University of Southampton Research Repository

Copyright © and Moral Rights for this thesis and, where applicable, any accompanying data are retained by the author and/or other copyright owners. A copy can be downloaded for personal non-commercial research or study, without prior permission or charge. This thesis and the accompanying data cannot be reproduced or quoted extensively from without first obtaining permission in writing from the copyright holder/s. The content of the thesis and accompanying research data (where applicable) must not be changed in any way or sold commercially in any format or medium without the formal permission of the copyright holder/s.

When referring to this thesis and any accompanying data, full bibliographic details must be given, e.g.

Thesis: Author (Year of Submission) "Full thesis title", University of Southampton, name of the University Faculty or School or Department, PhD Thesis, pagination.

Data: Author (Year) Title.

UNIVERSITY OF SOUTHAMPTON

FACULTY OF MEDICINE

Clinical & Experimental Sciences

VASCULAR DEMENTIA AND FAILURE OF INTRAMURAL PERIARTERIAL DRAINAGE – THE ROLE OF THE DYSTROPHIN ASSOCIATED PROTEIN COMPLEX

by

Matthew Thomas MacGregor Sharp

ORCID ID 0000-0002-6623-5078

Thesis for the degree of Doctor of Philosophy

OCTOBER 2020

UNIVERSITY OF SOUTHAMPTON

ABSTRACT

FACULTY OF MEDICINE

CLINICAL & EXPERIMENTAL SCIENCES

Thesis for the degree of Doctor of Philosophy

VASCULAR DEMENTIA AND FAILURE OF INTRAMURAL PERIARTERIAL DRAINAGE – THE ROLE OF THE DYSTROPHIN ASSOCIATED PROTEIN COMPLEX

By

Matthew Thomas MacGregor Sharp

Introduction: Cerebral small vessel disease (CSVD), a key aspect of vascular dementia (VaD), consists of pathological modifications to cerebral vessel walls and associated white matter lesions. Cerebral vessels have a dual function: perfusion of the brain and drainage of interstitial fluid and solutes along the walls of capillaries and arteries as Intramural Periarterial Drainage (IPAD). IPAD fails with age resulting in cerebral amyloid angiopathy (CAA), part of the spectrum of CSVD. Most animal models designed to study CAA are modified to overexpress amyloid proteins, but this is in contrast to the majority of CAA cases which occur due to a failure of clearance of soluble amyloid, rather than genetic mutations. The conduit for IPAD is the capillary and arterial basement membrane. This basement membrane is synthesised by cells of the vessel wall and its modification leads to a failure of IPAD and CAA. Polarised astrocytic extensions form end feet projections that encircle the abluminal side of the vessel wall attaching to basement membrane by the dystrophin associated protein complex (DPC), of which alpha dystrobrevin (α-DB) and aquaporin 4 (AQP4) are key components. Alterations to this complex disrupt the morphology of vessel walls, causing abnormalities to basement membranes and altering blood-brain barrier function.

This thesis aims to investigate the role of the DPC in the morphology and dynamics of IPAD pathways and to ascertain if mice with altered DPC can be used to model: 1) a failure of ISF fluid clearance by IPAD and 2) the features of CSVD and VaD. The following hypothesis are tested: 1) *In mice that do not express glial AQP4 the morphology of capillary IPAD pathways is altered; 2) In mice genetically modified* *for* α-DB*, the morphology and dynamics of IPAD pathways and cerebral perfusion are impaired.*

Methods: A detailed morphological study on the capillary wall from the white and grey matter in AQP4 and α-DB deficient mice was performed using quantitative electron microscopy and immunohistochemistry for collagen IV. The pattern of IPAD in white and grey matter was imaged and quantitatively measured in α-DB deficient and wild-type control mice. Cerebral perfusion under resting state and when challenged with hypercapnia was measured in α-DB deficient mice.

Results: 1) AQP4 deficient mice showed a reduction in the percentage surface area of basement membranes and an increase in the percentage surface area of intramural cells in the white matter. 2) In α-DB deficient mice, the percentage surface area occupied by basement membrane was increased in capillary walls in both grey and white matter, accompanied by an increased expression of collagen IV in the grey matter. 3) The pattern of IPAD in the grey matter of α-DB deficient mice showed fewer arterioles with fluorescent soluble Aβ in their walls compared to age matched controls. 4) Solutes from the normal white matter drain preferentially along the basement membranes of capillaries. 5) Absence of α-DB is associated with a normal perfusion but a lower capacity for adaptation to hypercapnia.

Conclusions. The results highlight an important role for α-DB and the DPC in maintaining the structural integrity of basement membranes, which is reflected in the capacity for draining interstitial fluid and solutes via IPAD. The localisation of AQP4 to astrocyte endfeet by its indirect association with α-DB and the DPC is not critical for the morphology of the basement membrane in the grey matter. As the capillary walls in the grey matter appear normal and the intramural cells in the white matter are enlarged, in contrast to the findings in human disease, AQP4 deficient mice do not replicate features of CSVD and may not be a suitable model for mechanistic insights into CSVD or VaD. Since this work highlighted that IPAD occurs preferentially along the capillary walls in the normal white matter with little involvement from arteries, it is important to consider the failure of IPAD as a key mechanistic feature of white matter hyperintensities. It remains to be seen if there are changes to α-DB and the DPC in the spectrum of CSVD in human brains, as this work points to it as a suitable model for further hypothesis-based studies of CSVD.

Table of Contents

List of Tables ... i

List of Figures ... iii

Research Thesis: Declaration of Authorship ... vii

Acknowledgements ... ix

Definitions and Abbreviations ... xi

Chapter 1 INTRODUCTION ... 1

1.1 Vascular dementia is the second most common type of dementia ... 3

1.1.1 Risk factors ... 4

1.1.2 Subtypes ... 5

1.1.2.1 Cerebral small vessel disease is a key feature of dementia and stroke ... 5

1.1.2.1.1 Cerebral small vessel disease: Cerebral amyloid angiopathy is represented by the deposition of amyloid protein ... 7

1.2 Vascular dementia and alterations to the blood-brain barrier and the vessel wall ... 11

1.2.1 The vessel wall: Endothelia ... 12

1.2.1.1 Endothelial disruption alters permeability of the blood-brain barrier ... 12

1.2.2 The vessel wall: Extracellular matrix ... 13

1.2.2.1 Extracellular matrix remodelling ... 15

1.2.3 The vessel wall: Pericytes ... 17

1.2.4 The vessel wall: Astrocytes ... 17

1.2.4.1 Astrocytes are anchored to the extracellular matrix by the dystrophin associated protein complex ... 18

1.2.4.2 Astrocytes and the transmembrane water channel aquaporin 4 ... 19

1.2.4.3 Aquaporin 4 is anchored to astrocyte cell membrane by the dystrophin associated protein complex ... 19

1.2.4.4 Targeting of aquaporin 4 to astrocyte endfeet is regulated by Dystrobrevin proteins ... 22

1.2.4.4.1 Beta dystrobrevin ... 23

1.2.4.4.2 Alpha dystrobrevin ... 24

1.2.4.4.3 Alpha dystrobrevin and Aquaporin 4 ... 24

1.3 Vascular dementia and fluid homeostasis ... 27

1.3.1 Regulation of cerebrospinal fluid (CSF) 27
1.3.1.1 Exchange of CSF with interstitial fluid (ISF)........ 27
1.3.2 Regulation of interstitial fluid 31
1.3.2.1 The intramural periarterial drainage pathway (IPAD) 31
1.3.2.1.1 The motive force for I intramural periarterial drainage pathway is derived from the contractions of smooth muscle cells within the walls of arteries 34
1.3.3 The role of Aquaporin 4 in fluid homeostasis in the brain........ 35
1.3.3.1 Aquaporin 4 responds to altered cerebral water homeostasis by the formation or prevention of oedema 35
1.3.3.1.1 Aquaporin 4 and cytotoxic oedema 36
1.3.3.1.2 Aquaporin 4 and vasogenic oedema 36
1.3.3.1.3 Aquaporin 4 and hydrocephalic oedema 37
1.3.4 Fluid homeostasis and the white matter abnormalities in vascular dementia 37
1.4 Modelling Vascular Dementia using animal models 42
1.4.1 Modelling macrovascular changes to cerebral blood vessels 42
1.4.1.1 Hypoperfusion 42
1.4.2 Modelling microvascular changes to cerebral blood vessels 43
1.4.2.1 Hypertension 43
1.4.2.2 Hyperhomocysteinemia........ 43
1.4.2.3 Vascular deposits of proteins as cerebral amyloid angiopathy 43
1.5 The potential of mice with altered dystrophin associated protein complex to model microvascular changes seen in cerebral small vessel disease........ 44
1.5.1 Altered structure and function of the endothelium and the blood-brain barrier 44
1.5.2 Altered fluid homeostasis 45
1.5.3 Basement membrane remodelling........ 46
1.5.4 Can mice with altered dystrophin associated protein complex be used to model intramural periarterial drainage to investigate its possible failure in vascular dementia? 48
1.6 Aims 49
1.7 Hypotheses 51
Chapter 2 MATERIALS & METHODS **53**

2.1 Animals 55
  2.1.1 Mice deficient for Aquaporin 4 (chapter 3) 55
  2.1.2 Mice deficient for Alpha dystrobrevin (B6;129-Dtna tm1Jrs/J) mice (chapters 4, 5 & 6) 55
    2.1.2.1 Genotyping mice deficient for alpha-dystrobrevin 56
      2.1.2.1.1 Preparation of mouse genomic DNA 56
      2.1.2.1.2 Polymerase chain reaction 57
2.2 Assessment of the capillary wall using transmission electron microscopy (chapters 3 and 4) 60
  2.2.1 Fixation of tissue for electron microscopy 60
  2.2.2 Preparing perfusion fixed brains for tissue processing 60
  2.2.3 Tissue processing for transmission electron microscopy 61
  2.2.4 Sectioning of processed tissue 62
  2.2.5 Imaging tissue sections for capillaries 63
  2.2.6 Calculating percentage surface area of the different components of the capillary wall 63
  2.2.7 Statistical analysis 63
2.3 Analysing the composition of the cerebrovascular basement membranes (chapter 4) 65
  2.3.1 Fixation of tissue for immunohistochemistry 65
  2.3.2 Tissue sectioning 65
  2.3.3 Enzyme linked immunohistochemistry for collagen IV 65
  2.3.4 Imaging for DAB staining of collagen IV 66
    2.3.4.1 Extracting regions of interest 66
    2.3.4.2 Analysing regions of interest for COL4 staining and vessel density 68
    2.3.4.3 Analysing regions of interest for vessel distribution and vessel specific COL4 staining 68
    2.3.4.4 Statistical analysis 69
2.4 Assessment of intramural periarterial drainage in alpha-dystrobrevin deficient mice (chapter 5) 73
  2.4.1 Stereotaxic injection of amyloid-beta (1-40) HiLyte Fluor 555 73
  2.4.2 Fixation of tissue and tissue sectioning for immunohistochemistry 75
  2.4.3 Tissue processing for immunohistochemistry 75
  2.4.4 Imaging tissue sections by confocal microscopy 75
  2.4.5 Assessment of intramural periarterial drainage 76

2.4.6 Statistical analysis 77

2.5 Assessment of cerebral blood flow in alpha-dystrobrevin deficient mice (chapter 6) 80

2.5.1 The Theory of arterial spin labelling 80

Chapter 3 LOSS OF AQUAPORIN 4 FROM ASTROCYTE ENDFEET AND THE MORPHOLOGY OF THE INTRAMURAL PERIARTERIAL DRAINAGE PATHWAY 83

3.1 Introduction 85
3.2 Hypothesis 87
3.3 Aims 88
3.4 Materials & methods 89
3.5 Results 90

3.5.1 Ultrastructural assessment of the capillary wall in grey and white matter in AQP4 deficient mice 90
3.5.2 Image segmentation and surface area measurements 93

3.5.2.1 Comparison of capillaries in white and grey matter in wild-type control mice 93
3.5.2.2 Comparison of capillaries in white and grey matter in AQP4 deficient mice 93
3.5.2.3 Comparison of capillaries in white and grey matter between wild-type control and AQP4 deficient mice 96
3.5.2.4 Comparison of vascular wall composition in capillaries from grey and white matter between wild-type control and AQP4 deficient mice 99

3.6 Discussion 101

3.6.1 AQP4 and grey mater 101
3.6.2 AQP4 and white matter 101
3.6.3 Conclusions 102

Chapter 4 LOSS OF ALPHA-DYSTROBREVIN FROM ASTROCYTE ENDFEET AND THE MORPHOLOGY OF THE INTRAMURAL PERIARTERIAL DRAINAGE PATHWAY 105

4.1 Introduction 107
4.2 Hypothesis 109
4.3 Aims 110
4.4 Materials & methods 111

4.4.1 Transmission electron microscopy 111
4.4.2 Immunohistochemistry 111

4.5 Results ... 112
  4.5.1 Ultrastructural assessment of the capillary wall in grey and white matter in alpha dystrobrevin deficient mice ... 112
  4.5.2 Image segmentation and surface area measurements ... 115
    4.5.2.1 Comparison of capillaries in white and grey matter in wild-type control mice ... 115
    4.5.2.2 Comparison of capillaries in white and grey matter in alpha dystrobrevin deficient mice ... 115
  4.5.3 Comparison of capillaries in white and grey matter between wild-type control and alpha dystrobrevin deficient mice ... 118
  4.5.4 Comparison of vascular wall composition in capillaries from grey and white matter between wild-type control and alpha dystrobrevin deficient mice ... 121
  4.5.5 Alterations to the biochemical composition of vascular basement membranes in alpha dystrobrevin deficient mice ... 123
    4.5.5.1 Comparison of the pattern of collagen IV staining between wild-type control and alpha dystrobrevin deficient mice ... 123
    4.5.5.2 Comparison of vessel density and amount of collagen IV staining between wild-type control and alpha dystrobrevin deficient mice ... 125
    4.5.5.3 Comparison of vessel distribution and amount of collagen IV staining in grey matter between wild-type control and alpha dystrobrevin deficient mice ... 129
4.6 Discussion ... 131
  4.6.1 The morphology of the blood-brain barrier is unaltered in young alpha dystrobrevin deficient mice ... 131
  4.6.2 The capillary basement membrane is thickened in alpha dystrobrevin deficient mice ... 131
  4.6.3 Why does removal of alpha dystrobrevin cause thickening of capillary basement membrane? ... 132
  4.6.4 Conclusions ... 133
Chapter 5 LOSS OF ALPHA-DYSTROBREVIN FROM ASTROCYTE ENDFEET AND THE DYNAMICS OF INTRAMURAL PERIARTERIAL DRAINAGE ... 135
5.1 Introduction ... 137
5.2 Hypotheses ... 140
5.3 Aims ... 141
5.4 Materials & methods ... 142

5.5 Results ... 143

5.5.1 Assessment of vessel density in grey and white matter ... 143

5.5.1.1 Wild-type control mice ... 143
5.5.1.2 Alpha dystrobrevin deficient mice ... 143
5.5.1.3 Wild-type and alpha dystrobrevin deficient mice – grey matter ... 144
5.5.1.4 Wild-type and alpha dystrobrevin deficient mice – white matter ... 144

5.5.2 Assessment of intramural periarterial drainage in the grey and white matter ... 147

5.5.2.1 Qualitative assessment ... 147
5.5.2.2 Quanitative assessment of IPAD between grey and white matter ... 152

5.5.2.2.1 Wild-type control mice ... 152
5.5.2.2.2 Alpha dystrobrevin deficient mice ... 152

5.5.2.3 Wild-type control vs. alpha dystrobrevin deficient mice ... 154
5.5.2.4 Assessment of fluorescent intensity of parenchymal amyloid beta ... 156

5.6 Discussion ... 159

5.6.1 The dynamics of intramural periarterial drainage in the white matter is different from that in the grey matter in wild-type control mice ... 159
5.6.2 The dynamics of intramural periarterial drainage are altered in alpha dystrobrevin deficient mice ... 160

5.6.2.1 Grey matter ... 160
5.6.2.2 White matter ... 161

5.6.3 Conclusions ... 162

Chapter 6 LOSS OF ALPHA-DYSTROBREVIN FROM ASTROCYTE ENDFEET AND CEREBRAL BLOOD FLOW ... 163

6.1 Introduction ... 165
6.2 Hypothesis ... 166
6.3 Aims ... 167
6.4 Materials & methods ... 168
6.5 Results ... 169

6.5.1 Assessment of resting cerebral blood flow ... 169
6.5.2 Assessment of cerebral blood flow in response to hypercapnia ... 170

6.6 Discussion ... 173

Chapter 7 GENERAL DISCUSSION ... 175

Redistribution of AQP4 in α-DB deficient mice has minimal effect on the IPAD pathway 180
The cerebral vasculature in α-DB deficient mice show signs of early ageing and reflect early changes seen in CAA 181
IPAD in the white matter is less efficient than that in the grey matter 183
IPAD is impaired in α-DB deficient mice 184
The removal of α-DB from the DPC of astrocyte endfeet is associated with normal perfusion but a lower capacity for adaptation to hypercapnia 186
Mice deficient for α-DB show potential as a model for the failure of IPAD in CSVD and VaD 187
Limitations and Future work 187
Overall summary, conclusions and implications 189

Appendix A List of Publications 191

Co-authored publications that include data generated as part of this thesis 193
Co-authored publications in which some of the data has been presented in the main introduction 193

Appendix B PUBLICATION - Demonstrating a reduced capacity for removal of fluid from cerebral white matter and hypoxia in areas of white matter hyperintensity associated with age and dementia 195
Appendix C METHOD FOR CEREBRAL BLOOD FLOW MEASUREMENTS USING ARTERIAL SPIN LABELLING 211

C.1 Aim 213
C.2 Method 213
C.3 Theory 213
C.4 Data Processing 215

List of References 217

List of Tables

Table 1: Comparison of capillary size metrics between grey and white matter in wild-type control mice 94

Table 2: Comparison of capillary size metrics between grey and white matter in AQP4 deficient mice 95

Table 3: Comparison of capillary size metrics between grey and white matter in wild-type control mice 116

Table 4: Comparison of capillary size metrics between grey and white matter in α-DB deficient mice 117

Table 5: Comparison of vessel density between grey and white matter in wild-type control and α-DB deficient mice 145

Table 6: Comparison of the density of vessels with fluorescent Aβ in their vessel walls between grey and white matter in wild-type control and α-DB deficient mice 153

Table 7: Comparison of area and mean pixel density of fluorescent amyloid beta remaining in the parenchyma of grey and white matter 157

List of Figures

Figure 1.1 Summary of the risk factors for vascular dementia and subtypes 5

Figure 1.2 Classification of lesions related to small vessel disease as per Wardlaw et.al. 6

Figure 1.3 Diagram of an arterial wall showing deposition of Aβ as cerebral amyloid angiopathy 9

Figure 1.4 The Modified Boston Criteria 10

Figure 1.5 The neurovascular unit 11

Figure 1.6 The extracellular matrix 14

Figure 1.7 Regional specific thickening of capillary basement membranes with age in wild-type mice 16

Figure 1.8 The structure of AQ4 21

Figure 1.9 Interactions of dystrophin associated proteins and AQP4 22

Figure 1.10 The structure of dystrobrevin 23

Figure 1.11 α-DB targets AQP4 to astrocyte endfeet 25

Figure 1.12 The dystrophin associated protein complex at astrocyte endfeet 26

Figure 1.13 The pathway in which nanoparticles enter the brain after injection into mouse CSF via cisterna magna 29

Figure 1.14 Arterioles in the midbrain have enlarged pial-glial basement membranes 30

Figure 1.15 The intramural periarterial drainage pathway 32

Figure 1.16 Flow of biotinylated Aβ 40 after injection into mouse hippocampus 33

Figure 1.17 The pattern of IPAD in the hippocampus after administration of the beta blocker Atenolol 34

Figure 1.18 Dilated perivascular space 39

Figure 1.19 The two leptomeningeal layers of the pial-glial basement membrane 40

Figure 1.20 Leptomeningeal layers form a distinct perivascular compartment that has the potential to expand forming dilated perivascular spaces 41

Figure 1.21 Summary of the microvascular changes observed in mice deficient for dystroglycan, AQP4, dystrophin and α-DB 47

Figure 2.1 Overview of the α-DB gene and its deletion in α-DB null (B6;129-Dtna tm1Jrs/J) mice 58

Figure 2.2 PCR results for the genotyping of α-DB null (B6;129-Dtna tm1Jrs/J) mice 59

Figure 2.3 Dissection of mouse brain for TEM analysis.................................. 62

Figure 2.4 Demarcation and analysis of components of the capillary wall....... 64

Figure 2.5 Sample sites for immunohistochemistry of collagen IV.................. 67

Figure 2.6 Custom macros used in Image J to analyse COL4 staining 70

Figure 2.7 Analysing regions of interest for number of vessels and COL4 staining.. 71

Figure 2.8 Analysing regions of interest for distribution of vessels and COL4 staining 72

Figure 2.9 Stereotaxic injection sites 74

Figure 2.10 Selection of regions of intertest for assessment of intramural periarterial drainage... 78

Figure 2.11 Assessment of the density of amyloid beta (1-40) in the parenchyma 79

Figure 3.1 AQP4 and its deletion from the dystrophin associated protein complex in astrocyte endfeet 88

Figure 3.2 The structural appearance of the capillary wall in the grey matter appears unaltered in mice deficient for AQP4..................... 91

Figure 3.3 The structural appearance of the capillary wall in the white matter appears unaltered in mice deficient for AQP4..................... 92

Figure 3.4 Summary of capillary size metrics in grey matter between wild-type control and AQP4 deficient mice... 97

Figure 3.5 Summary of capillary size metrics in white matter between wild-type control and AQP4 deficient mice.................................... 98

Figure 3.6 Summary showing overall mean values for the percentage of the vessel wall occupied by endothelium, intramural cells and basement membrane between wild-type control and AQP4 deficient mice in white and grey matter...................................... 100

Figure 4.1 alpha dystrobrevin and the dystrophin associated protein complex... 110

Figure 4.2 The structural appearance of the capillary wall in the grey matter appears altered in mice deficient for α-DB 113

Figure 4.3 The structural appearance of the capillary wall in the white matter appears altered in mice deficient for α-DB 114

Figure 4.4 Summary of capillary size metrics in grey matter between wild-type control and α-DB deficient mice 119

Figure 4.5 Summary of capillary size metrics in white matter between wild-type control and α-DB deficient mice 120

Figure 4.6 Summary showing overall mean values for the percentage of the vessel wall occupied by endothelium, intramural cells and basement membrane between wild-type control and α-DB deficient mice in white and grey matter 122

Figure 4.7 Immunostaining for COL4 in wild type control and α-DB deficient mice 124

Figure 4.8 Vessel density and COL4 staining per vessel between grey and white matter in wild-type control mice 126

Figure 4.9 Vessel density and COL4 staining per vessel between grey and white matter in α-DB deficient mice 127

Figure 4.10 Vessel density and COL4 staining per vessel in grey and white matter between wild-type control and α-DB deficient mice 128

Figure 4.11 Vessel distribution and COL4 staining in grey matter wild-type control and α-DB deficient mice 130

Figure 5.1 The IPAD pathway and accumulation of amyloid proteins as CAA 138

Figure 5.2 alpha dystrobrevin, the dystrophin associated protein complex and the intramural periarterial drainage pathway 141

Figure 5.3 Vessel density in grey and white matter between wild-type control and α-DB deficient mice 146

Figure 5.4 Composite tile scan of the distribution of Aβ injected into left hippocampus of wild-type control mice 148

Figure 5.5 Composite tile scan of the distribution of Aβ injected into left hippocampus of α-DB deficient mice 149

Figure 5.6 Composite tile scan of the distribution of Aβ injected into the corpus callosum of wild-type control mice 150

Figure 5.7 Composite tile scan of the distribution of Aβ injected into the corpus callosum of α-DB deficient mice 151

Figure 5.8 Comparison of the density of vessels with fluorescent Aβ in their vessel walls between wild-type control and α-DB deficient mice 155

Figure 5.9 Comparison of mean fluorescent area and mean pixel density of parenchymal fluorescent Aβ in grey and white matter between wild-type control and α-DB deficient mice 158

Figure 6.1 alpha dystrobrevin, the dystrophin associated protein complex and assessing cerebral blood flow 167

Figure 6.2 Assessment of cortical CBF between wild-type control and α-DB deficient mice 169

Figure 6.3 Assessment of hippocampal CBF between wild-type control and α-DB deficient mice 170

Figure 6.4 Visualisation of the relative change in cortical CBF in response to hypercapnia in wild-type control and α-DB deficient mice 171

Figure 6.5 Visualisation of the relative change in hippocampal CBF in response to hypercapnia in wild-type control and α-DB deficient mice.. 172

Research Thesis: Declaration of Authorship

Print name: Matthew MacGregor Sharp

Title of thesis: Vascular dementia and failure of intramural periarterial drainage – the role of the dystrophin associated protein complex

I declare that this thesis and the work presented in it are my own and has been generated by me as the result of my own original research.

I confirm that:

1. This work was done wholly or mainly while in candidature for a research degree at this University;
2. Where any part of this thesis has previously been submitted for a degree or any other qualification at this University or any other institution, this has been clearly stated;
3. Where I have consulted the published work of others, this is always clearly attributed;
4. Where I have quoted from the work of others, the source is always given. With the exception of such quotations, this thesis is entirely my own work;
5. I have acknowledged all main sources of help;
6. Where the thesis is based on work done by myself jointly with others, I have made clear exactly what was done by others and what I have contributed myself;
7. Parts of this work have been published as:-

MacGregor Sharp M, Saito S, Keable A, Gatherer M, Aldea R, Agarwal N, et al. Demonstrating a reduced capacity for removal of fluid from cerebral white matter and hypoxia in areas of white matter hyperintensity associated with age and dementia. Acta Neuropathol Commun. 2020;8(1):131.

Signature: ....Date: ....

Acknowledgements

This work is funded by a Stroke Association Priority Programme Award (PPA 2016/01, ARCP003059) entitled "Failure of drainage of fluid from the brain along the walls of blood vessels in vascular dementia". Tissue from aquaporin 4 deficient mice were kindly supplied by colleagues at Keio University, Japan. Mice deficient for alpha dystrobrevin were generated by colleagues in the Biomedical Research Facilities of the University of Portsmouth and the University of Southampton.

Unless specifically stated otherwise, all animal work, data analysis and interpretation of results was performed by myself, but I am extremely grateful for the help of James Lyles, who performed some of the electron microscopy (chapter 4), Jordan Cassidy who helped with immunohistochemistry (chapter 4) and Maureen Gatherer who has provided expert advice on all aspects of immunohistochemistry and performed confocal microscopy (chapter 5). Special thanks go to Jack wells and Yolanda Othene who kindly performed arterial spin labelling on alpha dystrobrevin deficient mice at University college London (chapter 6). I am grateful to David Johnston who has provided expert assistance with the confocal microscope and my mentor Professor Roxana Carare whose guidance, support and patience are valued enormously.

Finally, I would like to acknowledge my wife Helen, for her continuous encouragement, support, and strength. I would also like to say an enormous thank you to my daughter Harriet, her infectious smile and wicked sense of humour has helped me tremendously during some of the most challenging of times.

Definitions and Abbreviations

Aβ	Amyloid beta
α-DB	α-dystrobrevin
ACAS	Asymmetrical common carotid artery stenosis
AD	Alzheimer’s disease
APP	Amyloid precursor protein
AQP4	Aquaporin 4
BCAS	Bilateral common carotid artery stenosis
BMD	Becker muscular dystrophy
CAA	Cerebral amyloid angiopathy
CADASIL	Cerebral autosomal dominant arteriopathy with subcortical infarcts and leukoencephalopathy
COL4	Collagen IV
CNS	Central nervous system
CSF	Cerebrospinal fluid
CSVD	Cerebral small vessel disease
CT	computer tomography
DAB	3,3'-Diaminobenzidine
DMD	Duchenne muscular dystrophy
DNA	Deoxyribonucleic acid
DPC	Dystrophin associated protein complex
DP71	Dystrophin isoform 71
DPVS	Dilated perivascular space

ECM	Extracellular matrix
EDTA	Disodium ethylenediaminetetraacetic acid
HHcy	Hyperhomocysteinemia
HOTSHOT	Hot Sodium Hydroxide and Tris
ICP	Inter cranial pressure
IPAD	Intramural periarterial drainage
ISF	Interstitial fluid
KIR4.1	Potassium channel
LOX	Lysyl oxidase
MDX	Dystrophin deficient mice
MMP	Matrix metalloprotease
MPTP	1-methyl-4-phenyl-1,2,3,6-tetrahydropyridine
MRI	Magnetic resonance imaging
NAOH	Sodium hydroxide
NVU	Neurovascular unit
OAPS	Orthogonal array of particles
PCR	Polymerase chain reaction
PDZ	**P**ost synaptic density protein, **D**rosophila disc large tumor suppressor and **Z**onula occludens-1 protein
PBS	Phosphate buffered saline
PFA	Paraformaldehyde
PIPES	Piperazine-N,N’-bis(2-ethanesulfonic acid)
ROI	Region of interest
SHR	Spontaneously hypertensive rat

SHRSP	Spontaneously hypertensive stroke prone rat
SMC	Smooth muscle cells
TEM	Transmission electron microscopy
TGN-020	Inhibitor 2-(nicotinamide)-1,3,4-thiadiazole
TRIS-HCL	Tris (hydroxymethyl) aminomethane hydrochloride
VaD	Vascular dementia
WMH	White matter hyperintensities

Chapter 1 INTRODUCTION

1.1 VASCULAR DEMENTIA IS THE SECOND MOST COMMON TYPE OF DEMENTIA

The umbrella term “dementia” encompasses a wide range of neurodegenerative disorders characterised by a progressive decline in cognitive ability and capacity for independent living. It is a devastating disease that not only affects the individuals with the condition, but also friends and family who often have to respond to the changes in their loved ones needs while at the same time witnessing their decline. The disease has a large effect on wider society as sufferers of dementia require continual health and social care [1] and the economic burden is huge. In the UK, the current cost of dementia including healthcare, social care and unpaid care is £36.7 billion. This is predicted to rise by 172% to £94.1billion by 2040 [2].

Dementia is an ever-growing worldwide problem. The biggest risk factor is ageing and here lies the main issue: the world’s population is ageing. As of 2015, the worldwide population of people aged 60 or over was estimated to comprise over 900 million people. The number of people suffering from dementia was estimated to be around 47 million [3, 4]. As longevity and life expectancy continues to rise, this number is set to increase.

According to the World Alzheimer report 2019, almost 80% of the general public are concerned about developing dementia and there are currently no preventative measures [5]. In the UK, dementia is currently predicted to affect 883,100 people, increasing by 80% to 1,590,100 by 2040. Because of this, the UK and many other high-income countries now prioritise dementia for funding and research and have developed several specific plans and strategies to combat the health and social care burdens that arise from the condition.

Vascular dementia (VaD), the second most common type of dementia accounting for 17-20 % of all dementia patients [6] is the most severe form of vascular cognitive impairment (VCI), an umbrella term that is used to emphasise the vascular origins of cognitive deficits. VCI has recently been reconceptualised, with the severity of cognitive impairment subdivided into “minor” and “major (VaD)” divisions [7]. VaD is a mixed group of brain disorders in which cognitive abnormalities such as behavioural symptoms, locomotor abnormalities, dysarthria and autonomic dysfunction are attributable to pathological changes to the cerebrovasculature.

These include microvascular changes (e.g. arteriolosclerosis or microvascular protein deposition of amyloid, tau, alpha synuclein or TAR DNA-binding protein-43), macrovascular changes (e.g. atherosclerosis) and parenchymal changes (e.g. large and small infarcts, microinfarcts, haemorrhages or white matter abnormalities) [8]. VaD is associated with impaired cerebral blood flow (CBF) supplying the brain (hypoperfusion), that may or may not be associated with a stroke. The hippocampus, periventricular white matter and basal ganglia are particularly susceptible, with pathology in the basal ganglia strongly associated with the cognitive deficits typical of VaD [9].

1.1.1 RISK FACTORS

Similar to Alzheimer's disease (AD), ageing is the predominant risk factor for VaD. However, the incidence of VaD is higher in males. Age and vascular risk factors such as hypertension, diabetes, obesity, smoking and high plasma cholesterol [10] (**Figure 1.1**) lead to chronic hypoperfusion and thromboembolic events (development of a blood clot) that reduce CBF and perfusion. Impaired CBF initiates a cascade of hypoxic events that culminate in inflammation having a deleterious effect on the homeostasis of the brain. An example of this is the activation of matrix metalloproteinases which degrade vascular extracellular matrix and tight junction proteins to open the blood-brain barrier. This results in vasogenic oedema that in the white matter damages myelinated fibres [11, 12].

Alterations to cerebral perfusion correlates with severity of dementia and can be used as an indicator of disease progression [13, 14]. However, VaD is relatively under-diagnosed and treatment options are hampered by poor mechanistic understanding and identification of therapeutic targets [15].

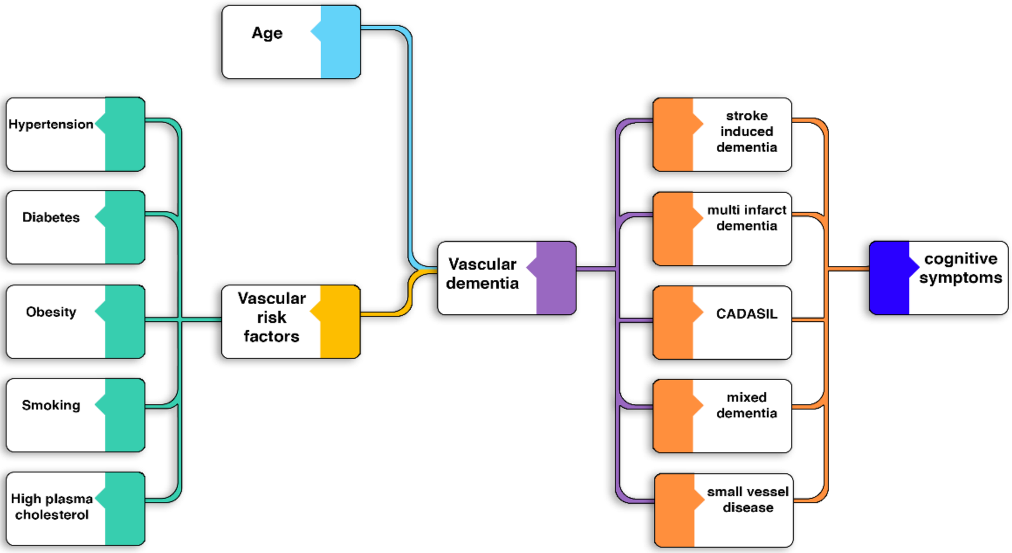
Age
Hypertension
Diabetes
Obesity
Smoking
High plasma cholesterol
Vascular risk factors
Vascular dementia
stroke induced dementia
multi infarct dementia
CADASIL
mixed dementia
small vessel disease
cognitive symptoms

Figure 1.1 Summary of the risk factors for vascular dementia and subtypes

1.1.2 SUBTYPES

Several subtypes of VaD have been classified including: (1) stroke induced dementia; (2) multi infarct dementia; (3) CADASIL (cerebral autosomal dominant arteriopathy with subcortical infarcts and leukoencephalopathy) and (4) mixed dementia [9] (**Figure 1.1**). However, the most prevalent cause of VaD is cerebral small vessel disease (CSVD), a syndrome of clinical, cognitive, neuroimaging and neuropathological findings arising from pathology of perforating cerebral arterioles, capillaries and venules [16].

1.1.2.1 CEREBRAL SMALL VESSEL DISEASE IS A KEY FEATURE OF DEMENTIA AND STROKE

CSVD forms a central pathway in the pathogenesis of dementia and stroke, accounting for one fifth of all strokes worldwide [17] and more than 90% of cases of intracerebral haemorrhage, the most devastating form of stroke [16]. Of an estimated 47 million people suffering from dementia globally [3, 4], 45% have CSVD as a major contributing pathology [18].

Current neuroimaging techniques used in clinical practice are restricted to the parenchymal lesions caused by CSVD and cannot easily visualise the small vessels in the brain. Therefore, the term CSVD is best used to describe the pathological consequences on the brain parenchyma. The exact aetiology of the vessels involved is not fully understood and subsequently, there are no efficient therapies for the syndrome, other than trying to manage metabolic and cardiovascular risk factors, of which age and hypertension are the most prevalent [19]. Nevertheless, diagnosis can be confirmed by neuroimaging the parenchymal lesions by magnetic resonance imaging (MRI) in both white and subcortical matter. A recent paper by Wardlaw et.al [20] (**Figure 1.2**) has classified these lesions as:

1. recent small subcortical infarcts (formerly categorized as acute lacunar stroke);
2. white matter hyperintensities (WMH) of presumed vascular origin;
3. lacunae (small fluid cavities in the brain) of presumed vascular origin;
4. cerebral microbleeds;
5. dilated perivascular spaces (DPVS);
6. brain atrophy.

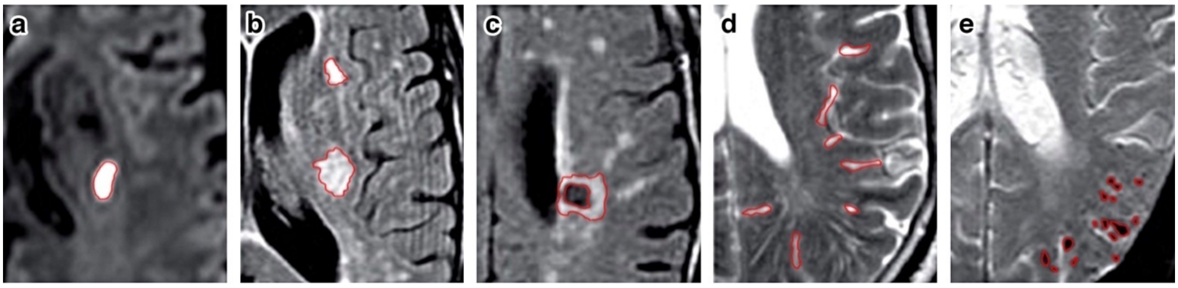

Figure 1.2 Classification of lesions related to small vessel disease as per Wardlaw et.al.

Lesions (highlighted in red) are classified as recent small subcortical infarcts (a), white matter hyperintensities (b), lacunae (c), dilated perivascular spaces (d) or cerebral microbleeds (e). Images adapted from [20]

Further classification has been suggested by Pantoni L [16] in an attempt to summarise the many different forms of CSVD into six different subtypes:

- Type 1 – deep perforator arteriopathy (arteriolosclerosis);
- Type 2 - sporadic and inherited cerebral amyloid angiopathy;
- Type 3 - inherited or genetic small vessel disease distinct from cerebral amyloid angiopathy;
- Type 4 - inflammatory and immunologically mediated small vessel diseases;
- Type 5 - venous collagenosis;
- Type 6 - other small vessel diseases.

Ultimately, progressive vascular age-related changes to vessels such as deep perforator arteriopathy (arteriolosclerosis) and cerebral amyloid angiopathy (CAA) alters cerebral blood flow and perfusion to deep brain structures. This causes lacunar infarcts (small areas (< 15mm) of loss of brain parenchyma traversed by fibrous strands) and microinfarcts (small strokes < 1mm in size) that are damaging to the blood-brain barrier and surrounding parenchyma [21, 22].

1.1.2.1.1 CEREBRAL SMALL VESSEL DISEASE: CEREBRAL AMYLOID ANGIOPATHY IS REPRESENTED BY THE DEPOSITION OF AMYLOID PROTEIN

CAA is represented by the deposition of amyloid proteins including amyloid beta (Aβ), cystatin C, prion protein, ABri/Adan, transthyretin, gelsolin and immunoglobulin light chain amyloid [23] in the walls of blood vessels. The vast majority (80% - 90%) of AD cases have CAA as a key pathological feature [24]. The disease can be sporadic, and associated with ageing, or hereditary and associated with various genetic mutations such as Down syndrome [25]. Typical characteristics include progressive accumulation of congophilic amyloid peptides of different amino acid lengths in the walls of leptomenigeal arteries, arterioles located in the cortex, capillaries and venules [16, 26] (**Figure 1.3**). Pathology is mainly observed in the occipital lobe and to a lesser extent in the hippocampus, cerebellum and basal ganglia. Deep central grey matter, subcortical white matter and brain stem are unaffected or involved in the final stages [27].

The exact aetiology of CAA is unclear. The most widely accepted amyloid cascade hypothesis suggests that an overproduction of Aβ is responsible. Indeed, several animal models have been developed that show this. The Swedish amyloid precursor protein (APP) transgenic mouse [28] for instance, has been genetically modified for the human APP by mimicking a mutation first identified in a Swedish family who were predisposed to developing early onset AD. This mutation leads to a 3 – 6 fold increase in the production of Aβ [29] and the mice go on to develop both parenchymal and vascular amyloid deposits [30]. Family forms of AD have known genetic mutations that increase extracellular concentrations of amyloid proteins [31]. While the amyloid cascade hypothesis may explain the pathology observed in the familial form of AD, the hypothesis does not explain the occurrence of CAA in sporadic non-familial AD, the most common form, where there is no evidence of Aβ overproduction [32]. This deviation from the amyloid hypothesis suggests that the deposition of Aβ as CAA could be due to an imbalance between its production and elimination [33, 34]. This theory is supported by the work of Mawuenyega *et.al.,* in which the development of CAA is shown to be most likely driven by failures of the clearance mechanisms of Aβ rather than its overproduction [35]. Such clearance mechanisms include phagocytosis of Aβ by glial cells [36-38]; carrier mediated transport of Aβ across the endothelium into the blood [39] and drainage of soluble Aβ within the interstitial fluid (ISF) along intramural periarterial drainage (IPAD) pathways.

Vessels laden with amyloid show severe ultrastructural abnormalities and alterations to the endothelium [40, 41], smooth muscle cells (SMC) [41, 42] and pericytes [27]. Until recently, definite diagnosis could only be made by the neuropathological grading of the severity of amyloid pathology (mild, moderate or severe) in tissue taken at autopsy or from a cortical biopsy [43]. In mild CAA, amyloid appears as a congophilic rim restricted around SMCs occurring initially in the outer portion of the tunica media. Vessels appear relatively normal with some loss of SMC nuclei [27]. In moderate CAA, amyloid is deposited throughout the tunica media with loss of SMC but no evidence of haemorrhage [27]. In severe CAA, amyloid is extensively deposited within the cerebrovasculature with focal fragmentation of the vessel wall and evidence of haemorrhage [27].

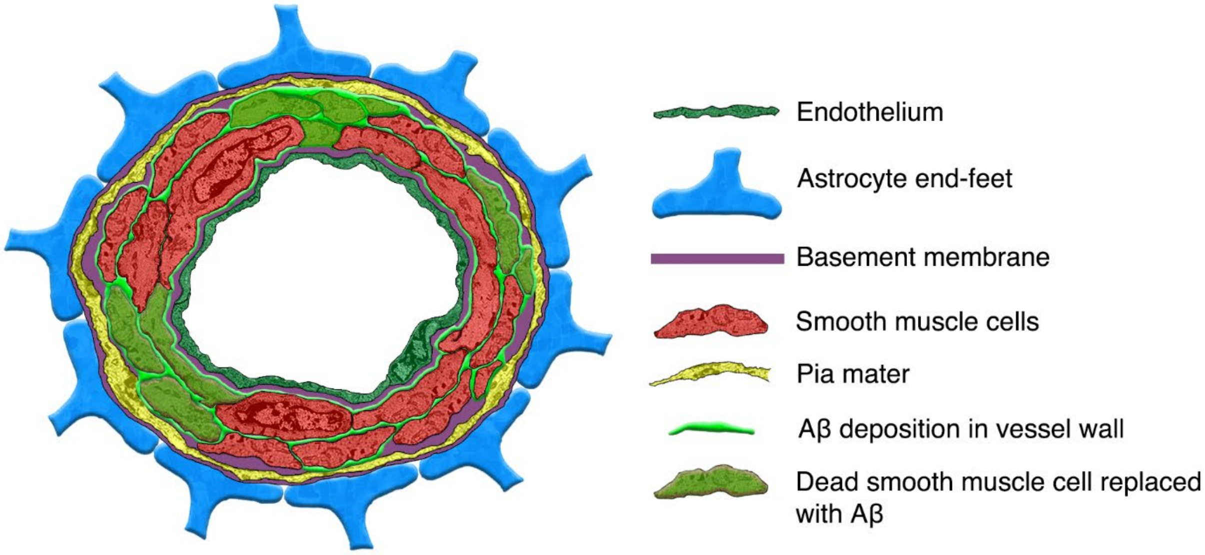
Endothelium
Astrocyte end-feet
Basement membrane
Smooth muscle cells
Pia mater
Aβ deposition in vessel wall
Dead smooth muscle cell replaced with Aβ

Figure 1.3 Diagram of an arterial wall showing deposition of Aβ as cerebral amyloid angiopathy

In CAA, progressive accumulation of congophilic amyloid peptides (green) of different amino acid lengths occurs in the walls of leptomenigeal arteries, arterioles located in the cortex and capillaries and venules. In mild CAA, amyloid appears as a congophilic rim restricted around SMCs. In moderate CAA, amyloid is deposited throughout the tunica media with loss of SMC. In severe CAA, amyloid is extensively deposited within the cerebrovasculature with focal fragmentation of the vessel wall.

Due to a lack of sensitive diagnostic in vivo techniques, it is difficult to detect CAA early. More recently, advancements in imaging techniques coupled with an increase in awareness of the different acute and progressive clinical syndromes has enabled the creation of diagnostic criteria for CAA known as the Modified Boston criteria [44]. Diagnosis can now be made based on four different severities of disease: 1) definite CAA, 2) probable CAA with supporting pathology, 3) probable CAA and 4) possible CAA (**Figure 1.4**).

The Modified Boston criteria has increased detection of the disease during life but CAA is still a leading causes of CSVD, occurring in approximately half of elderly individuals and up to 90% of AD cases [24].

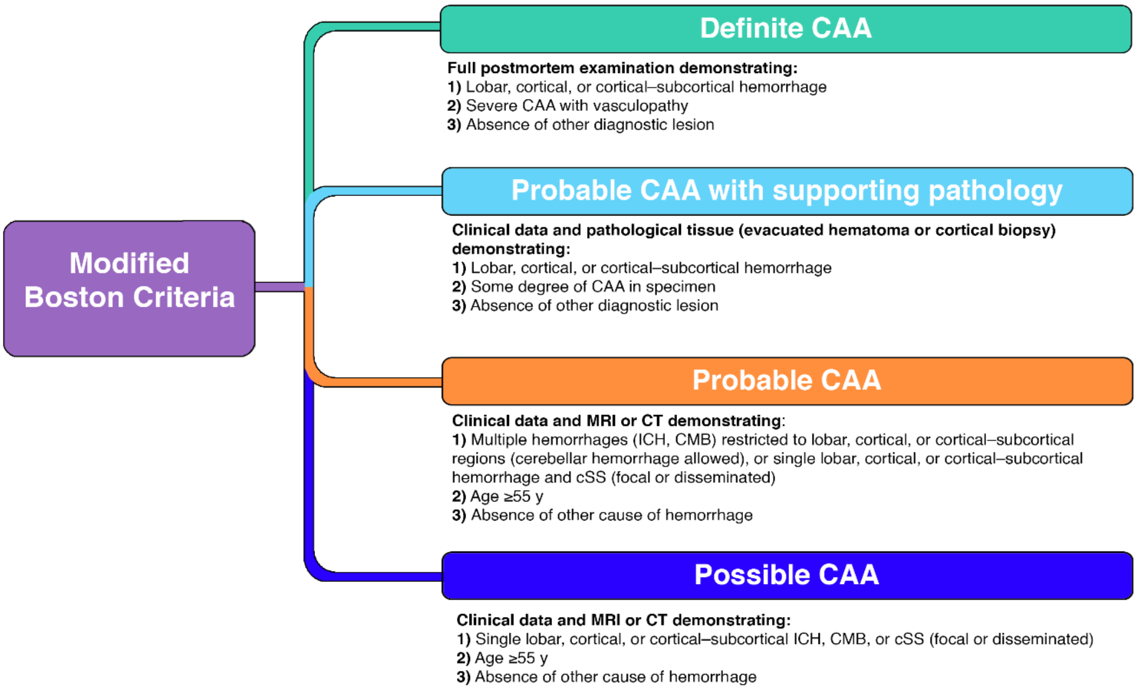

Full postmortem examination demonstrating:
1) Lobar, cortical, or cortical–subcortical hemorrhage
2) Severe CAA with vasculopathy
3) Absence of other diagnostic lesion

Clinical data and pathological tissue (evacuated hematoma or cortical biopsy) demonstrating:
1) Lobar, cortical, or cortical–subcortical hemorrhage
2) Some degree of CAA in specimen
3) Absence of other diagnostic lesion

Clinical data and MRI or CT demonstrating:
1) Multiple hemorrhages (ICH, CMB) restricted to lobar, cortical, or cortical–subcortical regions (cerebellar hemorrhage allowed), or single lobar, cortical, or cortical–subcortical hemorrhage and cSS (focal or disseminated)
2) Age ≥55 y
3) Absence of other cause of hemorrhage

Clinical data and MRI or CT demonstrating:
1) Single lobar, cortical, or cortical–subcortical ICH, CMB, or cSS (focal or disseminated)
2) Age ≥55 y
3) Absence of other cause of hemorrhage

Figure 1.4 The Modified Boston Criteria

Definite CAA (green), probable CAA with supporting pathology (light blue), probable CAA (orange) and possible CAA (dark blue). Adapted from [44].

1.2 VASCULAR DEMENTIA AND ALTERATIONS TO THE BLOOD-BRAIN BARRIER AND THE VESSEL WALL

The blood-brain barrier is a multicellular structure separating the central nervous system (CNS) from the peripheral blood circulation. As well as a barrier function to toxins and pathogens the blood-brain barrier regulates the influx and efflux of ions, nutrients and oxygen between the blood and brain parenchyma by fine interplay between the endothelium (the core anatomical unit of the blood-brain barrier) and elements of the neurovascular unit (NVU). The NVU is a conceptual model that describes the functional interactions and signalling between neurons, capillaries and glia consisting of cellular (neurons, microglial cells, astrocytes and pericytes) and noncellular (extracellular matrix) elements (**Figure 1.5**) [9, 45]. In VaD, pathological changes to the vascular wall alter the integrity and function of the blood-brain barrier [46].

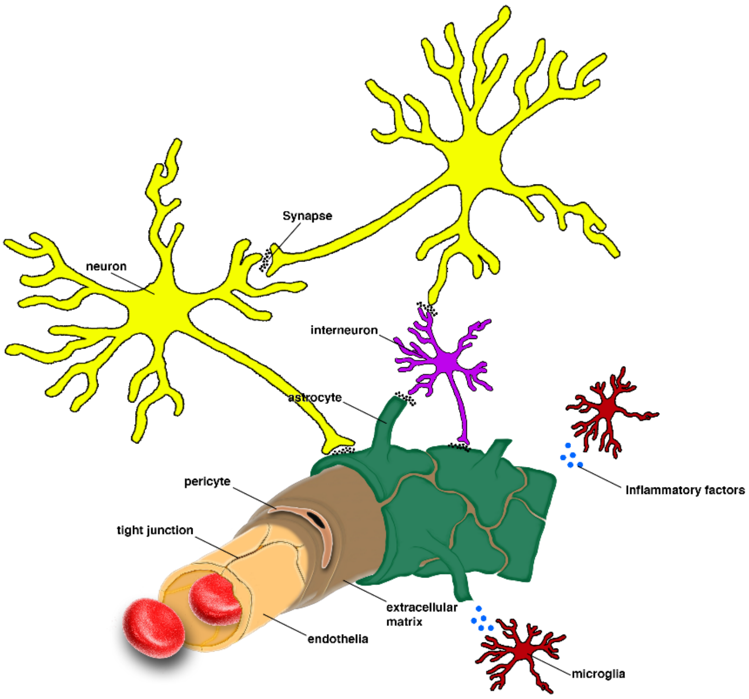
Synapse
neuron
interneuron
astrocyte
pericyte
tight junction
Inflammatory factors
extracellular matrix
endothelia
microglia

Figure 1.5 The neurovascular unit

The NVU consists of endothelia, neurons, microglial cells, astrocytes, pericytes and extracellular matrix (not drawn to scale).

1.2.1 THE VESSEL WALL: ENDOTHELIA

Cerebral endothelia, the core anatomical element of the blood-brain barrier, are highly specialised cells with specific transport receptor proteins [47], high electrical resistance tight junctions and no fenestrations [48]. Lipid-soluble molecules of < 180 Da in size with fewer than 10 hydrogen bonds diffuse passively across the endothelia [49] but tight junctions between neighbouring endothelial cells restrict paracellular diffusion of ions and macromolecules [48]. Instead, essential nutrients like glucose and fatty acids require carrier mediated transport. For example, glucose is transported via the solute carrier transporter GLUT1 [47]. Endothelial cells also release nitric oxide, which reduces contractile tone of SMCs, and the vasoconstrictor endothelin 1 [50].

1.2.1.1 ENDOTHELIAL DISRUPTION ALTERS PERMEABILITY OF THE BLOOD-BRAIN BARRIER

Disruption to normal endothelial function, as is the case in VaD during ischemic stroke and chronic neurodegeneration and in several other neurological diseases such as epilepsy or neuromyelitis [46] leads to leakage of fluid, macromolecules and migration of cells into the vessel wall. This inhibits normal blood-brain barrier regulation of leukocyte trafficking in response to brain infection and immune surveillance [51] or after damage to brain tissue in which macrophages are required to clear debris [52]. Oxidative stress induced damage to endothelia, initiated by chronic hypoperfusion and thromboembolic events, alters mitochondrial function and the balance of antioxidants and reactive oxygen species. Oxidative stress acts as a catalyst by initiating further reductions in CBF [53] and the triggering of inflammatory cascades. Inflammatory events perpetuate endothelial damage, further disrupts permeability of the blood-brain barrier and cause infarcts leading to fibrinoid necrosis (tissue death with accompanying accumulation of proteinaceous material with a staining pattern similar to fibrin) [54]. This results in damage to arteriole SMCs, fibrin deposition, perivascular oedema and damage to surrounding parenchyma [55]. This is typically seen as expansion of perivascular spaces in the white matter with pallor of adjacent myelin and astrocytic gliosis. Deep cerebral structures and white matter are particularly susceptible as vessels within these regions include end arteries with very little branching [8].

1.2.2 THE VESSEL WALL: EXTRACELLULAR MATRIX

Extracellular matrix (ECM) is formed of glycoproteins and proteoglycans that ensheath the abluminal side of endothelia separating the endothelia from pericytes and pericytes from astrocytes, forming basement membranes between different cell types [56]. Each cell type of the vessel wall contributes to the composition of the ECM producing structural and functional diversity between the basement membranes of different vessel types [57]. Basement membranes consist of highly crosslinked complexes of collagen IV (COL4), laminin, nidogen/entactin and heparin sulphate proteoglycan catalysed by the activity of Lysyl oxidase (LOX). Both COL4 and laminin are critical for basement membrane stability and can self-assemble into sheet like structures interacting with each other by nidogen/entactin. However, LOX, an ECM amine oxidase that converts amines into aldehdyes, forms covalent crosslinks between fibrillar collagens and elastins ensuring ECM structural integrity [58] (**Figure 1.6**).

Cells interact with the ECM by the association of the transmembrane proteoglycan dystroglycan and integrin adhesion receptors with laminin networks [59]. Dystroglycan is expressed in astrocytes, neurons and endothelial cells. Integrins are present on all cell types involved in the formation of the blood-brain barrier. These matrix receptors regulate signalling pathways but also anchor cells in place regulating their motility (reviewed in [60]). During ischemic events, such as those caused by occlusion of the middle cerebral artery in mice, expression of astrocyte dystroglycan and select integrins (e.g. $\alpha_6\beta_4$) are significantly reduced. This correlates with loss of dystroglycan expression in primary astrocytes subject to oxygen-glucose deprivation [61] and is thought to be associated with loss of integrity between the astrocyte and vessel wall in response to ischemia [62].

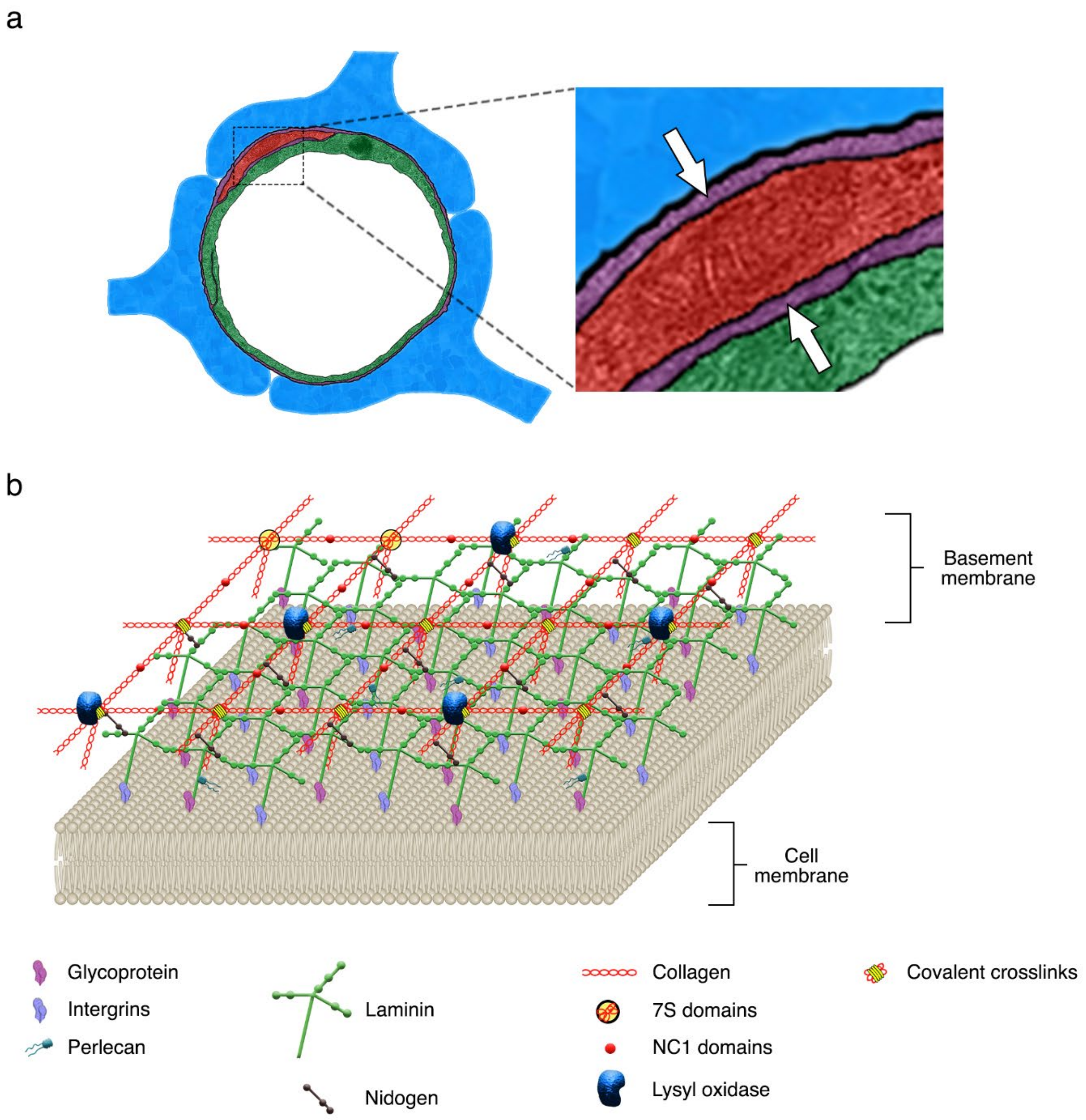
a
b
Basement membrane
Cell membrane
Glycoprotein
Intergrins
Perlecan
Laminin
Nidogen
Collagen
7S domains
NC1 domains
Lysyl oxidase
Covalent crosslinks

Figure 1.6 The extracellular matrix

Schematic diagram of a typical cerebral capillary (a). Basement membrane (purple) align along the abluminal side of endothelia (green) separating endothelia from pericytes (red) and pericytes from astrocytes (blue) (white arrows in enlarged inset in a). Basement membranes consist of highly crosslinked complexes of collagen IV, laminin, fibronectin, nidogen/entactin, and heparan sulphate proteoglycans (b). Lysyl oxidase reinforces collagen IV networks by forming covalent crosslinks at 7S domains. Diagram b adapted from [63, 64].

1.2.2.1 EXTRACELLULAR MATRIX REMODELLING

Ageing, the predominate risk factor for VaD, causes remodelling of the extracellular matrix. This has been observed as basement membrane splitting, duplication, thickening and presence of abnormal inclusions in ageing animal models and old human brains [65, 66]. Prominent fibrosis of the basement membrane, associated with severe degeneration of vascular SMCs [15, 67] has been linked to upregulation of COL4 [68, 69] and alterations to other key ECM proteins [70].

Expression of ECM proteins that directly interact with Aβ appear to be altered in CSVD creating an environment that favours the development of CAA. These proteins either promote Aβ aggregation (perlecan, fibronectin and agrin) [71, 72] or inhibit Aβ accumulation by destabilising its fibrilisation (laminin / nidogen and COL4) [73]. Studies of the changes to the ECM in the development of CAA in AD show that in the early stages of the disease, thickening of the basement membrane [74] is accompanied by increased levels of COL4, perlecan and fibronectin [70]. In latter stages, COL4 is reduced [75] and heparin sulphate proteoglycans such as agrin are increased [76, 77], promoting Aβ aggregation. We have previously shown a region-specific thickening of capillary basement membranes in aged mice occurring in areas more affected by CAA such as the cortex (young - 65.79 μm vs. old – 97.49 μm, $p < 0.05$) and hippocampus (young - 62.48 μm vs. old – 109.50 μm, $p < 0.05$) [74] (**Figure 1.7**).

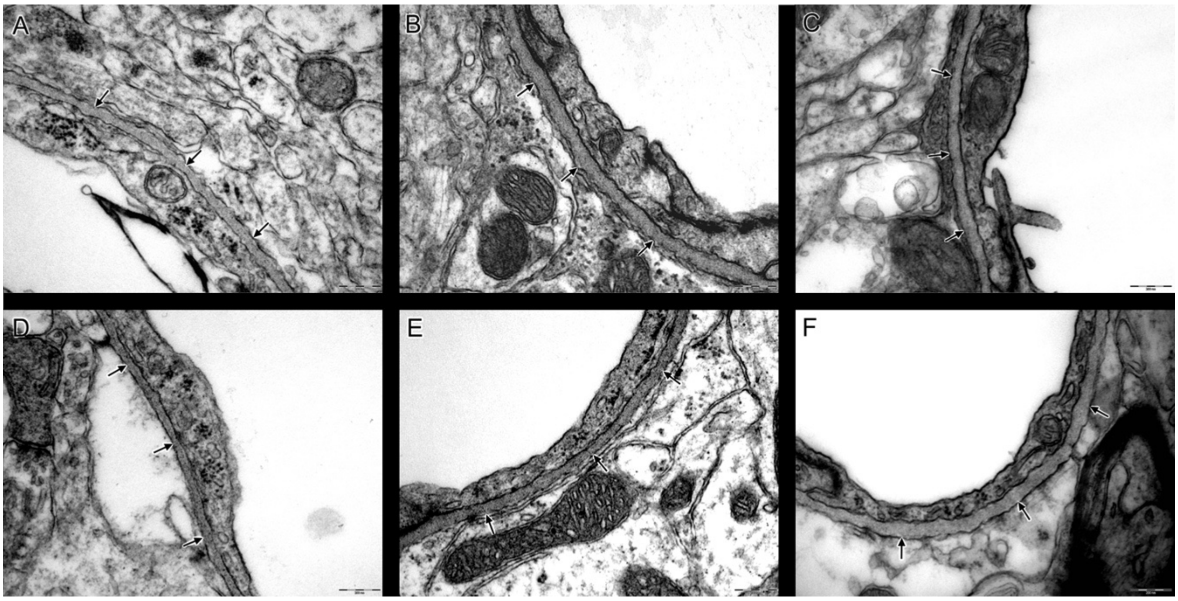

Figure 1.7 Regional specific thickening of capillary basement membranes with age in wild-type mice

Transmission electron micrographs showing regional differences in the thickness of capillary basement membranes (arrows) in 2 (A and D), 7 (B and E), and 23 (C and F) month-old mice between striatum (A-C) and frontoparietal cortex (D–F). Note the significant thickening of the capillary basement membrane in 23-month old mice in the cortex (F) compared to young 2-month-old mice (D). Original magnification = ×50 000. Published in [74].

1.2.3 THE VESSEL WALL: PERICYTES

Pericytes project stellate-shaped finger like elongated processes that ensheath the capillary wall connecting with endothelial membranes via direct peg-and socket contacts. These contacts contain cell-to-cell junction proteins enabling transfer of metabolites and ions between the two cell types (reviewed in [78]). Pericytes contribute to the integrity of the vessel wall by helping to regulate capillary diameter, CBF and levels of ECM proteins (reviewed in [48]). Pericytes have also been shown to mediate polarisation of astrocytic endfeet by helping to guide astrocyte foot processes to cerebral vessel walls [79]. Injury and degeneration of pericytes is associated with a breakdown of the blood-brain barrier in many neurological diseases including amyotrophic lateral sclerosis, AD, mild dementia and stroke (reviewed in [80]). Recent evidence from human post-mortem studies demonstrate a 35-45% reduction of pericytes in the white matter of VaD or AD [81].

1.2.4 THE VESSEL WALL: ASTROCYTES

Polarised astrocytic extensions form end feet projections that encircle the abluminal side of the vessel wall [45] interacting with intramural cells, extracellular matrix and the endothelium. Interaction with the endothelium is important for synchronising metabolite levels with CBF and vasodilation, and regulating brain water homeostasis [82]. Astrocytes contribute to normal function in the healthy CNS, including regulation of blood flow, participation in synaptic function and plasticity, and maintenance of the extracellular balance of ions, fluid balance and transmitters. They also respond to CNS insults caused by infection, trauma, ischemia and neurodegenerative disease by reactive astrogliosis and glial scar formation (reviewed in [83]). Glial scar formation enables repair to damaged elements of the blood-brain barrier, limits neuronal death, inhibits entry of inflammatory cells into the brain [84-86] but also impairs axonal regeneration [87]. Astrocytes contribute to the integrity of the blood-brain barrier by releasing several effector molecules that enhance and maintain barrier tightness [88-90].

Astrocytes are affected by ageing, changing to a more proinflammatory phenotype [91] that may contribute to decline in brain function by loss of function and neuroinflammation. Furthermore, oxidative stress has been shown to affect astrocytes in parallel to that seen in endothelium [92]. For an extensive overview of possible roles of astrocytes in CSVD see [93].

1.2.4.1 ASTROCYTES ARE ANCHORED TO THE EXTRACELLULAR MATRIX BY THE DYSTROPHIN ASSOCIATED PROTEIN COMPLEX

The cell membrane of astrocyte endfeet are anchored to endothelial or intramural cell ECM via components of a structurally unique protein complex that is associated with dystrophin protein (dystrophin associated protein complex (DPC)). DPCs are expressed in a variety of tissue types such as skeletal muscle, neurons and glia [94, 95]. The complex consists of the transmembrane matrix receptor dystroglycan, the intracellular proteins dystrophin and its associated dystrobrevins and syntrophins and localised transmembrane proteins such as the aquaporins (AQP) (**Figure 1.12**).

In skeletal muscle, DPCs afford structural integrity to muscle fibres by binding the ECM to the actin cytoskeleton. When this binding is compromised, muscle fibres become dystrophic. The most widely known of the muscle dystrophies are the Duchenne muscular dystrophy (DMD) and its milder form Becker muscular dystrophy (BMD). DMD and BMD are linked to X-linked recessive mutations in the dystrophin gene [96] that generates DPCs that either lack dystrophin entirely (DMD) or have a partially functioning dystrophin component (BMD). In both cases, dystrophic changes in muscle including muscle fibre degeneration and regeneration lead to loss of muscle function.

In the brain, different dystrophin isoforms and DPCs can be found in neurones and glia associated with astrocytic endfeet and GABA receptor clusters in cerebellar Purkinje cells and pyramidal neurons of the neocortex and hippocampus (reviewed in [95]). DPCs are thought to play a role in modulating synaptic function and approximately one third of DMD and BMD cases present with mild to moderate cognitive impairment [97]. While mutations in any part of the dystrophin gene can result in cognitive impairment, distal mutations affecting the dystrophin isoforms DP140 and DP71 appear to be most correlated [98, 99]. Language development is delayed, and IQ is diminished by one standard deviation compared to controls. Boys with DMD are more at risk of developing autism, obsessive compulsive disorder and attention-deficit / hyperactivity disorder [100].

In perivascular astrocytes, dystrophin is mainly expressed in the shorter DP71 isoform. DP71 contains binding sites for β-dystroglycan, the dystrobrevins and syntrophins. β-dystroglycan interacts with α-dystroglycan which in turn anchors the astrocyte end foot to the ECM by binding to a number of ECM proteins including laminins, perlecan, agrin and the neurexins. Attachment of the astrocyte end foot to the ECM is disrupted in mice deficient for the dystrophin protein suggesting a key role of the DPC in maintenance of the basement membrane [101] (**Figure 1.12).**

1.2.4.2 ASTROCYTES AND THE TRANSMEMBRANE WATER CHANNEL AQUAPORIN 4

Aquaporin 4 (AQP4) is the predominant AQP in mammalian brain expressed in astrocyte endfeet bordering the ventricles, subarachnoid space, blood vessels, non-endfeet glial processes of the granule cell layer in the cerebellum [102] and to a lesser extent in both adluminal and abluminal endothelial cell membranes [103].

AQP4 expression is upregulated in conditions that alter brain water homeostasis. Elevated levels of AQP4 have been observed in brain tumours [104, 105], cerebral ischemia (including stroke) [106, 107], traumatic brain injury [108] and dementia and other age related pathologies [109-114]. A recent study has shown elevated expression of AQP4 in grey mater from autopsied temporal lobes from eight patients with AD [114]. We have recently shown that in humans AQP4 expression is upregulated in both grey and white matter with normal ageing. However, in cases of moderate CAA, the percentage area immunostained for AQP4 in grey matter is significantly higher compared to age matched controls. In the white matter, the expression of AQP4 expression was reduced in CAA and in tissue from brains that had WMH, suggesting a loss of function of this channel in CSVD [115].

Expression of AQP4 in the white matter of experimental models of stroke and after focal ischemic stroke frequently accompanied by life-threatening cerebral edema in post mortem human brains [116] suggest an involvement of AQP4 in oedema resolution [117]. It has also been proposed that AQP4 expression on astrocytic endfeet represents a pathway in which AQP4 drives a directional clearance of solutes from the ISF into paravenous spaces via extracellular spaces [118]. This has been termed glymphatic flow and is discussed more in section 1.3.

1.2.4.3 AQUAPORIN 4 IS ANCHORED TO ASTROCYTE CELL MEMBRANE BY THE DYSTROPHIN ASSOCIATED PROTEIN COMPLEX

The distribution of AQP4 is polarised and particularly concentrated in the astrocytic endfeet that abut capillaries, the ependymal cells lining the ventricles and the pia [102].

Extensive studies using electron and X-ray crystallography of 2D crystals and 3D crystals, respectively, has revealed the tetrameric arrangement of AQP4. Typically, an AQP monomer contains six transmembrane helical segments oriented in a right-handed bundle. This produces funnel shaped cytoplasmic and extracellular vestibules interconnected by a 1.5 Å central pore, just large enough to allow the passage of a single file of hydrogen bonded water molecules [119-121]. This enables AQPs to respond to changes in osmotic gradients by facilitating passive water transport or sometimes small uncharged solutes, as the case with aquaglyceroporins, across cell plasma membranes. A detailed description of the structural basis of water transport through AQPs is explained in [122].

AQP4 tetramers contain ~30kDa monomeric units that have eight membrane embedded helical segments (M1 – M8), six of which are membrane spanning (M1 – 2, M4 – M6, M8) and two which form shorter segments with an aqueous pore (M3 and M7) all connected by five loops (loops a - e) [121] (**Figure 1.8**). Seven AQP4 isoforms have been identified in astrocytes (AQP4a – f) [123]. The two main isoforms, Met1 (AQP4a or AQP4M1) and Met23 (AQP4c or AQP4M23) [124] form higher order supramolecular assemblies (OAPs) [125] on astrocytic endfeet, first observed in 1974 by the freeze fracture analysis of astrocytic plasma membranes [126]. OAPs appear as distinctive rectangular particle array assemblies each containing 4 – 60 subunits packed in an orthogonal array with a periodicity of 6 – 7 nm [126]. They contain both AQP4M1 and AQP4M23 but only AQP4M23 can form independent orthogonal lattices [127]. OAPs can be immunogold labelled with antibodies to AQP4 [125] and identified by photoactivation localisation microscopy [128] but they are absent in astrocyte plasma membranes in mice that do not express AQP4 [129].

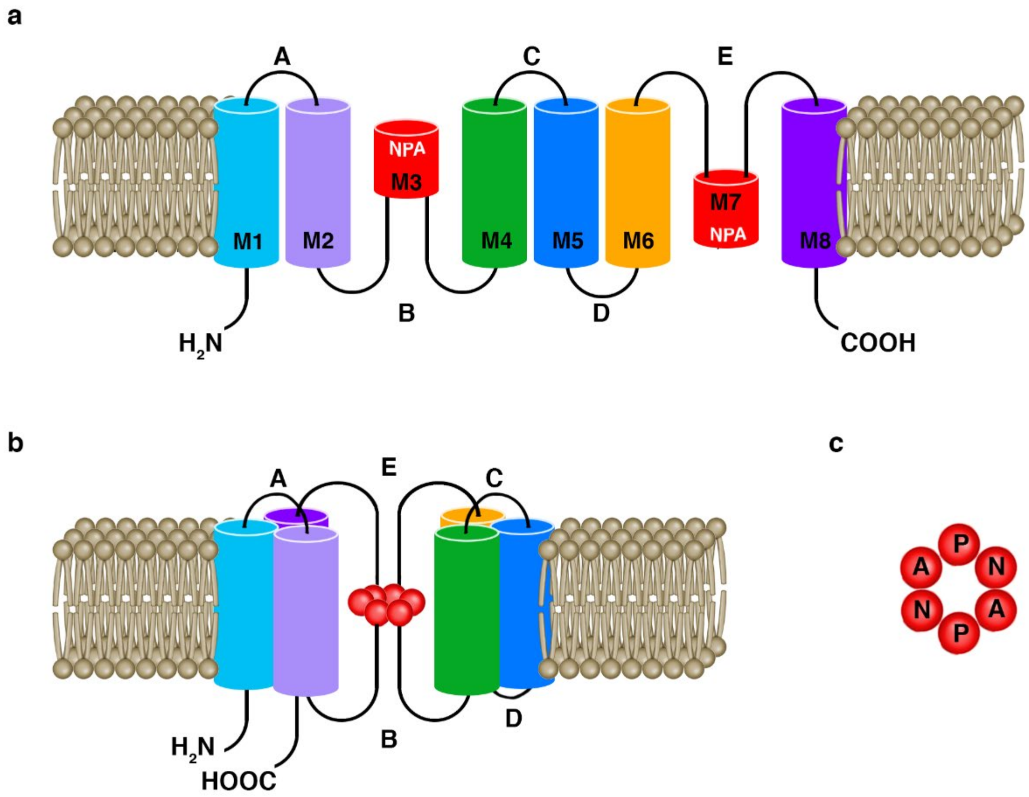

Figure 1.8 The structure of AQ4

AQP4 has six bilayer spanning domains with five interconnecting loops (a). The proposed molecular structure of a monomeric AQP4 as depicted in (b) contains highly conserved asparagine-proline-alanine (NPA) motifs in loops B and E that form a pore in the membrane bilayer (c).

The subcellular OAP arrangement of AQP4 in the plasma membrane of astrocyte endfeet is maintained by the indirect association with DP71 and α-dystrobrevin (α-DB) of the DPC [94]. α-DB binds directly to DP71 by reciprocal coiled-coil interactions. α-DB interacts with syntrophin which localises AQP4 to the cell membrane [130] (**Figure 1.9**).

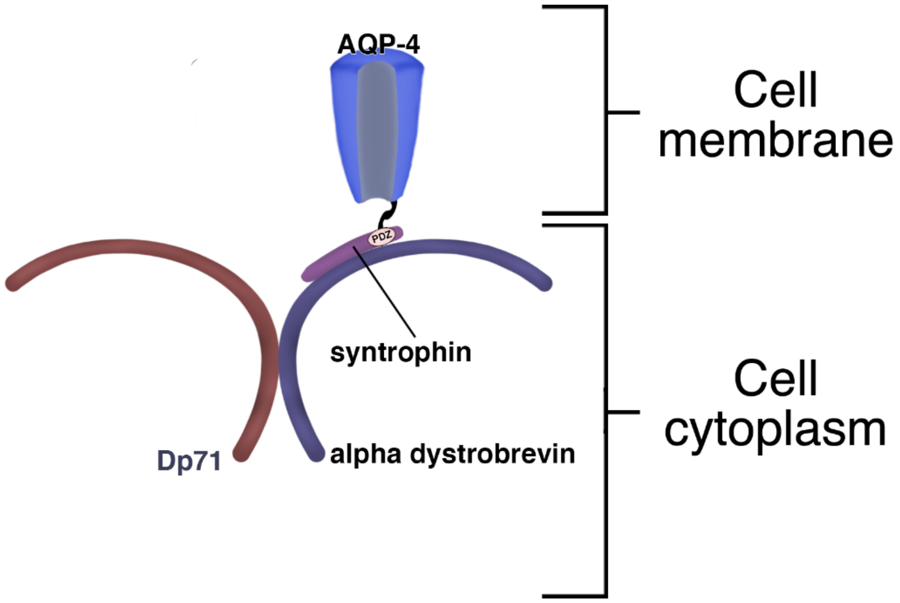

Figure 1.9 Interactions of dystrophin associated proteins and AQP4

1.2.4.4 TARGETING OF AQUAPORIN 4 TO ASTROCYTE ENDFEET IS REGULATED BY DYSTROBREVIN PROTEINS

Dystrobrevins are a group of dystrophin associated proteins with homology to the cysteine-rich C-terminal region and carboxy-terminal domains of dystrophin, showing similarity with protein binding sites such as ZZ domains, syntrophin binding sites and tandem α-helical coiled coils that binds with the reciprocal regions of dystrophin isoforms (**Figure 1.10**) [131]. The dystrobrevin protein was originally identified as an 87-kDa phosphoprotein localised to postsynaptic membranes in the *Torpedo californica* electric organ, copurifying with acetylcholine receptors [132, 133]. It was also found extrasynaptically in the sarcolemma of *Torpedo californica* electric organ and vertebrate skeletal muscle and in postsynaptic membranes of chick and rat endplates [133]. Two separate genes have been identified: β-dystrobrevin (β-DB) and α-DB [134-136].

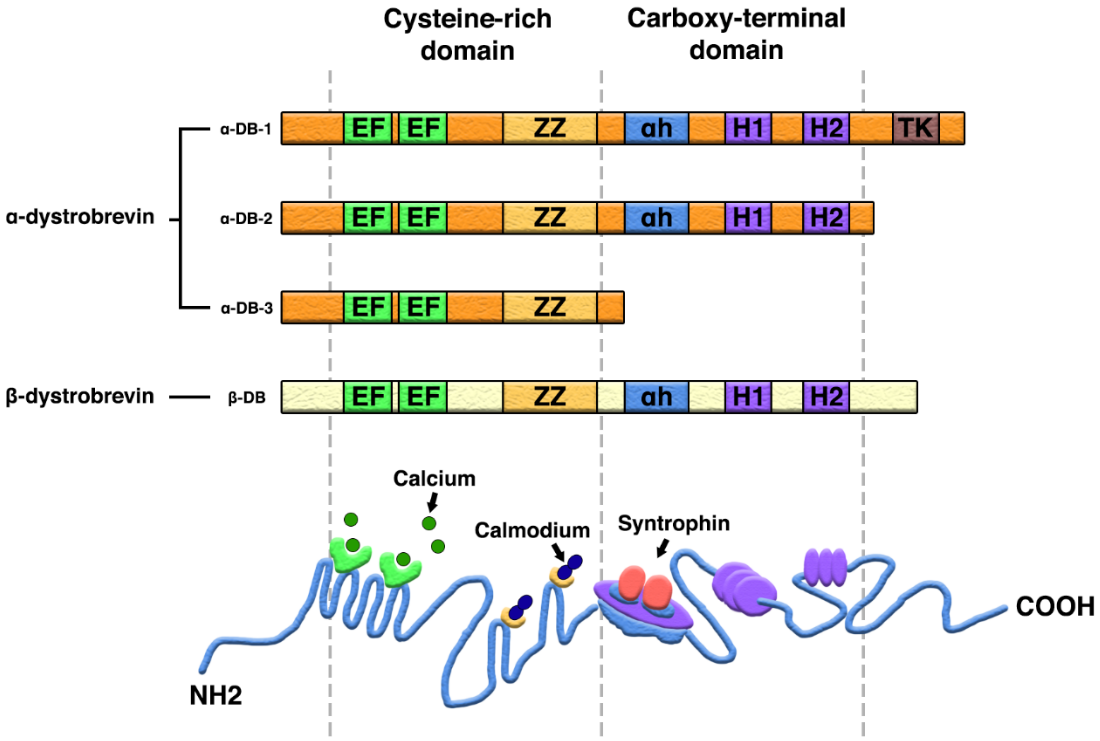
Cysteine-rich domain
Carboxy-terminal domain
α-dystrobrevin
α-DB-1
α-DB-2
α-DB-3
β-dystrobrevin
β-DB
EF
EF
ZZ
ah
H1
H2
TK
Calcium
Calmodium
Syntrophin
NH2
COOH

Figure 1.10 The structure of dystrobrevin

The dystrobrevins contain a cysteine-rich domain with two EF hand domains (EF, green) and one ZZ domain (ZZ, orange) and a carboxy-terminal domain with a a-helical region (ah, blue) and two sets of helical leucine-heptad motifs (H1 and H2, Purple). The hairpins of a-helices in EF domains can bind calcium. The zinc fingers of the ZZ domains are believed to bind Calmodium. The a-helical region contains two binding sites for the syntrophins. The helical leucine-heptad motifs can combine to form a coiled-coiled region that interacts with the coiled-coiled region of dystrophin. a-dystrobrevin-1 also contains sites of tyrosine phosphorylation by tyrosine kinase (TK, brown). Diagram adapted from [137].

1.2.4.4.1 BETA DYSTROBREVIN

The β-DB gene has been mapped to mouse chromosome 12 [138] and human chromosome 2p22-23 [139]. β-DB is considered as a non-muscle protein and is most abundant in the lung, liver, kidney and brain. In brain, β-DB is found in hippocampal and Purkinje neurons and postsynaptic densities but not within the microvasculature [140, 141]. β-DB deficient mice show no obvious histological abnormality and are both viable and fertile [131] but do show a loss of the membrane localisation of DP71 and syntrophin in basolateral region of epithelial cells of cortical renal tubules and collecting tubules [131].

1.2.4.4.2 ALPHA DYSTROBREVIN

The α-DB gene has been mapped to mouse chromosome 18 and human chromosome 18q12.1. α-DB is predominantly expressed in skeletal muscle, lung, heart and brain. In Torpedo, only a single transcript and protein of α-DB has been described. However, the mammalian α-DB gene gives rise to several isoforms by alternative splicing [135, 142] as shown by cloning in mouse [143] and human [144]. In mice, the α-DB gene consists of 24 coding exons. Alternative usage of exons 11, 18 & 24 generates transcripts that encode at least three major C-terminal-truncated α-DB isoforms: α-DB1, α-DB2 and α-DB3 [142].

1.2.4.4.3 ALPHA DYSTROBREVIN AND AQUAPORIN 4

In the brain, α-DBs are found in DPCs in cells forming tissue barriers such as blood-brain and blood-cerebrospinal fluid; mainly in glial end feet and neuroglia of the ependyma and choroid plexus but not endothelium [145]. In astrocyte endfeet, the α-DBs play a key role in the proper assembly of the DPC by targeting AQP4 to the cell membrane. α-DB binds directly to DP71 by reciprocal coiled-coil interactions. Both DP71 and α-DB interact with syntrophin which localises AQP4 to the cell membrane by C-terminal tail binding to PDZ domains (acronym for **P**ost synaptic density protein, **D**rosophila disc large tumor suppressor and **Z**onula occludens-1 protein) [139, 146, 147]. Rather than DP71, α-DB is thought to be the key anchoring molecule for AQP4 in astrocyte endfeet. In mice deficient for α-DB, there is no change in overall expression of AQP4 or syntrophin but AQ4 is redistributed to astrocyte cell bodies, impairing its function at the endfeet [146] (**Figure 1.11**).

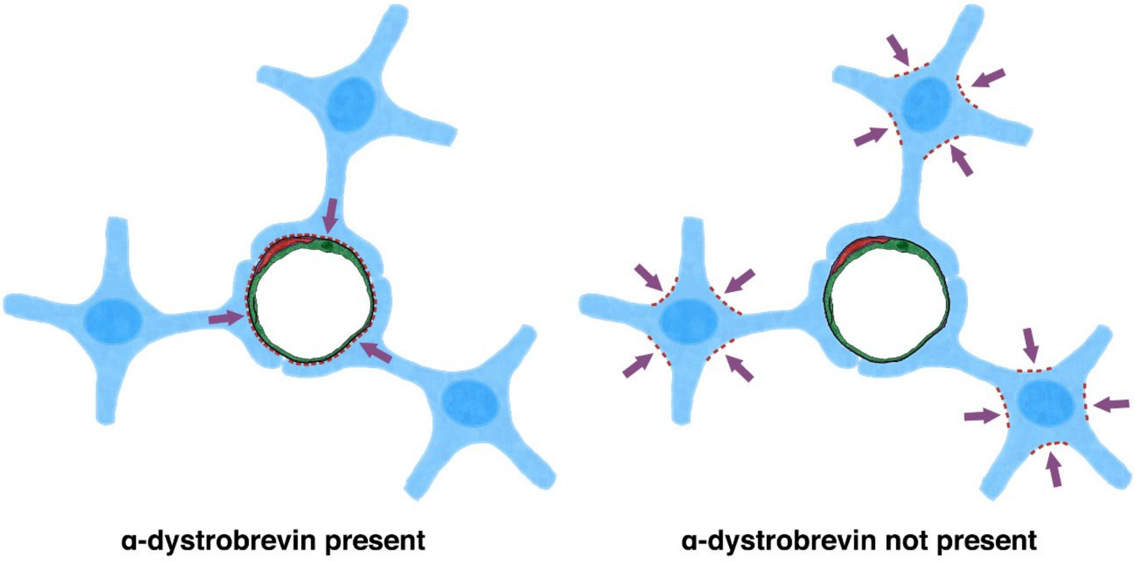
α-dystrobrevin present
α-dystrobrevin not present

Figure 1.11 α-DB targets AQP4 to astrocyte endfeet

AQP4 (red boxes) is anchored to astrocyte endfeet by association with syntrophin and α-DB. When syntrophin is not present, AQP4 expression is redistributed form astrocyte endfeet to astrocyte cell bodies (purple arrows).

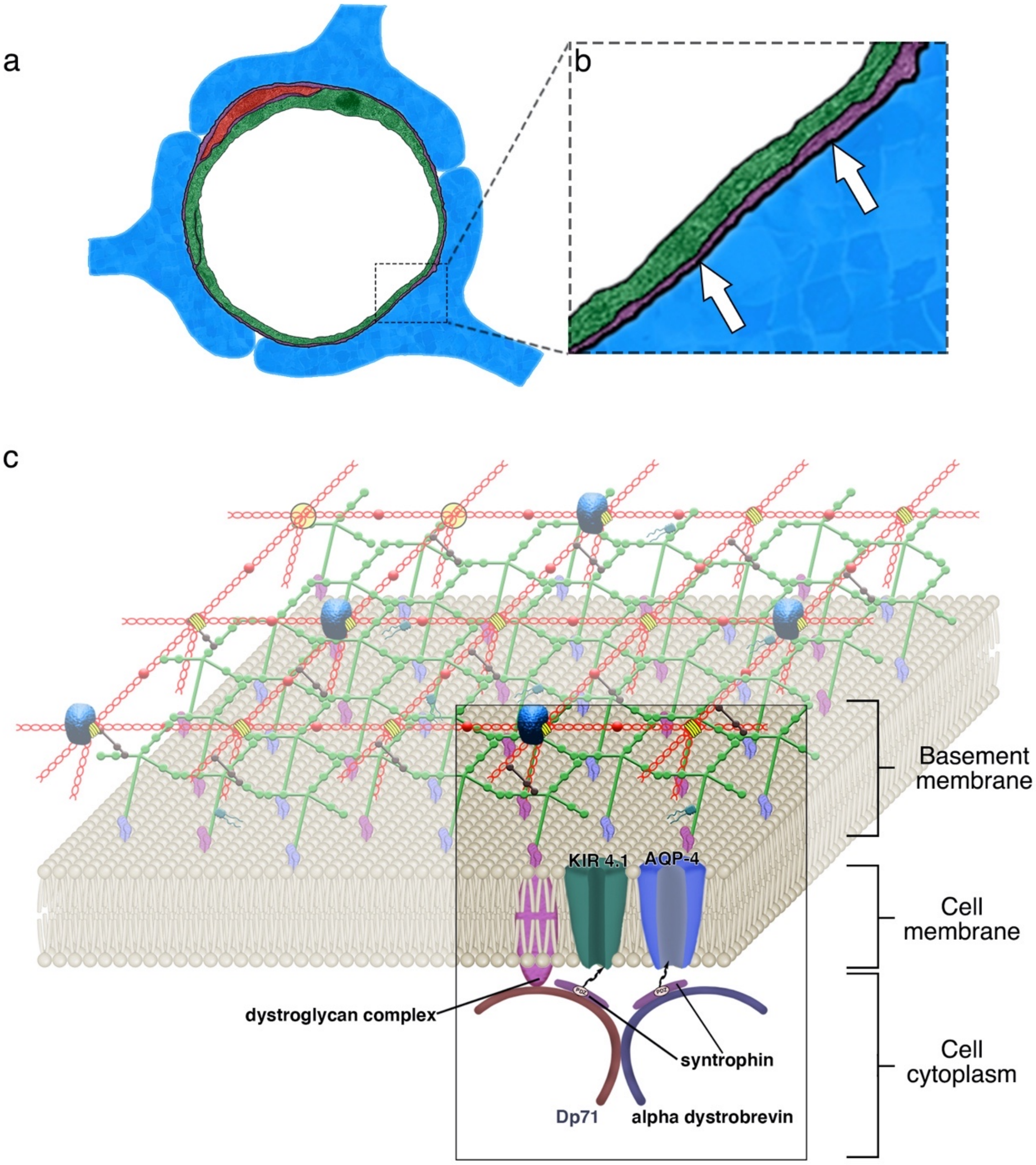
a
b
c
Basement membrane
Cell membrane
Cell cytoplasm
KIR 4.1
AQP-4
dystroglycan complex
syntrophin
Dp71
alpha dystrobrevin

Figure 1.12 The dystrophin associated protein complex at astrocyte endfeet

a) Astrocyte endfeet (blue) are anchored to the basement membrane (extracellular matrix) (purple) via the dystrophin associated protein complex located on the astrocyte cell membrane (b, white arrows). c) The dystrophin associated protein complex. Transmembrane proteins are localised to the cell membrane by C-terminal tail binding to PDZ domains of syntrophin. The dystroglycan complex anchors the cell membrane to laminin/agrin of the extracellular matrix. Dystrophin (Dp71) forms a bridge between the cell cytoskeleton and the cell membrane.

1.3 VASCULAR DEMENTIA AND FLUID HOMEOSTASIS

Despite its high metabolic demands [148], the brain lacks a traditional lymphatic system although there are lymphatic vessels within the dura mater [149, 150]. There are several mechanisms involved in the regulation of the two fluids that are associated with the brain; the cerebrospinal fluid (CSF) and the interstitial fluid (ISF). Dysfunction in these mechanisms alters fluid homeostasis and may provide a substrate for the WMH seen in VaD.

1.3.1 REGULATION OF CEREBROSPINAL FLUID (CSF)

CSF acts synergistically with blood circulation within the skull during the cardiac cycle and provides partial buoyancy for the brain affording protection against physical damage [151]. The classical view of CSF physiology assumes that 80% of CSF is secreted by the choroid plexuses in the lateral, third and fourth ventricles and 20% is produced by other structures such as the brain parenchyma [152, 153]. The CSF is then reabsorbed via bulk flow primarily through arachnoid granulations into venous sinuses [154] but also outflows from the brain via routes along olfactory nerves as they leave the central nervous system, draining into the lymphatics of extracerebral tissues such as the nasal mucosa and cervical lymphatics [155, 156]. CSF also mixes with ISF in the brain parenchyma via convective influx along pathways paralleling the intraparenchymal vasculature [157].

1.3.1.1 EXCHANGE OF CSF WITH INTERSTITIAL FLUID (ISF)

Early observations by Rennels et al suggested that tracers within the CSF can mix with ISF throughout the brain by “paravascular” fluid circulation along pathways paralleling the intraparenchymal vasculature [157]. Multiphoton studies by Iliff et al. [118] show that small molecular weight tracers injected into cisterna magna travel by convective flow into the brain along penetrating arteries and can reach the level of capillaries within 30 minutes. From here they mix with ISF within the parenchyma and exit the brain along large calibre veins. Further studies revealed that this movement is inhibited in mice lacking AQP4 [118], reduced by 50% [158] in mice undergoing unilateral carotid artery ligation but enhanced during the transition of wakefulness to sleep [159]. Controversially, Iliff et al. named this process glymphatic flow, concluding that AQP4 on astrocyte endfeet drives a directional clearance of solutes from the ISF into paravenous spaces via extracellular spaces [118]. Our electron microscopy studies using nanoparticle tracers injected into mouse cisterna magna show these spaces as channels of extracellular matrix that are continuous with the extracellular matrix of the cerebral vasculature and the basement membrane that separates the glia limitans from the outer leptomenigeal sheath of penetrating arterioles (pial-glial basement membrane). However, unlike Iliff et al. we only observed entry of nanoparticles at distances of approximately 100 μm from the meningeal surface of the brain and the nanoparticles remained within pial-glial basement membrane, without diffusion into the parenchyma [160] (**Figure 1.13**). Our contrast enhanced MRI studies assessing the inflow of tracers from the CSF in a beagle dog brain revealed enhanced penetration of tracers into the midbrain. This correlated with an enlarged arteriole pial-glial basement membrane in vessels within the midbrain, further highlighting the pial-glial basement membrane as an entry route of CSF into brain parenchyma (**Figure 1.14**) [161].

It has been hypothesised that changes in norepinephrine levels during altered states of consciousness expands extracellular spaces reducing tissue resistance and allowing faster glymphatic flow [159]. Although controversial, there are several schools of thought correlating the failure of glymphatic flow to VaD [162, 163].

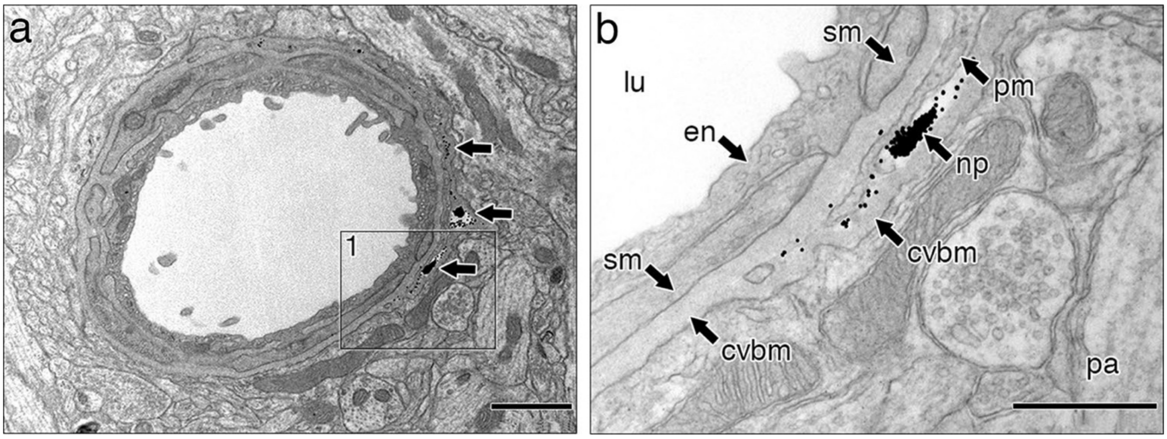

Figure 1.13 The pathway in which nanoparticles enter the brain after injection into mouse CSF via cisterna magna

a) A low power electron micrograph of an arteriole near the surface of the cortex showing dense nanoparticles (arrows) in pial-glial basement membrane between the pia mater and the glia limitans, 5 minutes after injection into mouse cisterna magna. b) Higher magnification of the box 1 in (a) showing the layers of the arterial wall. Dense groups and single nanoparticles (np) are located mainly in the pial-glial basement membrane (cvbm) between the pia mater (pm) and the adjacent glia limitans. (lu) lumen, (en) endothelium, (sm) smooth muscle cells, (pm) pia mater, (pa) parenchyma. Scale bars (a) = 1 μm; (b) 500 nm. Published in [160].

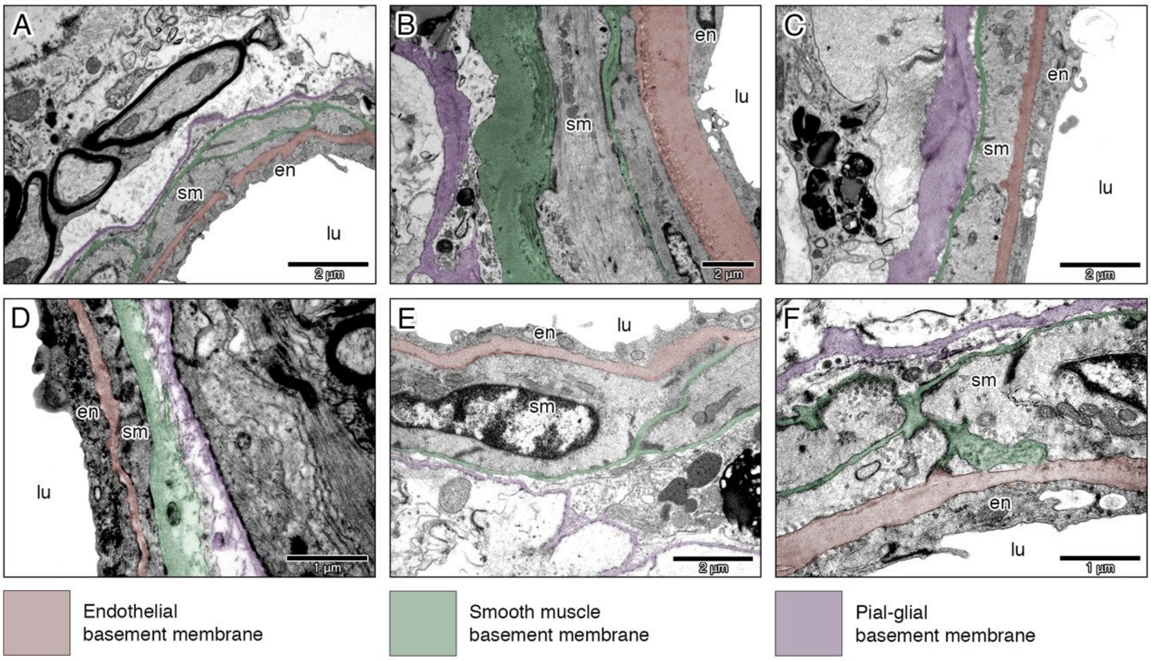
A
sm
en
lu
2 µm
B
en
lu
sm
2 µm
C
en
sm
lu
2 µm
D
en
sm
lu
1 µm
E
en
lu
sm
2 µm
F
sm
en
lu
1 µm
Endothelial basement membrane
Smooth muscle basement membrane
Pial-glial basement membrane

Figure 1.14 Arterioles in the midbrain have enlarged pial-glial basement membranes

False coloured electron micrographs showing regional differences in basement membrane thickness between arterioles in the cerebellum (A), hippocampus (B), midbrain (C), periventricular white matter (D), thalamus (E) and cortex (F) of beagle dog brain. The pial-glial basement membrane of arterioles in the midbrain were found to be at least three times the thickness of any other cerebrovascular basement membrane analysed. Abbreviations: lumen (lu); endothelium (en) and smooth muscle (sm). Published in [161].

1.3.2 REGULATION OF INTERSTITIAL FLUID

ISF provides the suitable ionic and nutrient microenvironment to allow the proper function of neurons and associated cells. The extracellular spaces of the brain accommodate ISF that is produced by diffusion of water across the blood-brain barrier driven by osmotic gradients generated by the active transport of solutes across the endothelium [151]. Nutrients, ions, oxygen and other molecules fundamental for metabolism of cerebral tissue cross the blood-brain barrier from the blood and diffuse 8 – 25 μm into surrounding parenchyma. It is also likely that small amounts of recycled CSF and water produced by brain metabolism contribute to ISF production [164].

1.3.2.1 THE INTRAMURAL PERIARTERIAL DRAINAGE PATHWAY (IPAD)

There are no lymphatic vessels in the brain parenchyma. Cerebral endothelium contains specific membrane transporters for the removal of waste substances from the brain into the blood (e.g. lipid soluble toxins) [165] but ISF and solutes are also eliminated from the brain along the walls of capillaries and arteries, via intramural periarterial drainage (IPAD) pathways. Tracers injected into mouse brain parenchyma diffuse at different rate constants, determined by molecular size and diffusion coefficient [166, 167], along extracellular spaces towards the capillary endothelial basement membrane, as observed by confocal microscopy [168]. Tracers enter capillary endothelial basement membrane and after five minutes drain via bulk flow against the direction of blood flow along smooth muscle basement membrane of cerebral arteries towards the surface of the brain and ultimately to the cervical lymph nodes adjacent to arteries under the base of the skull [168, 169] (**Figure 1.15**).

Our previous work using immuno transmission electron microscopy (TEM) show that after five minutes post injection of biotinylated Aβ 40 into mouse hippocampus the biotinylated Aβ 40 flows in the narrow extracellular spaces between neuronal and glial processes and within the capillary basement membrane [160] (**Figure 1.16**). This mirrors the deposition of Aβ in capillary basement membranes observed in CAA [16, 26].

Although not directly demonstrated in humans *per se*, the similarities between the deposition of Aβ within vessel walls in post-mortem human CAA and in experimental rodent models strongly support the concept of IPAD. Studies also show that the deposition of proteins as CAA inhibits IPAD along the affected vessel wall [170] and that several CSVD risk factors, such as age, hypertension, hyperhomocysteinemia and type 2 diabetes mellitus have altered IPAD [170-176]. Therefore, failure of IPAD appears to be an important factor of CSVD.

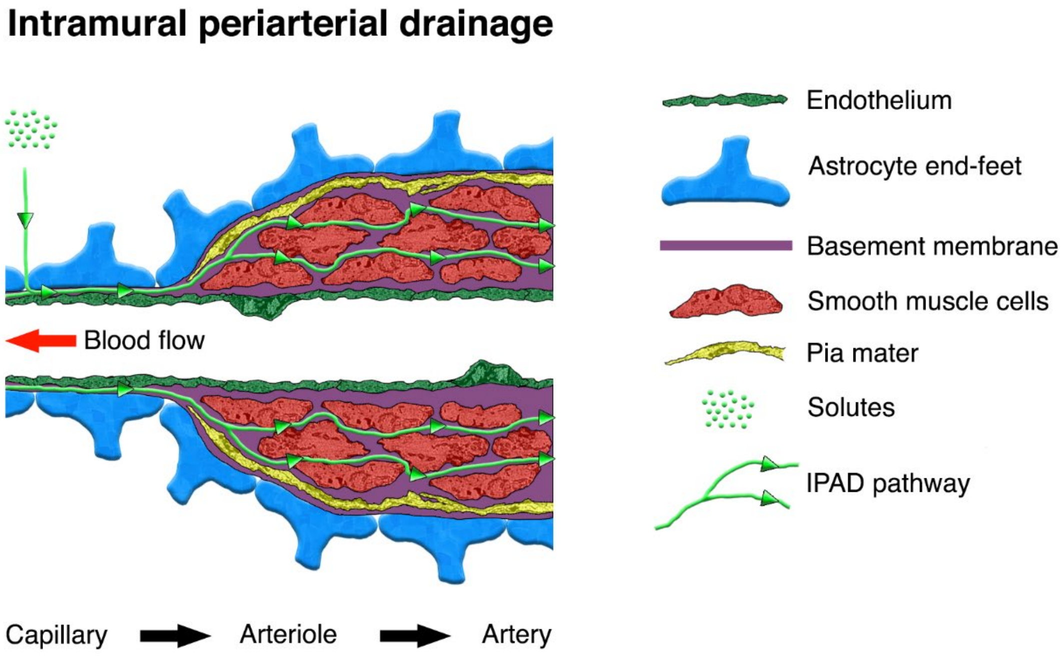
Intramural periarterial drainage
Endothelium
Astrocyte end-feet
Basement membrane
Smooth muscle cells
Pia mater
Solutes
IPAD pathway
Blood flow
Capillary
Arteriole
Artery

Figure 1.15 The intramural periarterial drainage pathway

Solutes (green) diffuse along extracellular spaces and enter capillary basement membranes (purple) via gaps between astrocytic endfeet (blue). Solutes then travel against the direction of blood flow (green arrows) towards arteriole smooth muscle basement membranes towards the surface of the brain and ultimately to the cervical lymph nodes adjacent to arteries under the base of the skull.

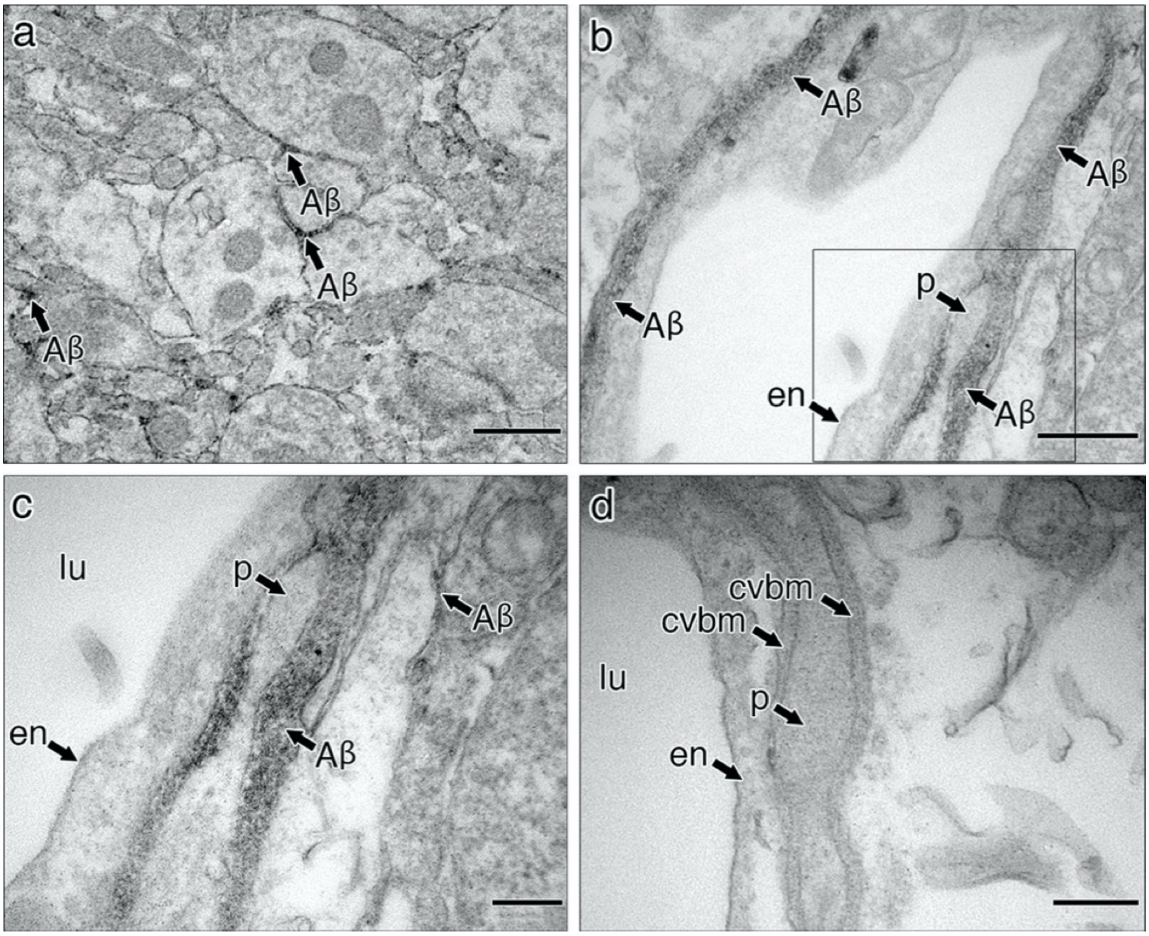

Figure 1.16 Flow of biotinylated Aβ 40 after injection into mouse hippocampus

5 minutes after injection into mouse hippocampus, biotinylated Aβ can be observed as darkly stained areas in extracellular spaces of the parenchyma (a) and extending into the capillary basement membrane (b) encapsulating a pericyte (c). d) hippocampal control tissue in which no biotinylated Aβ has been injected. No Aβ is present in the basement membrane (cvbm). Other abbreviations; pericyte (p); endothelium (en); lumen (lu). Scale bars a 500 nm; b – d 200 nm. Published in [160].

1.3.2.1.1 THE MOTIVE FORCE FOR I INTRAMURAL PERIARTERIAL DRAINAGE PATHWAY IS DERIVED FROM THE CONTRACTIONS OF SMOOTH MUSCLE CELLS WITHIN THE WALLS OF ARTERIES

The process of IPAD ceases upon cardiac arrest [168], therefore It was initially assumed that IPAD was driven by the pulsation force of cerebral vessels [177]. However, our mathematical simulations, confirmed by assessing the pattern of IPAD in mice after administrating the pulse modulator Atenolol (10mg kg−1) showed that this would not provide sufficient motive force [178] (**Figure 1.17**). More recently, new mathematical models and in-vivo 2 photon microscopy on awake mice suggest that it is vasomotion generated by cycles of contraction and relaxation of SMCs that drives IPAD. Vasomotion induces deformations of the basement membrane, effectively opening and closing a valve like system allowing for flow of IPAD in the direction of the vasomotion wave [179, 180].

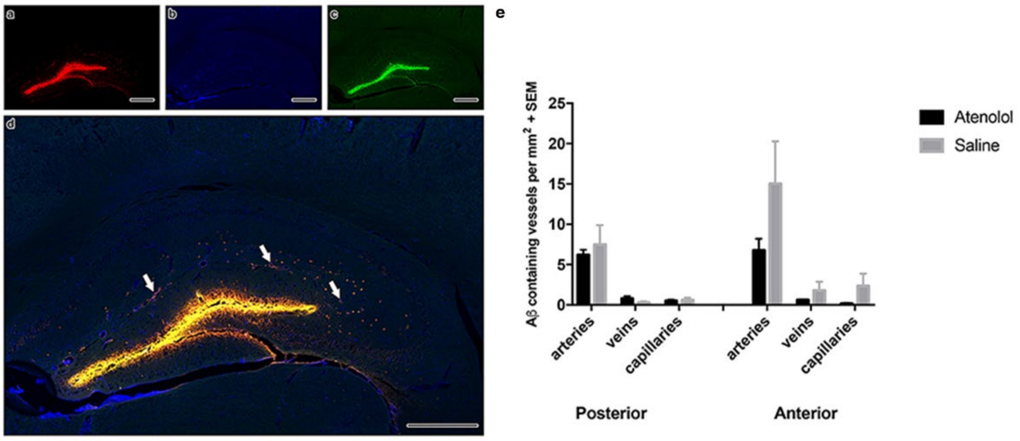

Figure 1.17 The pattern of IPAD in the hippocampus after administration of the beta blocker Atenolol

After administrating the beta blocker Atenolol, IPAD in mouse hippocampi was assessed using confocal microscopy (a-d). Assessment of the number of arteries, veins and capillaries with fluorescent Aβ in their vessel walls (e) revealed no statistical difference between mice injected with Atenolol or saline, confirming the findings of our mathematical simulations. a) fluorescent Aβ, b) collagen IV staining, c) smooth muscle actin staining & d) merged tile scan with arrows indicating arteries with Aβ in IPAD pathways. Scale bars = 400 μm. SEM: standard error of mean. Published in [178].

1.3.3 THE ROLE OF AQUAPORIN 4 IN FLUID HOMEOSTASIS IN THE BRAIN

Over the past ten years, the significance of AQP4 to key functional roles in the brain has received much attention. In mammalian brain the function of AQP4 has been linked to memory consolidation and neurotransmission [181-184], neuroinflammation [83-87, 185-189], and cerebral water homeostasis [118, 158, 159, 166, 190], mainly by the formation or prevention of oedema [102, 120, 188, 191-195]. Expression of AQP4 differs between brain regions such as the hippocampus [196], cerebellum [197], hypothalamus [198] and spinal cord [102] and appears to be altered with disturbances in fluid homeostasis [106, 107, 109-112, 186, 199-201], particularly in dementia and other age-related pathologies [109].

1.3.3.1 AQUAPORIN 4 RESPONDS TO ALTERED CEREBRAL WATER HOMEOSTASIS BY THE FORMATION OR PREVENTION OF OEDEMA

AQP4 expression is upregulated in conditions that alter brain water homeostasis. Elevated levels of AQP4 have been observed in brain tumours [104, 105], cerebral ischemia (including stroke) [106, 107], traumatic brain injury [108] and dementia and other age related pathologies [109-114]. A recent study has shown elevated expression of AQP4 in grey mater from autopsied temporal lobes from eight patients with AD [114]. We have recently shown that in humans AQP4 expression is upregulated in both grey and white matter with normal ageing. However, in cases of moderate CAA, the percentage area immunostained for AQP4 in grey matter is significantly higher compared to age matched controls. In the white matter, the expression of AQP4 expression was reduced in CAA and in tissue from brains that had WMH, suggesting a loss of function of this channel in CAA [115].

Expression of AQP4 in the white matter of experimental models of stroke and after focal ischemic stroke frequently accompanied by life-threatening cerebral edema in post mortem human brains [116] suggest an involvement of AQP4 in oedema resolution [117].

Oedema is a hallmark of most brain diseases. During oedema, an accumulation of excess water in the brain parenchyma causes the brain to swell having a detrimental effect on blood supply, increasing intercranial pressure (ICP) and disrupting tissue structure. Under normal physiological conditions AQP4 deficient mice show slightly raised basal water content [202, 203] and brain extracellular space volume fraction [204] but ICP is not significantly altered. The potential roles of AQP4 in cytotoxic (cellular), vasogenic and hydrocephalic oedema are summarised below.

1.3.3.1.1 AQUAPORIN 4 AND CYTOTOXIC OEDEMA

Cytotoxic oedema relates to the abnormal uptake of water intracellularly into injured brain cells without blood-brain barrier disruption. A net uptake of water from the blood compartment into the brain parenchyma causes astrocyte swelling, particularly at pre-capillary foot processes. Both white and grey matter regions are affected [192, 205]. AQP4 deficient mice are less affected by this form of brain oedema, evident by reduced astrocyte endfeet swelling, normal brain anatomy and intact blood-brain barrier [188, 191]. Indeed wild-type mice treated with the AQP4 inhibitor 2-(nicotinamide)-1,3,4-thiadiazole (TGN-020) after occlusion of the middle cerebral artery showed a reduction in oedema formation [206]. AQP4 deficient mice have a markedly reduced mortality rate in a model of serum hyponatremia [191] and lower ICP, less cerebral water accumulation and improved neurological status and survival when infected with Pneumococcal meningitis [188]. It has been suggested that a lack of AQP4 protects against cytotoxic oedema due to a reduced blood-brain barrier water permeability and reduced water flow into the brain parenchyma [192].

1.3.3.1.2 AQUAPORIN 4 AND VASOGENIC OEDEMA

Vasogenic oedema is associated with abnormal passage of water and proteins into the extracellular compartment due to a disrupted blood-brain barrier [207]. Differences in hydrostatic pressure drive iso-osmotic fluid and serum proteins from the bloodstream into the brain parenchyma, causing expansion of the extracellular space. This is observed most frequently in the white matter, as the extracellular spaces of the grey matter are tortuous, tight and with a higher resistance to flow of interstitial fluid [192, 193]. AQP4 deficient mice exposed to cortical freeze injury or brain tumor implantation in order to model vasogenic oedema are less effective at clearing the excess of brain water from the parenchyma. They show severe swelling of the brain, raised ICP and accelerated neurological deterioration.

Similarly, AQP4 deficient mice are less effective at eliminating intraparenchymal infusions [202].

1.3.3.1.3 AQUAPORIN 4 AND HYDROCEPHALIC OEDEMA

Hydrocephalic oedema refers to the movement of CSF from the ventricles across the ependyma into the interstitial space during hydrocephalus. In hydrocephalus, ventricles become enlarged due to an accumulation of CSF flow or impaired CSF absorption [192]. In a mouse model of hydrocephalus, in which kaolin was injected into the cisterna magna to generate CSF accumulation and ventricle enlargement, AQP4 deficient mice had significantly greater ventricular enlargement at 3 and 5 days post injection [194]. Up to 9% of AQP4 deficient mice produced by heterozygote-heterozygote or knockout-knockout breedings show sporadic obstructive triventricular hydrocephalus with raised ICP and lowered survival rate (most die by 6 weeks of age). The blood-brain barrier is unaffected in these models but the cerebral aqueduct is destroyed. In effect, AQP4 deletion in mice leads to an accelerated progression of obstructive hydrocephalus [194] but the link between AQP4 deficiency and ependymal cell abnormalities is unclear [195].

1.3.4 FLUID HOMEOSTASIS AND THE WHITE MATTER ABNORMALITIES IN VASCULAR DEMENTIA

Damage to the white matter is observed radiologically as white matter hyperintensities or leukoaraiosis [208] and reflects abnormalities in fluid homeostasis in the white matter, frequently observed in cerebrovascular pathology. White matter is highly susceptible to swelling after acute CNS injury [116, 209, 210] and WMH are a common finding on computer tomography (CT) or MRI in the elderly, particularly with stroke or dementia [211]. However, the reason as to why white matter is so susceptible to disturbances in fluid homeostasis has yet to be fully resolved. Various mechanisms for the aetiology of WMH have been proposed, they include ischaemia/hypoxia as a result of CSVD [212], loss of axons in the white matter associated with deposition of tau protein in parent neurons in the overlying grey matter [213] and a failure of elimination of ISF from the affected white matter along peri-capillary and peri-arterial drainage routes [208].

The clinical features of VaD as imaged by MRI (**see section 1.1.2.1**) suggest that in early stages of WMH the lesions are due to altered fluid homeostasis in the brain that could be reversible [211]. Damage to the endothelia of arterioles and capillaries and disruption to the blood-brain barrier leads to altered dynamics of the interstitial fluid and water content. These changes are typically seen by MRI as early lesion formation in the white matter as WMH [55, 214]. Dilated perivascular spaces (PVS), which can also be observed by MRI, are of particular interest as they are linked to altered fluid clearance by IPAD (see section 1.3.3) and have been described in the white matter of patients with CAA [215, 216]. In a recent electron micrograph study, in which we analysed tissue from the white matter of a patient with CAA, we showed the anatomical location of dilated PVS within an expanded region of the arterial wall in a location consistent with the pial-glial basement membrane (**Figure 1.18**) [217]. Our morphological studies on the cerebral vasculature in an elderly dog have revealed that this pial-glial basement membrane contains two layers of leptomeninges that forms a distinct perivascular compartment that potentially could be expanded to allow the formation of a dilated PVS (**Figure 1.19**) [218] (also confirmed with unpublished pilot data, see **Figure 1.20**). Therefore, a clearer picture of the relationship between the vasculature and the regulation of interstitial and cerebrospinal fluids is necessary in order to better understand the pathogenesis of WMH.

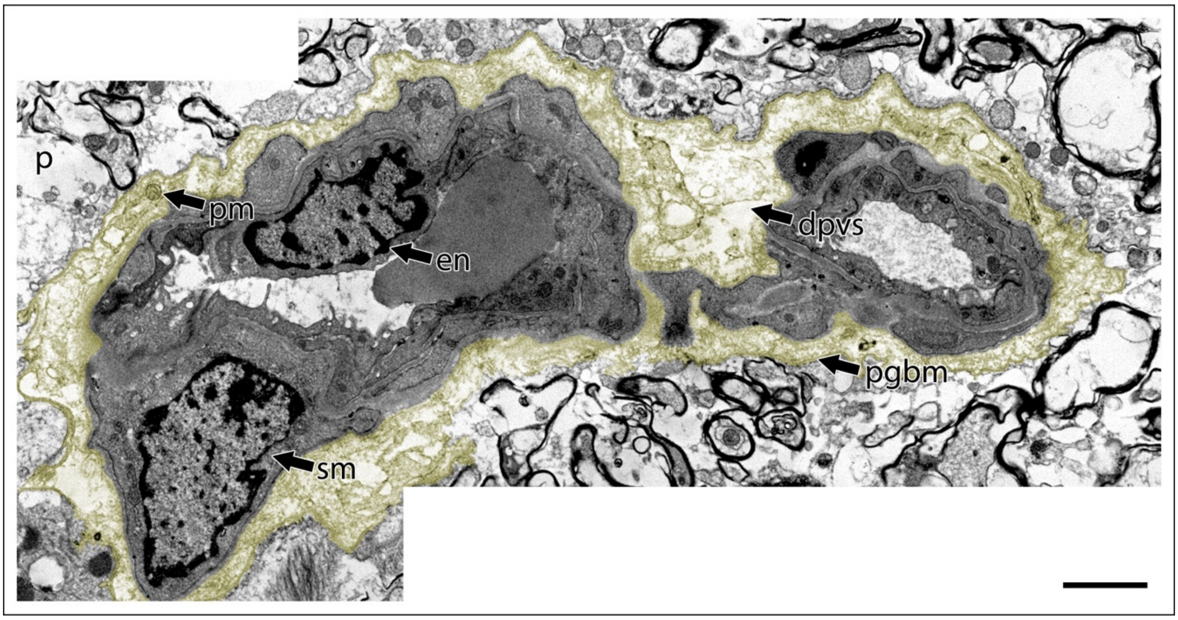

Figure 1.18 Dilated perivascular space

Electron micrograph of an artery from the right frontal subcortical white matter of a patient diagnosed with CAA. The endothelium (en) appears enlarged. The yellow region indicates a dilated perivascular space (dpvs) and expansion of the pial glial basement membrane (pgbm). The pia mater (pm) appears disrupted with only fragments visible. Other abbreviations; smooth muscle (sm); parenchyma (p). Scale bar 2 μm. Published in [217].

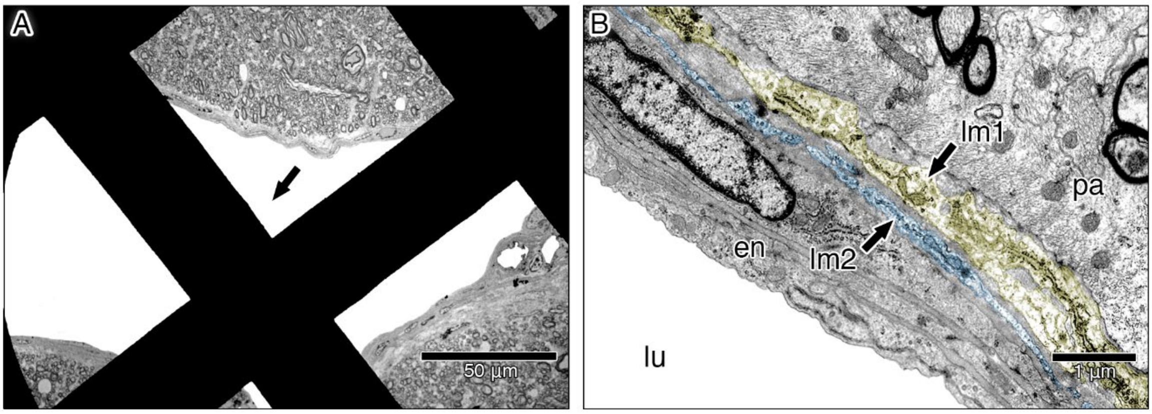

Figure 1.19 The two leptomeningeal layers of the pial-glial basement membrane

Electron micrograph of a large arterial in the subcortical WM of the parietal lobe from beagle dog brain. A) Low power image overview. Arrow points into the lumen of an arteriole of approximately 50 µm diameter. (B) High power of the wall of the vessel in (A) showing the lumen (lu), endothelial cell (en), two layers of leptomeninges (lm1 and lm2) and the adjacent parenchyma with myelin sheets in the WM. Published in [218].

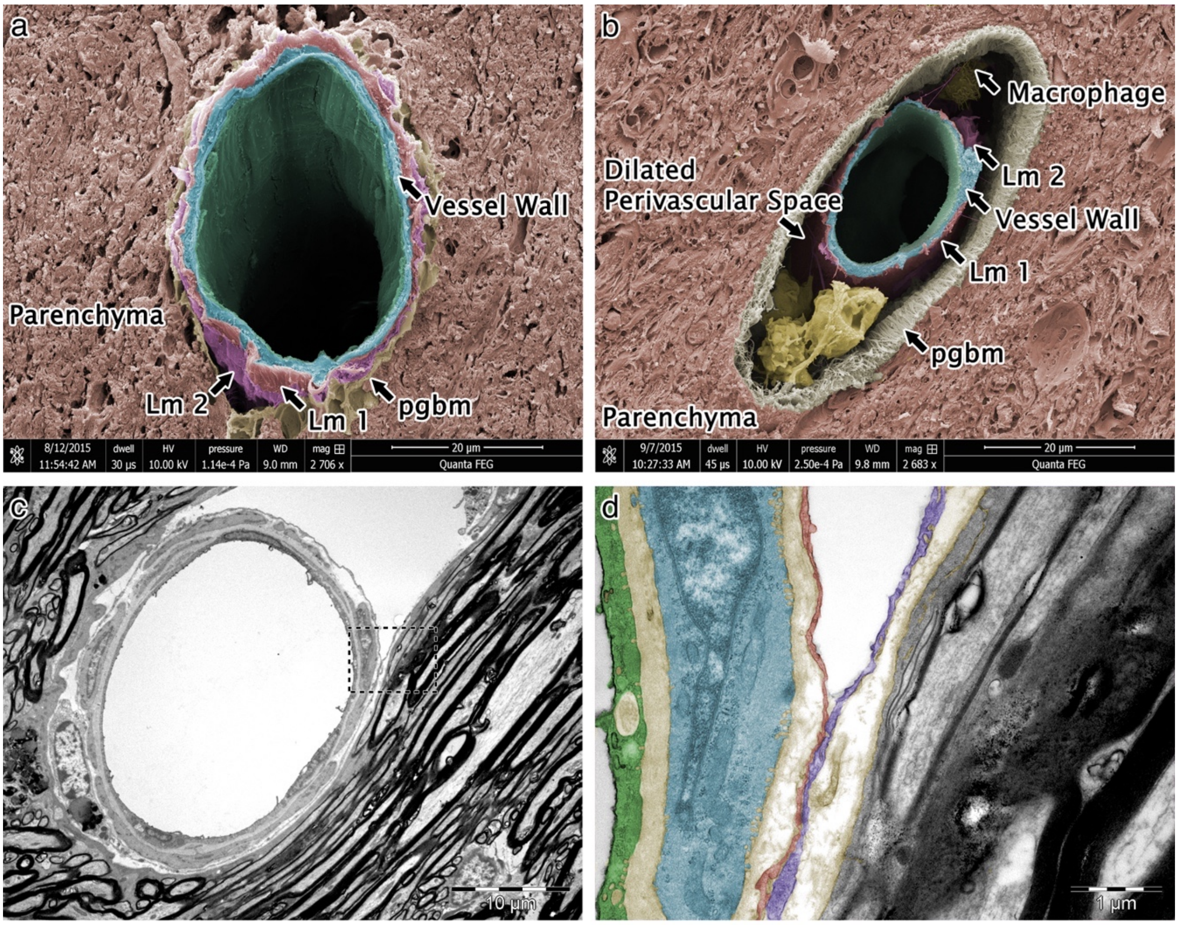
a
Vessel Wall
Parenchyma
Lm 2
Lm 1
pgbm
8/12/2015 11:54:42 AM
dwell 30 µs
HV 10.00 kV
pressure 1.14e-4 Pa
WD 9.0 mm
mag 2 706 x
20 µm
Quanta FEG
b
Macrophage
Dilated Perivascular Space
Lm 2
Vessel Wall
Lm 1
pgbm
Parenchyma
9/7/2015 10:27:33 AM
dwell 45 µs
HV 10.00 kV
pressure 2.50e-4 Pa
WD 9.8 mm
mag 2 683 x
20 µm
Quanta FEG
c
10 µm
d
1 µm

Figure 1.20 Leptomeningeal layers form a distinct perivascular compartment that has the potential to expand forming dilated perivascular spaces

False coloured freeze fracture scanning electron micrograph of a normal arteriole (a) and an arteriole with a dilated space (b). The normal arteriole (a) shows two leptomeningeal layers (Lm 1, red & Lm 2, purple) that envelop the vessel wall (blue). There is very minimal space between the outer leptomeningeal layer (LM 2) and the pial-glial basement membrane (pgbm). The dilated perivascular space in (b) can be seen separating the vessel wall and the Lm1 (red) from the pgbm (brown). Only fragments of Lm2 (purple) are visible. Transmission electron microscopy of an arteriole also showing a dilated space (c) demonstrates the potential for the two leptomenigeal layers to separate (red and purple colours in d) as shown in the boxed region and higher power in (d). Green; endothelium, Brown; basement membrane, Blue; smooth muscle cells. Data generated as part of a pilot study using tissue from the parietal lobe of beagle dog brain.

1.4 MODELLING VASCULAR DEMENTIA USING ANIMAL MODELS

A good animal model should mimic the particular disease conditions and outcomes as close as possible to human findings. Although an animal model will never truly recapitulate the exact aetiology of VaD as seen in humans, these models are needed to understand the role of the vascular risk factors in the microvascular, macrovascular and parenchymal changes observed in VaD with a view to identifying novel therapeutic targets. Due to the multi-factorial nature of VaD, it is difficult to model the disease to accurately reflect all the pathological changes. Rather, it is usual to isolate and focus on one specific aspect of the disease. This allows a more targeted approach which is vital to clearly identify the pathological mechanisms.

The majority of animal models currently available to investigate VaD all appear to target macrovascular or microvascular changes to cerebral blood vessels that lead to cerebral hypoperfusion. Most show white matter lesions and microinfarcts. However, other key pathology changes associated with VaD, such as break down of the blood-brain barrier, microhemorrhages and CAA are limited to specific models. All models share a similar end loss in cognitive abilities (for recent reviews see [9, 12, 219, 220]).

1.4.1 MODELLING MACROVASCULAR CHANGES TO CEREBRAL BLOOD VESSELS

1.4.1.1 HYPOPERFUSION

Macrovascular models include bilateral common carotid artery stenosis (BCAS), asymmetrical common carotid artery stenosis (ACAS) and 2, 3 or 4 vessel occlusion models (2-VO, 3-VO and 4-VO). These models require invasive surgical intervention using chronic cerebral hypoperfusion surgery to reduce blood flow to the brain triggering transient or prolonged hypotension. Both BCAS and ACAS models present with subcortical ischemic injury as the primary pathology whereas occlusion models present with global ischemia and neurodegeneration [219]. The key pathological features of these models are disruption to the blood-brain barrier, white matter lesions and microinfarcts.

1.4.2 MODELLING MICROVASCULAR CHANGES TO CEREBRAL BLOOD VESSELS

Microvascular models are used to replicate the changes to the walls of cerebral vessels observed in human dementia. Current models include the spontaneously hypertensive rat (SHR) [221], hyperhomocysteinemia (HHcy) [171] and amyloid precursor protein transgenic (APP) mice such as the Swedish APP transgenic mouse [28]. Although differing in their aetiology, the below models all appear to show failure of IPAD and the accumulation of Aβ in the perivascular drainage pathway as CAA.

1.4.2.1 HYPERTENSION

Arterial hypertension in young (<10 weeks) spontaneously hypertensive rats leads to arterial wall thickening, blood-brain barrier dysfunction and enlarged perivascular spaces [219]. In spontaneously hypertensive stroke prone rats (SHRSP), the thickening of the cerebrovascular basement membrane is in part, due to increased expression of Coll IV. There is also the accumulation of endogenous vascular Aβ deposits resembling CAA [173, 222].

1.4.2.2 HYPERHOMOCYSTEINEMIA

Elevated plasma levels of homocysteine are a major risk factor for VaD. The most common cause is vitamin B deficiency which is frequent in the elderly (reviewed in [223]). Mice modified for HHcy show thickened cerebral arteriolar walls [224], endothelial damage [225] and blood–brain barrier dysfunction [226]. A diet-inducing high homocysteinemia [227] in a transgenic mouse model of early AD (APP/ presenilin) appears to increase CAA [227].

1.4.2.3 VASCULAR DEPOSITS OF PROTEINS AS CEREBRAL AMYLOID ANGIOPATHY

Secondary vascular changes associated with CAA have been modelled in transgenic mice modified for the overexpression of Aβ. Degeneration of SMCs, endothelial cell loss and basement membrane thickening have been observed in Tg2576, PSAPP [228], APPDutch and TgSw/DI mutant mice [28, 229]. Interestingly, the blood-brain barrier often remains intact in APP mice [220].

While these models have provided key insights into vascular and parenchymal amyloid pathology [28] the significance of overexpression of Aβ to the development of CAA has been questioned. Findings show that in humans, the amyloid pathology observed in sporadic AD is likely due to reductions in the clearance mechanisms of Aβ40 and Aβ42 rather than its rate of production [35]. CAA occurs in approximately 80% of AD cases [230] suggesting a strong link between the failures of Aβ clearance and its accumulation in vessel walls. There is no reason to believe that that this would not be the case in VaD but further models are required to confirm this.

1.5 THE POTENTIAL OF MICE WITH ALTERED DYSTROPHIN ASSOCIATED PROTEIN COMPLEX TO MODEL MICROVASCULAR CHANGES SEEN IN CEREBRAL SMALL VESSEL DISEASE

Although not currently considered as models of CSVD, mice genetically modified for DPC show features of CSVD that are associated with microvascular changes to the cerebral vasculature (**summarised in Figure 1.21**). Alterations to the DPC alter the fine interactions between the astrocytes and the basement membrane of the ECM but also disturb the endothelium and the blood brain barrier. Blood brain barrier disruption leads to altered fluid homeostasis.

1.5.1 ALTERED STRUCTURE AND FUNCTION OF THE ENDOTHELIUM AND THE BLOOD-BRAIN BARRIER

Disruption to normal endothelial function, as is the case in VaD during ischemic stroke and chronic neurodegeneration [46] leads to leakage of fluid, macromolecules and migration of cells into the vessel wall. Mice deficient for dystrophin (mdx) and α-DB show alterations to endothelial tight junctions resulting in a leaky blood-brain barrier [146, 231]. Electron microscopy analysis of cerebral blood vessels from aged α-DB deficient mice show a damaged endothelium with numerous pinocytotic vesicles in the cytoplasm, microvilli on the abluminal surface, tight junction abnormalities and hyperplasia (multi-layered endothelium). These features were not observed in aged-matched controls. Analysis of blood-brain barrier permeability in these mice show abundant perivascular extravasations of both injected Evans blue and blood-borne proteins into the brain [146] indicating impaired blood-brain barrier function. Mdx mice show cognitive decline with decreased hippocampal spatial learning and memory which progressively worsens with age [232]. Cognitive function in α-DB deficient mice has not been investigated.

1.5.2 ALTERED FLUID HOMEOSTASIS

In a recent study, we showed a reduction of AQP4 in post-mortem human tissue from patients diagnosed with CAA and WMH, suggesting a loss of AQP4 regulated fluid homeostasis in CAA [115]. Both α-DB deficient and mdx mice show altered fluid homeostasis in the brain with loss of AQP4 function, particularly at astrocyte endfeet. In α-DB deficient mice, there is a redistribution of AQP4 and the potassium channel KIR4.1 from astrocyte endfeet to the astrocytic cell body [146]. This correlates with similar changes in AQP4 expression in experimental models of ischaemia and in the deep white matter of post stroke dementia [233, 234]. α-DB deficient mice appear to show altered fluid homeostasis that initially presents as swollen astrocyte endfeet but then extends into the surrounding parenchyma as oedema as the mice age [146]. This is most likely due to vasogenic oedema as a lack of AQP4 has protective effects against cytotoxic oedema [192]. Indeed, mdx mice also show swollen endfeet, and vasogenic oedema in the cortex and caudate putamen [101, 232].

It is not clear if the lack of AQP4 at astrocyte endfeet alone is solely responsible for the altered fluid homeostasis in these mice. Of the many different AQP4 deficient mouse models, only one shows any evidence of altered fluid homeostasis with abnormalities in the blood-brain barrier and swollen endfeet (Zhou *et al.*) [235]. The majority of AQP4 deficient mice show no alterations to the blood-brain barrier related to the absence of AQP4 [188, 191, 195, 203]. Even observations by Zhou *et al.* [235] have been questioned as further studies on the same AQP4 deficient model by Feng X *et al.* show no abnormalities in the blood-brain barrier [195]. A possible explanation for the altered blood-brain barrier function in mice with altered DPC has been suggested by Lien *et al.* They propose that a loss of both the AQP4 and KIR4.1 channel from astrocytic endfeet impairs ion and water homeostasis leading to osmotic opening of tight junctions in response to changes in cell volume [146]. Ideally, the blood-brain barrier would need to be assessed in

KIR4.1 deficient mice to help confirm this but this is difficult as these mice suffer severe ataxia, stress induced seizures and premature death [236].

1.5.3 BASEMENT MEMBRANE REMODELLING

Attachment of astrocyte endfeet to basement membrane appears to be regulated, in part, by dystrophin as this attachment is broken in mdx mice [101]. These mice also show a thickened and incomplete basement membrane [231] with significant reductions in laminin and agrin which may help to explain the disrupted astrocyte anchoring to the vessel wall [101].

Mice with partial deletion of the dystroglycan gene (DAG1) show an incomplete basement membrane [237]. Dystroglycan is essential for forming cross links between the DPC and the basement membrane as GFAP-Cre/DG-null mice show a substantial reduction in dystroglycan – laminin binding [237].

Aged α-DB deficient mice show a modified basement membrane that appears thicker but the biochemical changes responsible are not known [146].

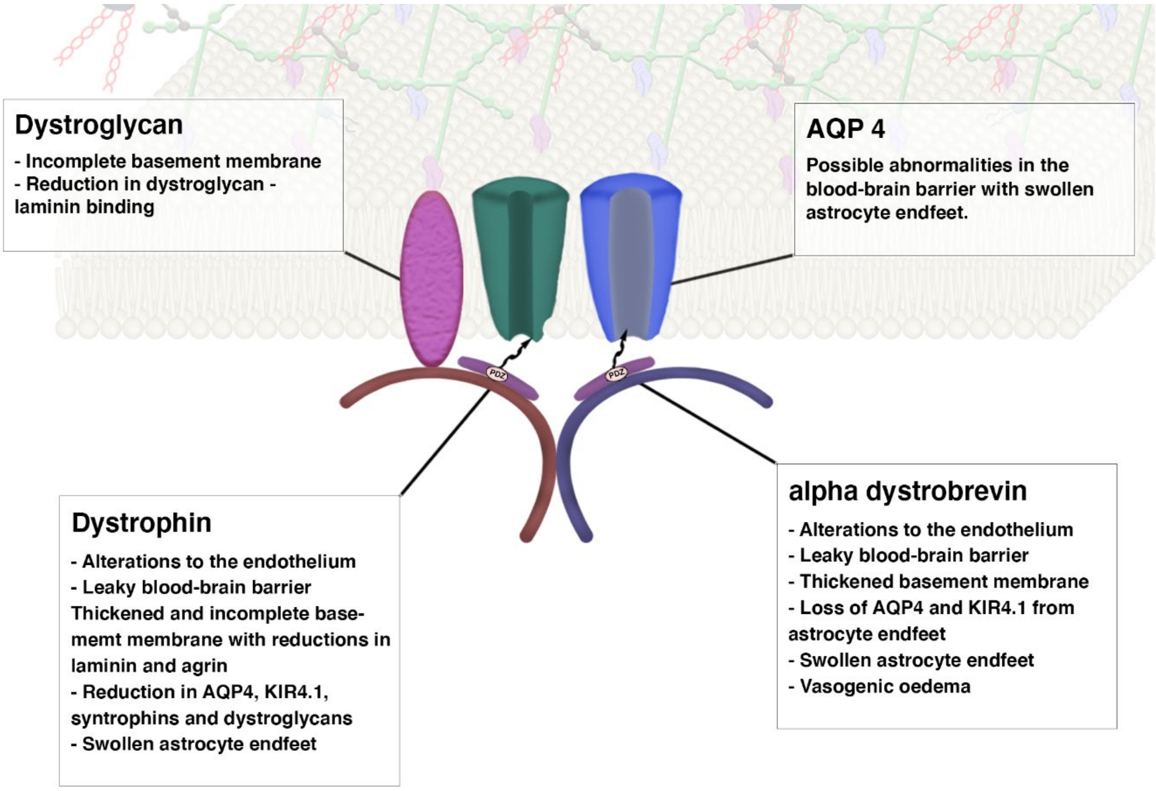

Dystroglycan

- Incomplete basement membrane
- Reduction in dystroglycan - laminin binding

AQP 4

Possible abnormalities in the blood-brain barrier with swollen astrocyte endfeet.

Dystrophin

- Alterations to the endothelium
- Leaky blood-brain barrier Thickened and incomplete basememt membrane with reductions in laminin and agrin
- Reduction in AQP4, KIR4.1, syntrophins and dystroglycans
- Swollen astrocyte endfeet

alpha dystrobrevin

- Alterations to the endothelium
- Leaky blood-brain barrier
- Thickened basement membrane
- Loss of AQP4 and KIR4.1 from astrocyte endfeet
- Swollen astrocyte endfeet
- Vasogenic oedema

Figure 1.21 Summary of the microvascular changes observed in mice deficient for dystroglycan, AQP4, dystrophin and α-DB

Other than AQP4, alterations to components of the DPC all appear to affect the vascular basement membrane. Modifications to dystrophin or alpha dystrobrevin alter the endothelium and blood-brain barrier resulting in abnormal fluid homeostasis and oedema. Changes due to deletion of AQP4 remain controversial

1.5.4 CAN MICE WITH ALTERED DYSTROPHIN ASSOCIATED PROTEIN COMPLEX BE USED TO MODEL INTRAMURAL PERIARTERIAL DRAINAGE TO INVESTIGATE ITS POSSIBLE FAILURE IN VASCULAR DEMENTIA?

As the accumulation of amyloid proteins in the walls of cerebral blood vessels as CAA is the most frequent form of CSVD, it is evident that the process of IPAD and its failure must play a significant role in the development of VaD. Experimental models highlighted in section 1.4.2 show that changes to the cerebral vasculature induced by hypertension [173], hyperhomocysteinemia [227], and overexpression of Aβ [28, 228, 229] all favour the accumulation of amyloid proteins in the IPAD pathway. All these models show a thickening of blood vessel walls that is most likely altering the compliance of the vessel wall for IPAD. Subsequently in these models, elimination of ISF by IPAD appears to have failed.

As demonstrated by the similarity between tracer studies in mice and the location of CAA in blood vessels in humans (see section 1.3.2) it has been established that the central component for IPAD is the cerebrovascular basement membranes. Pathological alterations to these membranes most likely alter IPAD. Perivascular cells, such as astrocytes, maintain the basement membrane and hence the IPAD pathway (see section 1.2.2.1) [57]. Therefore, regulation of the fine interaction between the astrocyte endfeet and the ECM of the basement membrane by the DPC must play a key role in ensuring the integrity and function of the IPAD pathway. This is evident in the altered basement membrane and hence IPAD pathway in mice deficient for dystrophin [231], dystroglycan [237] and α-DB [146].

Mice deficient for α-DB show promise as a potential model to test the role of the DPC in IPAD as the basement membrane, although thickened in older mice, remains intact [146] and is therefore a suitable target to assess IPAD. Changes in the basement membrane in mice deficient for dystrophin [231] and dystroglycan [237] are more severe. The incomplete basement membrane in these mice would most likely impede any investigative studies.

If α-DB deficient mice demonstrate a significant role for the DPC in the dynamics of IPAD, they may also provide an opportunity to further investigate the causes of failed ISF fluid clearance by IPAD and its significance to CSVD and VaD.

1.6 AIMS

The objective of the work presented in this thesis is to ascertain if the vascular DPC plays a key role in ensuring the integrity and efficiency of the IPAD pathways. The overall aim is to test if mice with altered DPC can be used to model failed ISF fluid clearance by IPAD and investigate if these mice show features of CSVD and VaD. This may help facilitate the identification of new novel therapeutic targets for the prevention or management of VaD.

Two existing animal models are analysed: 1) mice deficient for AQP4 and 2) mice deficient for α-DB *(B6;129-Dtna* ^{tm1Jrs}*/J)*. Expression of AQP4 on astrocyte endfeet is reliant on α-DB and is lost in α-DB deficient mice. Therefore, to assess the integrity and function of the IPAD pathways in α-DB deficient mice, the effect of AQP4 loss in these mice on the cerebral vasculature need to be assessed first.

The first aim is to test if loss of AQP4 in α-DB deficient mice affects the morphology of IPAD pathways. A specific mouse model with a knockout for AQP4 will be used to perform a detailed ultrastructural study of the vessel wall at cerebral capillary level, the first entry point for IPAD. Even though extensive work has been done using these mice with behavioural and fluid clearance studies well documented, there is much debate whether AQP4 is required for ISF clearance in the brain and the role of AQP4 in the structure and arrangement of the vessel wall has received little attention.

The second aim is to investigate how loss of α-DB at astrocyte endfeet affects the morphology and dynamics of IPAD pathways. α-DB deficient mice will be employed to repeat the detailed ultrastructural study of cerebral capillaries and if there are any modifications, the dynamics of IPAD and cerebral perfusion will be investigated in order to determine if they display a failure of IPAD seen in CAA and features of CSVD and VaD.

1.7 HYPOTHESES

1. *In mice that do not express glial aquaporin 4 the morphology of capillary intramural periarterial drainage pathways is altered.*

2. *In mice genetically modified for alpha dystrobrevin, the morphology and dynamics of intramural periarterial drainage pathways and cerebral perfusion are impaired.*

Chapter 2 MATERIALS & METHODS

2.1 ANIMALS

Experimental work within this thesis is performed using mice deficient for either aquaporin 4 (AQP4) **(chapter 3)** or alpha-dystrobrevin protein (α-DB) **(chapters 4, 5 and 6).** Mice deficient for AQP4 were generated by Ikeshima-Kataoka et el. at Keio University, Japan who kindly donated perfusion fixed brains for electron microscopy studies. Mice deficient for α-DB were purchased from The Jackson laboratory (010976) and rederived to establish colonies at the University of Portsmouth (colony 1) and the University of Southampton (colony 2). Unless otherwise stated, all procedures were carried out in accordance with animal care guidelines stipulated by the United Kingdom Animals (Scientific Procedures) Act 1986, Home Office licence (P12102B2A).

2.1.1 MICE DEFICIENT FOR AQUAPORIN 4 (CHAPTER 3)

The AQP deficient mouse model used in this thesis is a global AQP4 deficient model in which a 250-nucleotide sequence in exon 1 that corresponds to the region from Ser^{18} to Thr^{101} has been removed and replaced with GFP (green fluorescent protein) complimentary DNA and a PGK-neo cassette flanked by FRT sequences. This generates mice that express GFP under the AQP4 promotor instead of AQP4 [238].

2.1.2 MICE DEFICIENT FOR ALPHA DYSTROBREVIN (B6;129-DTNA TM1JRS/J) MICE (CHAPTERS 4, 5 & 6)

Mice deficient for alpha dystrobrevin (α-DB) were initially generated by Grady *et.al* [239] to investigate the pathogenesis of dystrophin-dependent muscular dystrophies by deletion of a segment common to the two alpha-dystrobrevin isoforms (α-DB1 and α-DB2) found in muscle (target mutation 1 made by Joshura R Sanes $^{(tm1Jrs)}$). Briefly, a 2.5 Kilobase [240] BstBI – Bg1I segment of the alpha-dystrobrevin gene containing exon 3 [142] was deleted and replaced with a neomycin – resistant gene (**Figure 2.1 a - c**). This mutation was then introduced into 129/SvJ-derived embryonic-stem cells by homologous recombination to produce heterozygous and homozygous independent recombinants. This strain was then backcrossed once with C57BL/6 mice and maintained on a mixed 129 and C57BL/6 background. Homozygous recombinants do not express the known alternatively spliced isoforms of α-DB in brains. Both heterozygous and homozygous mutant animals appear normal, show the expected lifespan and are fertile. These mice do show a subclinical muscular dystrophy but never develop the myofibrosis characteristic of the human disease [239].

For experimental work in this thesis, the same strain of α-DB deficient mice generated by Grady *et.al* [239] was purchased from The Jackson laboratory (010976). Homozygous mice were imported into the Bio-resources Unit at the University of Portsmouth and backcrossed with C57BL/6 wild-type mice to generate a colony consisting of mutant, wild type and heterozygous offspring. Mutant and wild-type control mice were perfused for transmission electron microscopy (chapter 4).

A second colony of α-DB deficient mice was established at the Bio-resources Unit at the University of Southampton by blastocyst transfer. Briefly, α-DB deficient male and wild-type control female mice were used for timed matings performed by our collaborators at the Bio-resources Unit at the University of Portsmouth. At 3.5 days post conception, uterus dissection was performed, and the uterus transferred to the Bio-resources Unit at the University of Southampton. Upon receipt, the uterus was flushed to obtain blastocysts that were transferred into recipient female C57BL/6 mice. These mice then produced a litter of heterozygous offspring that were further bred to produce α-DB deficient mice. α-DB deficient mice were used to access intramural periarterial drainage (chapter 4) or were transferred to the Centre for Advanced Biomedical Imaging at University College London (UCL) for assessment by arterial spin labelling (chapter 6).

2.1.2.1 GENOTYPING MICE DEFICIENT FOR ALPHA-DYSTROBREVIN

All mice deficient for α-DB used in this thesis underwent genotyping. This involved DNA extraction, polymerase chain reaction (PCR) and gel electrophoresis.

2.1.2.1.1 PREPARATION OF MOUSE GENOMIC DNA

PCR-quality mouse genomic DNA was prepared using HotSHOT (Hot Sodium Hydroxide and Tris) according to Truett GE *et al.* [241]. Ear punches from 4-week-old mice were placed in 0.2 ml PCR Tubes (STAR LAB, 11402-8100) with 75 µl of alkaline lysis reagent (25 mM sodium hydroxide (NaOH) in 0.2 mM disodium ethylenediaminetetraacetic acid (EDTA), pH 12) and heated to 89ºC for 2 hours. After heating, samples were cooled to 4ºC and 75 µl of neutralising reagent (40 mM Tris (hydroxymethyl) aminomethane hydrochloride (Tris-HCl) pH 5) was added to each sample. The samples were then stored at 4ºC.

2.1.2.1.2 POLYMERASE CHAIN REACTION

1 µl of HotSHOT DNA was added to 0.2 ml 8-strip PCR Tubes (STAR LAB 11402-2900) and mixed with 19 µl of PCR mixture containing 14.8 µl nuclease free water (Thermo Fischer, AM9930), 2 µl PCR buffer, 0.2 µl dNTPs, 0.2 µl Taq DNA polymerase, 0.6 µl $MgCl_2$ (Taq DNA Polymerase, recombinant kit, Thermo Fischer, 10342020) and 0.4 µl of 10 µmol mutant (TGC CAA GTT CTA ATT CCA TCA GAA GCT G), common (GGG CCT TAC CTA TGT GAC TGA GTG AC) and wild-type reverse (TGC TCG CCC CTA CAG CAC CCC TTA) primers (custom ordered, Merck KGaA) (**Figure 2.1 d**).

DNA was amplified in a DNA Engine Tetrad®2 (Peltier Thermal Cycler, Bio-Rad Laboratories, Inc.) by first heating to 94ºC for 5 minutes and then cycling 34 times at 94ºC for 30 seconds, 62ºC for 30 seconds and 72ºC for 30 seconds. Samples were then heated again at 72ºC for five minutes and cooled and stored at 4ºC. Following amplification 4 µl of gel loading dye (Purple (6X), New England Biolabs inc, B7025S) was added to each sample. 4 µl of sample was loaded onto a 2 % agarose in 1 x TBE buffer gel containing 2.5 µl Gel red (Cambridge Bioscience, BT41003) and electrophoresed at 120 V for 30 minutes. Gels were imaged under UV light using a High performance ultraviolet transilluminator imaging system (Ultra-violet Products Ltd). See **Figure 2.2** for results.

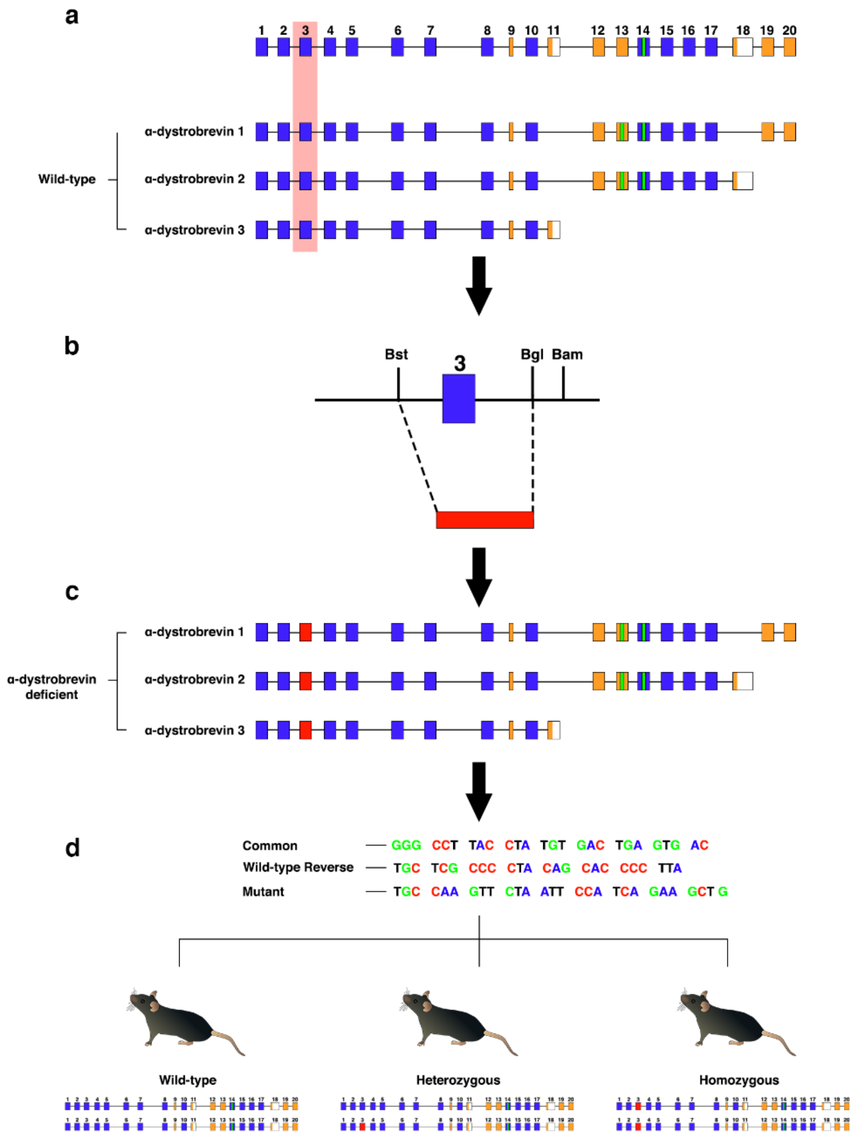
a
1 2 3 4 5 6 7 8 9 10 11 12 13 14 15 16 17 18 19 20
Wild-type
α-dystrobrevin 1
α-dystrobrevin 2
α-dystrobrevin 3
b
Bst
3
Bgl
Bam
c
α-dystrobrevin deficient
α-dystrobrevin 1
α-dystrobrevin 2
α-dystrobrevin 3
d
Common — GGG CCT TAC CTA TGT GAC TGA GTG AC
Wild-type Reverse — TGC TCG CCC CTA CAG CAC CCC TTA
Mutant — TGC CAA GTT CTA ATT CCA TCA GAA GCT G
Wild-type
Heterozygous
Homozygous

Figure 2.1 Overview of the α-DB gene and its deletion in α-DB null (B6;129-Dtna tm1Jrs/J) mice

a) Overview of the α-DB gene in mice showing the major exons (1 – 20). Blue boxes - constitutive coding exons. Orange boxes – alternatively spliced coding exons that result in the different isoforms. White boxes – untranslated regions. Green boxes – encoding regions for syntrophin binding sites. b) Exon 3, common to the major isotypes (red area in (a)), is deleted and replaced with a neomycin – resistant gene that effects all major isotypes (c) producing either wild-type, heterozygous or homozygous mice genotyped by standard PCR and custom common, wild-type reverse and mutant PCR primers (d). a & c adapted from [242]. b adapted from [239].

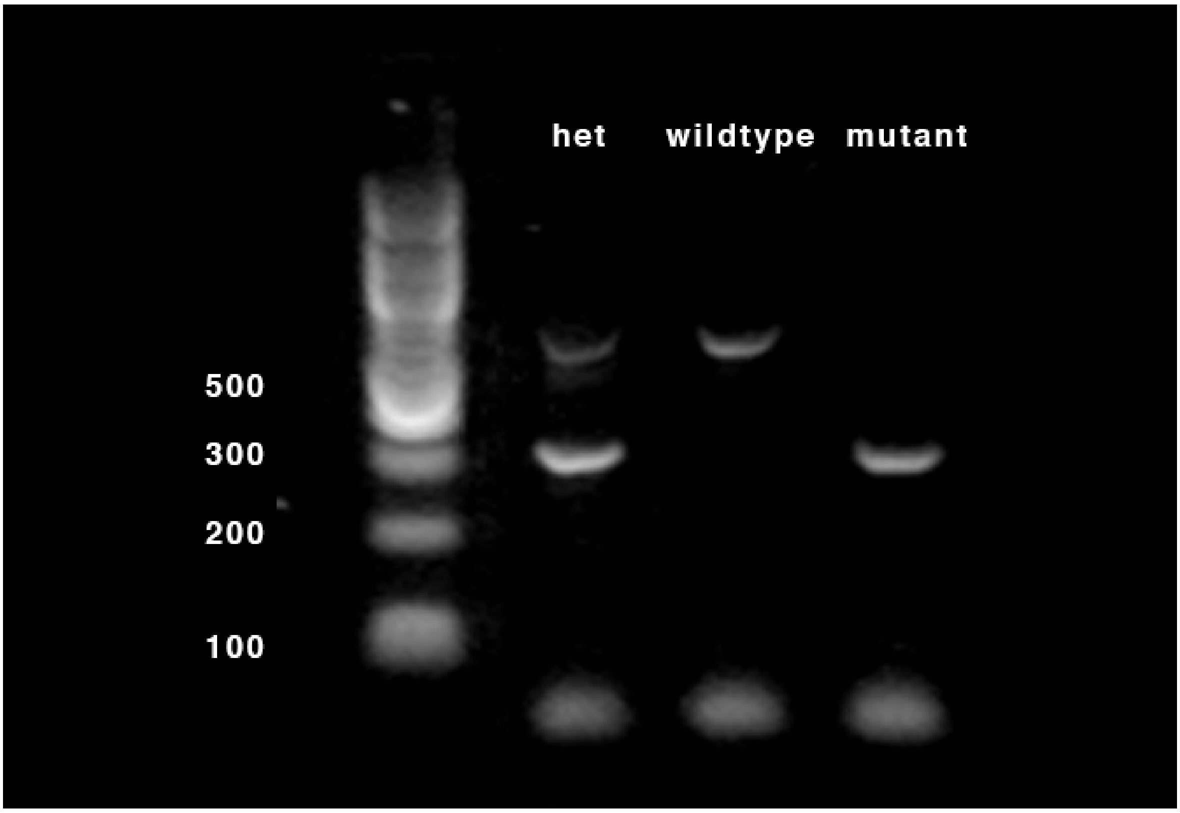
het
wildtype
mutant
500
300
200
100

Figure 2.2 PCR results for the genotyping of α-DB null (B6;129-Dtna tm1Jrs/J) mice

Mutant mice will show one 300 bp band. Wildtype mice will show one 574 bp band. Heterozygous (het) mice will show both a 300 bp and 574 bp band.

2.2 ASSESSMENT OF THE CAPILLARY WALL USING TRANSMISSION ELECTRON MICROSCOPY (CHAPTERS 3 AND 4)

To assess the effect of the removal of AQP4 or α-DB on the structure of cerebral capillaries in the grey and white matter (chapters 3 and 4), a subset of AQP4 deficient and α-DB deficient mice and associated wild-type controls were processed for transmission electron microscopy (TEM). This involved tissue fixation by perfusion, tissue processing for TEM and imaging and analysis by TEM. The following methods area adapted from our published protocols [243, 244] and have been utilised in several peer reviewed publications [160, 161, 173, 217, 218, 245].

2.2.1 FIXATION OF TISSUE FOR ELECTRON MICROSCOPY

AQP4 deficient (n=2) and wild-type control mice (n=2) or α-DB deficient (n=3) and wild-type control mice (n=3) were terminally anesthetised with pentobarbitone (200 mg/kg) and then intracardially perfused with 0.1M piperazine-N,N'-bis(2-ethanesulfonic acid) buffer (PIPES, pH 7.2) followed by 4% formaldehyde plus 3% glutaraldehyde in 0.1M PIPES buffer (pH 7.2). Brains were removed from the skull and subsequently placed in fresh 4% formaldehyde plus 3% glutaraldehyde in 0.1M PIPES buffer (pH 7.2) at 4°C for 24 hours.

2.2.2 PREPARING PERFUSION FIXED BRAINS FOR TISSUE PROCESSING

Perfusion fixed brains were sliced into 1mm thick coronal sections using a mouse brain tissue matrix (Fisher Scientific, 15344908). Upon exanimation of each 1mm slice, it was decided the seventh section (7mm from the olfactory bulbs) provided a good amount of both white and grey matter for sampling. This section was removed and further microdisected for regions of interest in the cortex (x5) and white matter (x5) by removing roughly 5mm of each region starting from the midline and extending into the left hemisphere. Each 5mm region was then divided into smaller 1mm^2 slices (**Figure 2.3**) and stored in fresh 4% formaldehyde plus 3% glutaraldehyde in 0.1M PIPES buffer (pH 7.2) at 4°C until processed for TEM. The other unused slices were stored in 4% formaldehyde plus 3% glutaraldehyde in 0.1M PIPES buffer (pH 7.2) at 4ºC.

2.2.3 TISSUE PROCESSING FOR TRANSMISSION ELECTRON MICROSCOPY

Tissue samples of cortex and white matter were processed for TEM following our optimised protocols [243, 244]. Sections were first washed in 0.01M PIPES buffer (pH7.2) for 5 min and then post fixed in 2% osmium tetroxide in 0.1M PIPES buffer (pH7.2) for I hour. After a further wash in 0.01M PIPES buffer (pH7.2) for 5 min samples were first dehydrated in 30% and then 50% ethanol for 10 mins each and then stained with 1% Uranyl acetate in 70% ethanol for 30 mins. Further dehydration in 95% ethanol for 10 mins and in 100% ethanol for 15 minutes (x2) was followed by 10 mins in acetonitrile, 12 hours in a 50:50 mixture of acetonitrile and TAAB resin (TAAB laboratories, UK) and 6 hours in fresh TAAB resin. Samples were embedded in flat bottomed resin capsules containing fresh TAAB resin and polymerised at 60ºC for 16 hours.

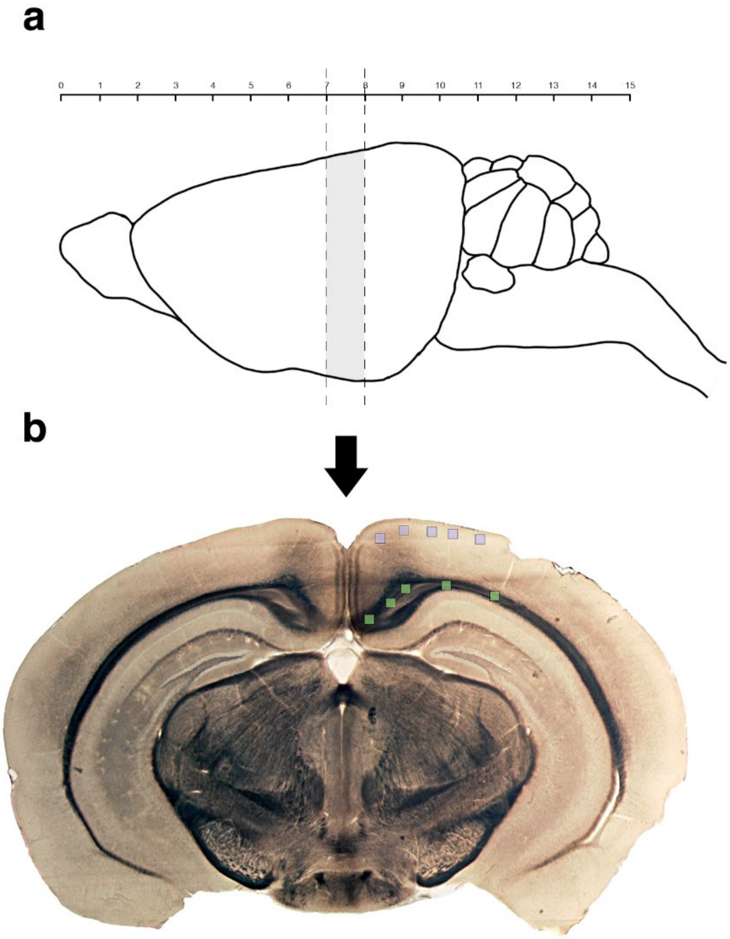

Figure 2.3 Dissection of mouse brain for TEM analysis

a) Brains were sliced into 1mm coronal sections using a mouse brain matrix. b) a representative coronal slice showing sample sites for grey matter (purple boxes) and white matter (green boxes).

2.2.4 SECTIONING OF PROCESSED TISSUE

Polymerised resin blocks were trimmed and sectioned using an Reichurt Ultracut E ultramicrotome (Reichurt, Germany). 80 nm ultrathin sections were cut, transferred onto copper grids (TAAB laboratories, UK) and counter-stained with lead citrate for 3 minutes.

2.2.5 IMAGING TISSUE SECTIONS FOR CAPILLARIES

Grids were examined using either a Hitachi HT7700 (**chapter 3**) or a Tecnai T12 (**chapter 4**) transmission electron microscope operating a Morada G3 digital camera and Radius image capture software (EMSIS, Münster, Germany). Each grid was methodically scanned from top right to bottom left. High resolution low power images of the first 20 capillaries in transverse section with well-defined and clearly resolved vessel walls from each brain region (40 per mouse) were digitally photographed.

2.2.6 CALCULATING PERCENTAGE SURFACE AREA OF THE DIFFERENT COMPONENTS OF THE CAPILLARY WALL

Images were first analysed qualitatively for ultrastructural changes to components of the capillary wall. These included the endothelium, basement membrane and intramural cells. Images were then analysed quantitatively for changes in expression of these components. Adobe Photoshop CS6 was used to manually demarcate the lumen, endothelium, intramural cells and basement membrane, based on electron dense staining of lipid bilayers. Once demarcated, each feature was segmented, measured for surface area in μm^2 and, other than the lumen, percentage area occupied of the vessel wall (**Figure 2.4**).

2.2.7 STATISTICAL ANALYSIS

The means of repeated measures (n = 20 per region per mouse) were analysed using SPSS and a univariate Analysis of Variance (two-way Anova). Repeated measures included the surface areas of the lumen, endothelium, intramural cells, basement membrane, vessel wall and overall vessel size and the percentage surface areas of the endothelium, intramural cells and basement membrane. Significance was set at $P < 0.05$.

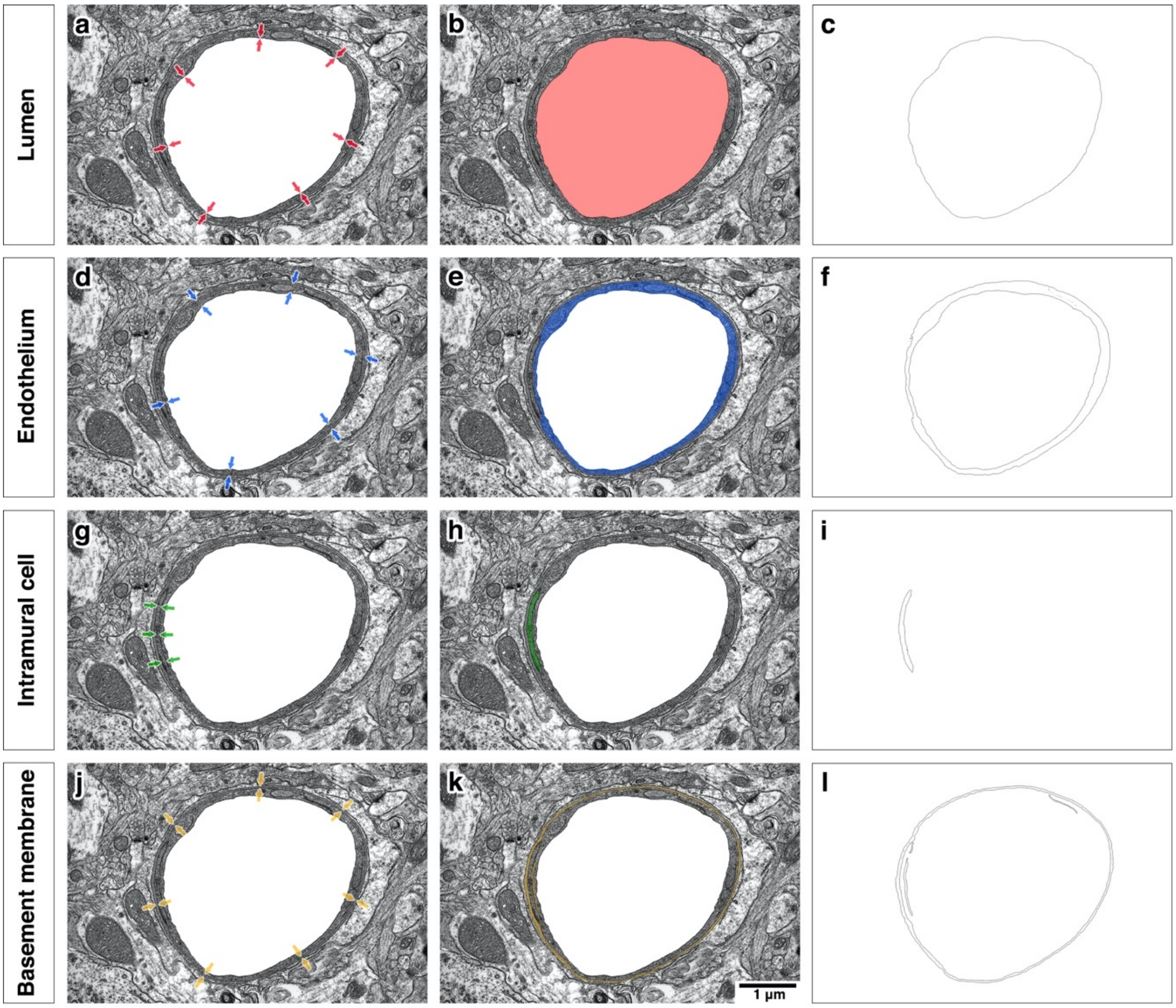

Figure 2.4 Demarcation and analysis of components of the capillary wall

Adobe Photoshop CS6 was used to demarcate and measure the surface area of the lumen (a – c, red), endothelium (d – f, blue), intramural cells (g - i), green and basement membrane (j – l, orange). The arrows in a, d, g & j point to electron dense staining of lipid bilayers that were used to define the edges of each feature. After defining the edges, each feature was segmented (represented as false coloured areas in b, e, h & k and outlined objects in c, f, i & l) and assessed for surface area using Adobe Photoshop inbuilt measure and analysis tools. For this image the lumen measured 7.62 µm^2, the endothelium 1.38 µm^2, the intramural cell 0.12 µm^2 and the basement membrane 0.46 µm^2. The endothelium occupied 70.41% of the vessel wall, the intramural cell 6.12% and the basement membrane 23.47%.

2.3 ANALYSING THE COMPOSITION OF THE CEREBROVASCULAR BASEMENT MEMBRANES (CHAPTER 4)

To assess for changes to the biochemical composition of capillary walls in α-DB deficient mice, immunohistochemistry (IHC) and brightfield microscopy was used to assess for changes in expression of collagen IV (COL4) in grey matter and white matter capillaries of α-DB deficient (n = 3) and wild-type control (n = 3) mice. This involved tissue fixation by perfusion, tissue processing for IHC and imaging and analysis by brightfield microscopy.

2.3.1 FIXATION OF TISSUE FOR IMMUNOHISTOCHEMISTRY

α-DB deficient mice (n = 3) and wild-type control (n = 3) mice were terminally anesthetised with pentobarbitone (200 mg/kg) and then intracardially perfused with 0.01 M phosphate buffered saline (PBS) followed by 4% Paraformaldehyde (PFA) in 0.01 M PBS, pH 7.4 at a rate of 5 ml min-1. Brains were dissected and post fixed for 6 hrs in fresh 4% PFA in 0.01 M PBS, pH 7.4 at 4ºC and then cryoprotected in 30% sucrose in distilled H_2O at 4ºC for a further 48 hrs.

2.3.2 TISSUE SECTIONING

Cryoprotected brains were removed from 30% sucrose and imbedded in OCT compound before serial sectioning into 20 μm coronal slices using a Leica CM1860 UV cryostat. Sections were collected onto SuperFrost Plus™ adhesion slides (Thermo Scientific™, 10149870) and stored at -20ºC.

2.3.3 ENZYME LINKED IMMUNOHISTOCHEMISTRY FOR COLLAGEN IV

Enzyme-linked immunohistochemistry using 3,3'-Diaminobenzidine (DAB) (Sigma-Aldrich, UK) as chromogen was used to visualise COL4 positive vessels in grey and white matter of α-DB deficient and wild-type control mice using 20 μm coronal frozen sections. One section per mouse was chosen based on matching the anatomy with sections used for TEM (**see section 2.2**). Adjacent sections posterior and anterior to the chosen section were used as negative controls.

Sections were first defrosted in an incubator at 37ºC for 15 mins and then washed 2 x 3 mins in 0.01M PBS, pH 7.4. To block endogenous peroxidase activity sections were incubated at room temperature in 3% hydrogen peroxide (Sigma-Aldrich, UK) in 0.01M PBS for 15 mins and then washed 4 x 3 mins in 0.01M PBS, pH 7.4. Antigen retrieval was performed by incubating the sections at 37ºC in pepsin digest (1mg / ml in 0.2 M hydrochloric acid) for 4 mins. Sections were then washed 4 x 3 mins in 0.01M PBS, pH 7.4 before being blocked with 15% normal goat serum (Sigma-Aldrich, UK) in 0.01M PBS at room temperature for 30 mins. After washing, the sections were probed overnight at 4ºC with Rabbit anti-COL4 (abcam, ab6586) diluted in in 0.1% triton in 0.01M PBS to a final dilution of 1:400. This step was omitted with the negative controls to ascertain the level of background non-specific antigen binding of the tissue. Sections were then washed in 0.1M PBS, 4 x 3 mins before being incubated for 1 hour at room temperature with goat anti-rabbit secondary antibody (ThermoFisher Scientific, 31820) diluted in 0.01M PBS to a final dilution of 1:200. Sections were then washed in 0.1M PBS, 4 x 3 mins, incubated at room temperature in ABC vector (Vector laboratories, PK-6100) for 1 hour, washed again in 0.01M PBS, 4 x 3 mins and then washed in 0.1M sodium acetate, 4 x 3 mins. Sections were developed using glucose oxidation enhancement with 3,3'-Diaminobenzidine (DAB) for 12 mins, dehydrated through an alcohol series (50%, 75%, 90%, 2 x 100% 2 mins each), washed in xylene (2 x 5 mins washes) and coverslipped using DPX mounting medium (Sigma-Aldrich, UK).

2.3.4 IMAGING FOR DAB STAINING OF COLLAGEN IV

2.3.4.1 EXTRACTING REGIONS OF INTEREST

An Olympus dotSlide digital virtual microscope was used to produce high powered tile scans of each section (magnification of x40) (1 x section per mouse). Tile scans were imported into VS Desktop imaging software (Olympus) to produce regions of interest (ROI)s for further image analysis. As the white matter (corpus callosum) in mice occupies less area than the grey matter, overall sample area was calculated based upon the size of the white matter in each image. The white matter was identified based on the orientation of the white matter tracts. We found that the white matter could be divided into 20 smaller ROIs with a size of 125 µm (width) by 125 µm (height) and an area of 15625 μm^2 (0.0156 mm^2). The total area of white matter sampled for each mouse was 312,500 μm^2 (0.313 mm^2). As the area of the grey matter is larger, we chose to use five ROIs with a size of 250 µm (width) by 250 µm (height) and an area of 62500 µm^2 (0.0625 mm^2) positioned to capture as much grey matter as possible while keeping the overall sample area the same as the white matter (0.313 mm^2) (**Figure 2.5**)

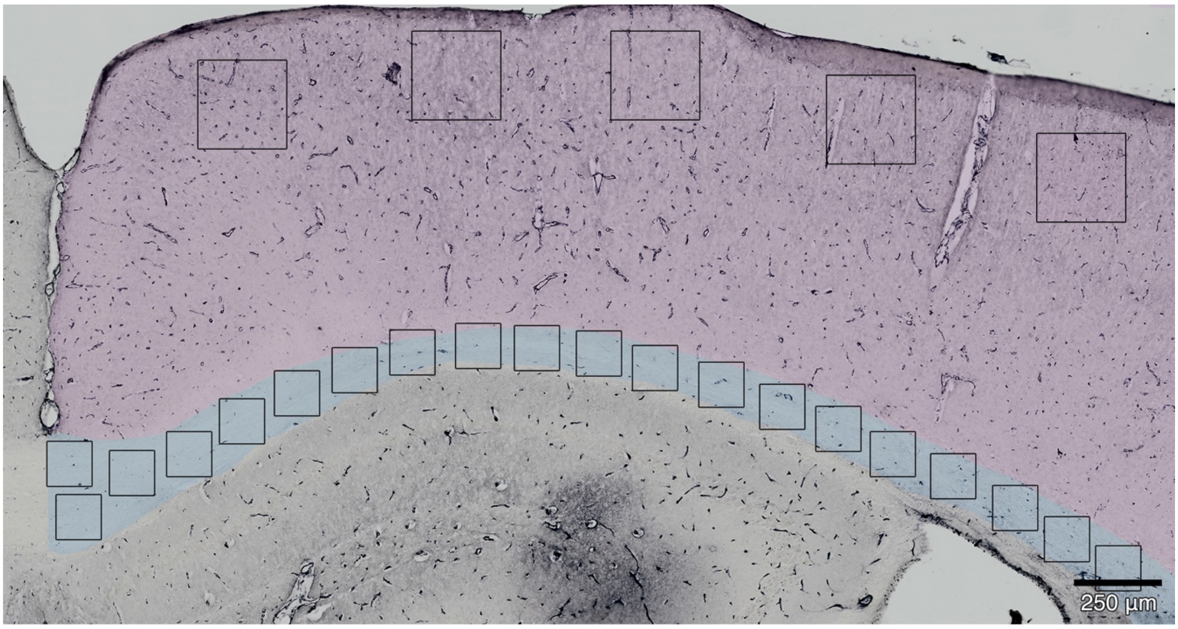

Figure 2.5 Sample sites for immunohistochemistry of collagen IV

One section per mouse was chosen based on matching the anatomy with sections used for TEM. The micrograph has been false coloured showing the grey matter (light purple) and white matter (light blue). The white matter is identified by the direction of the white matter tracts. The outlined boxes represent either 250 µm (width) by 250 µm (height) (grey matter) or 125 µm (width) by 125 µm (height) (white matter) regions of interest that were extracted for further analysis.

2.3.4.2 ANALYSING REGIONS OF INTEREST FOR COL4 STAINING AND VESSEL DENSITY

Each ROI was assessed for DAB (COL4) staining using Image J [246] and a custom macro (**Figure 2.6**) modified by colleagues from the Biomedical imaging Unit, Southampton University. The macro enables automatic thresholding of each region of interest (ROI) to just display vessels stained with DAB. The analyse particle function is then used to generate values for total number of vessels and total area of DAB staining from layer masks of each ROI (**Figure 2.7)**.

Values generated for each ROI were combined to give total number of vessels and total area of DAB staining per region per section. These values were then divided by the overall surface area (312500 μm^2) and multiplied by 500000 and expressed as total number of vessels (vessel density) and total area stained per $0.5mm^2$. The amount of COL4 per vessel was calculated by dividing the total area stained by the total number of vessels.

2.3.4.3 ANALYSING REGIONS OF INTEREST FOR VESSEL DISTRIBUTION AND VESSEL SPECIFIC COL4 STAINING

Grey matter ROI were further assessed for differences in vessel distribution by counting the number of capillaries (vessels with diameter of less than 10 μm) and arterioles and venules which, due to limitations of DAB staining, could not be easily differentiated and so were classified together as vessel with a diameter of 10 μm or larger. Inbuilt measurement and analysis tools in Adobe Photoshop CS6 were used to identify and count the number of vessels with a diameter of 10 μm or larger per ROI using imported layer masks of each ROI (generated from the ImageJ macros) (**Figure 2.8**). The number of capillaries of each ROI was calculated by deducting the counted number of arterioles/venules from the overall total vessel count (generated previously using the ImageJ macros). Values generated for each ROI were combined to give the total number of capillaries and arterioles/venules per region per section. These values were then divided by the overall surface area (312500 μm^2) and multiplied by 500000 and expressed per $0.5mm^2$.

Adobe Photoshop CS6 was also used to measure and calculate overall COL4 staining per vessel type. First, the arterioles/venules identified previously from the layer masks of each ROI were measured for total area of COL4 staining (**Figure 2.8**).

This value was then deducted from the overall area of COL4 staining to give total area of COL4 staining for capillaries per ROI. Values generated for each ROI were combined to give the total area of COL4 staining per capillaries and per arterioles / venules per region per section. These values were then divided by the overall surface area (312500 μm^2) and multiplied by 500000 to be expressed per $0.5mm^2$. The amount of COL4 per vessel was calculated by dividing the total area stained by the total number of vessels for each vessel group per $0.5mm^2$.

2.3.4.4 STATISTICAL ANALYSIS

Statistical analysis was performed using SPSS and an independent *t-test* with significance set at $P < 0.05$.

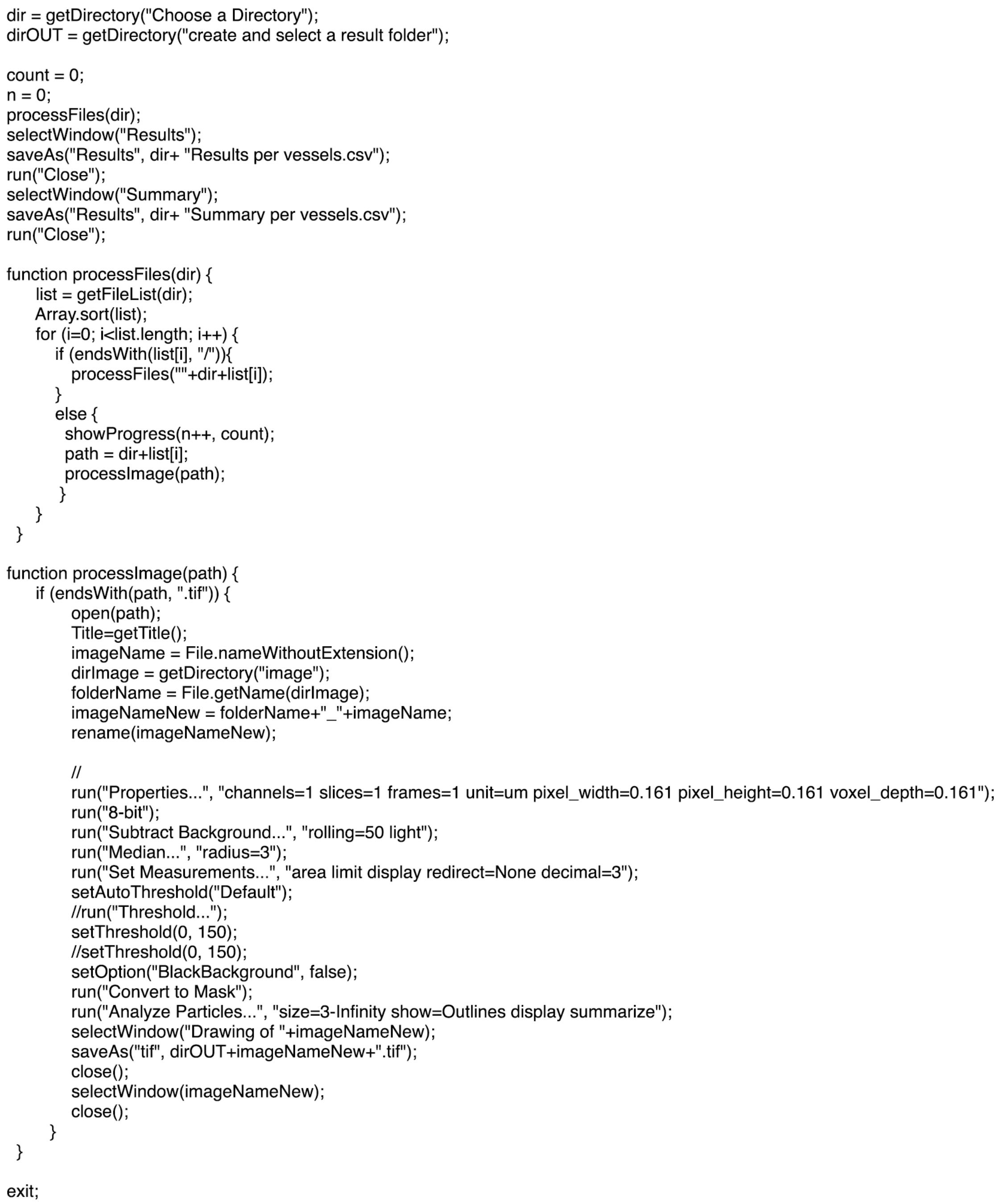

```
dir = getDirectory("Choose a Directory");
dirOUT = getDirectory("create and select a result folder");

count = 0;
n = 0;
processFiles(dir);
selectWindow("Results");
saveAs("Results", dir+ "Results per vessels.csv");
run("Close");
selectWindow("Summary");
saveAs("Results", dir+ "Summary per vessels.csv");
run("Close");

function processFiles(dir) {
     list = getFileList(dir);
     Array.sort(list);
     for (i=0; i<list.length; i++) {
         if (endsWith(list[i], "/")){
            processFiles(""+dir+list[i]);
         }
         else {
           showProgress(n++, count);
           path = dir+list[i];
           processImage(path);
          }
     }
 }

function processImage(path) {
     if (endsWith(path, ".tif")) {
            open(path);
            Title=getTitle();
            imageName = File.nameWithoutExtension();
            dirImage = getDirectory("image");
            folderName = File.getName(dirImage);
            imageNameNew = folderName+"_"+imageName;
            rename(imageNameNew);

            //
            run("Properties...", "channels=1 slices=1 frames=1 unit=um pixel_width=0.161 pixel_height=0.161 voxel_depth=0.161");
            run("8-bit");
            run("Subtract Background...", "rolling=50 light");
            run("Median...", "radius=3");
            run("Set Measurements...", "area limit display redirect=None decimal=3");
            setAutoThreshold("Default");
            //run("Threshold...");
            setThreshold(0, 150);
            //setThreshold(0, 150);
            setOption("BlackBackground", false);
            run("Convert to Mask");
            run("Analyze Particles...", "size=3-Infinity show=Outlines display summarize");
            selectWindow("Drawing of "+imageNameNew);
            saveAs("tif", dirOUT+imageNameNew+".tif");
            close();
            selectWindow(imageNameNew);
            close();
        }
 }

exit;
```

Figure 2.6 Custom macros used in Image J to analyse COL4 staining

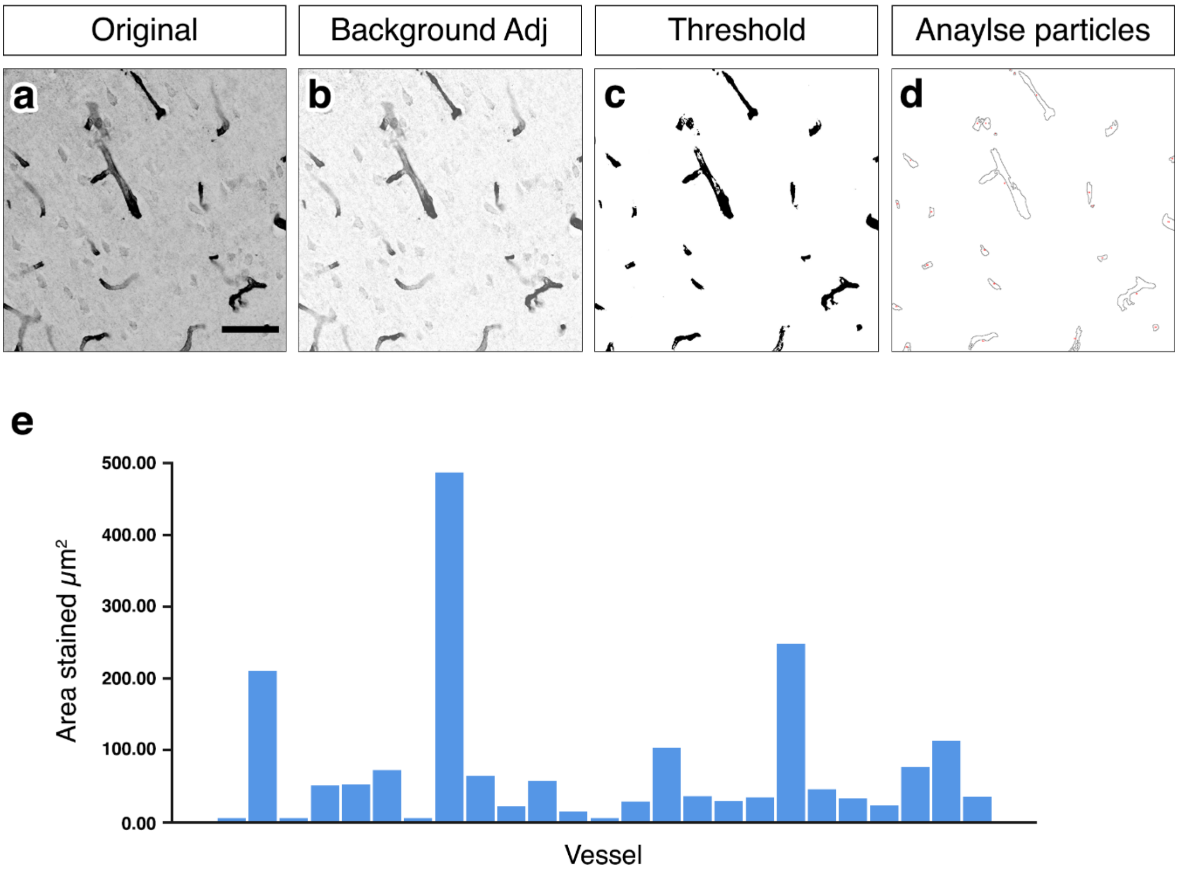

Figure 2.7 Analysing regions of interest for number of vessels and COL4 staining

Each region of interest is processed in Image J by a macro that automatically converts the image to 8 bit (a), subtracts unwanted background noise (b), applies auto threshold to display just DAB staining (C) and creates a layer mask to count the number of vessels and area staining of DAB by using analyse particle function (d). Scale bar = 25μm. The graph (e) shows the results with each column representing one vessel. In this sample, the area of the region of interest was 62500 μm^2, the total number of vessels was 25 and the total area of DAB staining was 1820.303 μm^2.

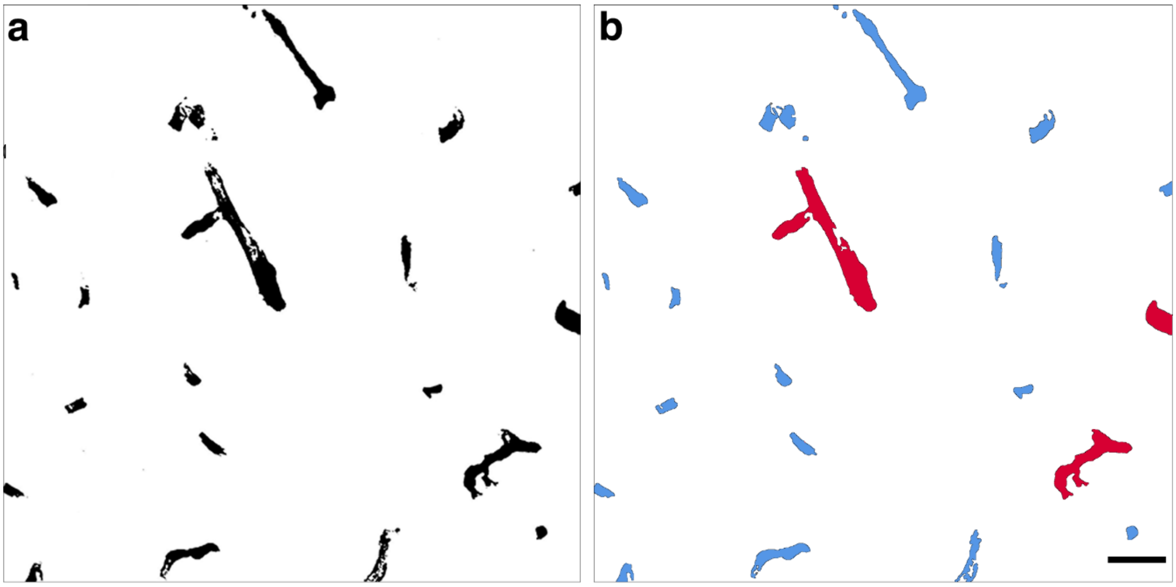

Figure 2.8 Analysing regions of interest for distribution of vessels and COL4 staining

Each ROI layer mask (a) was evaluated for the number and total area of DAB (COL4) staining of capillaries and arterioles / venules. Panel (b) has been false coloured to highlight the capillaries (blue) and arterioles / venules (red). The total number of capillaries for this ROI is 22 and arterioles / venules 3. The overall surface area of DAB staining for capillaries is 985.263 μm^2 and arterioles / venules 835.04 μm^2. Scale bar = 20μm

2.4 ASSESSMENT OF INTRAMURAL PERIARTERIAL DRAINAGE IN ALPHA-DYSTROBREVIN DEFICIENT MICE (CHAPTER 5)

To assess the dynamics of Intramural periarterial drainage (IPAD) in α-DB deficient mice, the clearance of a fluorescent tagged tracer (amyloid-beta (Aβ) (1-40) HiLyte Fluor 555 (Cambridge Bioscience)) injected into the hippocampus (grey matter) or corpus callosum (white matter) was assessed by confocal microscopy. This involved stereotaxic surgery, tissue fixation by perfusion, tissue sectioning, immunohistochemistry, confocal microscopy and image analysis.

The following methods have recently been published in [247]. Further work where we have utilised stereotaxic surgery can be found in [160, 178, 245, 248].

2.4.1 STEREOTAXIC INJECTION OF AMYLOID-BETA (1-40) HILYTE FLUOR 555

α-DB deficient (n = 5 per region) and wild type control (n = 5 per region) were anaesthetised with Isoflurane mixed with concentrated O_2 (1.7 L min-1). Mice were induced with 3% isoflurane and then maintained using 2% isoflurane. The level of anaesthesia was monitored by using pedal withdrawal reflex response. A rectal probe and homoeothermic blanket and temperature control system (BASi) was used to regulate internal body temperature at 37ºC. Lacri-lube ointment was applied to the eyes to preserve cornea during anaesthesia. Isoflurane was used rather than injectable anaesthetics based on our previous study which showed that isoflurane is better at maintaining a more physiologically relevant heart rate and oxygen saturation level [245].

A KOPH instruments stereotaxic frame (Model 900) with attached digital manipulator (World Precision Instruments) was used to precisely inject tracer into hippocampal grey matter (Anterior-Posterior - 2 mm; Medial-Lateral 1.5 mm; Dorsal-Ventral - 1.7 mm, n=5) or corpus callosum (white matter) (Anterior-Posterior -2 mm; Medial-Lateral 0.5 mm; Dorsal-Ventral - 1.3 mm, n= 5) of wildtype or mutant mice. The stereotaxic coordinates were obtained using The Allen mouse brain atlas (www.mouse.brain-map.org) (**Figure 2.9**).

The anaesthetized mouse was placed in the stereotaxic frame and the head secured with jaw bars. A midline incision was performed and a Tech2000 Micromotor drill (RAM Products, INC) with 0.7 mm burr was used to create a burr hole in the skull at the injection site. 0.5µl of 100µM Aβ (1-40) HiLyte Fluor 555 (Cambridge Bioscience) was injected into either the hippocampus or corpus callosum using a Hamilton Neuros Syringe with a 33 gauge needle (Essex Scientific Laboratory Supplies Ltd.) and Microinjection syringe pump (UMP3T-1; World Precision Instruments) at a rate of 0.25 µl min-1. The syringe was left in situ for 2 min to allow for bolus diffusion to prevent reflux. The tracers were allowed to drain for a further 5 min and then the mouse terminally anesthetised with pentobarbitone (200 mg/kg) for perfusion fixation.

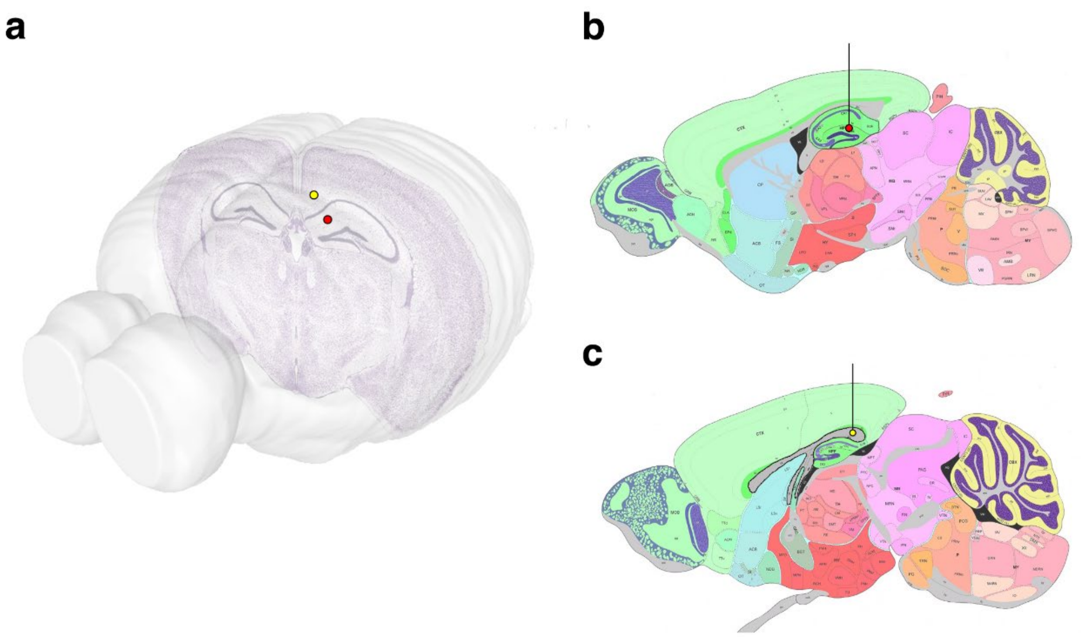

Figure 2.9 Stereotaxic injection sites

Injections were performed Anterior-Posterior -2mm from the Bregma represented by the red dot (hippocampus) and yellow dot (corpus callosum) in (a). Sagittal slices show the injection site for the hippocampus (Anterior-Posterior - 2 mm; Medial-Lateral 1.5 mm; Dorsal-Ventral 1.7 mm), red dot in (b) and corpus callosum (Anterior-Posterior -2 mm; Medial-Lateral 0.5 mm; Dorsal-Ventral - 1.3 mm), yellow dot in (c). Images adapted from www.mouse.brain-map.org

2.4.2 FIXATION OF TISSUE AND TISSUE SECTIONING FOR IMMUNOHISTOCHEMISTRY

Terminally anesthetised mice were intracardially perfused with 0.01 M phosphate buffered saline (PBS) followed by 4% Paraformaldehyde (PFA) in 0.01 M PBS, pH 7.4 at a rate of 5 ml min-1. Brains were dissected and post fixed for 6 hrs in fresh 4% PFA in 0.01 M PBS, pH 7.4 at 4ºC and then cryoprotected in 30% sucrose in distilled H_2O at 4ºC for a further 48 hrs. Brains were imbedded in OCT compound and then sectioned into 20 μm coronal slices using a Leica CM1860 UV cryostat. Sections were collected onto SuperFrost Plus™ adhesion slides (Thermo Scientific™, 10149870) and viewed using a Zeiss Axioskop 2 fitted with a rhodamine filter to identify the section containing the site of injection. In our previous studies we show that in mice the drainage of Aβ (1-40) occurs predominantly in a posterior direction and can be visualised in the wall of blood vessels as close as 200 μm to the injection site [74]. We therefore chose coronal sections 200 μm posterior to the injection site for immunohistochemistry. All sections were stored at -20ºC.

2.4.3 TISSUE PROCESSING FOR IMMUNOHISTOCHEMISTRY

Sections were defrosted in an incubator at 37ºC for 15 mins, washed 2 x 3 mins in 0.01M PBS, pH 7.4 and then blocked in 15% goat serum (Sigma 9023) for 1 hour at room temperature (RT). Sections were then incubated in rabbit anti-COL4 1/400 in 0.01M PBSt (AbCam, ab6586) and anti-smooth muscle actin (SMA) FITC conjugated 1/200 in 0.01M PBSt (Sigma F3777) overnight in a moist chamber at 4ºC. Sections were then washed 3 x 10 mins in 0.01M PBS and incubated in conjugated secondary antibody goat antirabbit Alexa Fluor 633 0.01M PBSt (ThermoFisher Scientific A-21070) for 1 hour RT. Sections were further incubated in 1% Sudan Black for 5 min to remove auto fluorescence before being mounted in mowiol citiflour and stored at 4ºC until imaged.

2.4.4 IMAGING TISSUE SECTIONS BY CONFOCAL MICROSCOPY

For each section, tile scans of the left hippocampus or corpus callosum were captured using a Leica SP8 confocal microscope fitted with x20 objective set at an optical zoom of 1. Laser power and detection windows were kept consistent for all scans. Sequential imaging was used to prevent cross excitement of fluorophores.

2.4.5 ASSESSMENT OF INTRAMURAL PERIARTERIAL DRAINAGE

Quantification of intramural periarterial drainage (IPAD) of Aβ (1-40) HiLyte Fluor 555 injected into the left hippocampus or corpus callosum was performed using a max projection of each tile scan uploaded into Adobe Photoshop CS6. We chose to use max projections of each tile scan as they provide a more precise and accurate method to assess IPAD, particularly when assessing vessel density.

IPAD was assessed by using Adobe Photoshop CS6 to manually measure vessel density of capillaries, arterioles and venules and counting the number of vessels containing Aβ (1-40) HiLyte Fluor 555 in their vessel walls. We also assessed fluorescence intensity to investigate for possible differences in the amount of amyloid-beta remaining in the parenchyma.

Vessel density was calculated by dividing the total number of capillaries, arterioles or venules by the overall surface area (in μm^2) and multiplying this value by 500000 to be expressed as number of vessels per $0.5mm^2$. This was also performed for the number of capillaries, arterioles or venules with Aβ in their vessel walls. Vessels were identified based on lumen diameter and immunoreactivity to SMA ($< 10\mu m$ = capillaries, ≥ 10 μm & SMA positive = arterioles, ≥ 10 μm & SMA negative = venules) [168, 170]. The overall surface area was determined by choosing regions of interest that were based on key anatomical features that could be observed in each section analysed. Regions of interest were outlined using Adobe Photoshop CS6. For the hippocampus, an area transversely extending from the edge of the suprapyramidal blade to the apex of the granule cell layer [178] was outlined. For the corpus callosum, the white matter tracts extending from the midline to a point directly above the suprapyramidal blade of the granule cell of the hippocampus were outlined (**Figure 2.10**).

The density of Aβ (1-40) in the parenchyma was assessed using Image J [246] and the RawIntDen function. Each tile region of interest was extracted from the confocal tile scan using Adobe Photoshop CS6 and split into its subsequent colour channels (blue – COL4, green – SMA, red - Aβ (1-40)). The red channel was then imported into Image J and converted into an 8-bit greyscale image. Areas of the image containing fluorescent signal was segmented using an auto-threshold algorithm and assessed for overall area and fluorescent intensity using the RawIntDen function to generate the sum of the values of all the fluorescent pixels. Values were divided by the overall surface area (in μm^2) of each region of interest and multiplied by 500000 to be expressed as overall area and fluorescent intensity per $0.5mm^2$ (**Figure 2.11**).

2.4.6 STATISTICAL ANALYSIS

Statistical analysis was performed using SPSS and an independent *t-test* with significance set at $P < 0.05$.

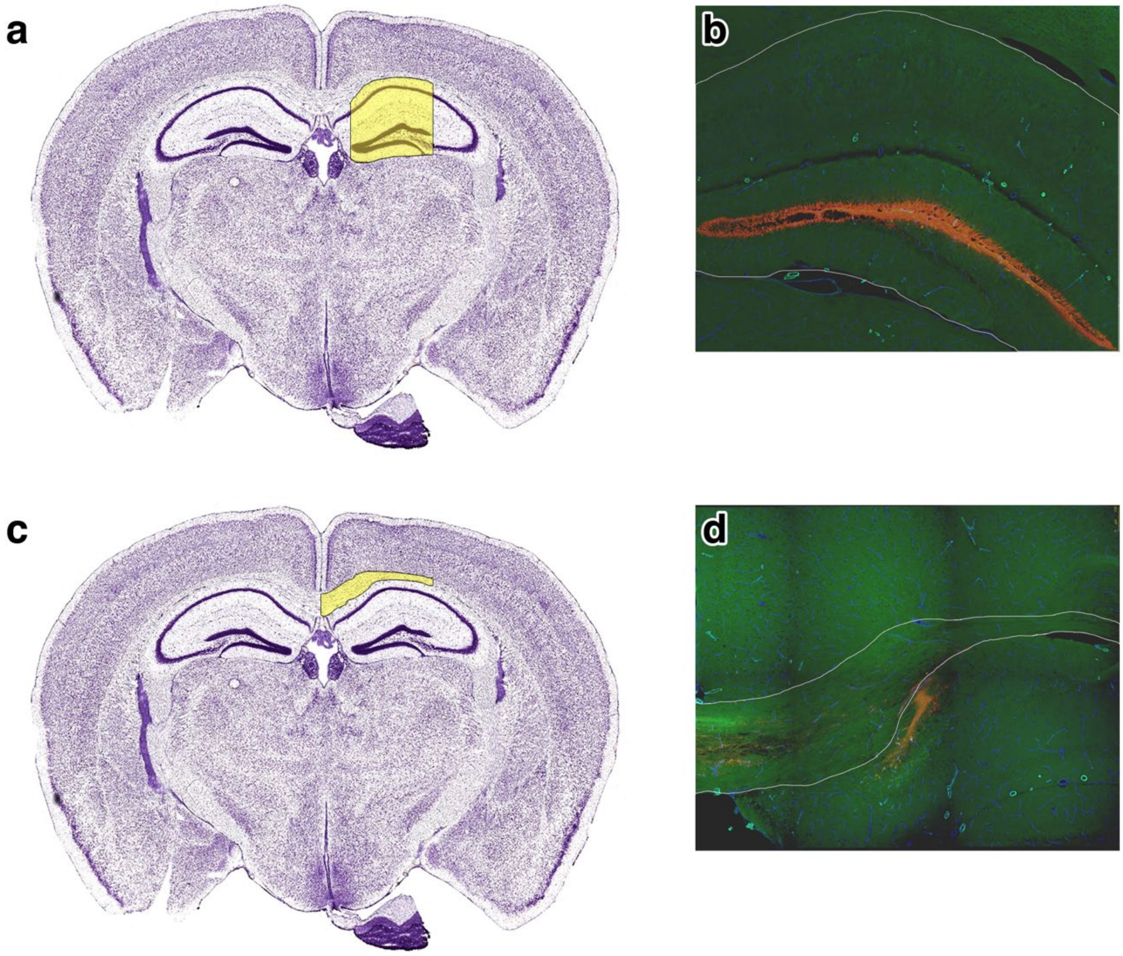

Figure 2.10 Selection of regions of intertest for assessment of intramural periarterial drainage

Regions of interest for assessment of IPAD in the hippocampus (a, yellow area) and corpus callosum (b, yellow area). Corresponding confocal images (b & c) show demarcated regions (white lines) manually drawn in Adobe Photoshop CS6. The distribution of vessels and the number of vessels with Aβ (1-40) HiLyte Fluor 555 in their vessel walls within these regions were manually counted using Adobe Photoshop analysis tools. Images (a & c) adapted from www.mouse.brain-map.org

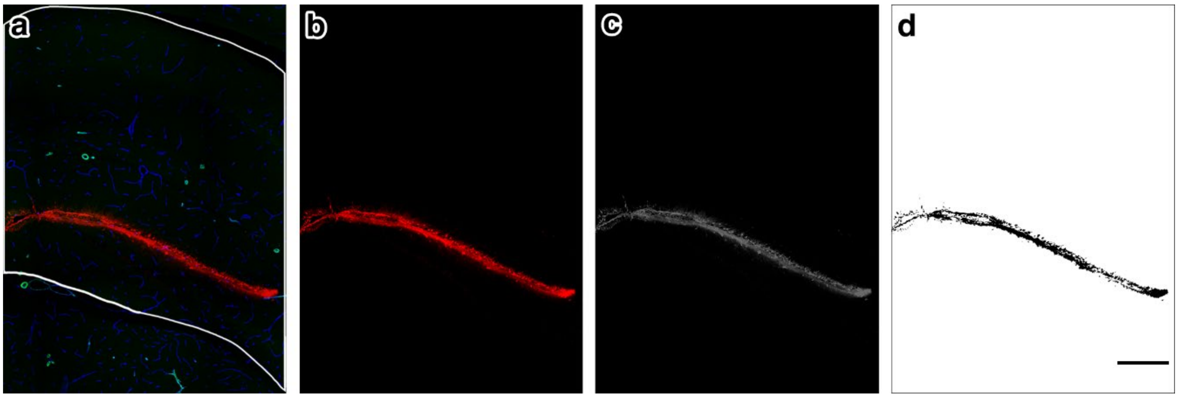

Figure 2.11 Assessment of the density of amyloid beta (1-40) in the parenchyma

Regions of interest were extracted from the confocal tile scan (a) and split into its subsequent colour channels. The red channel (Aβ (1-40)) (b) was imported into ImageJ, converted into a grey scale image (c) and segmented using Image thresholding (d). Fluorescent intensity was calculated using the ImageJ RawIntDen function and presented as overall fluorescent area and intensity per 0.5mm^2. For this sample the overall surface area of the region of interest is 1271335.49 μm^2, the surface area of the fluorescent signal is 108972.03 μm^2 and the RawIntDen fluorescent intensity is 17.13 x10^6 per 0.5mm^2.

2.5 ASSESSMENT OF CEREBRAL BLOOD FLOW IN ALPHA-DYSTROBREVIN DEFICIENT MICE (CHAPTER 6)

To asses for alterations to baseline cerebral blood flow (CBF) (12 – 16 week-old) α-DB deficient (B6;129-*Dtna* ^{tm1Jrs}/J) [239] (n = 10) and wild-type control mice (n = 12) were assessed using a non-invasive magnetic resonance imaging (MRI) technique (arterial spin labelling (ASL)) by colleagues at the Centre for Advanced Biomedical Imaging UCL. CBF values were generated by colleagues at UCL but statistical analysis was performed by myself using SPSS and an independent *t-test* with significance set at $P < 0.05$

A small pilot study was also performed assessing CBF in α-DB deficient mice after exposure to hypercapnia. Hypercapnia was generated by exposing 10-month old α-DB deficient (n=2) and wild-type control mice (n=3) to medical air for 5 mins, 10% CO_2 for 5 mins and then medical air for a further 10 mins. Baseline scans were normalised to the mean baseline signal (for the first 5 mins of scanning) to visualise the relative change in CBF.

2.5.1 THE THEORY OF ARTERIAL SPIN LABELLING

In ASL, tissue perfusion is quantitatively measured using magnetically labelled arterial blood water protons as an endogenous tracer [249]. The main goal is to produce two MRI images of the same static tissue slice that have different magnetisation of the inflowing blood. After acquisition of the first slice, a radiofrequency (RF) pulse is used to invert or saturate water protons in arterial blood in a second slice before it enters the region of interest. After a set delay (T1, Longitudinal relaxation) in which the magnetism of the water protons is slowly reverting back to their longitudinal magnetism (uninverted), a second slice is acquired that will have a decreased amplitude in the region of interest. A variation of this image acquisition sequence is flow alternating inversion recovery (FAIR) in which a RF pulse is applied to a large area that includes the slice that is going to be imaged. After a set T1 time, the slice is imaged to generate a control slice that contains signal from both inverted stationary water protons and non-stationary water protons. To ascertain flow or movement of the water protons, another RF pulse is then applied to the same slice to invert all the water protons just in that slice. At the same time uninverted non-stationary water protons from areas outside the slice will be flowing into the slice to generate an image that again contains both stationary (inverted) and non-stationary water protons. Both images are compared by subtraction in which the stationary inverted protons are eliminated to just leave a flow sensitive image showing signal form water photons that are uninverted and can be quantitatively assessed for CBF [249, 250]. A more detailed summary of the methods used by colleagues at the Centre for Advanced Biomedical Imaging UCL can be found in **appendix C**.

Chapter 3 LOSS OF AQUAPORIN 4 FROM ASTROCYTE ENDFEET AND THE MORPHOLOGY OF THE INTRAMURAL PERIARTERIAL DRAINAGE PATHWAY

3.1 INTRODUCTION

Aquaporin 4 (AQP4) is anchored to astrocyte endfeet by syntrophin through C-terminal tail binding to PDZ domains. Syntrophin interacts with both dystrophin (DP71) and α-dystrobrevin (α-DB) of the dystrophin associated protein complex (DPC) [139, 146] (**Figure 1.12**). In mice deficient for α-DB, AQP4 function at astrocytic endfeet is lost as AQP4 is redistributed from the endfeet to the cell body [146].

While extensive studies have investigated functional roles of AQP4, particularly in relation to oedema, the relationship between AQP4 and the structural integrity of the capillary wall and intramural periarterial drainage (IPAD) pathways has received little attention. In the limited instances where the vessel wall has been studied, the majority report no abnormalities in blood-brain barrier function or ultrastructural appearance related to the absence of AQP4 [188, 191, 195, 203]. It is worth noting that hyperpermeability of the blood-brain barrier accompanied by open endothelial tight junctions and swollen astrocyte end feet in grey matter have been reported by Zhou et al [235] in mice that do not express AQP4 [184]. However this is in direct contrast to reports by Feng X et al. who, in the same mouse model, reported no abnormalities in the blood-brain barrier, even with the presence of sporadic hydrocephalus and complete destruction of the cerebral aqueduct [195]. As yet, there are no reports of changes to other components of the vessel wall.

The majority of the aforementioned studies have focussed on cortical or striatal grey matter and not the white matter, where abnormalities in fluid homeostasis are frequently observed in cerebrovascular pathology. This is most likely due to the small amount of cerebral white matter available for study in small rodents and therefore evidence for how AQP4 relates to the structural integrity of the vessel wall, blood-brain barrier and IPAD pathways in the white matter is somewhat scarce. In a recent study we have shown a reduction in the expression of AQP4 in the white matter of human post mortem brains with cerebral amyloid angiopathy (CAA) and white matter hyperintensities (WMH) [115]. However, it is unclear if alterations in the expression of AQP4 in the white matter precede or are caused by abnormalities in fluid disturbances.

Chapter 3: Introduction

The primary aim of this chapter is to investigate whether the loss of AQP4 from astrocytic endfeet alters the morphology of the vessel wall and IPAD pathways. This is to support work in chapter 4 of this thesis in which mice deficient for αDB are investigated for morphology of the vessel wall and IPAD pathways. It is therefore essential to be able to distinguish any differences in the structure of the vessel wall and IPAD pathway between these mice.

Transmission electron microscopy (TEM) was applied to firstly analyse the ultrastructure of capillaries in the grey matter and secondly to compare these to capillaries in the white matter of mice deficient for AQP4.

3.2 HYPOTHESIS

In mice that do not express glial aquaporin 4, the morphology of capillary intramural periarterial drainage pathways is altered.

3.3 AIMS

The work detailed in this chapter aims to investigate whether the loss of AQP4 from astrocytic endfeet alters the morphology of the capillary wall and IPAD pathway. A mouse model that does not express glial AQP4 (see **section 2.1**) is used to perform a detailed ultrastructural study of the capillary wall (see **section 2.2**), the first entry point for periarterial drainage (**Figure 3.1**).

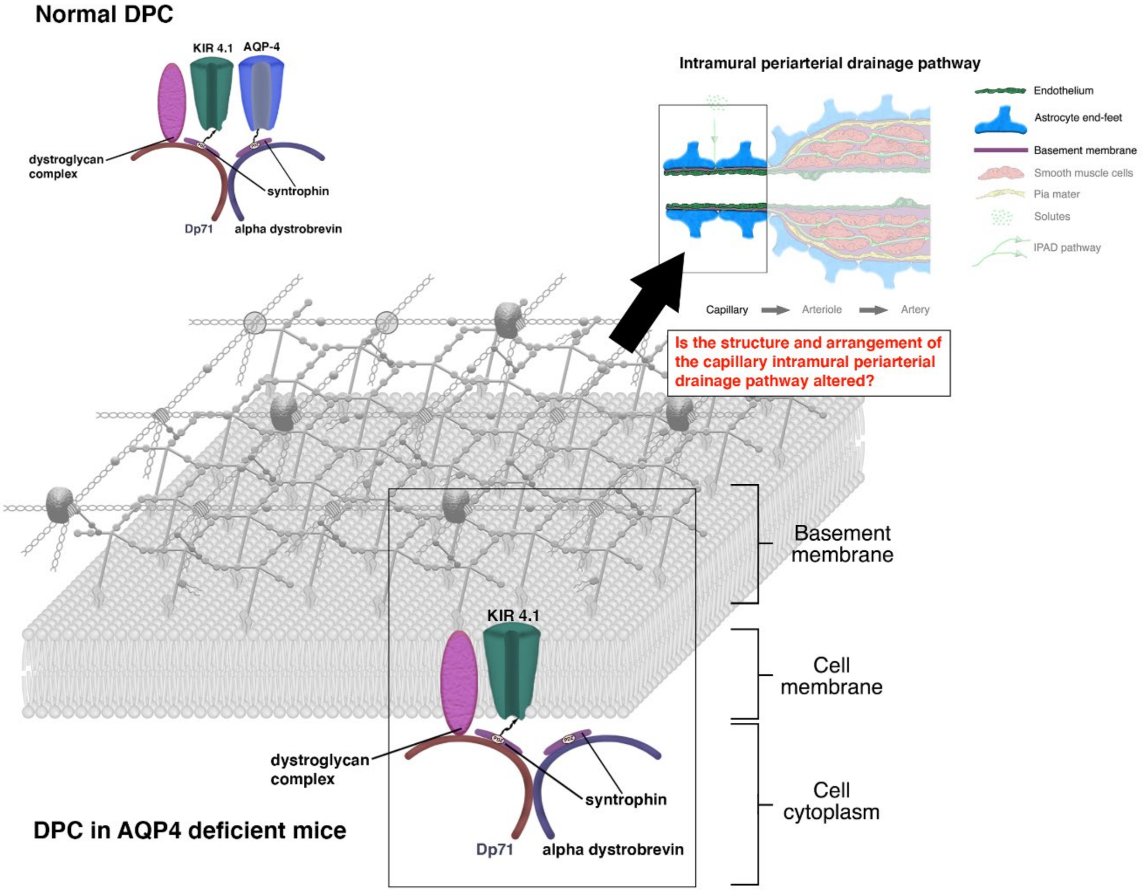
Normal DPC
KIR 4.1
AQP-4
dystroglycan complex
syntrophin
Dp71
alpha dystrobrevin
Intramural periarterial drainage pathway
Endothelium
Astrocyte end-feet
Basement membrane
Smooth muscle cells
Pia mater
Solutes
IPAD pathway
Capillary
Arteriole
Artery
Is the structure and arrangement of the capillary intramural periarterial drainage pathway altered?
Basement membrane
Cell membrane
Cell cytoplasm
KIR 4.1
dystroglycan complex
syntrophin
DPC in AQP4 deficient mice
Dp71
alpha dystrobrevin

Figure 3.1 AQP4 and its deletion from the dystrophin associated protein complex in astrocyte endfeet

Does the loss of AQP4 from astrocytic endfeet alter the morphology of the capillary intramural periarterial drainage pathway?

3.4 MATERIALS & METHODS

For this chapter, brains from AQP4 deficient (n = 2) (generated by Ikeshima-Kataoka et el. at Keio University, Japan [238]) and wild-type control mice (n = 2) were processed for TEM by colleagues in Keio University, Japan following our published protocols [160, 243]. For more details see **sections 2.1.1** and **2.2**

Tissue embedded in resin blocks was sectioned and prepared for TEM as detailed in **section 2.2**. Imaging and analysis of the structure and arrangement of the capillary wall in grey and white matter was performed as per **sections 2.2.5** and **2.2.6**. Briefly, high resolution low power images of 20 capillaries from grey matter and 20 capillaries from white matter from each mouse were digitally photographed and analysed qualitatively for ultrastructural changes to endothelial cells, intramural cells and basement membrane. Each capillary was also quantitatively assessed for surface area measurements by image segmentation.

Statistical analysis was performed using SPSS and a univariate Analysis of Variance (two-way Anova) adjusting for repeated measures (20 per region per mouse) with significance set at $P < 0.05$. For more details see **sections 2.2.7**

3.5 RESULTS

3.5.1 ULTRASTRUCTURAL ASSESSMENT OF THE CAPILLARY WALL IN GREY AND WHITE MATTER IN AQP4 DEFICIENT MICE

To establish whether a lack of AQP4 at astrocyte endfeet affects the morphology of the capillary wall, the structural appearance of endothelium, intramural cells and basement membrane of capillaries from the white matter and grey matter in AQP4 deficient mice were analysed by electron microscopy.

When compared to wild-type control mice, electron microscopy revealed the appearance of the capillary wall to be unaltered in AQP4 deficient mice with no visible differences in the endothelium, intramural cells or basement membrane in either grey or white matter capillaries. There was also no difference in the appearance of the surrounding parenchyma. However, in AQP4 deficient mice the majority of the capillaries analysed appeared to be bigger in overall size as shown with the variation in the size of the scale bars on the electron micrographs shown in **b** & **Figure 3.3 b**. This was confirmed with differences in capillary size metrics in **section 3.5.2** (**Figure 3.4 & Figure 3.5**).

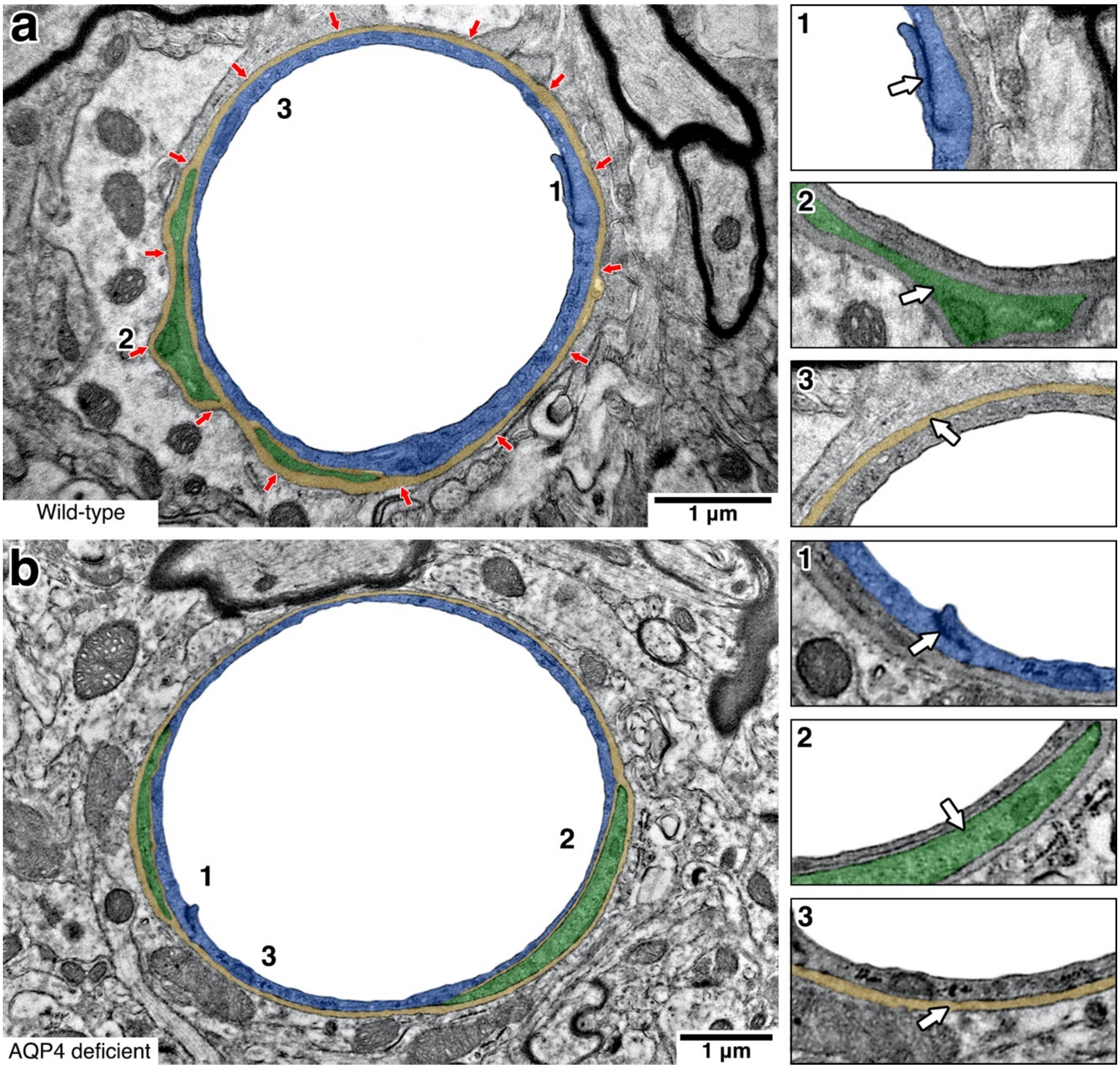

Figure 3.2 The structural appearance of the capillary wall in the grey matter appears unaltered in mice deficient for AQP4

Electron micrographs false coloured to highlight the endothelium (blue), intramural cells (green) and basement membrane (orange). The structural appearance of the capillary wall in AQP4 deficient mice (b) appears to be unaltered in the grey matter when compared to wild-type control mice (a). Endothelial cells and tight junctions (b1 & a1, blue), intramural cells (b2 & a2, green) and basement membranes (b3 & a3, orange) appeared similar in both genotypes. Note that in AQ4 deficient mice (b) the scale bar is smaller due to the majority of the capillaries appearing larger. The red arrows in (a) indicate the location of glial AQP4 in wild-type control mice.

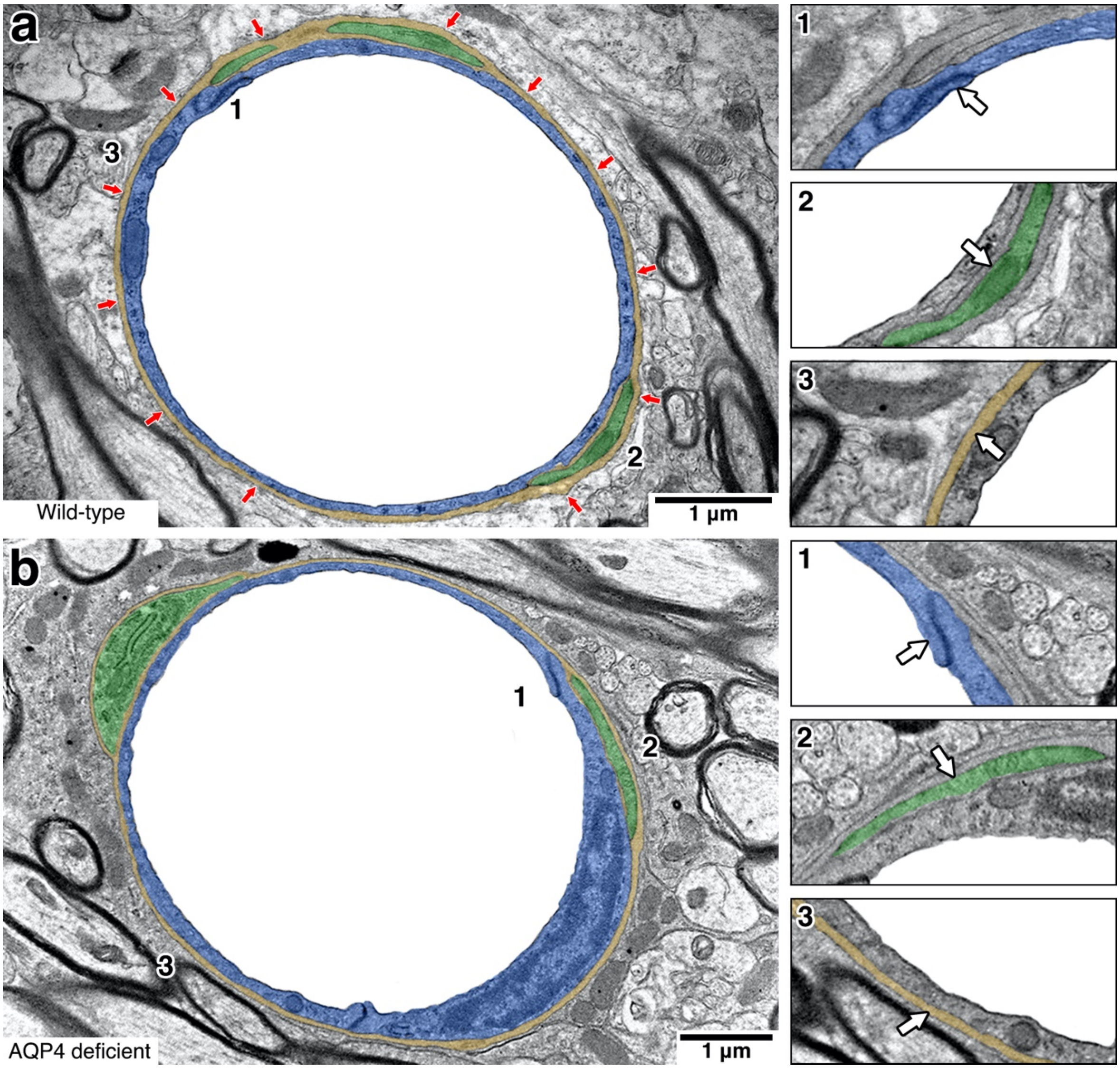

Figure 3.3 The structural appearance of the capillary wall in the white matter appears unaltered in mice deficient for AQP4

Electron micrographs false coloured to highlight the endothelium (blue), intramural cells (green) and basement membrane (orange). The structural appearance of the capillary wall in AQP4 deficient mice (b) appears to be unaltered in the white matter when compared to wild-type control mice (a). Endothelial cells and tight junctions (b1 & a1, blue), intramural cells (b2 & a2, green) and basement membranes (b3 & a3, orange) appeared similar in both genotypes. Note that as with capillaries in the grey matter, in AQ4 deficient mice (b) the scale bar is smaller due to the majority of the capillaries appearing larger in the white matter. The red arrows in (a) indicate the location of glial AQP4 in wild-type control mice.

3.5.2 IMAGE SEGMENTATION AND SURFACE AREA MEASUREMENTS

As no overall differences in structural appearance, other than size, was noted by electron microscopy in capillaries of grey matter and white matter between wild-type control and AQP4 deficient mice, we next assessed each capillary (n = 20 per region per mouse) for changes in composition of the vessel wall. Image segmentation was performed to measure each capillary for the surface area of the vessel wall, endothelium, intramural cells, basement membrane, lumen and overall area.

Differences between capillaries in grey and white matter in each genotype were analysed.

3.5.2.1 COMPARISON OF CAPILLARIES IN WHITE AND GREY MATTER IN WILD-TYPE CONTROL MICE

In wild-type control mice, Univariate Analysis of Variance (two-way Anova with $P < 0.05$) revealed no significant differences between any of the variables measured in capillaries between grey and white matter (**Table 1**).

3.5.2.2 COMPARISON OF CAPILLARIES IN WHITE AND GREY MATTER IN AQP4 DEFICIENT MICE

Similar to the wild-type control mice, in AQP4 deficient mice Univariate Analysis of Variance (two-way Anova with $P < 0.05$) also revealed no significant differences between any of the variables measured in capillaries between grey and white matter (**Table 2**).

		Grey matter	White matter	Sig.
Overall vessel size	Mean	**14.53 μm^2**	**15.16 μm^2**	0.675
	Range	(9.10 – 24.04 μm^2)	(8.57 – 29.63 μm^2)	
	S.D	4.52	4.76	
	S.E	1.01	1.06	
Lumen	Mean	**11.45 μm^2**	**8.50 μm^2**	0.057
	Range	(6.61 – 18.96 μm^2)	(6.10 – 23.36 μm^2)	
	S.D	3.76	3.95	
	S.E	0.84	0.88	
Vessel wall	Mean	**3.08 μm^2**	**3.29 μm^2**	0.454
	Range	(2.04 – 5.17 μm^2)	(2.23 – 6.27 μm^2)	
	S.D	0.93	0.96	
	S.E	0.21	0.22	
Endothelium	Mean	**1.93 μm^2**	**1.87 μm^2**	0.773
	Range	(1.27 – 3.16 μm^2)	(1.15 – 3.28 μm^2)	
	S.D	0.60	0.54	
	S.E	0.13	0.12	
Intramural cells	Mean	**0.35 μm^2**	**0.45 μm^2**	0.228
	Range	(0.06 – 0.77 μm^2)	(0.10 – 1.31 μm^2)	
	S.D	0.17	0.27	
	S.E	0.04	0.06	
Basement membrane	Mean	**0.80 μm^2**	**0.88 μm^2**	0.271
	Range	(0.46 – 1.38 μm^2)	(0.64 – 1.68 μm^2)	
	S.D	0.24	0.26	
	S.E	0.05	0.06	

Table 1: Comparison of capillary size metrics between grey and white matter in wild-type control mice

		Grey matter	White matter	Sig.
Overall vessel size	Mean	**19.90 μm^2**	**21.32 μm^2**	0.463
	Range	(11.10 – 34.06 μm^2)	(11.39 – 35.51 μm^2)	
	S.D	6.42	6.84	
	S.E	1.44	1.53	
Lumen	Mean	**15.58 μm^2**	**17.16 μm^2**	0.295
	Range	(8.75 – 27.44 μm^2)	(9.07 – 29.60 μm^2)	
	S.D	5.22	5.61	
	S.E	1.17	1.25	
Vessel wall	Mean	**4.32 μm^2**	**4.16 μm^2**	0.764
	Range	(2.35 – 8.79 μm^2)	(2.32 – 7.56 μm^2)	
	S.D	1.59	1.52	
	S.E	0.35	0.34	
Endothelium	Mean	**2.65 μm^2**	**2.43 μm^2**	0.547
	Range	(1.43 – 5.73 μm^2)	(1.37 – 4.14 μm^2)	
	S.D	1.10	0.90	
	S.E	0.25	0.20	
Intramural cells	Mean	**0.59 μm^2**	**0.72 μm^2**	0.286
	Range	(0.19 – 1.39 μm^2)	(0.25 – 1.77 μm^2)	
	S.D	0.33	0.44	
	S.E	0.07	0.10	
Basement membrane	Mean	**1.08 μm^2**	**1.00 μm^2**	0.511
	Range	(0.60 – 2.28 μm^2)	(0.57 – 1.73 μm^2)	
	S.D	0.37	0.31	
	S.E	0.08	0.07	

Table 2: Comparison of capillary size metrics between grey and white matter in AQP4 deficient mice

3.5.2.3 COMPARISON OF CAPILLARIES IN WHITE AND GREY MATTER BETWEEN WILD-TYPE CONTROL AND AQP4 DEFICIENT MICE

In the grey matter of AQP4 deficient mice, capillaries had significantly larger lumina (15.58 μm^2 vs. 11.45 μm^2, $p < 0.001$). A significant difference in vessel area (19.90 μm^2 vs. 14.53 μm^2, $p < 0.001$) was accompanied by significant changes to the endothelium (2.65 μm^2 vs. 1.93 μm^2, $p < 0.05$), intramural cells (0.59 μm^2 vs. 0.35 μm^2, $p < 0.05$) and basement membrane (1.08 μm^2 vs. 0.80 μm^2, $p < 0.01$) (**Figure 3.4**).

Similar differences were observed in the white matter. Again, capillaries were found to be larger in AQP4 deficient mice with significantly larger lumina (21.32 μm^2 vs. 15.16 μm^2, $p < 0.001$). The vessel wall area was again significantly different (4.16 μm^2 vs. 3.29 μm^2, $p < 0.05$) with significant changes to the endothelium (2.43 μm^2 vs. 1.87 μm^2, $p < 0.05$) and intramural cells (0.72 μm^2 vs. 0.45 μm^2, $p < 0.05$) but not basement membrane (1.00 μm^2 vs. 0.88 μm^2, $p = 0.208$) (**Figure 3.5**).

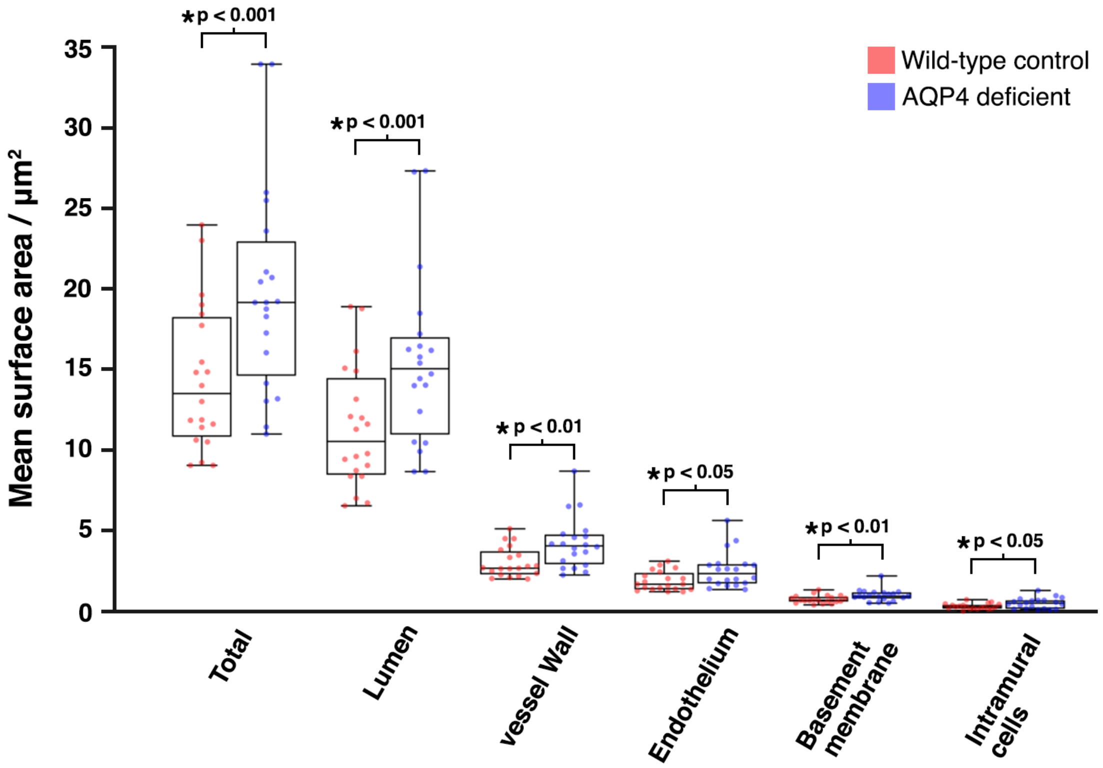

Figure 3.4 Summary of capillary size metrics in grey matter between wild-type control and AQP4 deficient mice

Significant differences were observed in mean total vessel surface area and areas of lumen, vessel wall, endothelium, basement membrane and intramural cells in the grey matter between wild-type control (red) and AQP4 deficient mice (blue). Total mean vessel surface area is the sum of vessel wall area and lumen area. Each box plot represents the range of data from two mice. The scatter plots represent the means of repeated measures (20 per mouse, n = 2).

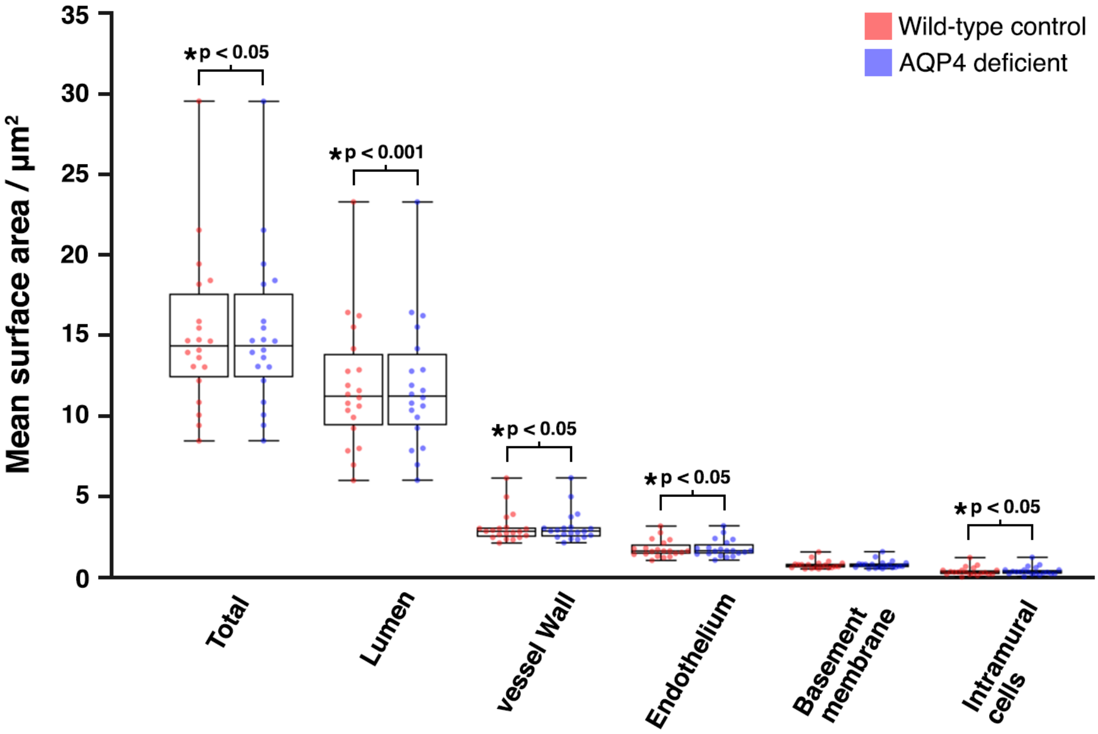

Figure 3.5 Summary of capillary size metrics in white matter between wild-type control and AQP4 deficient mice

Significant differences were observed in mean total vessel surface area and areas of lumen, vessel wall, endothelium, intramural cells but not basement membrane in the white matter between wild-type control (red) and AQP4 deficient mice (blue). Each box plot represents the range of data from two mice. The scatter plots represent the means of repeated measures (20 per mouse, n = 2).

3.5.2.4 COMPARISON OF VASCULAR WALL COMPOSITION IN CAPILLARIES FROM GREY AND WHITE MATTER BETWEEN WILD-TYPE CONTROL AND AQP4 DEFICIENT MICE

As capillaries in AQP4 deficient mice appeared significantly larger than those in wild-type control mice we next investigated if the differences in the size of the vessel and thickness of the vessel wall in the white vs. grey matter rather than genotype were responsible for the observed changes in endothelium, intramural cells and basement membrane. To account for variation in vessel size, the surface areas obtained for endothelium, intramural cells and basement membrane were normalised against the surface area of the capillary wall by converting into percentage surface area.

We first assessed each genotype for differences between grey and white matter. In wild-type control mice there were no differences in the percentage surface area of the vessel wall occupied by endothelium (62.13% vs. 58.78%, $p = 0.068$), intramural cells (11.30% vs. 13.37%, $p = 0.205$) or basement membrane (26.57% vs. 27.85%, $p = 0.199$). This was also observed in AQP4 deficient mice (endothelium, 60.98% vs. 58.17%, $p = 0.156$, basement membrane 26.28% vs. 25.12%, $p = 0.291$), other than the surface area occupied by intramural cells which was higher in the white matter (12.83% vs. 16.71%, $p < 0.05$) (**Figure 3.6**).

We next analysed for differences in the percentage surface area of the vessel wall occupied by endothelium, intramural cells or basement membrane in grey and white matter between the genotypes. In grey matter, there was no significant difference but in the white matter there was a significant difference in the percentage surface area of the vessel wall occupied by basement membrane (27.85 vs. 25.12%, $p < 0.01$) (**Figure 3.6**).

These results suggest that our first observations showing changes in the surface areas of the vessel wall, endothelium, basement membrane and intramural cells between genotypes were most likely influenced by differences in the vessel size and it appears that only the capillary basement membrane is altered in the white matter of AQP4 deficient mice when compared to wild-type control mice. Capillaries in the grey matter show no alterations to the endothelium, basement membrane or intramural cells.

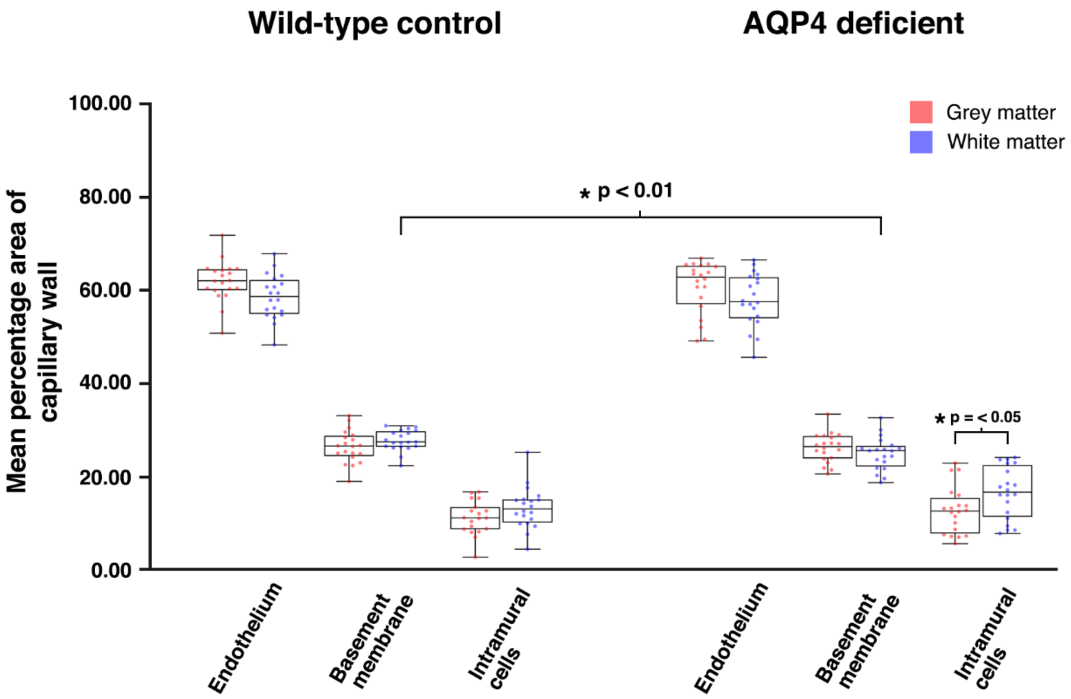

Figure 3.6 Summary showing overall mean values for the percentage of the vessel wall occupied by endothelium, intramural cells and basement membrane between wild-type control and AQP4 deficient mice in white and grey matter

In wild-type control mice, no significant differences were observed in the mean percentage area of the capillary wall occupied by endothelium, basement membrane or intramural cells between grey and white matter. In AQP4 deficient mice intramural cells occupied a larger surface area of the vessel wall in the white matter compared to grey matter. There was no significant difference in the percentage surface area of the vessel wall occupied by the endothelium, intramural cells and basement membrane in capillaries from grey matter between wild-type control and AQP4 deficient mice. In the white matter, AQP4 deficient mice showed a significantly lower percentage surface area of the vessel wall occupied by basement membrane compared to the white matter of wild-type control mice. Each box plot represents the range of data from two mice. The scatter plots represent the means of repeated measures (20 per mouse, n = 2).

3.6 DISCUSSION

The objective of the work in this chapter was to test the hypothesis that in mice that do not express glial aquaporin 4 the morphology of capillary intramural periarterial drainage pathways will be altered. This was investigated by using TEM to perform a detailed analysis of the size, structure and cellular composition of the capillary wall in grey and white matter of AQP4 deficient mice. This information is needed so that any differences in the structure of the vessel wall and IPAD pathway between mice deficient for AQP4 and αDB can be distinguished.

3.6.1 AQP4 AND GREY MATER

The results in this chapter suggest that in the grey matter, the presence of AQP4 anchored to astrocyte endfeet by the DPC does not appear to be essential for the morphology of the capillary wall. In AQP4 deficient mice there were no notable differences in the ultrastructural appearance or surface area of the capillary wall occupied by endothelium, intramural cells or basement membrane. Endothelial tight junctions appeared normal and there were no obvious signs of altered fluid homeostasis such as swollen astrocyte end feet. These findings are in agreement with other studies that also show AQP4 deficient mice have no abnormalities in the function of the blood-brain barrier in the grey matter [188, 191, 195, 203].

3.6.2 AQP4 AND WHITE MATTER

In the white matter, the ultrastructural appearance of the endothelium, intramural cells and basement membrane was not affected by AQP4 genotype. Similar to grey matter, there were no morphological indicators of altered fluid homeostasis and the endothelial tight junctions appeared normal in AQP4 deficient mice. Quantitative assessment showed that in AQP4 deficient mice there was a significant reduction in the percentage surface area of the vessel wall occupied by basement membrane with a corresponding upwards trend in percentage surface area of intramural cells but no evidence of astrocyte swelling or disrupted vessel wall. This suggests that either the loss of AQP4 function is altering the capillary basement membrane without showing any morphological indicators of altered fluid homeostasis or the presence of AQP4 anchored by the DPC to astrocyte endfeet in some way, helps to maintain the integrity of the basement membranes in the white matter. The white matter is highly susceptible to alterations in fluid homeostasis, as seen with swelling after acute CNS injury [116, 209, 210] in the elderly, after stroke and in dementia [211]. It is most likely that the modifications seen accompanying the loss of AQP4 function impact upon the interstitial fluid homeostasis (ISF) in the white matter.

The increase in the surface area of intramural cells seen in AQP4 deficient mice suggests that the number and/or size of pericytes are increased, reflecting an increase in their function of maintaining an efficient blood-brain barrier [251]. Recent evidence from human post-mortem studies demonstrate there is a reduction of 35-45% of pericytes in the white matter of vascular dementia (VaD) or Alzheimer's disease [81], which is in contrast to the findings in the AQP4 deficient model, suggesting that this model does not reflect the pathological findings of VaD. Furthermore, there were no morphological modifications observed in the capillary wall in the grey matter of mice deficient for AQP4. Since there are functional changes to AQP4 in brain tumours [104, 105], cerebral ischemia [106, 107] and traumatic brain injury [108], it appears that the predominant role of AQP4 in the brain is to respond to altered water homeostasis initiated by pathology, playing a fundamental role in oedema resolution associated with modifications of the vascular wall.

3.6.3 CONCLUSIONS

In the grey matter of AQP4 deficient mice, the morphology of the capillary wall is similar to that of the wild-type mice. However, the surface area occupied by basement membrane is reduced in capillary walls in the white matter of AQP4 deficient mice compared to wild-type mice. AQP4 deficient mice also showed an increase in surface area occupied by intramural cells in the white matter compared to grey matter in contrast to recent evidence from human post-mortem studies [81]. Other cerebral vessels such as arterioles were not analysed for possible changes to the vessel wall. Future work incorporating other vessels types would help to ascertain if the observations reported here are limited to capillaries.

The AQP4 deficient mice used in this study were not tested for their efficiency in the IPAD of solutes. However, recent studies have demonstrated that in AQP4 deficient mice there is a normal interchange of cerebrospinal fluid with ISF and the diffusion of tracers through the brain parenchyma was non-directional and size dependent suggesting that drainage by IPAD would be unaffected [166, 252, 253].

In conclusion, the results in this chapter demonstrate that anchoring of AQP4 to astrocyte endfeet by association with α-DB and the DPC is important for the structure and arrangement of the capillary wall in the white matter alone and not the grey matter.

It is important to note that sample group size was limited in this study due to tissue samples used from our collaborators in Japan. This was mitigated by increasing the number of vessels analysed per sample.

Chapter 4 LOSS OF ALPHA-DYSTROBREVIN FROM ASTROCYTE ENDFEET AND THE MORPHOLOGY OF THE INTRAMURAL PERIARTERIAL DRAINAGE PATHWAY

4.1 INTRODUCTION

α-dystrobrevin (α-DB), a key intracellular protein of the dystrophin associated protein complex (DPC), indirectly anchors transcellular proteins such as aquaporin 4 (AQP4) to the cell membrane through its interaction with syntrophin [139, 146] (**Figure 1.12**). This interaction is disrupted in mice deficient for α-DB, as the mutation leads to mislocalisation of transcellular proteins (potassium channel Kir4.1 and AQP4) from astrocyte endfeet to the astrocyte cell body [139, 146, 147]. Work in the previous chapter demonstrated that loss of AQP4 from astrocyte endfeet does not significantly alter morphology of the capillary wall and IPAD pathways in the grey matter. A reduction in the percentage surface area of capillary basement membrane was observed in the white matter, most likely as a consequence of loss of AQP4 function.

Previous studies show that in α-DB deficient mice, there are alterations to blood-brain barrier function at 3 months of age, demonstrated by increased perivascular extravasations of both injected Evans blue dye and blood-borne proteins in the brain. At 18 months of age these mice display disrupted endothelial cells and astrocyte endfeet [146] but there are no reports detailing the anatomy of the cerebral vasculature in young α-DB deficient mice.

A key feature in cerebral small vessel disease (CSVD) and vascular dementia (VaD) is remodelling of the extracellular matrix (ECM). In particular, changes to collagen IV (COL4) and laminin, critical proteins for ECM stability, are altered in animal models of ageing [74], in animal models of vascular dysfunction such as the spontaneously hypertensive rat (SHR) [173], in human ageing [68] and in neurodegenerative disease such as Alzheimer's Disease (AD) [69] and Parkinson's disease [254]. Reduced levels of laminin have been associated with changes in capillary basement membrane in aged mice in regions of the brain most affected by CSVD. The occurrence of cerebral amyloid angiopathy (CAA) in these regions, together with alterations to other extracellular matrix proteins such as fibronectin, perlecan, nidogens and COL4 [74] suggest a strong link between alterations to ECM proteins and reduced fluid clearance by intramural periarterial drainage (IPAD). Astrocytes cultured from α-DB deficient mice produce ECM with less laminin compared to normal wild-type astrocytes and have abnormal interactions with brain endothelial cells [146]. However, the effect of the α-DB protein on other ECM proteins, such as COL4 is not known. This is important in the context of understanding the mechanisms behind CSVD.

In this chapter, mice that do not express α-DB are used to test the hypothesis that the absence of α-DB from astrocyte endfeet alters the morphology of the capillary wall and IPAD pathways. Transmission electron microscopy (TEM) is used to analyse the ultrastructure of capillaries in the grey matter and then compare these to those in the white matter. Immunohistochemistry for components of the ECM is used on both white and grey matter to analyse changes in composition of capillary basement membrane.

4.2 HYPOTHESIS

In mice genetically modified for alpha-dystrobrevin, the morphology of capillary intramural periarterial drainage pathways are altered.

4.3 AIMS

The work detailed in this chapter aims to investigate whether the loss of α-DB from astrocytic endfeet alters the morphology of the capillary wall and IPAD pathways. Mice deficient for α-DB are used to perform a detailed ultrastructural study of the capillary wall in grey and white matter using electron microscopy. The basement membrane marker COL4 is assessed using immunohistochemistry (**Figure 4.1**).

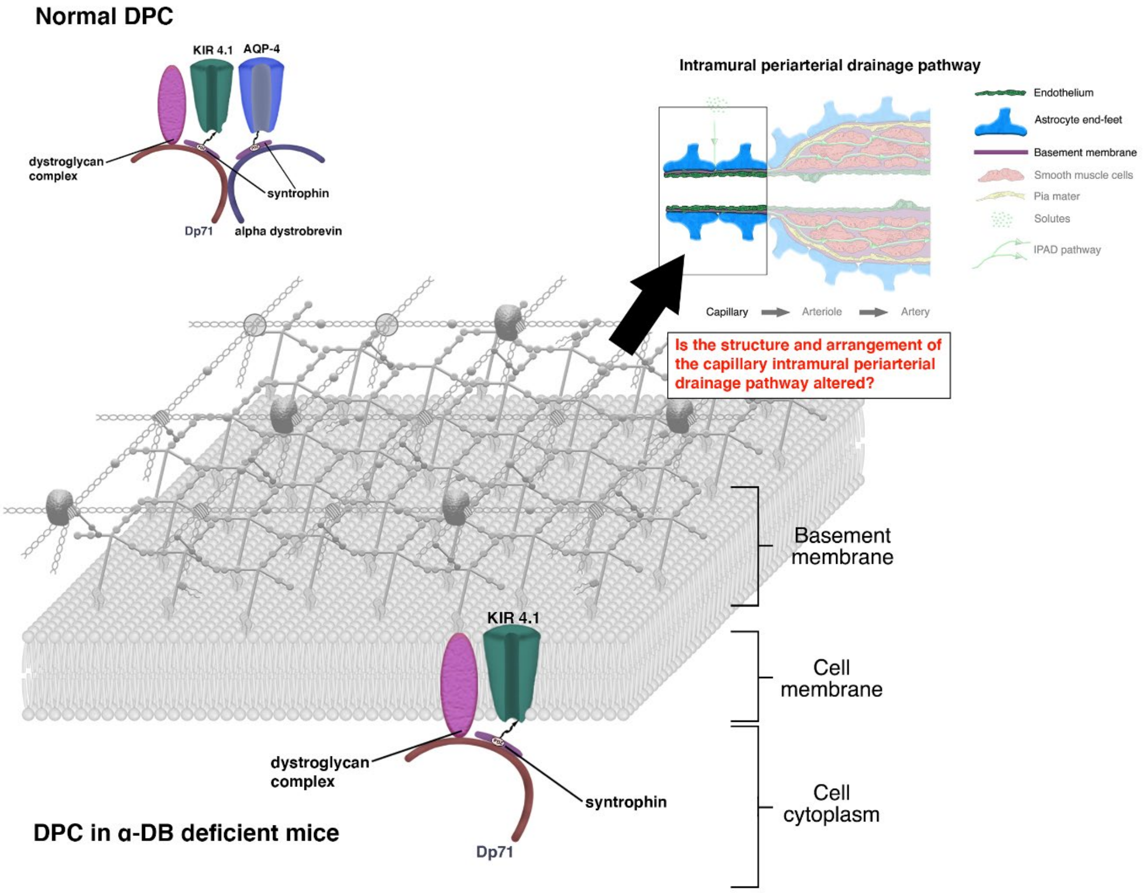
Normal DPC
KIR 4.1
AQP-4
dystroglycan complex
syntrophin
Dp71
alpha dystrobrevin
Intramural periarterial drainage pathway
Endothelium
Astrocyte end-feet
Basement membrane
Smooth muscle cells
Pia mater
Solutes
IPAD pathway
Capillary
Arteriole
Artery
Is the structure and arrangement of the capillary intramural periarterial drainage pathway altered?
Basement membrane
Cell membrane
Cell cytoplasm
KIR 4.1
dystroglycan complex
syntrophin
Dp71
DPC in α-DB deficient mice

Figure 4.1 alpha dystrobrevin and the dystrophin associated protein complex

Does the loss of α-DB from astrocytic endfeet alter the morphology of the capillary intramural periarterial drainage pathway?

4.4 MATERIALS & METHODS

For this chapter, brains from α-DB deficient mice (B6;129-*Dtna* ^{tm1Jrs}/J) [239] and wild-type control mice were either processed for TEM (n = 3 per genotype) or for immunohistochemistry (n = 3 per genotype) for COL4 (Rabbit anti-collagen IV, abcam, ab6586) following our published protocols [160, 243]. For more details see **sections 2.1.2** and **2.2**

4.4.1 TRANSMISSION ELECTRON MICROSCOPY

Tissue imbedded in resin blocks was sectioned and prepared for TEM as detailed in **section 2.2**. Imaging and analysis of the structure and arrangement of the capillary wall in grey and white matter was performed as per **sections 2.2.5** and **2.2.6**. Briefly, high resolution low power images of 20 capillaries from grey matter and 20 capillaries from white matter from each mouse were digitally photographed and analysed qualitatively for ultrastructural changes to endothelial cells, intramural cells and basement membrane. Each capillary was also quantitatively assessed for surface area measurements by image segmentation. Statistical analysis was performed using SPSS and a univariate Analysis of Variance (two-way Anova) adjusting for repeated measures (20 per region per mouse) with significance set at $P < 0.05$. For more details see **sections 2.2.7**

4.4.2 IMMUNOHISTOCHEMISTRY

Enzyme-linked immunohistochemistry using 3,3'-Diaminobenzidine (DAB) as chromogen was used to visualise COL4 positive vessels in grey and white matter using 20 μm coronal frozen sections as detailed in **section 2.3**. Statistical analysis was performed using SPSS and an independent *t-test* with significance set at $P < 0.05$.

4.5 RESULTS

4.5.1 ULTRASTRUCTURAL ASSESSMENT OF THE CAPILLARY WALL IN GREY AND WHITE MATTER IN ALPHA DYSTROBREVIN DEFICIENT MICE

To establish whether a lack of α-DB at astrocyte endfeet affects the morphology of the capillary wall, the structural appearance of endothelium, intramural cells and basement membrane of capillaries from the white matter and grey matter between α-DB deficient and wild-type control mice were compared by electron microscopy.

When compared to wild-type control mice, electron microscopy revealed the appearance of the capillary wall to be altered with a thickened basement membrane in α-DB deficient mice in both grey and white matter. There were no notable differences in the appearance of the endothelium and intramural cells or the surrounding parenchyma (**Figure 4.2** and **Figure 4.3**).

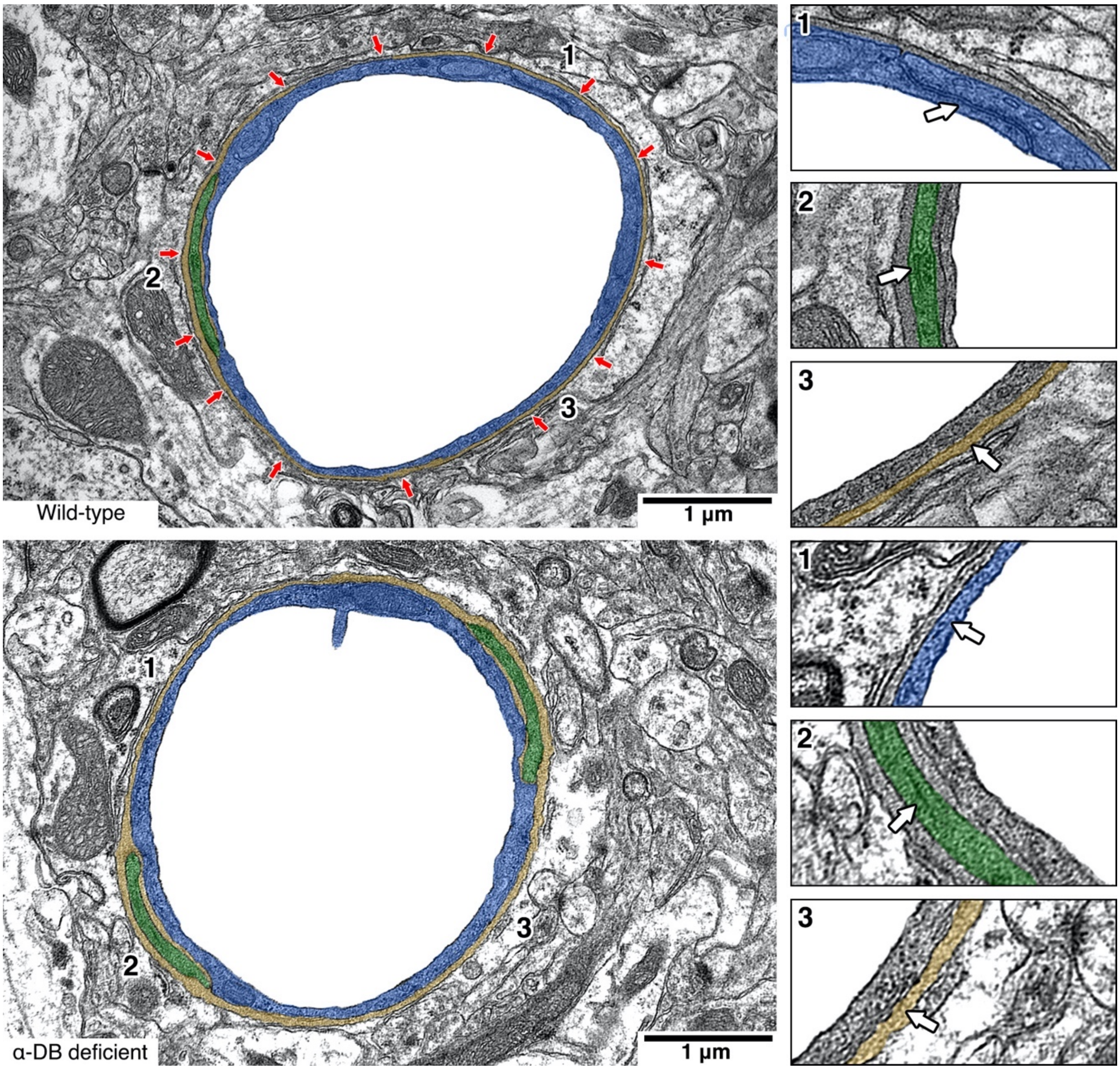

Figure 4.2 The structural appearance of the capillary wall in the grey matter appears altered in mice deficient for α-DB

Electron micrographs false coloured to highlight the endothelium (blue), intramural cells (green) and basement membrane (orange). The structural appearance of the capillary wall in α-DB deficient mice (b) appears to be altered in the grey matter when compared to wild-type control mice (a). Basement membranes (b3 & a3, orange) appear notably thicker in α-DB deficient mice. Endothelial cells and tight junctions (b1 & a1, blue) and intramural cells (b2 & a2, green) appeared similar in both genotypes. The red arrows in (a) indicate the location of glial α-DB in wild-type control mice.

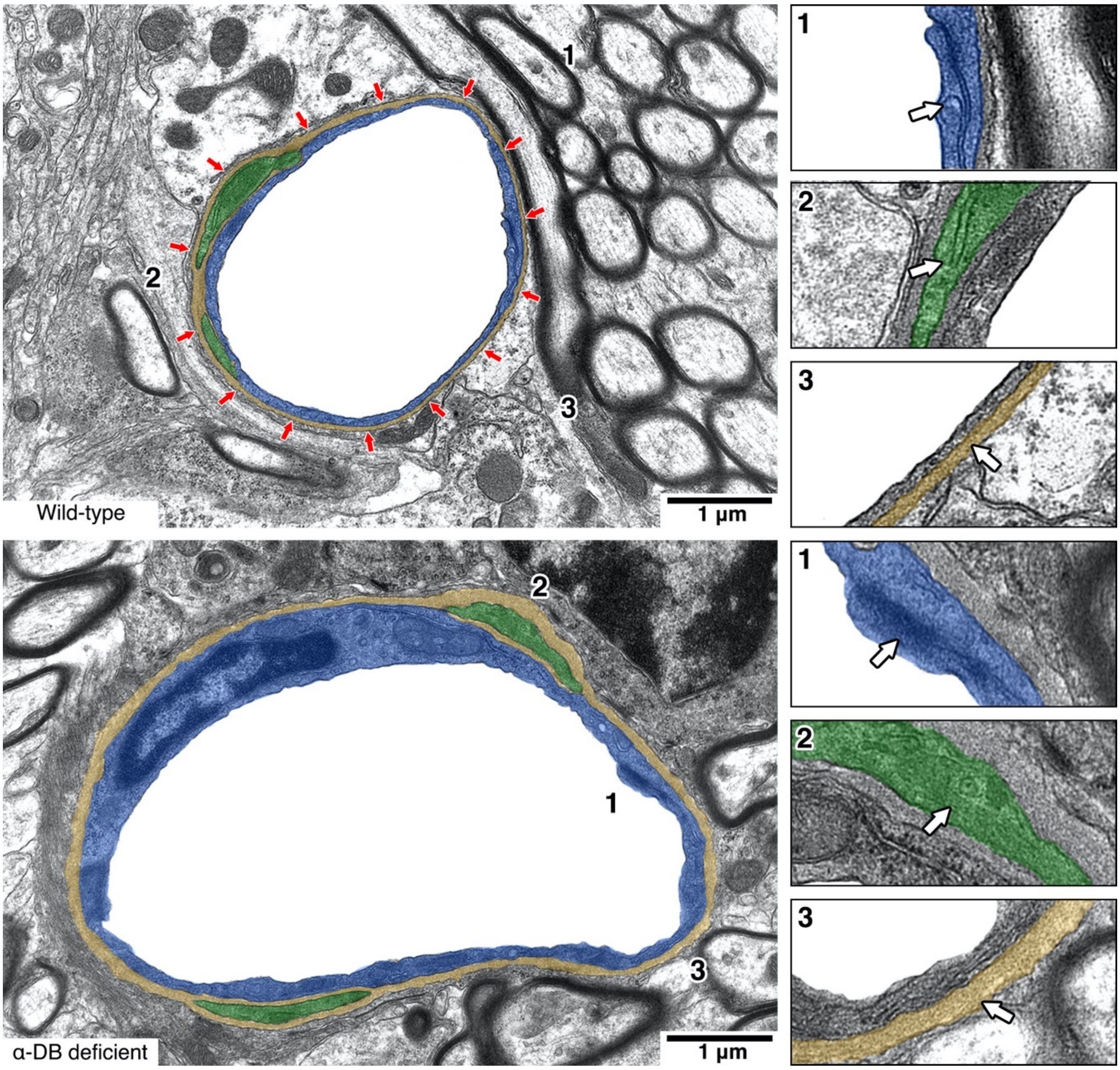

Figure 4.3 The structural appearance of the capillary wall in the white matter appears altered in mice deficient for α-DB

Electron micrographs false coloured to highlight the endothelium (blue), intramural cells (green) and basement membrane (orange). The structural appearance of the capillary wall in α-DB deficient mice (b) appears to be altered in the white matter when compared to wild-type control mice (a). Basement membranes (b3 & a3, orange) appear thicker in α-DB deficient mice. Endothelial cells and tight junctions (b1 & a1, blue) and intramural cells (b2 & a2, green) appeared similar in both genotypes. The red arrows in (a) indicate the location of glial α-DB in wild-type control mice.

4.5.2 IMAGE SEGMENTATION AND SURFACE AREA MEASUREMENTS

To confirm our observations that the capillary basement membrane appeared thicker in α-DB deficient mice, each capillary (n = 20 per region per mouse) was analysed for changes in composition of the vessel wall. Image segmentation as per chapter 3 was performed to measure each capillary for the surface area of the vessel wall, endothelium, intramural cells, basement membrane, lumen and overall area. Similar to the previous chapter, we first assessed for differences between capillaries in grey and white matter in each genotype and then compared these differences between genotypes.

4.5.2.1 COMPARISON OF CAPILLARIES IN WHITE AND GREY MATTER IN WILD-TYPE CONTROL MICE

In wild-type control mice, capillaries in the white matter appeared larger than those in the grey matter. Univariate Analysis of Variance (two-way Anova with $P < 0.05$) revealed significant differences in the surface areas of endothelium (2.37 μm^2 vs. 1.43 μm^2, $p < 0.001$), intramural cells (0.60 μm^2 vs. 0.32 μm^2, $p < 0.001$) and basement membrane (1.18 μm^2 vs. 0.65 μm^2, $p < 0.001$) resulting in larger white matter capillaries (10.59 μm^2 vs. 8.02 μm^2, $p < 0.01$) with thicker vessel walls (4.16 μm^2 vs. 2.40 μm^2, $p < 0.001$). There was no difference in the surface area of the lumen (5.62 μm^2 vs. 5.43 μm^2, $p = 0.219$) (**Table 3**).

4.5.2.2 COMPARISON OF CAPILLARIES IN WHITE AND GREY MATTER IN ALPHA DYSTROBREVIN DEFICIENT MICE

In α-DB deficient mice, capillaries in the white matter showed significantly larger surface areas of endothelium (2.16 μm^2 vs. 1.79 μm^2, $p < 0.05$), basement membrane (1.16 μm^2 vs. 0.92 μm^2, $p < 0.05$) and vessel wall (3.79 μm^2 vs. 3.08 μm^2, $p < 0.05$). However, there was no difference in overall vessel size, possibly due to the lack of significant change in the surface area of intramural cells (0.48 μm^2 vs. 0.38 μm^2, $P = 0.094$). There was also no difference in the surface area of the lumen (8.74 μm^2 vs. 8.91 μm^2, $p = 0.409$) (**Table 4).**

		Grey matter	White matter	Sig.
Overall vessel size	Mean	**8.02 µm^2**	**10.59 µm^2**	**< 0.01**
	Range	(5.67 – 10.88 µm^2)	(6.22 – 19.95 µm^2)	
	S.D	1.33	3.24	
	S.E	0.30	0.73	
Lumen	Mean	**5.62 µm^2**	**6.43 µm^2**	0.219
	Range	(3.57 – 7.71 µm^2)	(2.91 – 12.86 µm^2)	
	S.D	1.10	2.37	
	S.E	0.25	0.53	
Vessel wall	Mean	**2.40 µm^2**	**4.16 µm^2**	**< 0.001**
	Range	(2.00 – 3.22 µm^2)	(2.43 – 7.08 µm^2)	
	S.D	0.33	1.08	
	S.E	0.07	0.24	
Endothelium	Mean	**1.43 µm^2**	**2.37 µm^2**	**< 0.001**
	Range	(1.06 – 1.84 µm^2)	(1.30 – 3.81 µm^2)	
	S.D	0.19	0.58	
	S.E	0.04	0.13	
Intramural cells	Mean	**0.32 µm^2**	**0.60 µm^2**	**< 0.001**
	Range	(0.17 – 0.58 µm^2)	(0.29 – 127 µm^2)	
	S.D	0.10	0.26	
	S.E	0.02	0.06	
Basement membrane	Mean	**0.65 µm^2**	**1.18 µm^2**	**< 0.001**
	Range	(0.52 – 0.98 µm^2)	(0.84 – 2.00 µm^2)	
	S.D	0.10	0.33	
	S.E	0.02	0.07	

Table 3: Comparison of capillary size metrics between grey and white matter in wild-type control mice

		Grey matter	White matter	Sig.
Overall vessel size	Mean	**11.82 µm²**	**10.68 µm²**	0.353
	Range	(8.04 – 22.34 µm²)	(6.47 – 14.57 µm²)	
	S.D	3.34	2.82	
	S.E	0.755	0.63	
Lumen	Mean	**8.74 µm²**	**8.91 µm²**	0.409
	Range	(5.54 – 17.88 µm²)	(3.52 – 12.86 µm²)	
	S.D	2.80	2.54	
	S.E	0.63	0.57	
Vessel wall	Mean	**3.08 µm²**	**3.79 µm²**	**< 0.05**
	Range	(2.49 – 5.17 µm²)	(2.84 – 4.82 µm²)	
	S.D	0.70	0.61	
	S.E	0.16	0.14	
Endothelium	Mean	**1.79 µm²**	**2.16 µm²**	**< 0.05**
	Range	(1.24 – 2.97 µm²)	(1.61 – 2.91 µm²)	
	S.D	0.44	0.40	
	S.E	0.10	0.09	
Intramural cells	Mean	**0.38 µm²**	**0.48 µm²**	0.094
	Range	(0.18 – 0.67 µm²)	(0.22 – 0.83 µm²)	
	S.D	0.12	0.17	
	S.E	0.03	0.04	
Basement membrane	Mean	**0.92 µm²**	**1.16 µm²**	**< 0.05**
	Range	(0.67 – 1.53 µm²)	(0.83 – 1.47 µm²)	
	S.D	0.22	0.19	
	S.E	0.05	0.04	

Table 4: Comparison of capillary size metrics between grey and white matter in α-DB deficient mice

4.5.3 COMPARISON OF CAPILLARIES IN WHITE AND GREY MATTER BETWEEN WILD-TYPE CONTROL AND ALPHA DYSTROBREVIN DEFICIENT MICE

As observed in the previous chapter with AQP4 deficient mice, capillaries in the grey matter of α-DB deficient mice were also significantly larger in overall surface area (11.82 μm^2 vs. 8.02 μm^2, $p < 0.01$) with larger lumina (8.74 μm^2 vs. 5.62 μm^2, $p < 0.001$) than those in wild-type controls. A Significant difference in vessel wall area was observed (3.08 μm^2 vs. 2.40 μm^2, $p = < 0.001$) with changes to the endothelium (1.79 μm^2 vs. 1.43 μm^2, $p < 0.01$) and basement membrane (0.92 μm^2 vs. 0.65 μm^2, $p < 0.001$) (**Figure 4.4**). No differences were observed in the white matter (**Figure 4.5).**

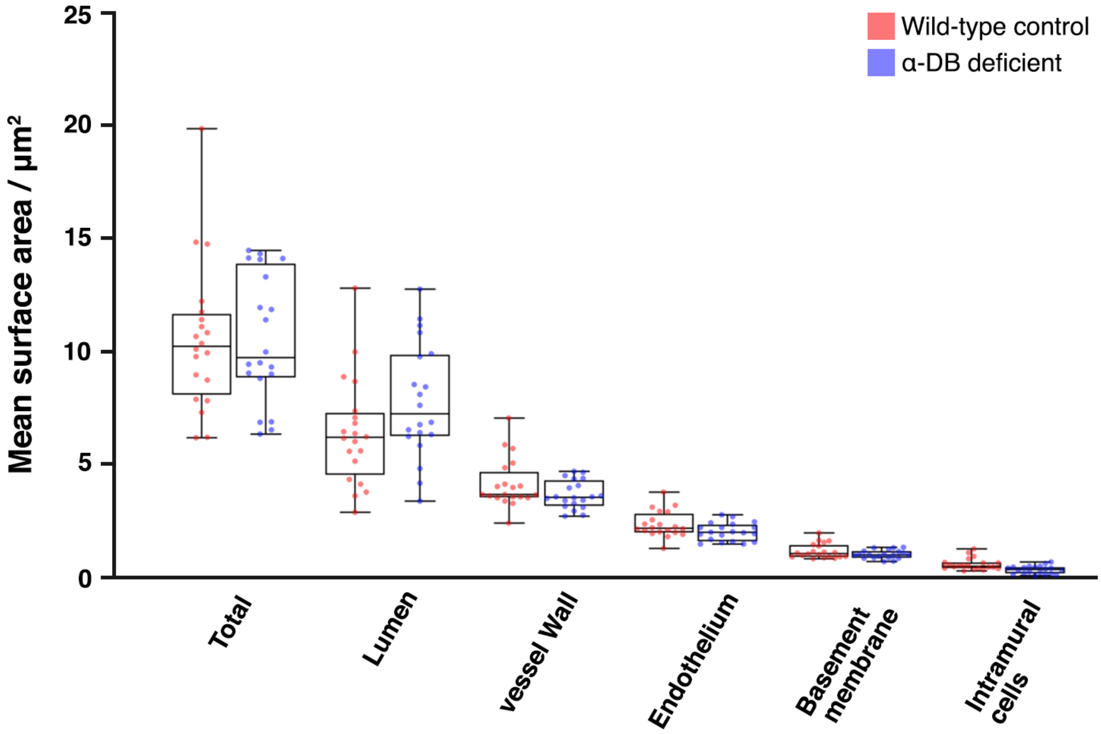

Figure 4.4 Summary of capillary size metrics in grey matter between wild-type control and α-DB deficient mice

Significant differences were observed in the mean total vessel surface area and areas of lumen, vessel wall, endothelium and basement membrane in the grey matter between wild-type control (red) and α-DB deficient mice (blue). Each box plot represents the range of data from three mice. The scatter plots represent the means of repeated measures (20 per mouse, n = 3).

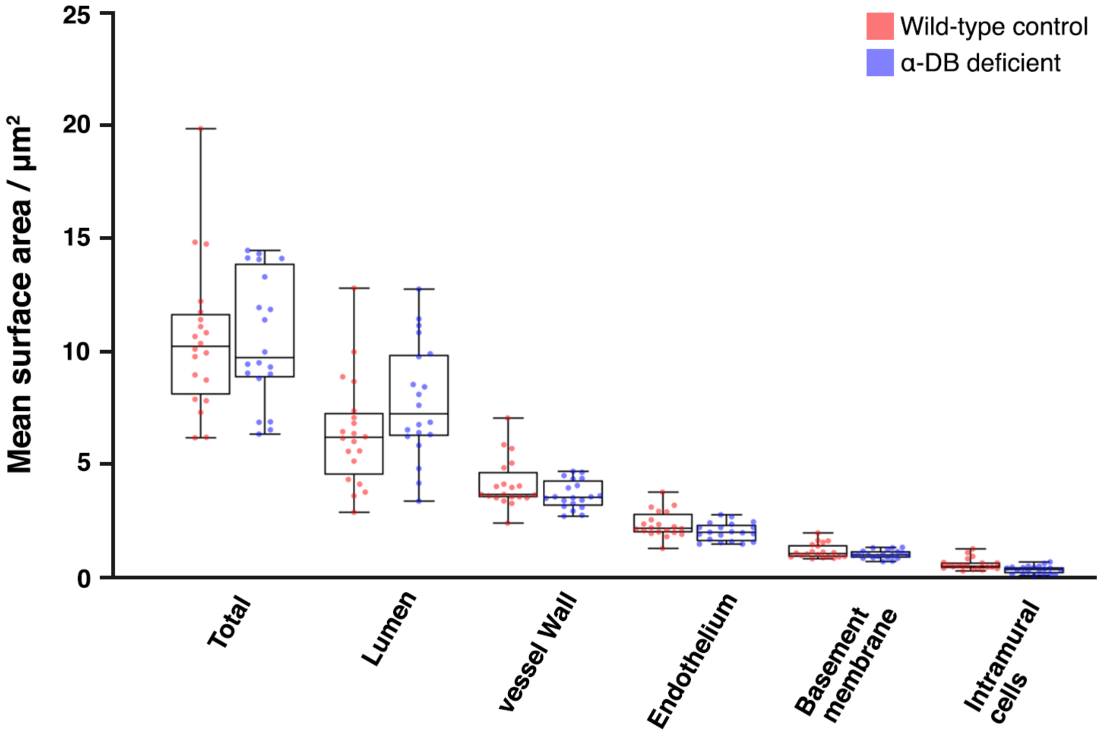

Figure 4.5 Summary of capillary size metrics in white matter between wild-type control and α-DB deficient mice

There were no significant differences in mean total vessel surface area and areas of lumen, vessel wall, endothelium, basement membrane or intramural cells in the white matter between wild-type control (red) and α-DB deficient mice (blue). Each box plot represents the range of data from three mice. The scatter plots represent the means of repeated measures (20 per mouse, n = 3).

4.5.4 COMPARISON OF VASCULAR WALL COMPOSITION IN CAPILLARIES FROM GREY AND WHITE MATTER BETWEEN WILD-TYPE CONTROL AND ALPHA DYSTROBREVIN DEFICIENT MICE

Work in the previous chapter (**chapter 3**) demonstrated that the removal of AQP4 from astrocyte endfeet in the grey matter had very little effect on the morphology of the capillary wall, after accounting for differences in vessel size by normalising data into percentage surface area. As capillaries were significantly larger in the grey matter but not in the white matter of α-DB deficient mice the same normalisation step was repeated to assess whether the differences observed in grey matter capillaries were due to vessel size or genotype.

Each genotype was analysed for differences between grey and white matter. In wild-type control mice there were no differences in the percentage surface area of the vessel wall occupied by endothelium (59.82% vs. 57.07%, $p = 0.051$), intramural cells (12.88% vs. 14.41%, $p = 0.349$) or basement membrane (27.27% vs. 28.52%, $p = 0.128$). This was also observed in α-DB deficient mice (endothelium, 58.78% vs. 57.25%, $p = 0.156$, intramural cells, 11.00% vs. 12.51%, $p = 0.206$ and basement membrane 30.22% vs. 30.24%, $p = 0.291$) (**Figure 4.6**).

The percentage surface area of the vessel wall occupied by endothelium, intramural cells or basement membrane in grey and white matter were analysed and compared between the genotypes. In both grey and white matter, there was no significant difference in the percentage surface area of the vessel wall occupied by the endothelium or intramural cells. However, the surface area of the vessel wall occupied by basement membrane was significantly higher in α-DB deficient mice in both grey matter (27.28% vs. 30.22%, $p < 0.01$) and white matter (28.52% vs. 30.24%, $p < 0.05$) (**Figure 4.6**).

As with our findings for the AQP4 deficient mice (**chapter 3**) these results suggest that changes in capillary size metrics between genotypes (**Figure 4.4** and **Figure 4.5**) was most likely influenced by differences in the vessel size rather than genotype. These results show that only the capillary basement membrane and not other components of the vessel wall are altered in the grey ($p < 0.01$) and white matter ($p < 0.05$) of α-DB deficient mice. This is supported by the appearance of the basement membrane as observed by transmission electron microscopy (**Figure 4.2** and **Figure 4.3**).

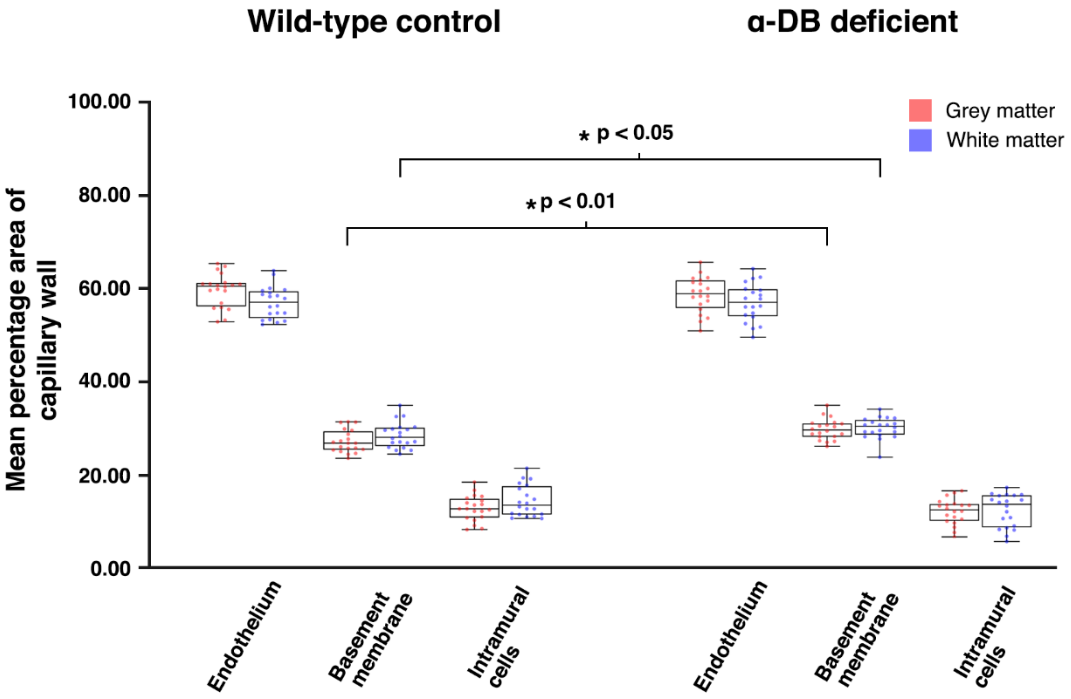

Figure 4.6 Summary showing overall mean values for the percentage of the vessel wall occupied by endothelium, intramural cells and basement membrane between wild-type control and α-DB deficient mice in white and grey matter

In both wild-type control and α-DB deficient mice there was no significant difference in the percentage surface area of the vessel wall occupied by the endothelium, basement membrane or intramural cells between capillaries from grey or white matter in the same mouse. However, when compared to wild-type control mice, the surface area of the vessel wall occupied by basement membrane was significantly higher in both grey and white matter in α-DB deficient mice. Each box plot represents the range of data from three mice. The scatter plots represent the means of repeated measures (20 per mouse, n = 3).

4.5.5 ALTERATIONS TO THE BIOCHEMICAL COMPOSITION OF VASCULAR BASEMENT MEMBRANES IN ALPHA DYSTROBREVIN DEFICIENT MICE

Morphological changes to cerebral vascular basement membranes, such as thickening have long been associated with alterations to their biochemical composition. The next questioned addressed was whether the morphological alterations (**Figure 4.2** and **Figure 4.3**) and changes in percentage surface area of the vessel wall occupied by basement membrane (**Figure 4.6**) in α-DB deficient mice were accompanied by changes in expression of COL4, a key structural component of vascular basement membranes.

Immunohistochemistry for COL4 was performed on grey matter and underlying white matter as detailed in **section 2.3**. Qualitative assessment by light microscopy was accompanied by quantitative analysis of the expression of COL4 between vessels in the grey matter and white matter by comparing the number of vessels (vessel density), mean area stained per vessel and in the grey matter, vessel distribution.

4.5.5.1 COMPARISON OF THE PATTERN OF COLLAGEN IV STAINING BETWEEN WILD-TYPE CONTROL AND ALPHA DYSTROBREVIN DEFICIENT MICE

Qualitative assessment revealed that the majority of COL4 immunoreactivity was confined to vascular walls that appeared more intense and less diffuse in the grey matter of α-DB deficient mice. There were no notable differences in the white matter which appeared similar to the pattern of COL4 staining seen in the grey matter of wild-type control mice (**Figure 4.7**).

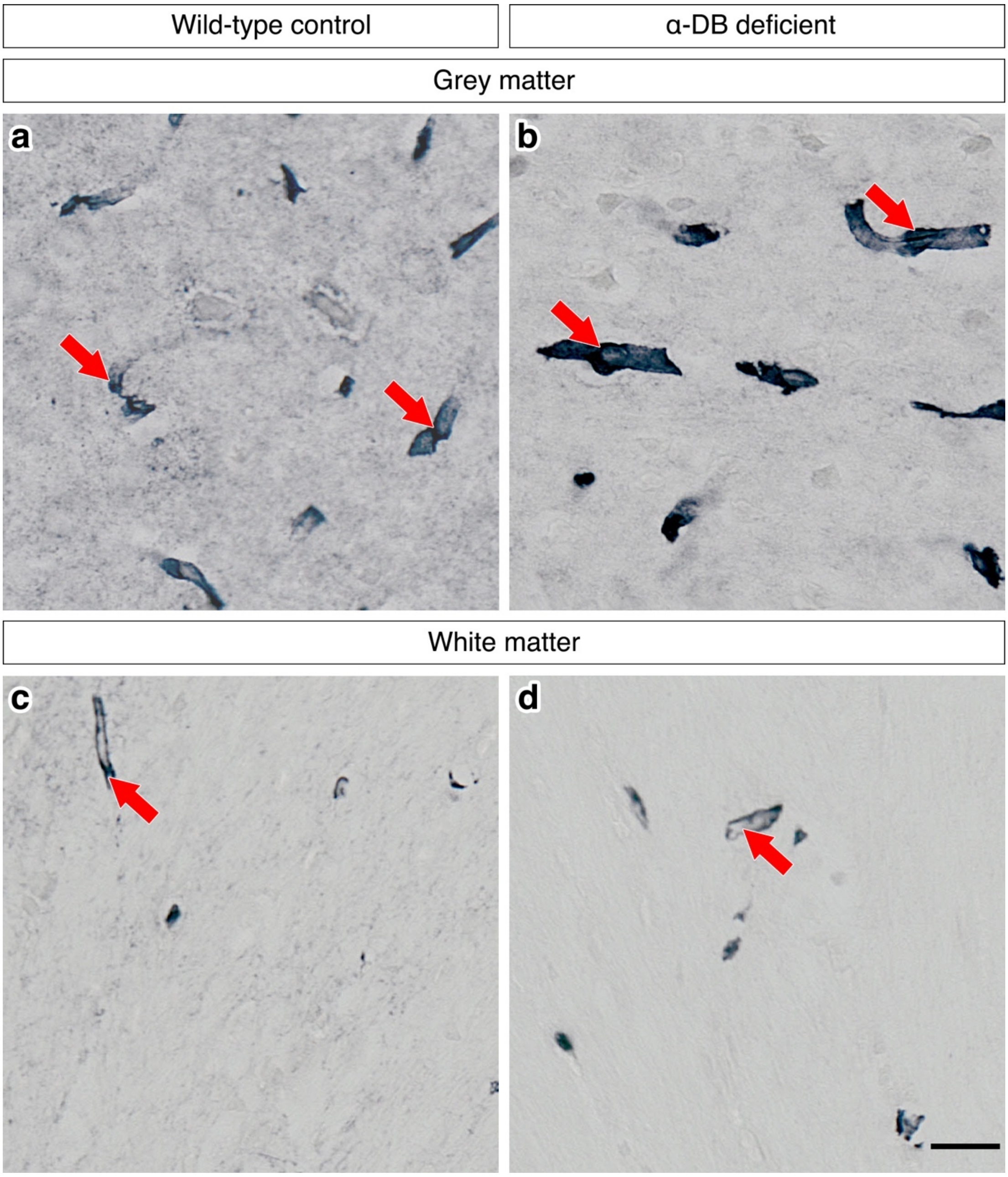
Wild-type control
α-DB deficient
Grey matter
a
b
White matter
c
d

Figure 4.7 Immunostaining for COL4 in wild type control and α-DB deficient mice

Staining for COL4 (black) appears more intense and less diffuse (red arrows) in the grey matter of α-DB deficient mice (b) when compared to wild-type control mice (a). There are no obvious differences in staining for COL4 in the white matter between wild-type control and α-DB deficient mice (c & d) which appeared similar to that of grey matter in wild-type control mice (a). Scale bar = 20 μm.

4.5.5.2 COMPARISON OF VESSEL DENSITY AND AMOUNT OF COLLAGEN IV STAINING BETWEEN WILD-TYPE CONTROL AND ALPHA DYSTROBREVIN DEFICIENT MICE

Vessels from each genotype were analysed for differences in vessel density (mean number of vessels per 0.5mm^2) and mean area of COL4 staining per vessel (expressed as μm^2) by using micrographs of grey and white matter and a custom macro in Image J (see **section 2.3** for detailed methods).

Analysis in wild-type control mice revealed a significant higher density of vessels in the grey matter (196.27 vessels per 0.5 mm^2) compared to the white matter (112 vessels per 0.5 mm^2) $p = < 0.05$ but no difference in the mean area of COL4 staining per vessel (14.48 μm^2 vs. 18.16 μm^2, $p = 0.765$) (**Figure 4.8**). A similar pattern of vessel density was seen in α-DB deficient mice, but the differences were not significant with 166.4 vessels per 0.5 mm^2 in grey matter compared to 133.33 vessels per 0.5 mm^2 in the white matter, $p = 0.065$. However, in α-DB deficient mice the mean area of COL4 staining per vessel was significantly higher in the grey matter (56.04 μm^2) than the white matter (19.31 μm^2), $p < 0.05$ (**Figure 4.9**).

Comparison of vessel density between wild-type control and α-DB deficient mice revealed no differences in either grey matter (196.27 vs.166.4 vessels per 0.5 mm^2, $p = 0.222$) or white matter (112 vs.133.33 vessels per 0.5 mm^2, $p = 0.207$). There were no differences in mean area of COL4 staining per vessel in the white matter (18.16 μm^2 vs. 19.31 μm^2, $p = 0.926$) but in the grey matter, α-DB deficient mice showed a significant higher mean area of COL4 staining per vessel when compared to the grey matter of wild-type control mice (56.05 μm^2 vs. 14.48 μm^2, $p < 0.01$) (**Figure 4.10**).

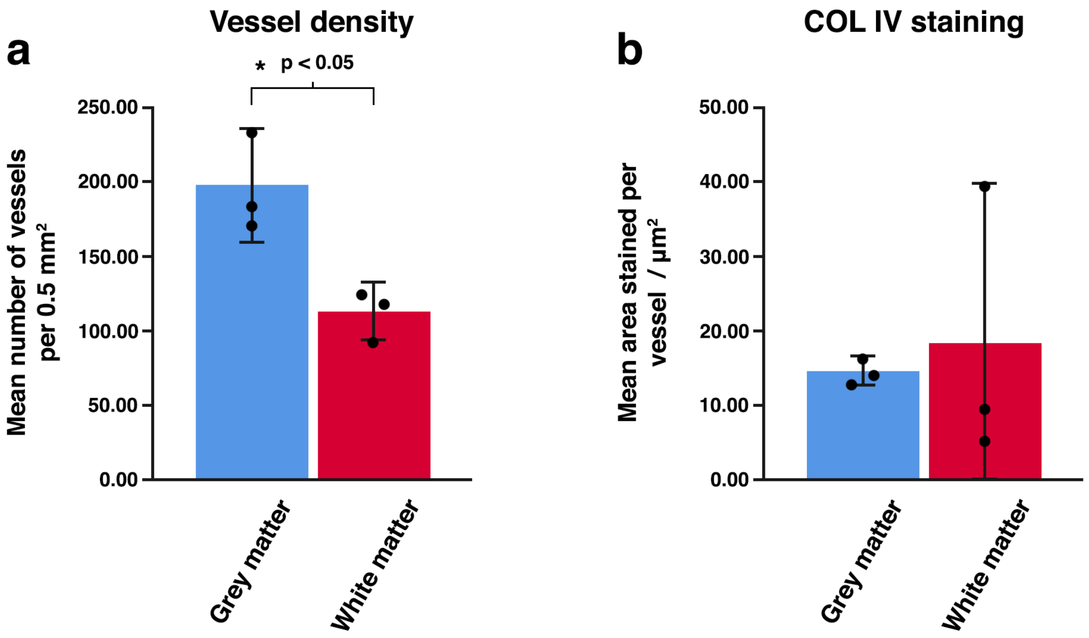

c

		Grey matter	White matter	Sig.
Vessel density per 0.5 mm^2	Mean	**196**	**112**	**< 0.05**
	Range	(171 – 233)	(93 – 125)	
	S.D	32.96	16.93	
	S.E	19.03	9.78	
Mean area of COL4 staining per vessel	Mean	**14.48 μm^2**	**18.16 μm^2**	0.765
	Range	(12.91 – 16.37 μm^2)	(5.32 – 39.54 μm^2)	
	S.D	1.75	18.64	
	S.E	1.01	10.76	

Figure 4.8 Vessel density and COL4 staining per vessel between grey and white matter in wild-type control mice

Comparison of the number of vessels per 0.5mm² revealed significant differences between grey and white matter (a & c). There were no differences in the mean area of COL4 staining per vessel (b & c). The scatter plots represent mean values for each mouse. Each column represents overall mean values (n = 3). Error bars: +/- 2 SE

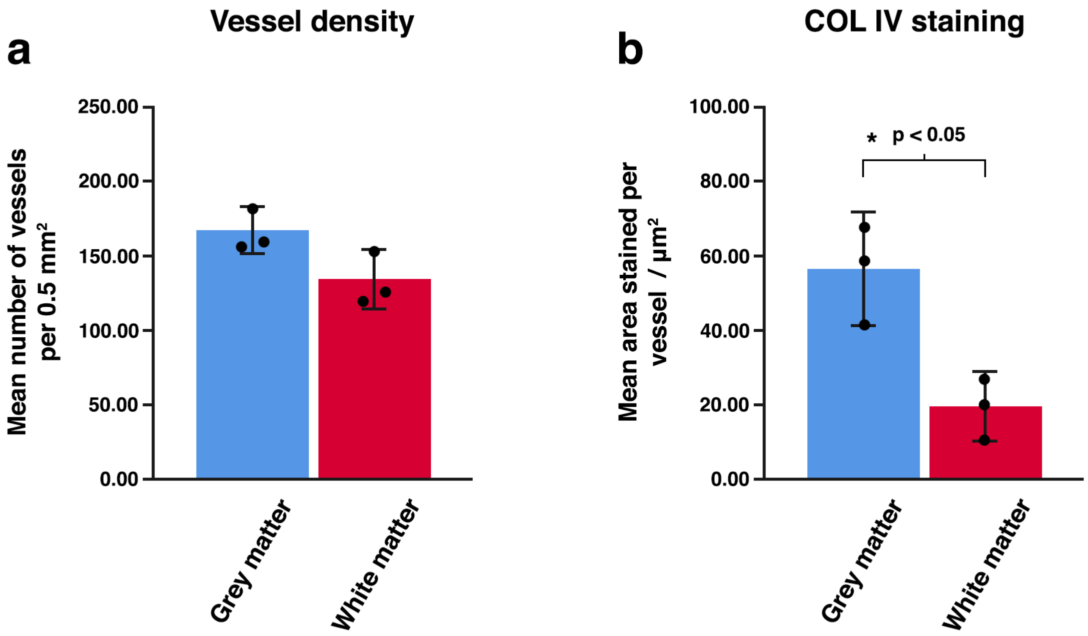

c

		Grey matter	White matter	Sig.
Vessel density per 0.5 mm^2	Mean	**166**	**133**	**0.065**
	Range	(157 – 183)	(75 – 96)	
	S.D	13.95	17.84	
	S.E	8.05	10.30	
Mean area of COL4 staining per vessel	Mean	**56.04 μm^2**	**19.31 μm^2**	**< 0.05**
	Range	(41.62 – 67.75 μm^2)	(10.70 – 27.00 μm^2)	
	S.D	13.27	8.19	
	S.E	7.67	4.73	

Figure 4.9 Vessel density and COL4 staining per vessel between grey and white matter in α-DB deficient mice

Comparison of the number of vessels per 0.5 mm^2 revealed no significant differences between grey and white matter (a & c) but there was a significant difference in the mean area of COL4 staining per vessel, which was higher in the grey matter (b & c). The scatter plots represent mean values for each mouse. Each column represents overall mean values (n = 3). Error bars: +/- 2 SE

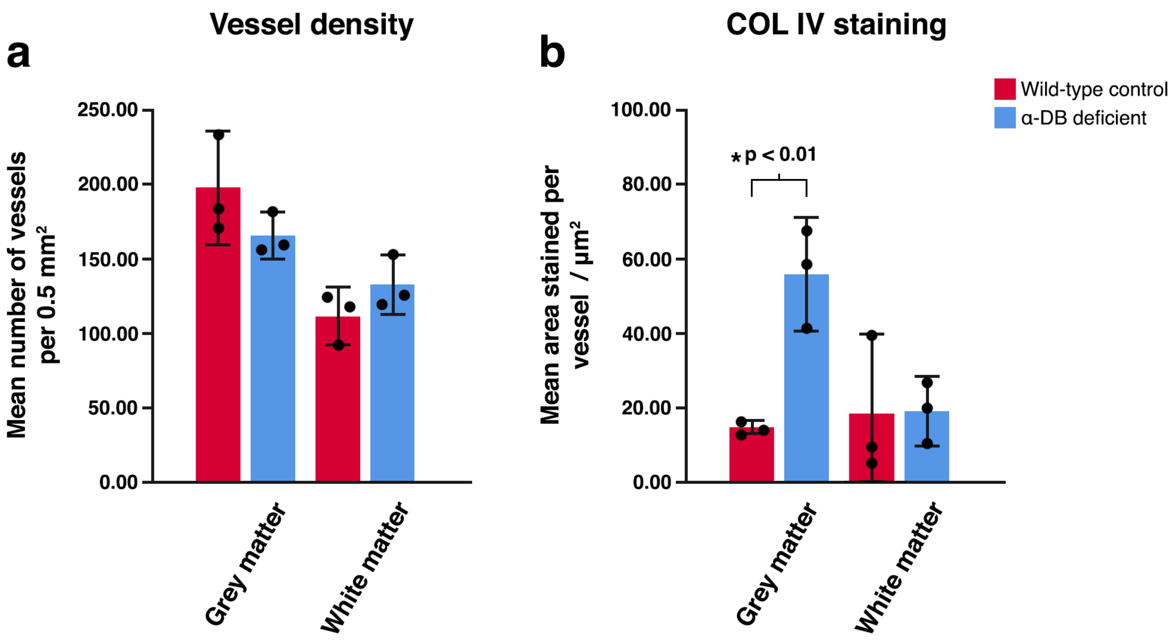

Figure 4.10 Vessel density and COL4 staining per vessel in grey and white matter between wild-type control and α-DB deficient mice

Comparison of the number of vessels per 0.5 mm² revealed no significant differences in grey and white matter (a) between wild-type control (red columns) and α-DB deficient mice (blue columns). There was a significant difference in the mean area of COL4 staining per vessel, which was higher in the grey matter of α-DB deficient mice compared to the grey matter of wild-type control mice (b). The scatter plots represent mean values for each mouse. Each column represents overall mean values (n = 3). Error bars: +/- 2 SE

4.5.5.3 COMPARISON OF VESSEL DISTRIBUTION AND AMOUNT OF COLLAGEN IV STAINING IN GREY MATTER BETWEEN WILD-TYPE CONTROL AND ALPHA DYSTROBREVIN DEFICIENT MICE

As there was no difference in vessel density but a large difference in mean area staining per vessel of COL4 in the grey matter between wild-type control and α-DB deficient mice, we next assessed whether this large difference could be attributed to possible changes in the pattern of distribution of the individual type of blood vessels.

Vessel density in the grey matter of wild-type control and α-DB deficient mice was reclassified into the number of capillaries (vessels with diameter of less than 10 µm) or larger vessels (vessels with a diameter of 10 µm or larger). DAB staining did not allow for the differentiation of arterioles from venules, so these were classified together as vessel with a diameter of 10 µm or larger.

There was no significant difference in the distribution of capillaries in the grey matter between wild-type control (188 per 0.5 mm^2) and α-DB deficient mice (156 per 0.5 mm^2) $p = 0.173$. There was also no difference in the distribution of arterioles and venules (8 per 0.5 mm^2 vs. 10 per 0.5 mm^2, $p = 0.275$). However, in α-DB deficient mice, capillaries and arterioles and venules showed a significantly higher mean area staining of COL4 per vessel (capillaries, 49.25 μm^2 vs 11.00 μm^2, $p <0.05$, arterioles and venules, 162.75 μm^2 vs 96.27 μm^2, $p < 0.05$) (**Figure 4.11**).

These data suggest that the large difference in mean area staining per vessel of COL4 observed in the grey matter of α-DB deficient mice is most likely linked to a loss of α-DB and not due to any alterations to the anatomical pattern of distribution of blood vessel type.

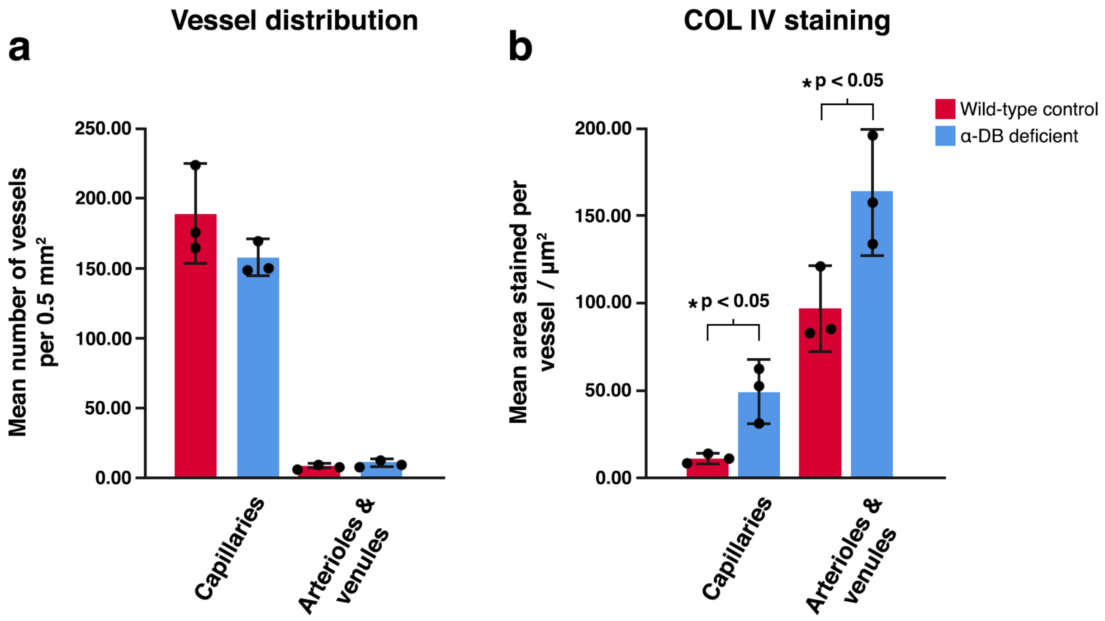

c

		Wild-type control	α-DB deficient mice	Sig.
Mean number of capillaries per 0.5 mm ^{2}	Mean	**188**	**156**	**0.173**
	Range	(165 – 224)	(149 – 170)	
	S.D	31.45	11.57	
	S.E	18.16	6.69	
Mean number of arterioles & venules per 0.5 mm ^{2}	Mean	**8**	**10**	**0.275**
	Range	(6 – 10)	(8– 13)	
	S.D	1.60	2.44	
	S.E	0.92	1.41	
Mean area stained per vessel / capillaries	Mean	**11.00 µm ^{2}**	**49.25 µm ^{2}**	**< 0.05**
	Range	(8.28 - 13.79 µm ^{2})	(31.75 - 62.90 µm ^{2})	
	S.D	2.76	15.92	
	S.E	1.59	9.20	
Mean area stained per vessel / arterioles & venules	Mean	**96.27 µm ^{2}**	**162.75 µm ^{2}**	**< 0.05**
	Range	(82.78 - 120.99 µm ^{2})	(134.20 - 196.19 µm ^{2})	
	S.D	21.44	31.28	
	S.E	12.38	18.06	

Figure 4.11 Vessel distribution and COL4 staining in grey matter wild-type control and α-DB deficient mice

There was no difference in the number of capillaries or arterioles and venules in the grey matter (a & c). However, in α-DB deficient mice the mean area of COL4 staining was significantly higher in capillaries, arterioles and venules when compared to wild-type control mice (b & c). The scatter plots represent mean values for each mouse. Each bar column represents overall mean values (n = 3). Error bars: +/- 2 SE

4.6 DISCUSSION

The objective of the work detailed in this chapter was to investigate whether the loss of α-DB from astrocytic endfeet alters the structure and arrangement of the capillary wall and IPAD pathways. The hypothesis tested was: *In mice genetically modified for alpha-dystrobrevin, the morphology of capillary intramural periarterial drainage pathways are altered.* This was investigated by using TEM to perform a detailed analysis of the size, structure and cellular composition of the capillary wall in grey and white matter of α-DB deficient mice. Vascular basement membranes were also assessed for compositional changes in expression of COL4, a key structural protein that is altered in neurodegenerative diseases.

4.6.1 THE MORPHOLOGY OF THE BLOOD-BRAIN BARRIER IS UNALTERED IN YOUNG ALPHA DYSTROBREVIN DEFICIENT MICE

Earlier studies of the cerebral vasculature in α-DB deficient mice showed the importance of the DPC in the maintenance and function of the blood-brain barrier in the grey matter but up until now, no one has investigated the white matter. Observations by Lien et.al in 18-month-old mice revealed that in the grey matter, deleting α-DB from astrocyte endfeet resulted in a leaky blood-brain barrier, structural abnormalities to the capillary endothelium, thickened capillary basement membranes and swollen astrocytic endfeet [146]. This in part, could be linked to loss of AQP4 function at astrocyte endfeet as a lack of α-DB causes a redistribution of AQP4 from astrocyte endfeet to the astrocytic cell body [146]. Although we did not test our mice for blood-brain barrier function, electron microscopy did not reveal any notable abnormalities in the capillary endothelium or surrounding parenchyma in either grey or white matter to suggest a link between a lack of glial α-DB and impaired blood-brain barrier function in young adult α-DB deficient mice. It appears therefore, that redistribution of AQP4 away from astrocyte endfeet in young α-DB deficient mice has minimal effect on BBB function.

4.6.2 THE CAPILLARY BASEMENT MEMBRANE IS THICKENED IN ALPHA DYSTROBREVIN DEFICIENT MICE

Morphological changes to cerebral vascular basement membranes are associated with modifications to their biochemical composition. Alterations to laminins and increases in the expression of COL4 have been measured in cerebral vessel basement membranes in aged human brains [68] and neurodegenerative conditions such as AD and Parkinson's disease [69, 254]. Glycoprotein components of the ECM such as COL4, laminin and nidogens interact with amyloid beta (Aβ) and destabilise preformed Aβ fibrils [73] while proteoglycans, such as perlecan and agrin appear to accelerate Aβ aggregation [71, 72].

In α-DB deficient mice a thickening of capillary basement membrane in the grey matter accompanied by an increase in the expression of COL4 were observed. In the grey matter we showed that all vessels (capillaries, arterioles and venules) display an increase in COL4 expression. The thickening of the capillary basement membranes was also observed in the white matter, but to a lesser extent compared to the grey matter. Although electron microscopy on arterioles or venules was not performed, the data does suggest that an altered DPC affects the ECM around all vessel types in the grey matter. It is not known if expression of other ECM proteins would also be altered but experiments showing altered laminin production in co-cultures of α-DB deficient astrocytes and endothelial cells [146] suggest that this may be the case. Further work utilising a more detailed approach to fully appreciate changes to the biochemical profile of the ECM with a focus on cerebrovascular basement membranes will clarify the exact components of the cerebrovascular basement membranes that are at risk from the modifications of the DPC.

4.6.3 WHY DOES REMOVAL OF ALPHA DYSTROBREVIN CAUSE THICKENING OF CAPILLARY BASEMENT MEMBRANE?

The exact reasons as to why the removal of α-DB disrupts the capillary basement membrane are unclear but considering that α-DB is entirely an intracellular protein its role in the formation and maintenance of the basement membrane must include indirect interactions via the DPC. Astrocyte endfeet are anchored to the vessel wall by interactions between α-dystroglycan and ECM proteins including laminins, perlecan, agrin, and the neurexins. α-dystroglycan binds to β-dystroglycan which is anchored to the cell membrane by dystrophin (DP71). α-DB binds directly to DP71 by reciprocal coiled-coil interactions. This binding helps stabilise transmembrane proteins which are anchored to the cell membrane by syntrophins and C-terminal tail binding to PDZ domains (acronym for **P**ost synaptic density protein, **D**rosophila disc large tumor suppressor and **Z**onula occludens-1 protein) **(Figure 1.12** & **Figure**

4.1) [139, 146]. It is entirely possible that deletion of α-DB from the DPC destabilises the interaction between DP71 and the dystroglycan proteins weakening the connection between α-dystroglycan and ECM proteins. This may stimulate over production of the ECM proteins resulting in a thickened basement membrane with altered morphology.

Conversely, a lack of α-DB may also down regulate other DPC proteins which, in turn, may indirectly affect remodelling of the ECM and basement membrane by the actions of matrix metalloproteases (MMP)s. ECM is regulated by a homeostatic balance of MMPs which are endopeptidases that digest ECM proteins, and TIMPs that inhibit the activity of MMPs [255]. In particular, MMP9, also known as Gelatinase B, is a COL4 collagenase [256] implicated in synaptic plasticity, memory and learning [257, 258] and several neurological disorders such as stroke and small vessel disease [259]. Expression patterns of DPC proteins are altered in α-DB deficient astrocytes with decreased levels of DP71 and α- and β-dystroglycans [146]. β-dystroglycan has been identified as a substrate for MMP 9 and is digested in response to enhanced synaptic activity [260]. It is possible that in α-DB deficient mice the regulation of the ECM and capillary basement membrane by the actions of MMP9 is altered as a direct result of reduced availability of β-dystroglycan substrate. Further work is required to confirm this as although reductions of DPC proteins have been observed in α-DB deficient astrocytes, this has not been elucidated in α-DB deficient mice. In future work, other components of the basement membranes as well as levels of MMP9 and its substrate TIMP3 will be analysed in α-DB deficient mice. In order to back-translate the significance of these results, the expression of α-DB should be analysed in post-mortem human brains from CSVD and VaD.

4.6.4 CONCLUSIONS

The structure and arrangement of the capillary wall and IPAD pathway is affected by a lack of α-DB at astrocyte endfeet in both the grey and white matter. The surface area occupied by basement membrane is increased in capillary walls and appears thickened as seen with TEM. This is accompanied by alterations in overall expression of COL4 in the grey matter but not the white matter. Other cerebral vessels such as arterioles were not analysed by TEM but the increase in expression of COL4 in larger vessels in the grey matter suggest that the basement membrane would also be altered in these vessels. Future work incorporating other vessels types would help to confirm this.

The alterations to the IPAD pathway at capillary level reported here suggest that disruption of the DPC at glial endfeet by the removal of α-DB alters the biochemical and structural properties of the IPAD pathway. Thickening of the capillary basement membrane and remodelling of the microvascular ECM are common features in CSVD [15, 67]. Therefore, α-DB deficient mice may provide a suitable model to investigate the potential role of a failure of IPAD in CSVD and VaD. These findings may also have wider implications for other drainage pathways in the brain (**see section 1.3.4**) such as convective influx of CSF that occurs along pial-glial basement membranes [245] which may also be directly influenced by α-DB.

The next logical step is to assess for IPAD in α-DB deficient mice to ascertain if changes to the IPAD pathway observed in this chapter are reflected in failed fluid clearance by IPAD

Chapter 5 LOSS OF ALPHA-DYSTROBREVIN FROM ASTROCYTE ENDFEET AND THE DYNAMICS OF INTRAMURAL PERIARTERIAL DRAINAGE

5.1 INTRODUCTION

Work detailed in the previous chapter demonstrates how the structure and arrangement of the capillary wall and the intramural periarterial drainage (IPAD) pathway is affected by removal of α-dystrobrevin (α-DB) from the dystrophin associated protein complex (DPC) of astrocyte endfeet. In particular, the surface area occupied by basement membrane is increased in capillary walls in both grey and white matter in α-DB deficient mice. This is accompanied by alterations to the biochemical composition of basement membrane in grey matter with cerebral vessels showing an increase in expression of collagen IV (COL4), mirroring the increase in COL4 and thickening of basement membranes observed in normal ageing [68], Alzheimer's disease (AD) and Parkinson's disease [69, 254].

Cerebral amyloid angiopathy (CAA), a major contributor to the spectrum of cerebral small vessel disease (CSVD) contributing to Vascular dementia (VaD), is the accumulation of amyloid-beta (Aβ) in the walls of leptomenigeal arteries, cortical arterioles, capillaries and very rarely venules [16, 26] (**see section 1.1.2**). Human in vivo studies by Batemen *et al.* suggest that CAA results from a failure of Aβ clearance from the brain [35]. A key pathway for the removal of Aβ from the brain is via IPAD pathways within the basement membrane of the capillary wall (**detailed in section 1.3.2**). As shown by confocal and electron microscopy in animal models, tracers injected into hippocampal grey matter diffuse from the parenchyma within extracellular spaces firstly into capillary endothelial basement membrane and then along smooth muscle basement membrane of cortical and leptomeningeal arteries and out of the base of the skull to cervical lymph nodes [74, 160, 168] **(Figure 5.1)** Recent multiscale models of arteries suggest that this process is driven by vasomotion generated by cycles of contraction and relaxation of vascular smooth muscle cells (SMC) [179].

In humans, CAA is mainly observed in the occipital lobe and to a lesser extent in the hippocampus, cerebellum and basal ganglia [27]. In animal models, such as transgenic models of AD, CAA predominantly affects the cortex and hippocampus [261]. We have previously shown that in aged mice, alterations to the cerebral vasculature, such as thickening of capillary basement membrane and remodelling of the extracellular matrix occur in a region-specific manner, particularly in those affected by CAA [74]. These alterations are also observed in CSVD [15, 67].

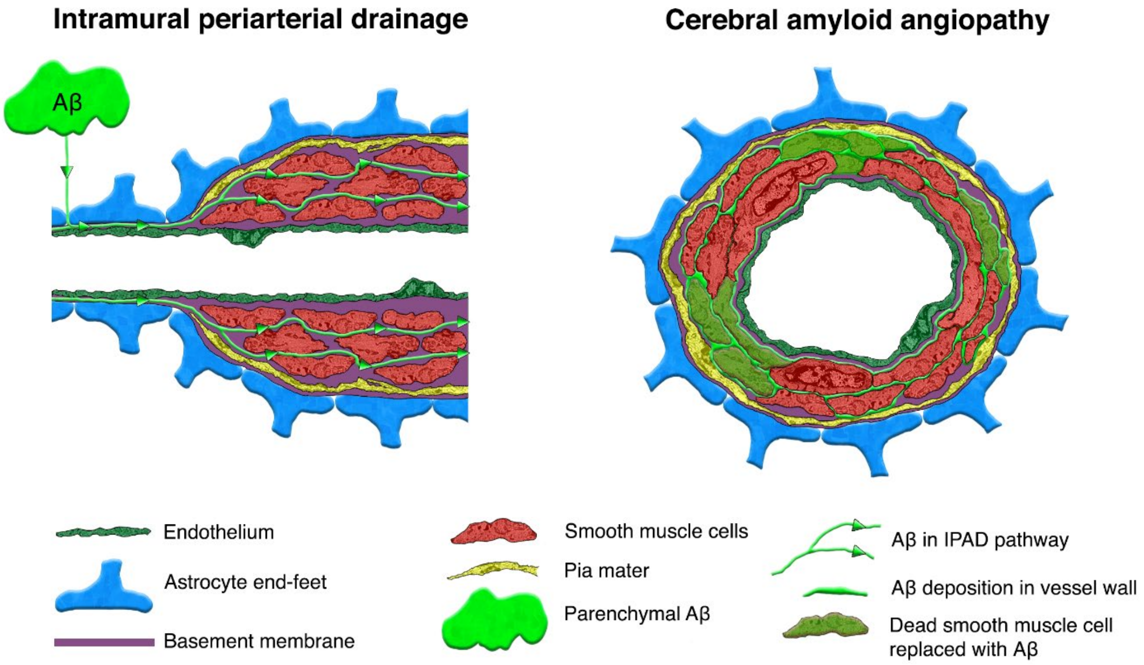
Intramural periarterial drainage
Cerebral amyloid angiopathy
Aβ
Endothelium
Astrocyte end-feet
Basement membrane
Smooth muscle cells
Pia mater
Parenchymal Aβ
Aβ in IPAD pathway
Aβ deposition in vessel wall
Dead smooth muscle cell replaced with Aβ

Figure 5.1 The IPAD pathway and accumulation of amyloid proteins as CAA

Solutes such as Aβ (green) diffuse along extracellular spaces and enter capillary basement membranes (purple) via gaps between astrocytic endfeet (blue). Solutes then travel against the direction of blood flow (green arrows) towards arteriole smooth muscle basement membranes. In CAA, progressive accumulation of Aβ occurs in the IPAD pathways of leptomenigeal arteries, arterioles located in the cortex and capillaries and venules. In mild CAA, Aβ appears as a congophilic rim restricted around SMCs. In moderate CAA, Aβ is deposited throughout the tunica media with loss of SMC. In severe CAA, Aβ is extensively deposited within the cerebrovasculature with focal fragmentation of the vessel wall.

Radiological hallmarks of CAA include abnormalities to the white matter, such as white matter hyperintensities (WMH) or leukoaraiosis [208] which are common findings on computer tomography (CT) or magnetic resonance imaging (MRI) in the elderly, particularly with stroke or dementia [211]. The clinical features of VaD as imaged by MRI (**see section 1.1.2.1**) suggest that in early stages of WMH the lesions are due to altered fluid homeostasis in the brain [211]. However, it is unclear why the white matter is so susceptible to disturbances in fluid homeostasis. A clearer picture of the regulation of interstitial and cerebrospinal fluids in the white matter by processes such as IPAD is necessary in order to better understand the pathogenesis of WMH.

As α-DB deficient mice show alteration to the IPAD pathway, with a thickening of capillary basement membrane and remodelling of the extracellular matrix, particularly in the grey matter (**chapter 4**), the dynamics of IPAD both in grey and white matter warrants further investigation. If these mice show alterations to IPAD, they may provide a suitable model to further investigate the role of IPAD in CSVD and VaD.

5.2 HYPOTHESES

1) *In wild-type control mice, the dynamics of intramural periarterial drainage pathways are different in the white matter of the corpus callosum compared to hippocampal grey matter.*
2) *In mice genetically modified for alpha dystrobrevin, the dynamics of intramural periarterial drainage pathways are altered in hippocampal grey matter and the white matter of the corpus callosum.*

5.3 AIMS

The work detailed in this chapter firstly aims to assess the dynamics of IPAD in white and grey matter of wild-type control mice and then investigate if IPAD is altered when α-DB is not present at astrocytic endfeet. Wild-type control and α-DB deficient mice received a stereotaxic injection of fluorescent Aβ (1-40) into either hippocampal grey matter or the white matter of the corpus callosum and the dynamics of IPAD was assessed by confocal microscopy (**Figure 5.2**).

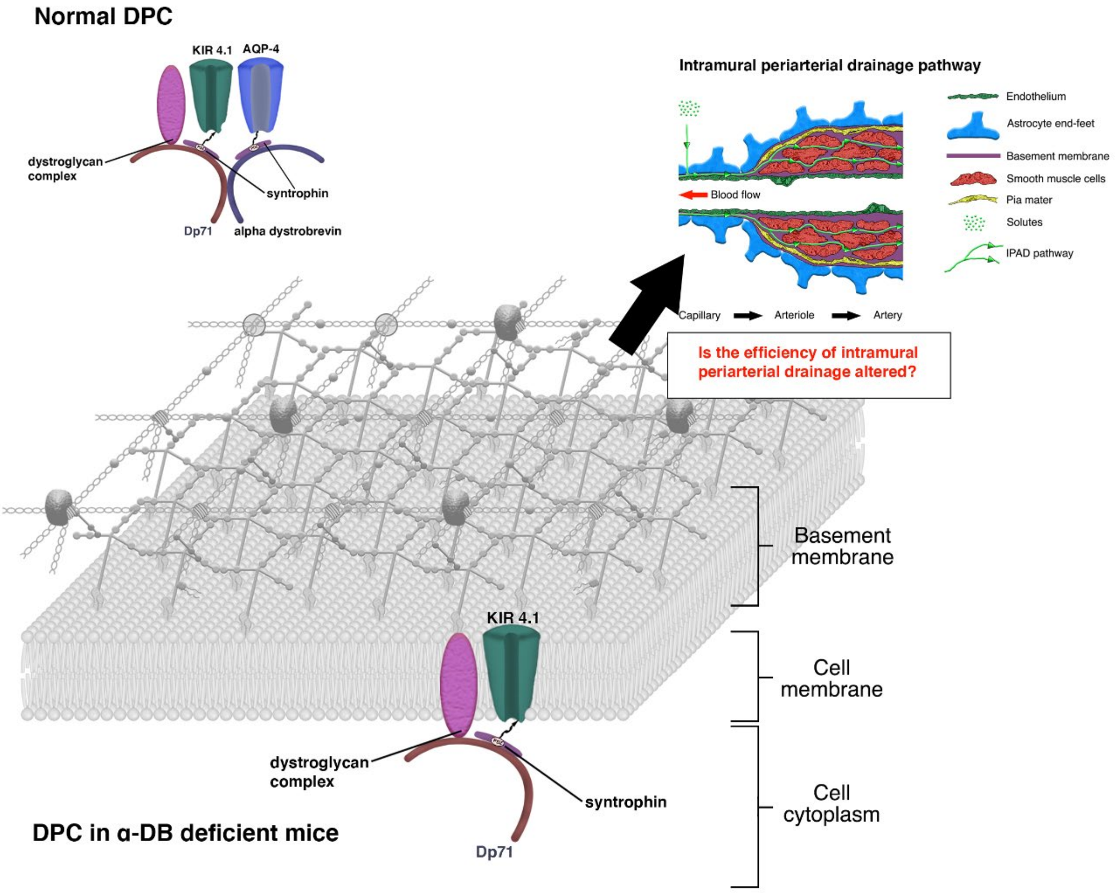
Normal DPC
KIR 4.1
AQP-4
dystroglycan complex
syntrophin
Dp71
alpha dystrobrevin
Intramural periarterial drainage pathway
Endothelium
Astrocyte end-feet
Basement membrane
Smooth muscle cells
Pia mater
Solutes
IPAD pathway
Blood flow
Capillary
Arteriole
Artery
Is the efficiency of intramural periarterial drainage altered?
Basement membrane
Cell membrane
Cell cytoplasm
KIR 4.1
dystroglycan complex
syntrophin
DPC in α-DB deficient mice
Dp71

Figure 5.2 alpha dystrobrevin, the dystrophin associated protein complex and the intramural periarterial drainage pathway

Does the loss of α-DB from astrocytic endfeet alter the dynamics of the intramural periarterial drainage pathway?

5.4 MATERIALS & METHODS

α-DB deficient (B6;129-*Dtna* ^{tm1Jrs}/J) [239] (n = 10) and wild-type control mice (n = 10) received a stereotaxic injection of amyloid-beta (Aβ) (1-40) HiLyte Fluor 555 into either the hippocampus (grey matter) (n = 5) or the corpus callosum (white matter) (n = 5) and assessed for the pattern of IPAD.

After receiving the stereotaxic injection, mice were fixed by perfusion, the brains removed and sectioned into 20μm slices for immunohistochemistry. Confocal microscopy was used to produce tile scans of tissue sections 200μm posterior to the site of injection. Adobe Photoshop CS6 was used to demarcate either the hippocampus or corpus callosum from each tile scan so that each region could be assessed for vessel density (per 0.5mm^2 of tissue), the density of vessels with Aβ in their vessel walls (per 0.5mm^2 of tissue) and the fluorescent intensity of parenchymal Aβ (per 0.5mm^2 of tissue). More details about the methods are in **section 2.4**.

Statistical analysis was performed using SPSS and an independent *t-test* with significance set at $P < 0.05$.

5.5 RESULTS

To establish whether a lack of α-DB at astrocyte endfeet affects the dynamics of IPAD from the grey and white matter, wild-type control and α-DB deficient mice received a stereotaxic injection of Aβ HiLyte Fluor 555 into either the hippocampus (grey matter) or the corpus callosum (white matter). IPAD was assessed using confocal microscopy.

5.5.1 ASSESSMENT OF VESSEL DENSITY IN GREY AND WHITE MATTER

The current method for analysing IPAD in mice requires calculating the number of vessels with Aβ in their vessel walls. Therefore, we first assessed for differences in the number (vascular density) of arterioles, capillaries and venules present in each region analysed, for each genotype. We then assessed for differences between genotypes. Vessels were identified based on the pattern of COL4 and smooth muscle actin (SMA) staining and vessel diameter size (**see section 2.4.5 for further details**). All data is presented per 0.5mm^2 of tissue.

5.5.1.1 WILD-TYPE CONTROL MICE

In wild-type control mice, the vessel density of arterioles (4.4 vs. 2.3 per 0.5 mm^2, $p = 0.134$) and venules (1.9 vs.1.1 per 0.5 mm^2, $p = 0.063$) did not differ significantly between grey and white matter. However, the density of capillaries was significantly reduced in the white matter (84 vs 54.5 per 0.5mm^2, $p < 0.05$) (**Table 5**). Data published [247].

5.5.1.2 ALPHA DYSTROBREVIN DEFICIENT MICE

In α-DB deficient mice, the vessel density of arterioles (5.4 vs. 4.0 per 0.5 mm^2, $p = 0.139$), venules (1.3 vs. 2.0 per 0.5 mm^2, $p = 0.354$) and capillaries (74.7 vs.85 per 0.5 mm^2, $p = 0.188$) did not differ significantly between grey and white matter (**Table 5**).

5.5.1.3 WILD-TYPE AND ALPHA DYSTROBREVIN DEFICIENT MICE – GREY MATTER

In grey matter the vessel density of arterioles (4.4 vs. 5.4 per 0.5 mm^2, $p = 0.270$) or capillaries (84 vs. 74.7 per 0.5 mm^2, $p = 0.270$) did not differ between wild-type control and α-DB deficient mice. However, the density of venules was significantly decreased in α-DB deficient mice (1.9 vs. 1.3 per 0.5 mm^2, $p < 0.05$) (**Figure 5.3**).

5.5.1.4 WILD-TYPE AND ALPHA DYSTROBREVIN DEFICIENT MICE – WHITE MATTER

In white matter the vessel density of arterioles (2.3 vs. 4 per 0.5 mm^2, $p = 0.216$) or venules (1.1 vs. 2.0 per 0.5 mm^2, $p = 0.261$) did not differ between wild-type control and α-DB deficient mice. However, the density of capillaries was significantly increased in α-DB deficient mice (54.5 vs. 85 per 0.5 mm^2, $p < 0.05$) (**Figure 5.3**).

			Grey matter	White matter	Sig.
Wild-type control	**Capillaries / 0.5mm^2**	Mean	**84.03**	**54.46**	**< 0.05**
		Range	(71.67 - 95.88)	(37.70 - 98.42)	
		S.D	9.49	25.55	
		S.E	4.25	11.42	
	Arterioles / 0.5mm^2	Mean	**4.39**	**2.28**	0.134
		Range	(3.48 - 6.29)	(0 - 5.68)	
		S.D	1.11	2.45	
		S.E	0.50	1.10	
	Venules/ 0.5mm^2	Mean	**1.91**	**1.12**	0.063
		Range	(1.24 - 2.18)	(0 - 1.80)	
		S.D	0.39	0.73	
		S.E	0.17	0.32	
α-DB deficient	**Capillaries / 0.5mm^2**	Mean	**74.70**	**84.97**	0.188
		Range	(62.19 - 93.74)	(72.52- 97.25)	
		S.D	12.29	10.16	
		S.E	5.50	4.55	
	Arterioles / 0.5mm^2	Mean	**5.39**	**3.98**	0.139
		Range	(3.22 - 7.05)	(2.99 - 5.84)	
		S.D	1.52	1.18	
		S.E	0.68	0.53	
	Venules / 0.5mm^2	Mean	**1.31**	**2.02**	0.354
		Range	(1.01 - 1.70)	(0 - 3.89)	
		S.D	0.30	1.49	
		S.E	0.13	0.67	

Table 5: Comparison of vessel density between grey and white matter in wild-type control and α-DB deficient mice

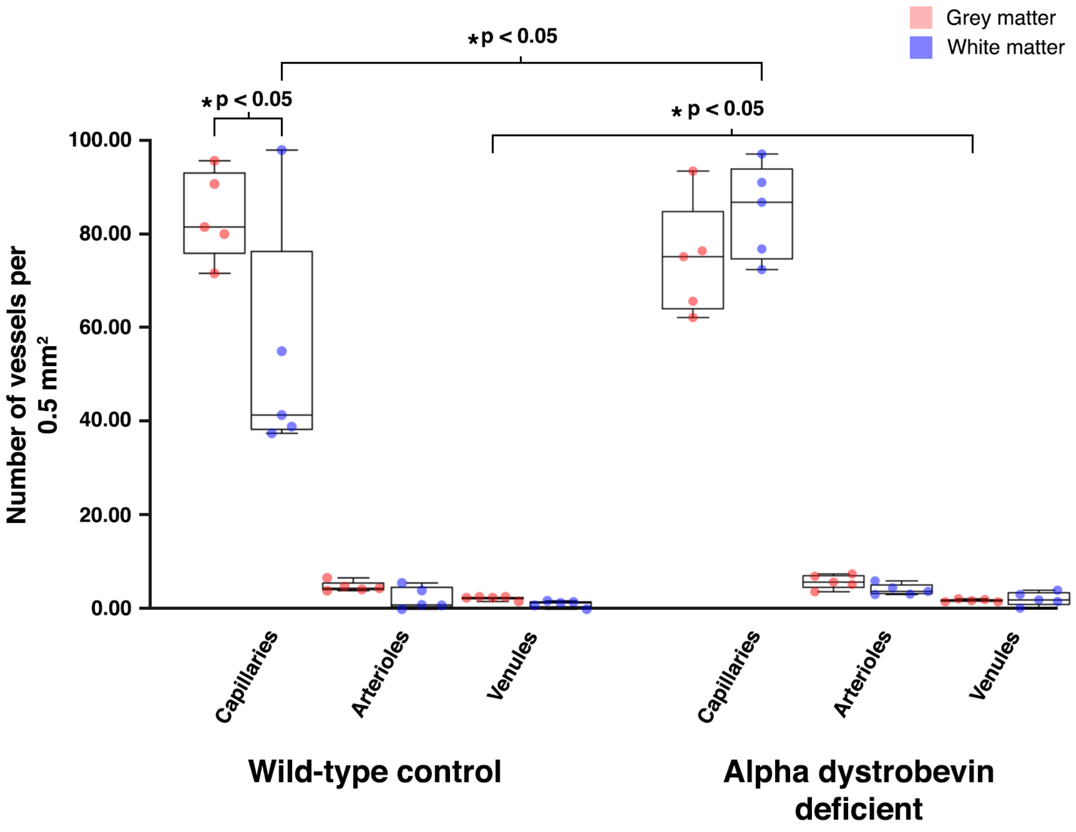

Figure 5.3 Vessel density in grey and white matter between wild-type control and α-DB deficient mice

Comparison of the number of vessels per 0.5 mm^2 revealed significant differences in the number of capillaries between grey matter (red) and white matter (blue) in wild-type control mice. In α-DB deficient mice there were no significant differences between grey and white matter but when compared to wild-type control mice, α-DB deficient mice showed a significantly higher number of capillaries in the white matter and significantly lower number of venules in the grey matter. Each box plot represents the range of data from five mice. The scatter plots represent vessel density from each mouse.

5.5.2 ASSESSMENT OF INTRAMURAL PERIARTERIAL DRAINAGE IN THE GREY AND WHITE MATTER

5.5.2.1 QUALITATIVE ASSESSMENT

After assessing for differences in vessel density between the grey and white matter of wild-type control and α-DB deficient mice, each region was analysed for qualitative differences in the distribution of the fluorescent Aβ after injection.

Within 5 mins of injection into the hippocampus, fluorescent Aβ was observed in the parenchyma and colocalising with COL4 within the walls of arterioles and capillaries and few venules in both wild-type control and α-DB deficient mice. In wild-type control mice, fluorescent Aβ was distributed diffusely (**Figure 5.4**) while in α-DB deficient mice, Aβ appeared less diffuse and more focally concentrated within the parenchyma. Aβ was also seen aggregating around arterioles that did not have Aβ in their basement membranes, in a location consistent with glia limitans, a feature not observed in wild-type mice (**Figure 5.5**).

Within 5 mins of injection into the corpus callosum, fluorescent Aβ was observed mainly along the white matter tracts and colocalising with collagen IV within the walls of capillaries, some arterioles and few venules in both wild-type control and α-DB deficient mice (**Figure 5.6 & Figure 5.7**).

Data for wild-type control mice has been published [247].

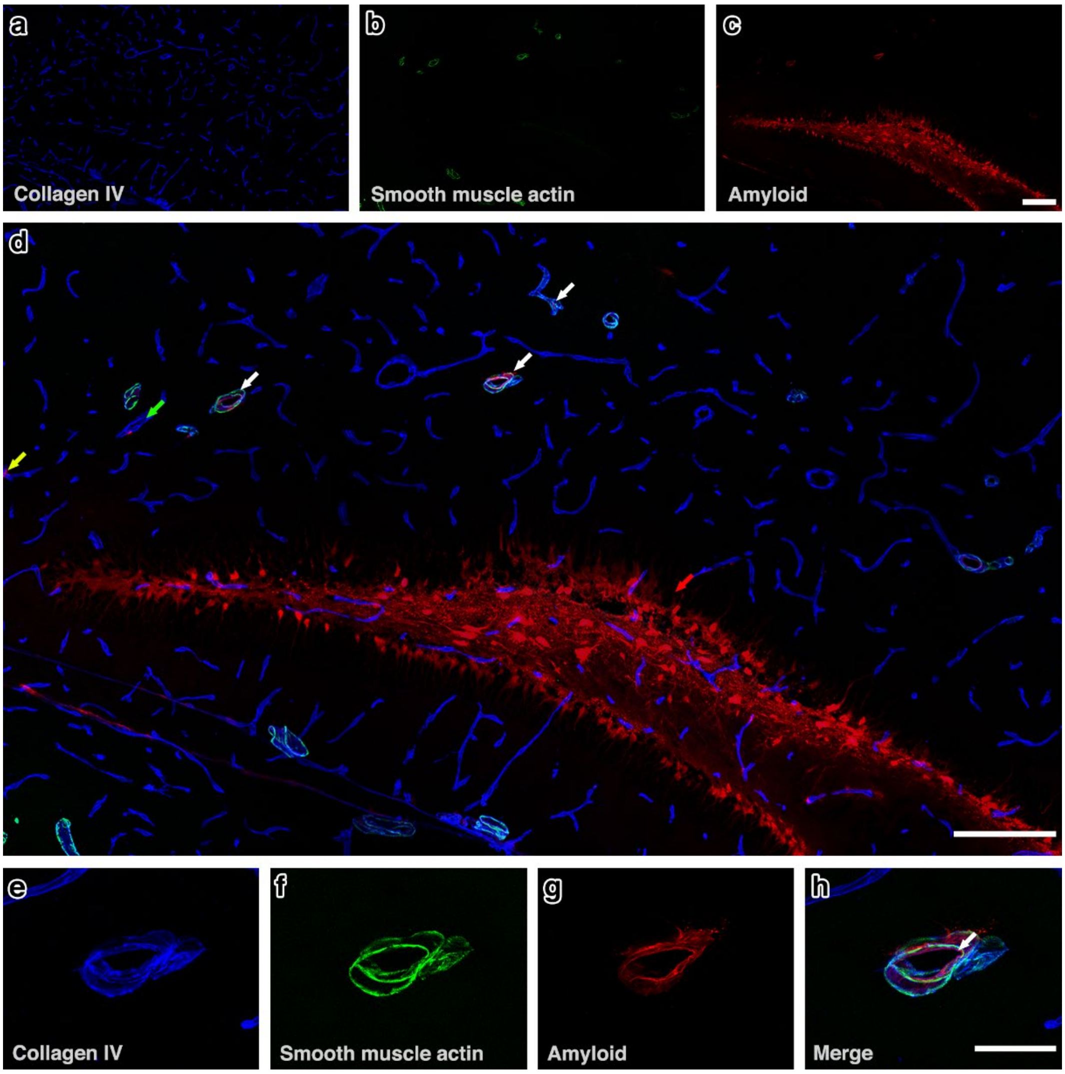
a
Collagen IV
b
Smooth muscle actin
c
Amyloid
d
e
Collagen IV
f
Smooth muscle actin
g
Amyloid
h
Merge

Figure 5.4 Composite tile scan of the distribution of Aβ injected into left hippocampus of wild-type control mice

The distribution of Aβ (c) in relation to collagen IV (a) and smooth muscle actin (b). Aβ was observed diffusely in the parenchyma (c & d) and co-localised with collagen IV in the walls of arterioles (white arrows), capillaries (yellow arrow) and few venules (green arrow). A representative high power of an arteriole (e-h) shows Aβ in the wall of the blood vessel as indicated by the white arrow in (h). Scale bars a-d = 200 μm, e – h = 10 μm. Figure published [247]

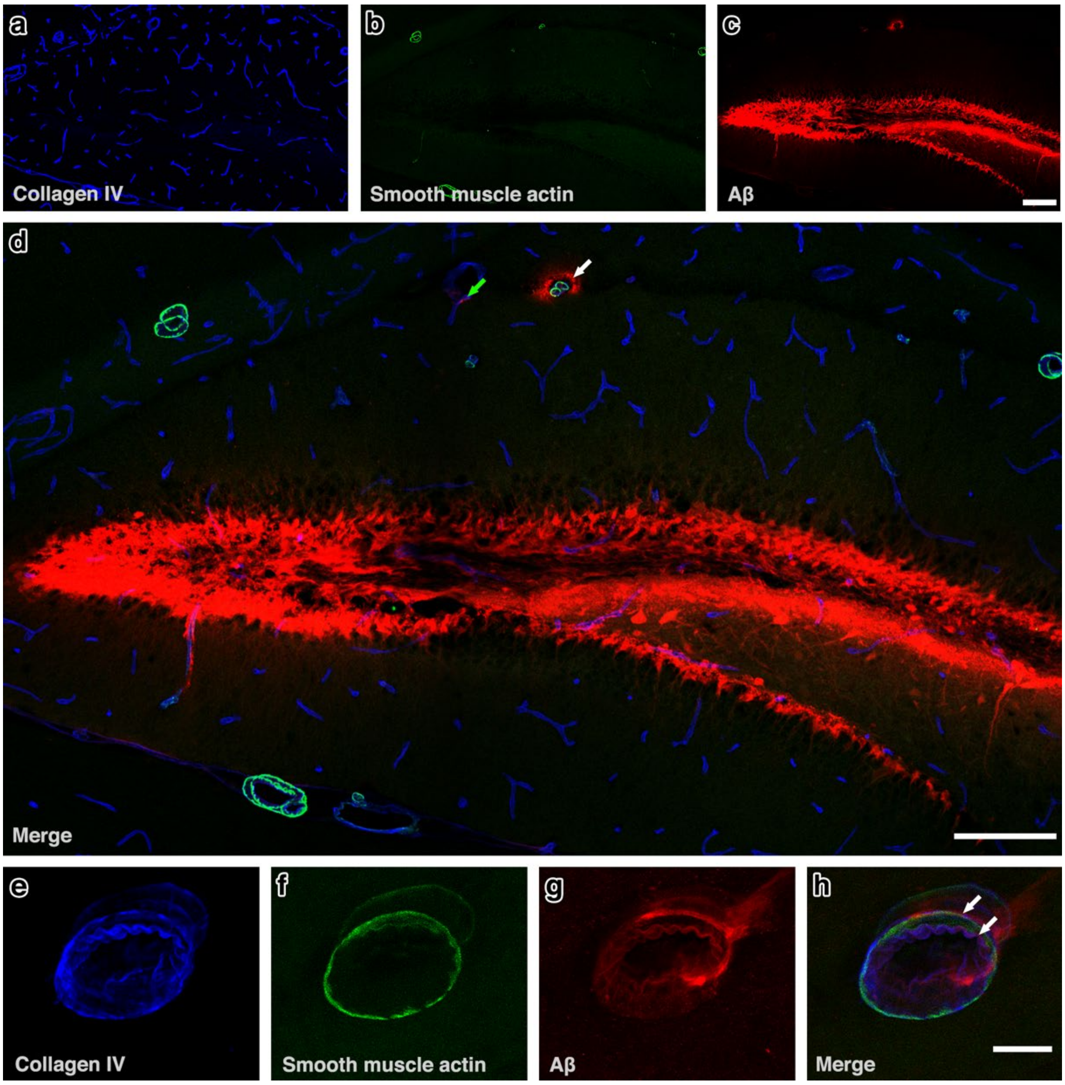
a
Collagen IV
b
Smooth muscle actin
c
Aβ
d
Merge
e
Collagen IV
f
Smooth muscle actin
g
Aβ
h
Merge

Figure 5.5 Composite tile scan of the distribution of Aβ injected into left hippocampus of α-DB deficient mice

The distribution of Aβ (c) in relation to collagen IV (a) and smooth muscle actin (b). Aβ was observed less diffusely in the parenchyma, accumulating mainly within extracellular spaces (c & d) but also co-localising with collagen IV in the walls of arterioles (e-h), capillaries and few venules (green arrow in d). Clumping of amyloid beta was also observed around arterioles that did not have Aβ within their walls (white arrow in d). A representative high power of an arteriole (e-h) shows Aβ in the wall of the blood vessel as indicated by the white arrows in (h). Scale bars a-d = 200 μm, e – h = 10 μm.

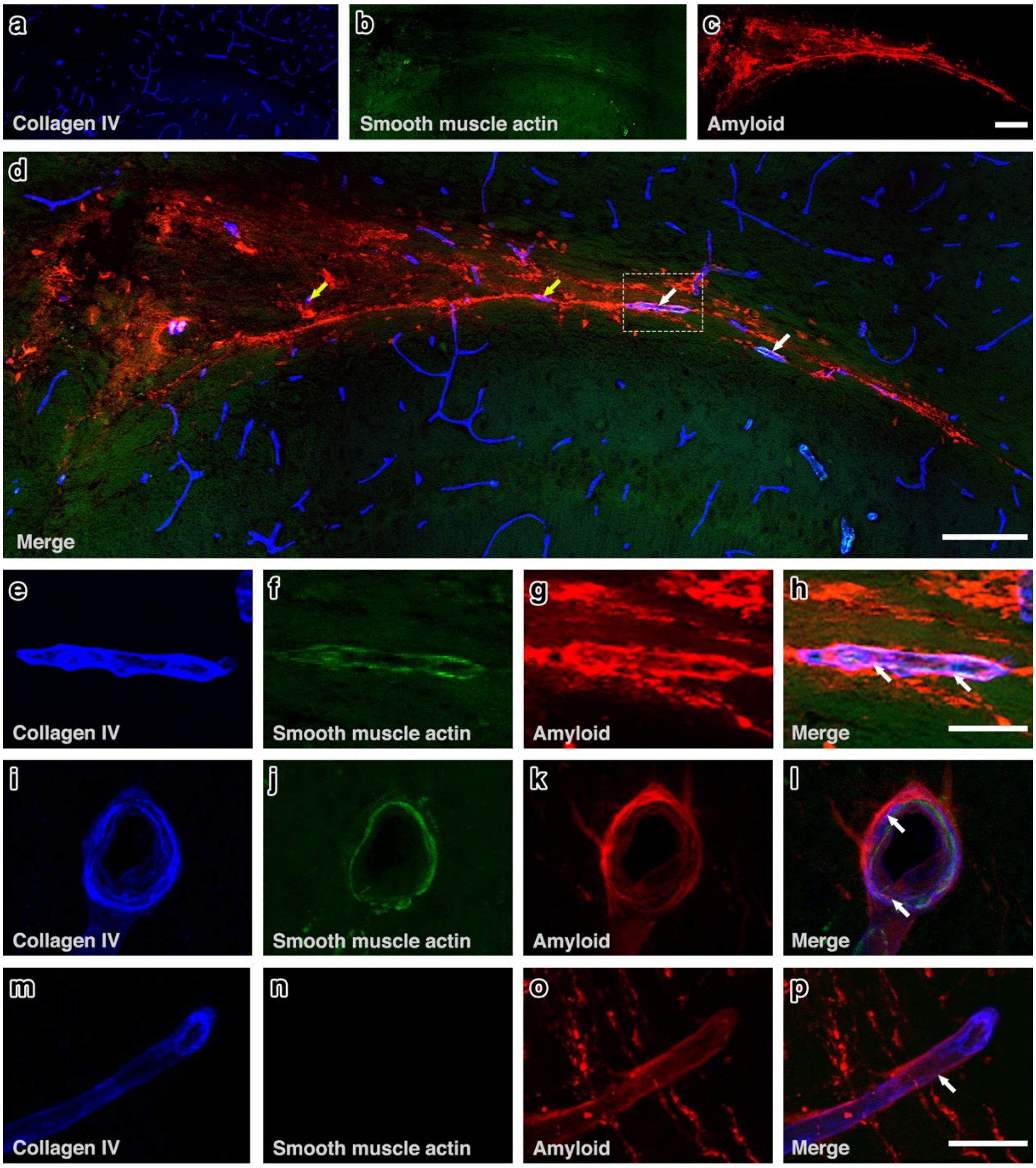
a
Collagen IV
b
Smooth muscle actin
c
Amyloid
d
Merge
e
Collagen IV
f
Smooth muscle actin
g
Amyloid
h
Merge
i
Collagen IV
j
Smooth muscle actin
k
Amyloid
l
Merge
m
Collagen IV
n
Smooth muscle actin
o
Amyloid
p
Merge

Figure 5.6 Composite tile scan of the distribution of Aβ injected into the corpus callosum of wild-type control mice

The distribution of Aβ (c) in relation to collagen IV (a) and smooth muscle actin (b). Aβ was observed along the white matter tracts (c & d) and co-localising with collagen IV in the walls of capillaries (yellow arrows) and few arterioles (white arrows). (e-h) An arteriole in the white matter - see box in (d) - with Aβ in the tunica media (white arrows). (i-l) A leptomeningeal artery in the hippocampal fissure abutting on to the white matter showing Aβ in the tunica media (lower arrow) and in the adventitia (upper arrow). (m-p) A capillary with Aβ (arrow) in the vessel wall. Scale bars a-d = 200 μm, e – h, i – l & m – p = 10 μm. Figure published [247]

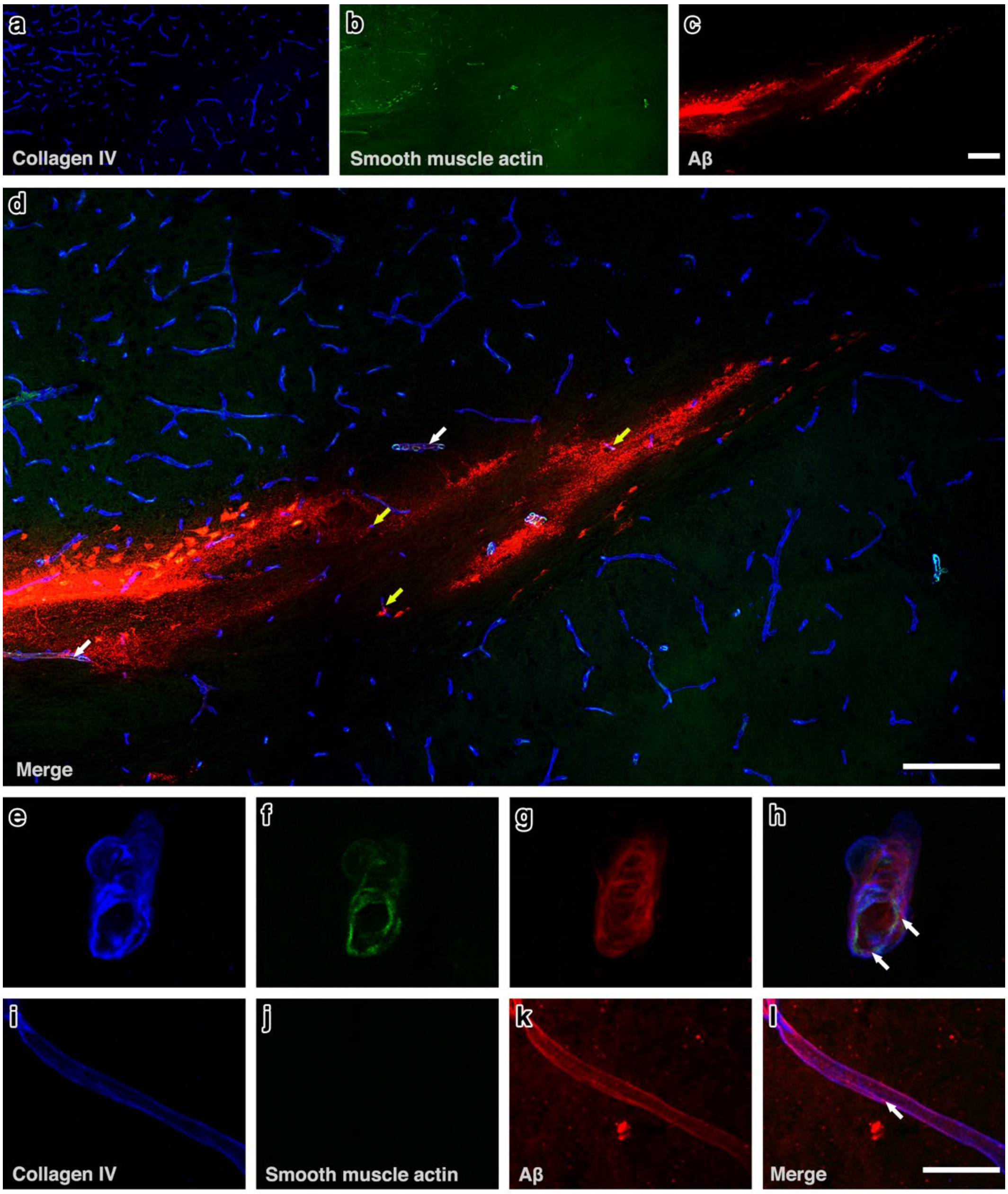
a
Collagen IV
b
Smooth muscle actin
c
Aβ
d
Merge
e
f
g
h
i
Collagen IV
j
Smooth muscle actin
k
Aβ
l
Merge

Figure 5.7 Composite tile scan of the distribution of Aβ injected into the corpus callosum of α-DB deficient mice

The distribution of Aβ (c) in relation to collagen IV (a) and smooth muscle actin (b). Aβ was mainly observed along the white matter tracts (d) and co-localising with collagen IV in the walls of capillaries (yellow arrows) and few arterioles (white arrows). Representative high power of an arteriole (e-h) and capillary (i – l) shows Aβ in the wall of the blood vessel (white arrows in h & l). Scale bars a-d = 200 µm, e – h & i – l = 10 µm.

5.5.2.2 QUANITATIVE ASSESSMENT OF IPAD BETWEEN GREY AND WHITE MATTER

Each region was analysed for quantitative differences in IPAD by calculating the density of capillaries, arterioles and venules with fluorescent Aβ in their vessel walls. We first compared the grey and white matter for each genotype (wild-type control and α-DB deficient). We then assessed the changes to IPAD between the genotypes. As per our assessment of vessel density (**see 5.5.1**) all data in this section is presented per 0.5mm^2 of tissue.

5.5.2.2.1 WILD-TYPE CONTROL MICE

In wild-type control mice, quantitative assessment of IPAD revealed significant differences in the density of capillaries and arterioles with fluorescent Aβ in their vessel walls between the hippocampal grey matter and the white matter. The density of arterioles with fluorescent Aβ in their vessel walls was significantly higher in the grey matter (2.3 vs 0.6 per 0.5 mm^2, $p < 0.05$). Conversely, the density of capillaries with fluorescent Aβ in their vessel walls was significantly higher in the white matter (1.1 vs. 6.3 per 0.5 mm^2, $p < 0.05$). There was no significant difference in the density of venules with fluorescent Aβ in their vessel walls (0.84 vs. 0.16 per 0.5 mm^2, $p = 0.058$) (**Table 6**). Data published [247].

5.5.2.2.2 ALPHA DYSTROBREVIN DEFICIENT MICE

In α-DB deficient mice, quantitative assessment of IPAD revealed no significant difference in the density of arterioles (0.9 vs 2.1 per 0.5 mm^2, $p = 0.132$) or venules (0.29 vs 0.32 per 0.5 mm^2, $p = 0.897$) with fluorescent Aβ in their vessel walls between grey and white matter. However, the density of capillaries with fluorescent Aβ in their vessel walls was significantly higher in the white matter (0.37 vs. 5.51 per 0.5 mm^2, $p < 0.005$) (**Table 6**).

			Grey matter	White matter	Sig.
Wild-type control	**Capillaries / 0.5mm^2**	Mean	**1.13**	**6.31**	**< 0.05**
		Range	(0.39 – 2.69)	(1.40 – 11.36)	
		S.D	1.09	4.34	
		S.E	0.49	1.94	
	Arterioles / 0.5mm^2	Mean	**2.27**	**0.64**	**< 0.05**
		Range	(1.57 – 3.70)	(0 – 2.43)	
		S.D	0.90	1.05	
		S.E	0.40	0.47	
	Venules/ 0.5mm^2	Mean	**0.84**	**0.16**	0.058
		Range	(0.31 - 1.74)	(0 - 0.80)	
		S.D	0.59	0.36	
		S.E	0.26	0.16	
α-DB deficient	**Capillaries / 0.5mm^2**	Mean	**0.37**	**5.51**	**< 0.005**
		Range	(0 - 0.99)	(3.51- 9.11)	
		S.D	0.51	2.22	
		S.E	0.23	0.99	
	Arterioles / 0.5mm^2	Mean	**0.90**	**2.07**	0.132
		Range	(0 - 1.01)	(0 - 3.90)	
		S.D	0.52	1.47	
		S.E	0.23	0.66	
	Venules / 0.5mm^2	Mean	**0.29**	**0.32**	0.897
		Range	(0 - 0.66)	(0 - 0.88)	
		S.D	0.30	0.44	
		S.E	0.13	0.20	

Table 6: Comparison of the density of vessels with fluorescent Aβ in their vessel walls between grey and white matter in wild-type control and α-DB deficient mice

5.5.2.3 WILD-TYPE CONTROL VS. ALPHA DYSTROBREVIN DEFICIENT MICE

In hippocampal grey matter, the density of arterioles with fluorescent Aβ in their vessel walls was significantly reduced in α-DB deficient mice compared to wild-type controls (2.27 vs 0.90 per 0.5 mm^2, $p < 0.05$). The density of capillaries (1.13 vs 0.37 per 0.5 mm^2, $p = 0.193$) and venules (0.84 vs 0.29 per 0.5 mm^2, $p = 0.98$) with fluorescent Aβ in their vessel walls also decreased in α-DB deficient mice but not significantly. IPAD appeared to be less efficient in α-DB deficient mice (**Figure 5.8**).

In white matter, the density of arterioles with fluorescent Aβ in their vessel walls decreased, but not significantly in α-DB deficient mice (2.06 vs. 0.64 per 0.5 mm^2, $p = 0.118$). There was no obvious difference in the density of capillaries (6.31 vs 5.51 per 0.5 mm^2, $p = 0.723$) but the density of venules with fluorescent Aβ in their vessel walls increased, but again not significantly in α-DB deficient mice (0.16 vs 0.32 per 0.5 mm^2, $p = 0.543$) (**Figure 5.8**).

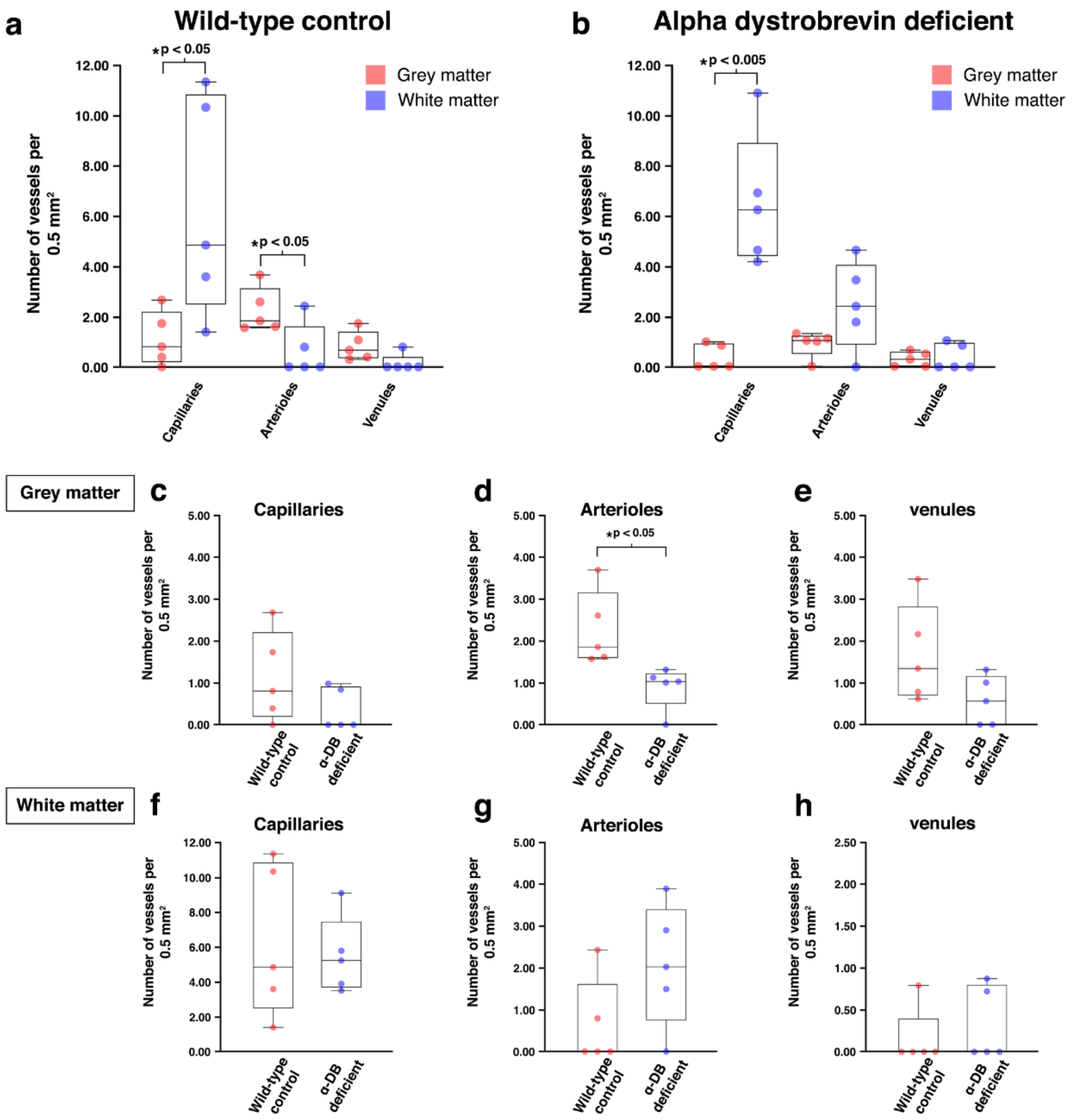

Figure 5.8 Comparison of the density of vessels with fluorescent Aβ in their vessel walls between wild-type control and α-DB deficient mice

There were significant differences between the number of capillaries and arterioles with fluorescent Aβ in their vessel walls between grey matter (red) and white matter (blue) in wild-type control mice (a). In α-DB deficient mice there was only a significant difference in the number of capillaries between grey and white matter (b). When compared to wild-type control mice, α-DB deficient mice showed significantly fewer arterioles with fluorescent Aβ in their vessel walls in the grey matter (d). There were no other significant differences between capillaries or venules in grey matter (c & e) or between capillaries, arterioles or venules in the white matter (f - h). Each box plot represents the range of data from five mice. The scatter plots represent vessel density from each mouse.

5.5.2.4 ASSESSMENT OF FLUORESCENT INTENSITY OF PARENCHYMAL AMYLOID BETA

To ascertain if the differences observed to IPAD in α-DB deficient mice were accompanied by alterations to parenchymal distribution of Aβ, fluorescent density analysis was performed on the same sections.

In the white matter, mean fluorescent area and mean pixel density was higher, although not significantly, than that in the grey matter in both wild-type control (mean fluorescent area 0.02 mm^2 vs. 0.05 mm^2, $p = 0.060$, mean pixel density 2.18 x 10^6 vs. 6.46 x 10^6 pixels, $p = 0.079$) and α-DB deficient mice (mean fluorescent area 0.03 mm^2 vs. 0.07 mm^2, $p = 0.063$, mean pixel density 4.25 x 10^6 vs. 9.32 x 10^6 pixels, $p = 0.099$). There was no significant difference in the white matter between wild-type and α-DB deficient mice but the values were higher in α-DB deficient mice (mean fluorescent area 0.05 mm^2 vs. 0.07 mm^2, $p = 0.388$, mean pixel density 6.46 x 10^6 vs. 9.32 x 10^6 pixels, $p = 0.368$). In the grey matter, there was no significant difference in the mean fluorescent area (0.02 mm^2 vs. 0.03 mm^2, $p = 0.199$) but there was a significant increase in mean pixel density in α-DB deficient mice (2.18 x 10^6 vs. 4.25 x 10^6 pixels, $p < 0.05$). This suggests that in α-DB deficient mice, a higher proportion of the injected Aβ tracer is taken up by the granule cell layer of the hippocampus (**Table 7** and **Figure 5.9**).

			Grey matter	White matter	Sig.
Wild-type control	**Fluorescent area / 0.5mm^2**	Mean	**0.02 mm^2**	**0.05 mm^2**	0.060
		Range	(0.01 - 0.03)	(0.02 - 0.08)	
		S.D	0.009	0.027	
		S.E	0.004	0.012	
	Mean pixel density raw IntDent / 0.5mm^2	Mean	**2.18 x 10^6 pixels**	**6.46 x 10^6 pixels**	0.079
		Range	(1.16 - 4.67)	(1.26 - 10.18)	
		S.D	1.47	4.10	
		S.E	0.66	1.83	
α-DB deficient	**Fluorescent area / 0.5mm^2**	Mean	**0.03 mm^2**	**0.07 mm^2**	0.063
		Range	(0.02 - 0.04)	(0.04 - 0.12)	
		S.D	0.009	0.037	
		S.E	0.003	0.017	
	Mean pixel density raw IntDent / 0.5mm^2	Mean	**4.25 x 10^6 pixels**	**9.32 x 10^6 pixels**	0.099
		Range	(3.07 - 5.97)	(4.15 - 15.39)	
		S.D	1.28	5.31	
		S.E	0.57	2.38	

Table 7: Comparison of area and mean pixel density of fluorescent amyloid beta remaining in the parenchyma of grey and white matter.

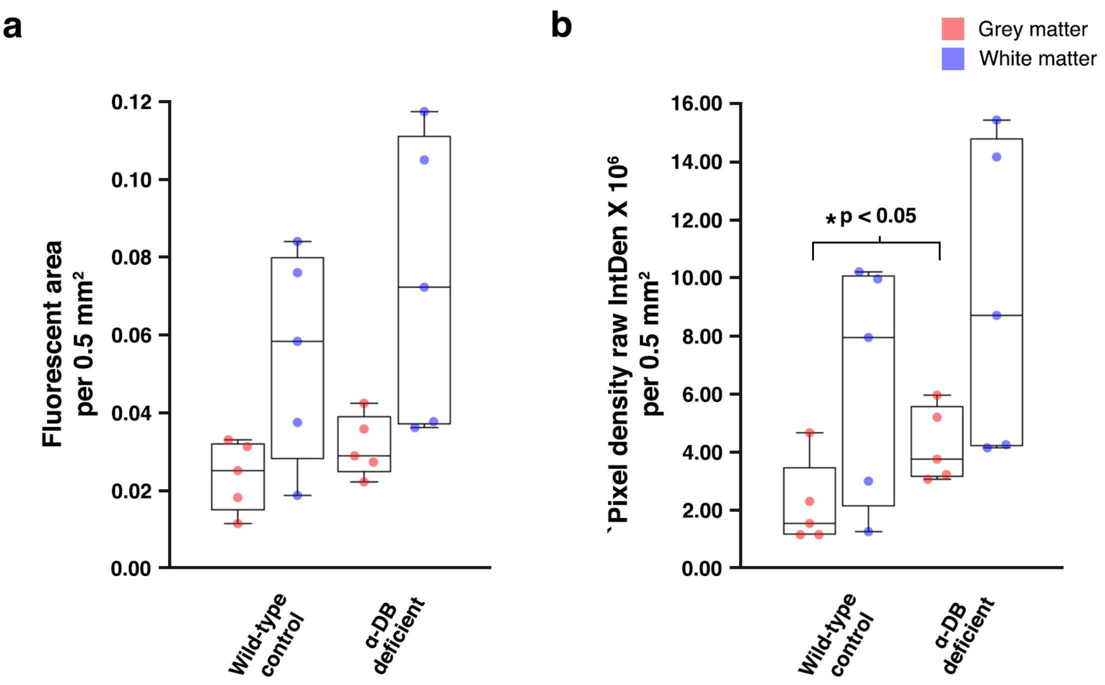

Figure 5.9 Comparison of mean fluorescent area and mean pixel density of parenchymal fluorescent Aβ in grey and white matter between wild-type control and α-DB deficient mice

Comparison of mean fluorescent area (a) and mean pixel density (b) of parenchymal fluorescent Aβ per $0.5mm^2$ *of grey matter (red) and white matter (blue) between wild-type control and α-DB deficient mice revealed a significant increase in mean pixel density in the grey matter of α-DB deficient mice. Each box plot represents the range of data from five mice. The scatter plots represent fluorescent area (a) and pixel density (b) from each mouse.*

5.6 DISCUSSION

The objectives of the work detailed in this chapter were to test the following hypotheses: 1) In wild-type control mice, the dynamics of IPAD are different in the white matter of the corpus callosum compared to hippocampal grey matter. 2) In mice genetically modified for alpha dystrobrevin, the dynamics of IPAD are altered in hippocampal grey matter and the white matter of the corpus callosum. These hypotheses were tested by a) comparing the density of capillaries in grey and white matter and b) injecting soluble Aβ as a tracer independently into the grey matter of the hippocampus and into the white matter of the corpus callosum of wild-type control and α-DB deficient mice and comparing the dynamics of drainage of tracer along IPAD pathways from each of these regions of the brain.

5.6.1 THE DYNAMICS OF INTRAMURAL PERIARTERIAL DRAINAGE IN THE WHITE MATTER IS DIFFERENT FROM THAT IN THE GREY MATTER IN WILD-TYPE CONTROL MICE

In our wild-type control mice, we observed injected fluorescent Aβ mainly within the walls of capillaries or within intracellular spaces of the white matter fibre tracts, in direct contrast to hippocampal grey matter in which fluorescent Aβ was present mainly in arteriole walls or in the parenchyma. The involvement of very few arterioles in the white matter may help to explain why the white matter is mostly spared from CAA. It is most likely that interstitial fluid (ISF) entering the capillary bed in the white matter either drains directly to grey matter arterioles or first enters the walls of coiled tortuous arterioles in the white matter and then into grey matter arterioles. Therefore, these grey matter arterioles are likely coping with the drainage of ISF from the grey matter as well as the underlying white matter. Failure of IPAD in these arterioles, such as seen with CAA [208] would alter drainage of ISF from the white matter contributing to white matter abnormalities such as WMH.

Cerebral white matter is more susceptible than grey matter to ischemic injury as capillary distribution in the white matter is relatively smaller [262]. In humans for example, the density of capillaries in the white matter is estimated to be around 49% lower than that in grey matter [263, 264]. Studies show an association with decline of capillary density and abnormalities in the white matter both in humans [262, 264, 265] and animal models [266, 267] suggesting a link between reduced perfusion of the white matter and white matter abnormalities. In wild-type control mice, we observed a 39.19% reduction in the density of capillaries in the white matter, a similar observation to that observed in humans [264]. As delivery of nutrients to the brain is via vascular capillaries, the lower density in the white matter suggests a lower capacity in white matter compared to grey matter for the delivery of oxygen and other nutrients. This may result in an increased risk of ischaemia/ hypoxia in the white matter over grey matter in the presence of diseases such as arteriosclerosis and CAA. As the capillary basement membrane is the main conduit for IPAD, the lower density of capillaries in the white matter also suggests that there is a lower capacity for IPAD in white matter when compared to grey matter ([247] **see appendix A**).

5.6.2 THE DYNAMICS OF INTRAMURAL PERIARTERIAL DRAINAGE ARE ALTERED IN ALPHA DYSTROBREVIN DEFICIENT MICE

5.6.2.1 GREY MATTER

Previous animal studies show the pattern of IPAD from hippocampal grey matter as the labelling of the walls of capillaries, arterioles and leptomenigeal arteries with fluorescent tracer within 5 minutes after injection into parenchyma. The majority of labelling is in arteriole walls followed by capillaries and a few venules [74, 160, 168, 170]. Alterations to this pattern, such as a reduction in the labelling of arterial walls in the hippocampus, have been attributed to a failure of IPAD. Previous studies have reported this in aged mice [74] and transgenic mouse models such as in the Tg2576 mouse model of AD [170] but up until now, not in young adult mice as shown here. In 12-week-old α-DB deficient mice, fluorescent Aβ was still present in the walls of capillaries and arterioles of the grey matter suggesting a functional IPAD pathway, but the number of vessels involved was much lower than that observed in wild-type control mice. Similarly, the parenchyma of the hippocampus in α-DB deficient mice appeared to accumulate more fluorescent Aβ suggesting reduced efficiency of IPAD as well as other clearance mechanisms.

The Tg2576 mouse model of AD is transgenic for amyloid precursor protein (APP), expressing human APP with a double mutation that favours the formation of Aβ-40 (Swedish mutation) [268]. At around 10 months of age these mice show CSVD in the form of CAA and also the accumulation of Aβ in the parenchyma as plaques

[269]. Tracer studies show that these mice have altered IPAD with a reduction in arterioles laden with fluorescent dextran. Interestingly, an increase in severity of CAA caused a redistribution of fluorescent dextran from the vessel walls of capillaries to the vessel walls of venules [170]. A significant redistribution of fluorescent Aβ from capillaries to venules was not observed in α-DB deficient mice, although there was more Aβ in the parenchyma, suggesting that other clearance mechanisms may also be impaired in this model. In this study young adult mice that still have a functioning IPAD pathway were used, so the pattern will likely change in older α-DB deficient mice.

In a previous study, we have demonstrated that in aged wild-type mice the pattern of IPAD is altered in a region-specific manner, favouring areas most affected by CAA. We associated these changes with age associated alterations to basement membrane composition [74]. In this chapter, the region of grey matter we assessed for IPAD (hippocampus) was based on the occurrence of CAA in the hippocampus of APP transgenic mouse models [261, 270]. However, in humans CAA is predominantly observed in the parietal and occipital cortices [271]. Therefore, it would be of interest to assess IPAD in other grey matter regions in α-DB deficient mice to compare the present findings to the pathology observed in human CAA cases.

5.6.2.2 WHITE MATTER

The dynamics of IPAD in the white matter of α-DB deficient mice was not dissimilar from that observed in wild-type control mice. However, there did appear to be more arterioles involved in α-DB deficient mice perhaps as a compensatory mechanism due to the reduced efficiency of IPAD observed in the grey matter altering the pattern of IPAD in the white matter. We only focused on drainage of ISF within white matter tracts so further animal tracer studies are required to ascertain this. For reasons as yet unknown, our α-DB deficient mice showed a 12.09% increase in capillary density in the white matter, possibly as a compensatory mechanism in the face of decreased perfusion. It is possible that this may offer some protection against ischemic damage to the white matter, but further work is required to investigate this.

5.6.3 CONCLUSIONS

The lower density of capillaries in the white matter of wild-type control mice suggests a lower capacity in white matter compared to grey matter for the delivery of oxygen and other nutrients. This may predispose the white matter to an increased risk of ischaemia/ hypoxia. When fluorescent Aβ was injected as a tracer into the normal white matter of wild-type control mice it was cleared more slowly from the capillaries compared to grey matter. The lower density of capillaries in the white matter also suggest that the white matter has a reduced capacity for IPAD when compared to grey matter.

In α-DB deficient mice, the dynamics of IPAD are altered in the grey matter but not in the white matter. IPAD in the grey matter occurs along fewer arterioles accompanied by an increase in diffuse fluorescent Aβ within the extracellular spaces of the hippocampus. When considered with results from the previous chapter (chapter 4) it appears that the thickening of the capillary basement membrane and remodelling of the microvascular extracellular matrix seen in α-DB deficient mice is intrinsically linked to alterations in IPAD in the grey matter of these mice. This is similar to findings observed in other experimental models that show that the changes to the cerebral vascular induced by hypertension [173], hyperhomocysteinemia [227], and overexpression of Aβ [28, 228, 229] all favour the accumulation of amyloid proteins in the IPAD pathway. As thickening of the capillary basement membrane and remodelling of the microvascular extracellular matrix are concurrent to the common features of CSVD [15, 67], α-DB deficient mice provide an opportunity to further investigate the role of IPAD in CSVD and VaD.

As the function of the cerebral vessels is to both supply blood to the brain as well as clear interstitial fluid, the next step is to determine if α-DB deficient mice display any alterations in cerebral blood flow (CBF). A key feature of CSVD and VaD is reduced efficiency of neurovascular coupling and CBF. Abnormalities in the cerebral vasculature, such as thickening of the basement membrane, have been linked to a failure of neurovascular coupling and hypoperfusion [272] so assessment of the CBF in α-DB deficient mice warrants further investigation.

Chapter 6 LOSS OF ALPHA-DYSTROBREVIN FROM ASTROCYTE ENDFEET AND CEREBRAL BLOOD FLOW

6.1 INTRODUCTION

The vessel wall is a key functional component of the neuro-vascular unit (NVU). The NVU plays a key role in the autoregulation of cerebral blood flow (CBF). Vascular cells (endothelium, pericytes and smooth muscle cells (SMC)), glial cells (astrocytes, microglia and oligodendroglia) and neurons of the NVU functionally integrate in a process called neurovascular coupling or functional hyperemia. In normotensive adults, autoregulation of CBF by the NVU ensures that CBF is maintained at about 60 mL per 100 g of brain tissue per minute [273] irrespective of changes to perfusion pressure. Dilation or constriction of blood vessels by the depolarisation and contraction or hyperpolarisation and relaxation of SMCs and pericytes in response to different stimuli, such as neuronal stimulation, decreases or increases blood flow ensuring an adequate supply of blood to active brain regions [274, 275].

Neurovascular coupling becomes less efficient with age as CBF has been shown to be reduced with normal ageing accompanied by attenuated responses to hypoxia, hypercapnia and alterations to blood pressure [276]. A key pathological feature of vascular dementia (VaD) is also a failure of neurovascular coupling and impaired CBF, particularly in the hippocampus, periventricular white matter and basal ganglia in which reductions in CBF can trigger a cascade of hypoxic events and inflammation, having a deleterious effect on cerebral homeostasis [9]. Alterations to cerebral perfusion often correlate with severity of dementia and can be used as an indicator of disease progression [7, 8].

Abnormalities in the cerebral vasculature, such as loss of pericytes, thickening of the basement membrane or reductions in the overall vascular bed have been linked to a failure of neurovascular coupling [272]. As α-dystrobrevin (α-DB) deficient mice show similar alterations to the vasculature, it is important to ascertain if these alterations are also accompanied by abnormal neurovascular coupling and reductions in CBF, an area that has not been investigated before in these mice.

In this chapter, CBF is assessed in cortical and hippocampal grey matter of α-DB deficient mice to assess if the thickening of the cerebral basement membrane observed in these mice are also accompanied by alterations to CBF. Data from a small pilot study testing CBF in α-DB deficient mice when challenged with hypercapnia is also presented.

6.2 HYPOTHESIS

In mice genetically modified for alpha dystrobrevin, cerebral blood flow is impaired under normal conditions and when challenged in hypercapnia.

Testing this hypothesis has been performed at the University College London, by colleagues at the Centre for Advanced Biomedical Imaging.

6.3 AIMS

The work detailed in this chapter aims to investigate whether the loss of α-DB from astrocytic endfeet alters CBF. Mice deficient for α-DB underwent non-invasive MRI imaging with CBF in the cortex and hippocampal grey matter assessed by arterial spin labelling (**Figure 6.1**).

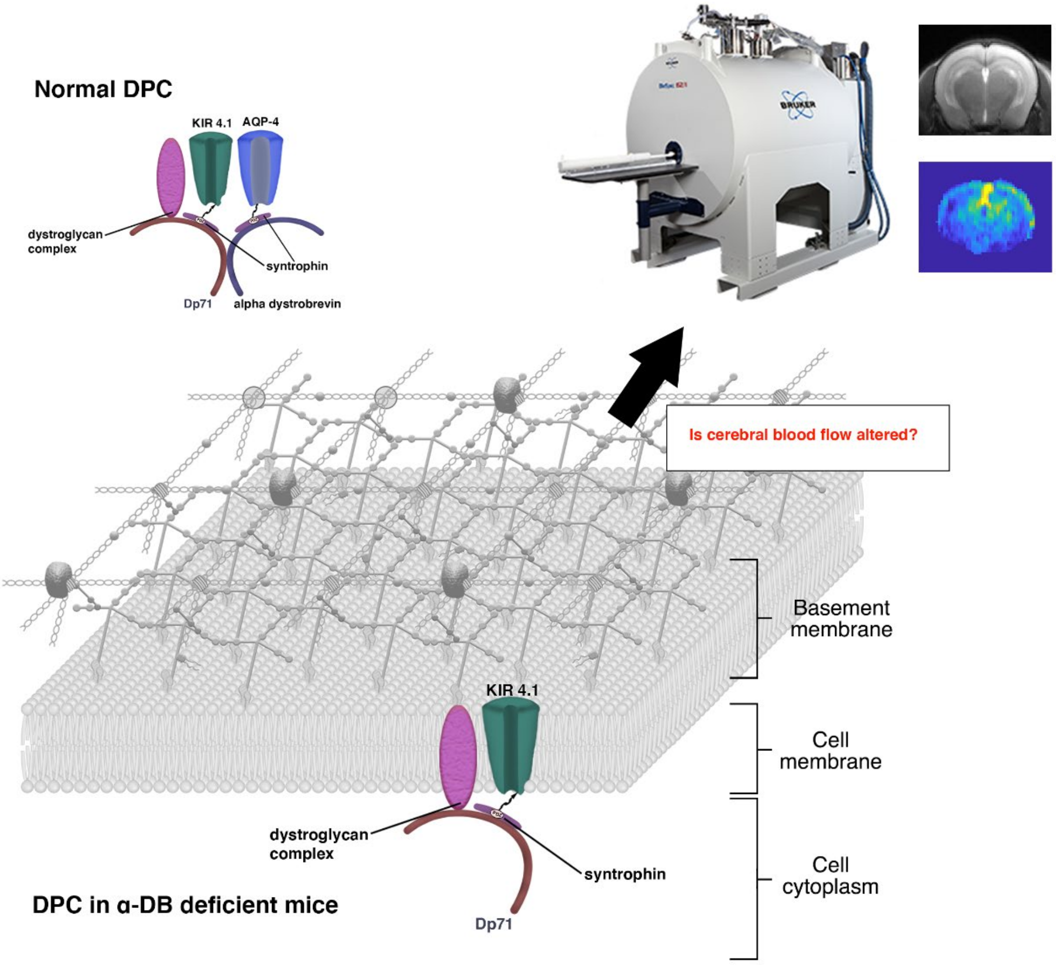
Normal DPC
KIR 4.1
AQP-4
dystroglycan complex
syntrophin
Dp71
alpha dystrobrevin
Is cerebral blood flow altered?
Basement membrane
Cell membrane
Cell cytoplasm
KIR 4.1
dystroglycan complex
syntrophin
DPC in α-DB deficient mice
Dp71

Figure 6.1 alpha dystrobrevin, the dystrophin associated protein complex and assessing cerebral blood flow

Does the loss of αDB from astrocytic endfeet alter cerebral blood flow?

6.4 MATERIALS & METHODS

In this chapter, adult (12 – 16 week-old) α-DB deficient (B6;129-*Dtna*^{tm1Jrs}/J) [239] (n = 10) and wild-type control mice (n = 12) were assessed for CBF using a non-invasive MRI technique (arterial spin labelling (ASL)) by colleagues at the Centre for Advanced Biomedical Imaging UCL.

Anaesthetised mice (2% isoflurane) were imaged using a horizontal bore 9.4T Bruker preclinical system (BioSpec 94/20 USR) using 440 mT/m gradient set with outer/ inner diameter 205 mm /116 mm respectively (BioSpec B-GA 12S2), a 86mm volume transit RF coil and a four-channel receiver array coil designed for the mouse brain (Bruker). CBF was assessed using the standard Buxton general kinetic perfusion model [277]. All imaging data was processed using Matlab 2018 (Mathworks) (**see section 2.5 and appendix C for more detailed methods**).

Statistical analysis was performed using SPSS and an independent *t-test* with significance set at $P < 0.05$.

A small pilot study was also performed assessing CBF in α-DB deficient mice after exposure to hypercapnia. Hypercapnia was generated by exposing 10-month old α-DB deficient (n=2) and wild-type control mice (n=3) to medical air for 5 mins, 10% CO_2 for 5 mins and then medical air for a further 10 mins. Baseline scans were normalised to the mean baseline signal (for the first 5 mins of scanning) to visualise the relative change in CBF.

6.5 RESULTS

To establish whether a lack of α-DB at astrocyte endfeet affects CBF of the cortex and hippocampal grey matter, wild-type control and α-DB deficient mice underwent non-invasive MRI imaging with CBF assessed by arterial spin labelling.

6.5.1 ASSESSMENT OF RESTING CEREBRAL BLOOD FLOW

In α-DB deficient mice there was a small but non-significant reduction in both cortical CBF (202 ± 35 ml/min/100g vs. 185 ± 55 ml/min/100g, p = 0.41) (**Figure 1.2**) and hippocampal CBF (206 ± 45 ml/min/100g vs. 191 ± 55 ml/min/100g, p = 0.49) (**Figure 1.3**).

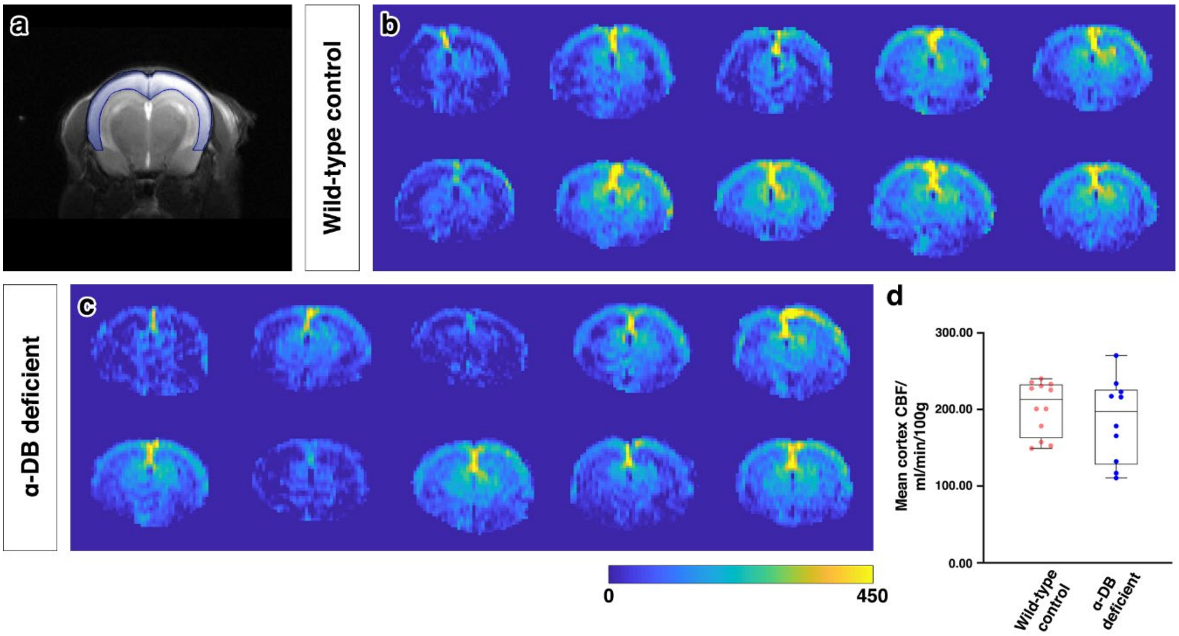
a
Wild-type control
b
α-DB deficient
c
0
450
d
Mean cortex CBF/ ml/min/100g
300.00
200.00
100.00
0.00
Wild-type control
α-DB deficient

Figure 6.2 Assessment of cortical CBF between wild-type control and α-DB deficient mice

Assessment of cortical CBF (region highlighted blue in (a) using ASL between wild-type control (b) and α-DB deficient mice (c) revealed no significant differences in CBF (d). Each box plot in d represents the range of data from all mice in that group (red, n = 12, blue, n = 10). The scatter plots represent mean CBF from each mouse.

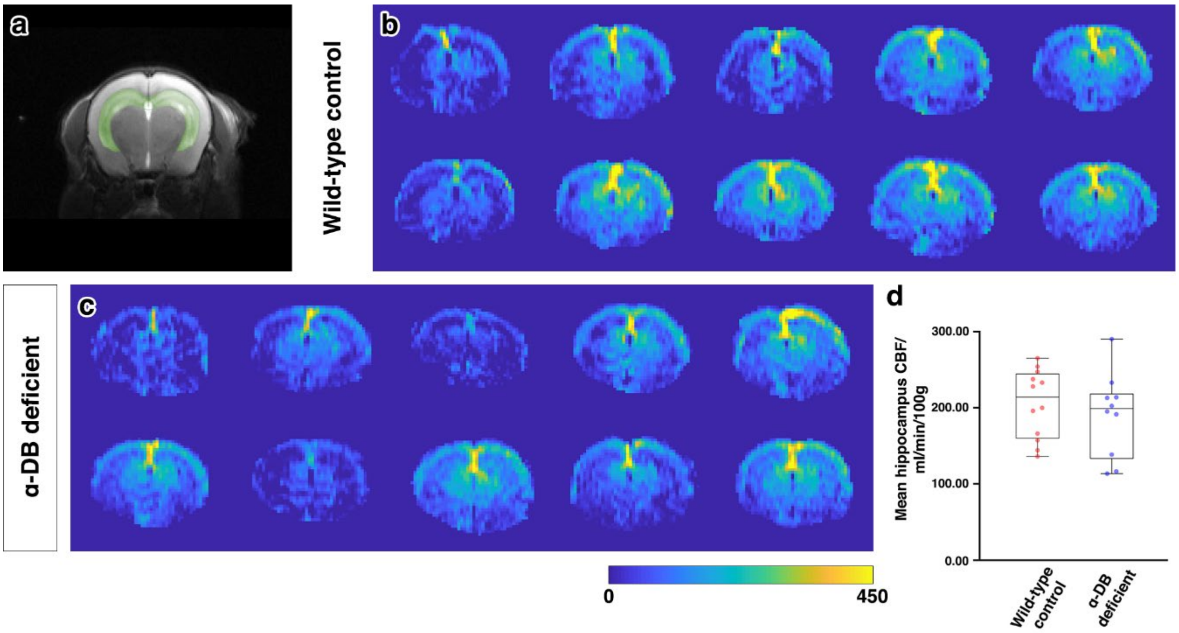
a
Wild-type control
b
α-DB deficient
c
d
0
450
Mean hippocampus CBF/ ml/min/100g
300.00
200.00
100.00
0.00
Wild-type control
α-DB deficient

Figure 6.3 Assessment of hippocampal CBF between wild-type control and α-DB deficient mice

Assessment of hippocampal CBF (region highlighted green in (a) using ASL between wild-type control (b) and α-DB deficient mice (c) revealed no significant differences in CBF (d). Each box plot in d represents the range of data from all mice in that group (red, n = 12, blue, n = 10). The scatter plots represent mean CBF from each mouse.

6.5.2 ASSESSMENT OF CEREBRAL BLOOD FLOW IN RESPONSE TO HYPERCAPNIA

Both wild-type control and α-DB deficient mice appeared to show alterations to cortical (**Figure 1.4**) and hippocampal (**Figure 1.5**) CBF in response to hypercapnia. However, there were differences in the level of relative change of CBF from base values. In wild-type control mice, there was an obvious elevation of CBF upon administration of 10% CO_2 that returned to baseline values once medical air was restored. In α-DB deficient mice, the elevation of CBF was less obvious and fluctuated more widely in both medical air and in 10% CO_2.

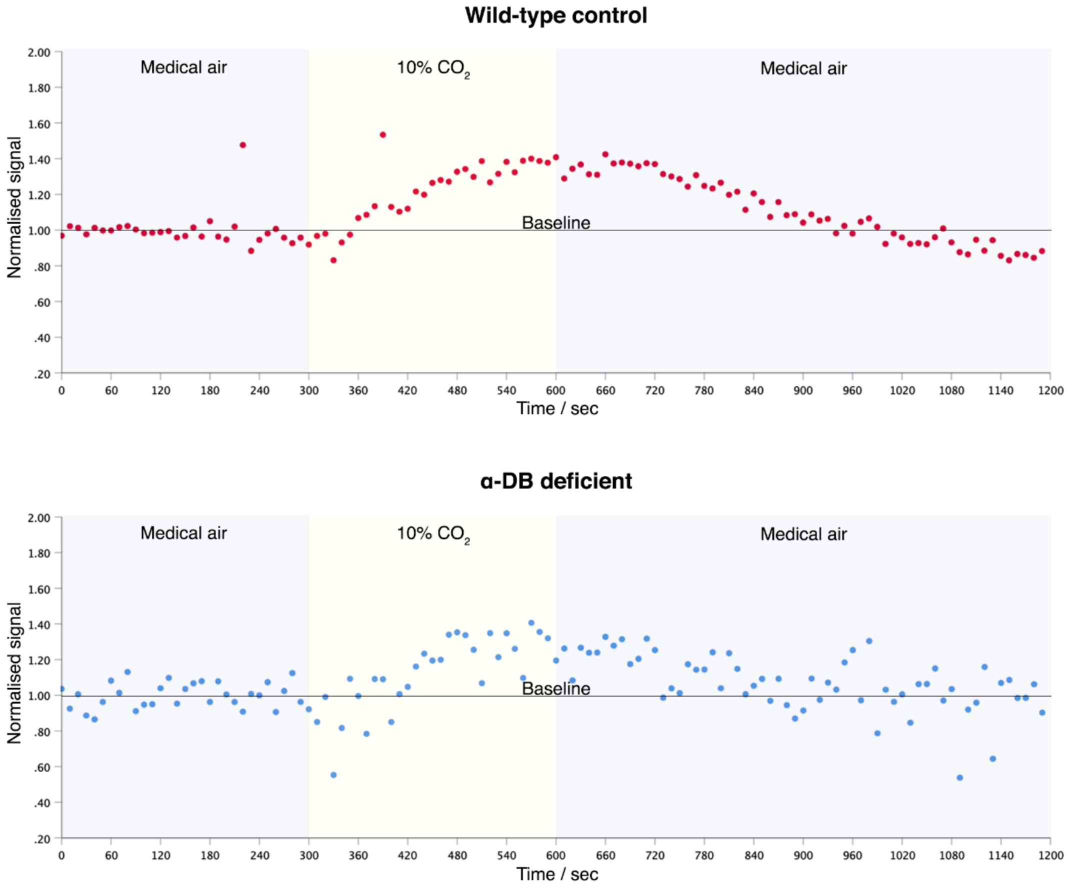

Figure 6.4 Visualisation of the relative change in cortical CBF in response to hypercapnia in wild-type control and α-DB deficient mice

In wild-type mice (red) there is an obvious increase in relative CBF in response to hypercapnia (10% CO_2). In α-DB deficient mice (blue) CBF appeared to fluctuate more during and after hypercapnia.

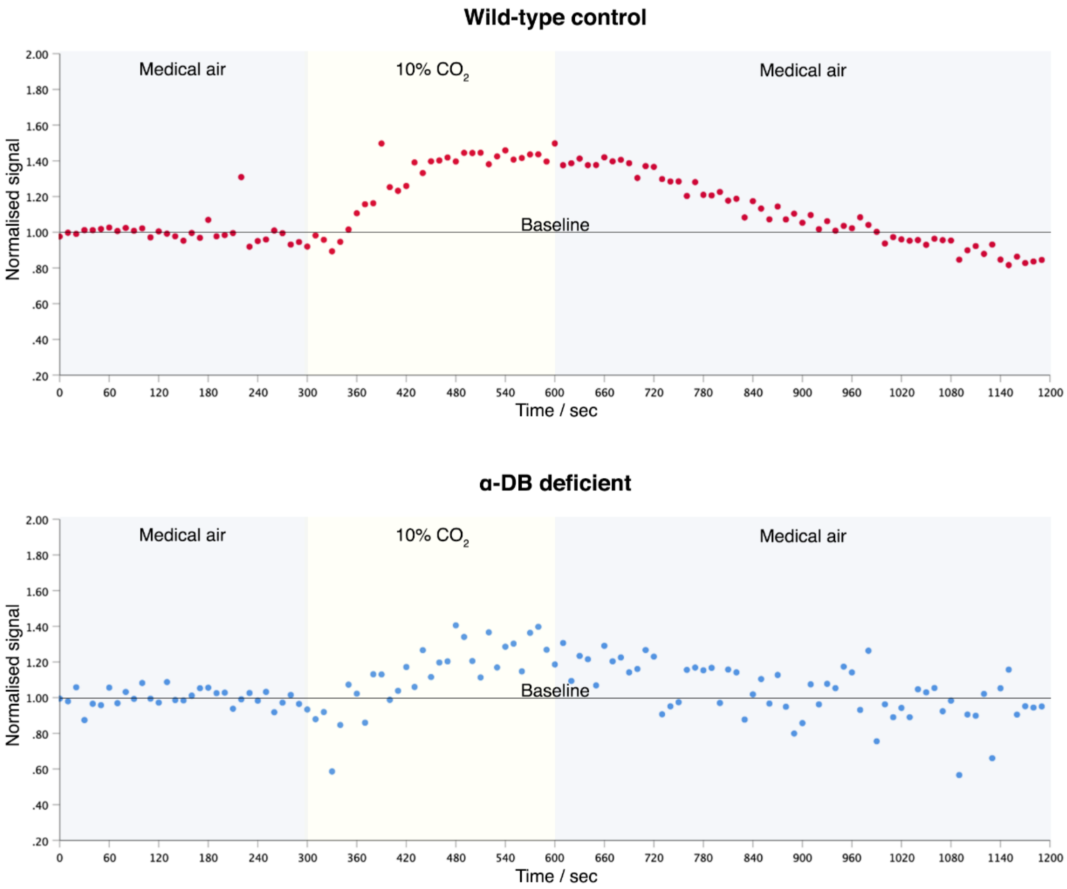

Figure 6.5 Visualisation of the relative change in hippocampal CBF in response to hypercapnia in wild-type control and α-DB deficient mice

In wild-type mice (red) the increase in relative CBF in response to hypercapnia (10% CO_2) is similar to that seen in the cortex. In α-DB deficient mice (blue) CBF appeared to fluctuate more in a similar pattern to that seen in the cortex.

6.6 DISCUSSION

The objective of this chapter was to test the hypothesis that in mice genetically modified for α-DB, CBF will be reduced. This was investigated by performing non-invasive MRI imaging and arterial spin labelling (ASL).

Reduced CBF has been associated with ageing [278, 279] particularly in older individuals with high vascular risk burdens [280]. In α-DB deficient mice, in which the thickening of capillary basement membranes and remodelling of the extracellular matrix of all cortical vessels (chapter 4) is similar to that observed in animal models of ageing [74], in animal models of vascular dysfunction [173] and in human ageing [68], baseline cortical and hippocampal CBF did not appear to be significantly altered. Therefore, adult α-DB deficient mice do not appear to be affected by hypoperfusion. It is interesting to note that transmission electron microscopy (chapter 4) revealed that grey matter capillary lumens were significantly larger in α-DB deficient mice when compared to wild-type controls. It is possible that this may be a compensatory mechanism to counteract any negative effect of vascular wall remodelling on CBF. Further studies using aged α-DB deficient mice may help to elucidate this.

The small pilot study assessing CBF response to hypercapnia revealed an attenuated response in both the cortex and hippocampus in older α-DB deficient mice. This suggest that neurovascular coupling in older α-DB deficient mice may be different from that in wild-type controls and that regulation of blood flow by dilation or constriction of blood vessels in the hippocampus and cortex is altered. Only a small number of animals were tested, so more work utilising a much larger cohort of mice is required to confirms this. Also, due to restrictions caused by the COVID 19 pandemic, we were unable to test response to hypercapnia in younger α-DB deficient mice. Future work will incorporate younger mice (12-16 weeks).

Chapter 7 GENERAL DISCUSSION

Vascular dementia (VaD) is defined as a progressive decline in cognitive ability associated with a broad etiology of vascular insults, the most common affecting the smaller vessels in the brain as cerebral small vessel disease (CSVD) [16]. In CSVD, modifications to the vessel wall such as those caused by arteriolosclerosis and cerebral amyloid angiopathy (CAA) impact upon efficient cerebral blood flow and perfusion to the brain [21, 22].

Cerebral blood vessels serve a dual function. In conjunction with neurons, they form an essential component of the neuro-vascular unit (NVU) to autoregulate cerebral blood flow (CBF), ensuring an adequate supply of blood flow to the brain, irrespective of changes to perfusion pressure [273]. However, an important function of the cerebral blood vessels is the removal of waste from the brain along the intramural periarterial drainage (IPAD) pathways. Alterations to cerebral blood vessels, such as modifications to the vessel walls likely has an impact on both perfusion [272] and IPAD [173] [227] [28, 228, 229].

A very well recognized subgroup in the spectrum of CSVD is CAA, characterized by the deposition of amyloid proteins in the walls of blood vessels [281]. Based on the pattern of deposition of amyloid in the walls of blood vessels in both humans and transgenic mouse models, as well as experimental studies involving the study of drainage of tracers from the brain, it is recognized that in CAA and other protein elimination failure arteriopathies there is a likely failure of clearance of amyloid along IPAD pathways [160, 282, 283].

The risk factors for CSVD are dyslipidemia, hypertension, obesity, age, stroke, and diabetes mellitus [284-287]. Experimental models of hypertension, diabetes and dyslipidemia replicate some of the changes in the walls of the vessels observed in humans. In vivo experimental work shows the failure of IPAD in some of these models [172-176]. Alterations to the cerebral vascular induced by hypertension [173], hyperhomocysteinemia [227], and overexpression of Aβ [28, 228, 229] include a thickening of blood vessel walls that is most likely altering the compliance of the vessel wall for IPAD. Subsequently in these models, IPAD also appears to have failed.

The main conduit for IPAD is the extracellular matrix (ECM) of the cerebral vascular basement membrane. This basement membrane is regulated and hence maintained by perivascular cells (astrocytes) and the cells that reside within it. Each cell type of the vessel wall contributes to the composition of the ECM but also interacts with laminin networks of the basement membrane by association with the transmembrane proteoglycan dystroglycan and integrin adhesion receptors [59]. Polarised astrocytic extensions form endfeet projections that encircle the abluminal side of the vessel wall [45]. 3D modelling and electron microscopy show that these endfeet projections almost cover the entire cerebral vasculature [288], interacting with ECM of the cerebrovascular basement membrane. This interaction is regulated by the dystrophin associated protein complex (DPC) [94, 95] and disruptions to this complex result in alterations to the basement membrane [231] [237] [146]. This suggest that the regulation of the fine interaction between the astrocyte endfeet and the ECM of the basement membrane by the DPC must play a key role in ensuring the integrity and function of basement membranes. As the ECM of the basement membrane is the conduit for IPAD, the DPC must also contribute to the integrity and function of IPAD pathways. This highlights two important questions that formed the basis of this thesis; 1) Is the morphology and the efficiency of IPAD pathways dependent on vascular DPC? and 2) Can mice with altered DPC be used to model a failure of fluid clearance by IPAD and the features of CSVD and VaD?

To address these questions, mice deficient for the dystrophin associated protein alpha dystrobrevin (α-DB), a key intracellular protein of vascular DPC [146] were chosen as a suitable model to assess both the morphology and dynamics of the IPAD pathway in the absence of a complete DPC at astrocyte endfeet. These mice show a redistribution of the water channel AQP4 from astrocyte endfeet to the cell body [146] so the role of AQP4 in maintaining the structure of the IPAD pathway was also assessed using mice deficient for AQP4.

The key aims of this thesis were:

1. To test if loss of AQP4 in α-DB deficient mice affects the morphology of IPAD pathways.
2. To investigate how loss of α-DB at astrocyte endfeet affects the morphology and dynamics of IPAD pathways and if these mice show features of CSVD and VaD.

The hypothesis tested were:

1. *In mice that do not express glial aquaporin 4 the morphology of capillary intramural periarterial drainage pathways is altered.*
2. *In mice genetically modified for alpha-dystrobrevin, morphology of capillary intramural periarterial drainage pathways are altered.*
3. *In wild-type control mice, the dynamics of intramural periarterial drainage pathways are different in the white matter of the corpus callosum compared to hippocampal grey matter.*
4. *In mice genetically modified for alpha dystrobrevin, the dynamics of intramural periarterial drainage pathways are altered in hippocampal grey matter and the white matter of the corpus callosum.*
5. *In mice genetically modified for alpha dystrobrevin, cerebral blood flow is impaired under normal conditions and when challenged in hypercapnia.*

In summary, the key findings of this thesis are:

1. **Redistribution of AQP4 in α-DB deficient mice has minimal effect on the IPAD pathway.** The loss of AQP4 from the DPC at astrocyte endfeet does not significantly alter morphology of the capillary wall and IPAD pathways in the grey matter but a reduction in the percentage surface area of capillary basement membrane accompanied by an increase in the surface area of the intramural cells were observed in the white matter.
2. **The cerebral vasculature in young adult α-DB deficient mice show signs of early ageing and reflect early changes seen in CAA.** The removal of α-DB from the DPC of astrocyte endfeet alters the morphology of the capillary wall and IPAD pathways. The surface area occupied by basement membrane is increased in capillary walls in both grey and white matter. The ECM of basement membranes are altered in the grey matter vessels with elevated expression of collagen IV (COL4).
3. **IPAD in the white matter is less efficient than that in the grey matter.** In the white matter, fluorescent amyloid-beta (Aβ) (1-40) preferentially drains along capillary walls in both α-DB deficient and wild-type control mice.
4. **IPAD is impaired in α-DB deficient mice.** The removal of α-DB from the DPC of astrocyte endfeet alters the dynamics of IPAD in the grey matter but not the white matter. The pattern of IPAD in the grey matter of α-DB deficient

mice showed fewer arterioles with fluorescent amyloid-beta (Aβ) (1-40) in their walls but more fluorescent amyloid-beta (Aβ) (1-40) in the parenchyma compared to wild-type control mice.

5. **The removal of α-DB from the DPC of astrocyte endfeet does not alter resting CBF.** CBF in the cortex and hippocampus was not altered in α-DB deficient mice but the challenge with hypercapnia revealed a trend consisting of a lower capacity for vasodilation.

Redistribution of AQP4 in α-DB deficient mice has minimal effect on the IPAD pathway

The function of AQP4 in the regulation of cerebral fluid homeostasis has been well documented [118, 158, 159, 166, 190] and It is accepted that AQP4 plays a significant role in the formation or prevention of oedema [102, 120, 188, 191-195]. Its expression differs between different brain regions [102, 196-198] and it is altered In response to disturbed fluid homeostasis [106, 107, 199] [109-112, 186, 200, 201] such as In dementia and other age related pathologies where its activity increases [109] [110-114].

As an absence of α-DB causes a redistribution of AQP4 from astrocyte endfeet to the cell body [146], the first question asked in this thesis was: *does a loss of AQP4 from astrocyte endfeet alter the structure and arrangement of the IPAD pathway?* Several pre-existing studies showed that loss of AQP4 from astrocyte endfeet does not directly alter the morphology of the capillary wall in grey matter [188, 191, 195, 203]. These studies were purely observational and lacked any rigorous quantification of the capillary wall. However, the quantitative electron microscopy performed on AQP4 deficient mice in chapter 3 of this thesis confirmed that there is no alteration to the endothelium, pericytes or basement membranes in vessels from the grey matter. The lack of consistent morphological modifications to the basement membranes suggests that the localisation of AQP4 to astrocyte endfeet by its indirect association with α-DB and the DPC is not critical for the morphology of the IPAD pathways. The dynamics of IPAD drainage in AQP4 deficient mice was not assessed in this thesis but several other studies support the concept that the function of IPAD would also be unaffected in mice deficient for AQP4 [252, 253] [166].

Loss of AQP4 from perivascular astrocyte endfeet is associated with increased severity of Aβ deposition in brain parenchyma. In particular, AQP4 is found concentrated within reactive astrocytes surrounding cortical plaques [289]. Expression of AQP4 is elevated in moderate CAA but decreased in severe CAA. Elevated AQP4 expression in moderate CAA might be due to an increase in reactive astrocytes to clear excess fluid resulting from the altered fluid homeostasis that accompanies CAA. Decreased AQP4 expression in severe CAA suggest this process is lost [115]. However, it is also entirely possible that the severe disruption and focal fragmentation to the vessel wall in severe CAA [27] is disrupting the anchoring of AQP4 by the DPC to the astrocyte endfeet causing its displacement from the cell membrane.

The effect of AQP4 deficiency from astrocyte endfeet in the white matter, which is highly susceptible to alterations in fluid homeostasis [116, 209, 210] [211] is not well understood. In post-mortem tissue from white matter of CAA and hyperintensities (WMH), there is a general reduction in expression of AQP4 compared to aged-matched control tissue [115]. In chapter 3, the loss of AQP4 from corpus callosum white matter resulted in an altered capillary wall. Capillary basement membranes appeared thinner with reduced surface area. The reason for this reduction in basement membrane area is unclear but could be due to alterations in the balance of synthesis and resorption of certain basement membrane components, such as Coll IV, laminin or perlecan. Further work is required to confirm this.

The cerebral vasculature in α-DB deficient mice show signs of early ageing and reflect early changes seen in CAA

After confirming that the redistribution of AQP4 from astrocyte endfeet to the cell body in α-DB deficient mice does not alter the capillary wall in the grey matter but does in the white matter, the second question asked in this thesis was: *Does a loss of alpha-dystrobrevin from astrocyte endfeet alter the structure and arrangement of the intramural periarterial drainage pathway*? Existing electron microscopy studies by Lien *et al.* suggest that a lack of α-DB causes abnormalities to the endothelium, basement membrane and blood-brain barrier in the grey matter of α-DB deficient mice [146]. In chapter 4 of this thesis, quantitative electron microscopy performed on the same strain of α-DB deficient mice revealed no structural abnormalities to the endothelium. The difference between the results presented in chapter 4 and those by Lien *et al* are most likely due to the fact that Lien *et al.* used aged mice whereas the mice used in this thesis were young adults. However, like older α-D deficient mice, young α-DB deficient mice showed alterations to the basement membrane of capillaries that affected not only vessels in the grey but also in the white matter. The basement membrane appeared thicker and occupied a larger area of the vessel wall. This is similar to the thickening of cerebral basement membranes in aged wild-type control mice [74] suggesting that young α-DB deficient mice are already displaying age associated changes to the vessel wall. Alterations to the vessel wall are not just limited to mice deficient for α-DB as other mice with different alterations to the DPC also display similar changes [101, 231, 237].

In aged mice, quantification of the ECM reveals remodelling of vascular basement membranes. A thickening of basement membranes was found to be associated with reductions in the levels of COL4 [74]. However in humans, ageing has been associated with increased expression of COL4 in the basement membrane of cerebral microvessels [68, 69]. When α-DB deficient mice were investigated for potential changes to the ECM, thickening of the cerebral basement membrane was associated with an increase in the level of COL4 in the vessels of the grey matter, mimicking more closely the aged associated changes observed in humans. This reaffirms the idea that α-DB deficient mice are displaying age associated changes to vessel walls.

Changes to the ECM of cerebral basement membranes are common features in CSVD [15, 67]. For instance, in the early stages of CAA, vascular basement membranes appear thickened [74] and are remodelled with increases in expression of COL4, perlecan and fibronectin [70]. Although in this thesis α-DB deficient mice were not assessed for changes in expression of perlecan or fibronectin, the changes that were observed to the vasculature in the grey matter do reflect some of the early changes to the vessel wall seen in CAA.

It appears that a lack of α-DB at astrocyte endfeet is influencing the way in which the basement membrane is remodelled, perhaps forcing an overproduction of COL4 to maintain structural integrity. It would be of interest to characterise the mechanical properties of specific layers of the vessel wall using Atomic force microscopy to help measure this [290]. It is not clear as to why vessels in the white matter of α-DB deficient mice did not display the same overproduction of COL4 as those of the grey matter, despite showing a thickening of the vessel wall. It is likely that other ECM proteins are being altered but further work is required to confirm this.

IPAD in the white matter is less efficient than that in the grey matter

A clinically important finding of this thesis was that the dynamics of IPAD in the cerebral white matter are different from that in the grey matter. This has been suspected for some time, but until now not demonstrated in an animal model. In the normal white matter of humans, the total number of capillaries is at least 49% lower compared to the grey matter [263]. In subjects with WMH, the capillary density decreases further, along with thickening of the capillary wall, leading to hypoperfusion [264]. This is important as the lower density of the capillary bed in the white matter suggests that the white matter has a lower capacity compared to grey matter for the delivery of oxygen and other nutrients. This potentially renders the white matter more vulnerable to ischaemia/hypoxia in the presence of diseases such as arteriosclerosis and CAA in the arteries supplying the white matter. In chapter 5, the density of capillaries in the white matter of wild-type control mice was found to be lower than those in the grey matter. As the capillary basement membrane is the main conduit for IPAD, the lower density of capillaries in the white matter suggests that there is also a lower capacity for IPAD in the white matter. When fluorescent Aβ40 was injected as a tracer into the white matter of wild-type control mice, it was cleared more slowly from the capillaries compared to grey matter. A similar effect is seen with increasing age in the grey matter [170]. It seems therefore that the lower capacity of IPAD in the white matter renders it to be more vulnerable to failure especially when its arterial supply is affected by age-related changes and/or CAA [208]. The corpus callosum was chosen to assess IPAD as it is the only part of the white matter that is large enough for intracerebral injections. There may be differences in the pattern of IPAD from the different parts of the white matter (for example subcortical or periventricular), as there are differences in the grey matter reflected also in different patterns of CAA [74, 281].

There are other pathologies in the white matter that may also reflect a reduced capacity for IPAD in the white matter, supporting the notion that in vivo imaging indicates that water shifts are prominent and represent early changes in WMH [211]. Vasogenic oedema that results from tumours in the brain or subarachnoid acute hydrocephalus mainly involves the white matter [291, 292]. This suggests that fluid dynamics in the white matter may differ from those in the grey matter. Obstruction of CSF drainage from the cerebral ventricles results in dilatation of the ventricular system and the accumulation of fluid in the periventricular white matter in the acute stages of hydrocephalus with the slowly progressive destruction of white matter fibers and gliosis [293]. The grey matter is only affected to a minor degree by the accumulation of fluid at its junction with the white matter even when the white matter is very severely damaged [294]. These observations support the concept that the capacity of IPAD to eliminate fluid is lower in the white matter than in the grey matter (also see [247] & Appendix A). This may explain some of the radiological effects observed after immunization against Aβ such as Amyloid Related Imaging Abnormalities (ARIA) and the radiological signs of small vessel disease [295, 296] [20].

In α-DB deficient mice, and for reasons not known, the capillary density in the white matter was not dissimilar to that of the grey matter in wild-type control mice. This may increase the capacity for the delivery of oxygen and other nutrients to the white matter and offer some protection against ischaemia/hypoxia, but further work is required to confirm this (e.g. assess for changes in CBF response to hypercapnia in adult (12 – week old) α-DB deficient mice).

IPAD is impaired in α-DB deficient mice

It is recognized that a failure of clearance of amyloid along IPAD pathways is a key contributor to CAA [160, 282, 283]. In an ageing mouse model, failure of IPAD has been demonstrated in brain regions that show alterations to the ECM of the basement membrane including basement membrane thickening [74]. As α-DB deficient mice showed a thickening of cerebral basement membranes, the third question asked in the thesis was: *Does a loss of alpha-dystrobrevin from astrocyte endfeet alter the dynamics of intramural periarterial drainage?* In chapter 5, assessment of the pattern of IPAD in α-DB deficient mice revealed a reduced efficiency of IPAD in the grey matter. Whereas in wild-type control mice the fluorescent Aβ40 was distributed mainly in arteriole walls, in α-DB deficient mice fluorescent Aβ40 was mainly observed in capillary walls and in the parenchyma. Both wild-type control mice and α-DB deficient mice showed similar densities of capillaries with fluorescent Aβ40 in the vessel walls so IPAD appeared to be functioning to some degree at capillary level. However, in α-DB deficient mice less fluorescent Aβ40 reached the arterioles and so accumulated in the parenchyma. In chapter 4, it was demonstrated that all vessels in the grey matter of α-DB deficient mice showed elevated levels of COL4 and this was reflected in a thickened capillary basement membrane. It is most likely that the basement membrane around arterioles would also be affected in the same way, although further examination by electron microscopy would be needed to confirm this. Nether the less, the importance of the structure of the vascular basement membrane to IPAD has recently been highlighted by new mathematical modelling of the driving factors for IPAD. Originally, IPAD was assumed to be driven by the pulsation force of cerebral vessels [177] but mathematical simulations by Diem *et al.* confirmed that this would not provide sufficient motive force [178]. The most current mathematical model suggests that it is vasomotion generated by cycles of contraction and relaxation of smooth muscle cells (SMC) that induces deformations of the basement membrane, effectively opening and closing a valve like system. In this model IPAD flows in the direction of the vasomotion wave [179] and would be sensitive to alterations to the biochemical composition of the basement membrane. Alterations, such as an increase in COL4 may stiffen the vessel wall reducing deformations induced by the SMCs. This may help to explain why in α-DB deficient mice the efficiency of IPAD appeared to be significantly reduced in the grey matter.

WMH on magnetic resonance imaging (MRI) occur in the cerebral hemispheres mainly in elderly patients and are particularly associated with dementia [212]. Hyperintensity on MRI suggests that there is fluid in the white matter and is typically referred to as leukoaraiosis on computer tomography (CT) [211, 213]. Various mechanisms for the aetiology of WMH have been proposed, they include ischaemia/hypoxia as a result of CSVD [212] loss of axons in the white matter associated with deposition of tau protein in parent neurons in the overlying grey matter [213] and a failure of elimination of interstitial fluid (ISF) from the affected white matter along peri-capillary and peri-arterial drainage routes [208].

In the white matter, basement membrane thickening in α-DB deficient mice did not correlate with elevated levels of COL4 or in the reduced efficiency of IPAD. Therefore, it appears that a loss of α-DB from astrocyte endfeet does not alter the dynamics of IPAD in the white matter. This suggests that not all changes to the ECM of cerebral basement membranes are reflected in a modification of IPAD, but some changes such as increased expression of COL4, as the case in grey matter of α-DB deficient mice are associated with a failure of IPAD, consistent with experimental findings in rodent models of ageing or transgenic models of Alzheimer's disease [28, 74, 228, 229].

The removal of α-DB from the DPC of astrocyte endfeet is associated with normal perfusion but a lower capacity for adaptation to hypercapnia

CBF reduces with age as the process of neurovascular coupling become less efficient at responding to hypoxia, hypercapnia and alterations to blood pressure [276]. A key feature of CSVD and VaD is reduced neurovascular coupling and CBF. Abnormalities in the cerebral vasculature, such as thickening of the basement membrane have been linked to cerebral hypoperfusion [272]. As α-DB deficient mice showed a thickening of cerebral basement membranes, the fourth question asked in this thesis was: *Does a loss of alpha-dystrobrevin from astrocyte endfeet alter cerebral blood flow?* In VaD, the hippocampus, periventricular white matter and basal ganglia are particularly susceptible to impaired CBF [9]. In chapter 6, assessment of resting CBF in α-DB deficient mice using arterial spin labelling revealed no significant difference in CBF compared to wild-type control mice in the hippocampal or cortical grey matter. We were unable to assess CBF in the white matter due to limitations with the technique. As noted in chapter 6, electron microscopy (chapter 4) revealed that grey matter capillaries in α-DB deficient mice showed significantly larger lumen areas, possibly as a compensatory mechanism to counteract any negative effect of vascular wall remodelling on CBF but further imaging studies would be needed to confirm this. A limitation with this section of work is that we were unable to assess the efficiency of neurovascular coupling in the same age of mice used for assessing resting CBF. However, we did perform a small pilot study in older 10-month old α-DB deficient mice that did show abnormal adaptation to hypercapnia. Future imaging experiments incorporating arterial spin labelling of younger α-DB deficient mice when exposed to different hypoxic conditions would help elucidate the effect of the DPC on the vascular response to hypoxia, hypercapnia and alterations to blood pressure [276].

Mice deficient for α-DB show potential as a model for the failure of IPAD in CSVD and VaD

There are three key findings of this thesis that suggest mice deficient for α-DB are a possible model to investigate failure of IPAD in CSVD and VaD. Firstly, the cerebral vasculature in young adult α-DB deficient mice show signs of early ageing, the predominant risk factor for VaD [10]. Secondly, the cerebral vasculature in young adult α-DB deficient reflect early changes seen in CAA, a significant form of CSVD. Thirdly, young adult α-DB deficient mice display impaired IPAD in the grey matter. Vessels of the grey matter are most affected by CAA [16, 26]. However, one key question that is highlighted by these findings is: *whether the changes observed to the cerebral vasculature and IPAD pathways in α-DB deficient mice predispose these mice to developing CAA and VaD.*

Limitations and Future work

The disadvantage of the current in vivo technique used in this thesis to assess IPAD is that only one time point (5 minutes post injection) was used. The fact that significant differences were observed in the pattern of IPAD in α-DB deficient mice just 5 minutes post injection of tracer into the parenchyma is very promising. However, in transgenic mouse models of CAA, the earliest age in which mice develop CAA is in the Tg-SwDI model in which vascular deposits of amyloid occur at 3 months of age [270]. Some models don't show any sign of CAA until 12 months (Tg2576) [297] or even 24 months (APPDutch) [298]. Therefore, to test if the reduction in the efficiency of IPAD in α-DB deficient mice is a predisposing factor to CAA, the clearance of fluids by IPAD needs to be assessed over a longer period of time. This can be achieved in two ways:

1. By administrating a tracer substance, such as fluorescent Aβ40 into the brain over a prolonged period of time and assessing the accumulation of fluorescent Aβ40 in the vessel walls at different time points. This could be

achieved by performing multiple stereotaxic injections. However, a more robust approach would be to use a miniosmotic pump under the scalp attached to a catheter that is inserted into the brain parenchyma. Miniosmotic pumps enable delivery of a substance into the brain at a controlled and known rate lasting up to 6 weeks, negating the need for multiple stereotaxic injections [299]. Pumps can also be replaced to extend experimental duration times.

2. By introducing a genetic mutation, such as that of Tg-SwDI mice [270], to cause overexpression of Aβ and then assessing the accumulation of the Aβ in the vessel walls, again at different time points.

It is also necessary to ascertain if the alterations to the vasculature and IPAD pathway in α-DB deficient mice lead to the cognitive abnormalities that are attributable to VaD. These abnormalities are variable and depend on the type of vascular insult and the pursuing pathology. Frequent abnormalities include deficits in attention, information processing and executive functions (e.g. working memory), mainly as a result of subcortical vascular pathology (reviewed in [285]). Assessment of behaviour on mice deficient for dystrophin (mdx mice) reveals decreased hippocampal spatial learning and memory and elevated anxiety related behaviour [232]. Currently, α-DB deficient mice have not been assessed for cognitive abnormalities. Therefore, animal behavioural studies that incorporate testing for key deficits associated with VaD should be included in future work and are essential to determine the suitability of using α-DB deficient mice to model the cognitive abnormalities seen in VaD.

It is important to note while mice deficient for α-DB deficient do show abnormalities to the structure of the vessel wall and IPAD pathways, it cannot be guaranteed that these abnormalities are due to loss of α-DB function rather than a functional consequence of what remains of the DPC. Further work incorporating functional inhibition of α-DB may help elucidate this.

Overall summary, conclusions and implications

In this thesis, several areas of novelty have been presented:

1. In the absence of AQP4 at astrocyte endfeet there is a decrease in the surface area of basement membranes and an increase in the surface area of intramural cells in the white matter.
2. In normal white matter, there is a reduced capacity for IPAD compared to the grey matter.
3. In the absence of α-DB at astrocyte endfeet capillary basement membranes are thickened accompanied by an increase in collagen IV, mimicking the ageing morphological changes in the cerebrovasculature. These changes are accompanied by a decreased efficiency of IPAD along arterioles in the grey matter of α-DB deficient mice with an increase in the soluble Aβ that remains in the extracellular spaces of the grey matter. Mice deficient for α-DB display a trend of an inability of its cerebral blood flow to adapt to hypercapnia.

Taken together with clinical and neuropathological findings from the literature, it appears that α-DB deficient mice represent a suitable model for the study of CSVD and VaD away from the confounding factors of overexpression of amyloid as in the transgenic models of AD or introducing metabolic risk factors such as hypertension or diabetes mellitus. As IPAD appears to be altered in α-DB deficient mice without any other metabolic involvement, these mice are an ideal candidate to test possible therapeutic interventions targeted at facilitating and improving IPAD.

Further work is required to ascertain if the modifications to the IPAD pathway in these mice are linked to the development of CAA and cognitive abnormalities seen in human VaD. However, since this work highlighted that IPAD occurs preferentially along the capillary walls in the normal white matter with little involvement from arteries, it is important to consider the failure of IPAD as a key mechanistic feature of WMH. It remains to be seen if there are changes to α-DB and the DPC in the spectrum of CSVD in human brains, as this work points to it as a suitable model for further hypothesis-based studies of CSVD. Therefore, future work should incorporate a detailed investigation of α-DB and other components of the DPC in human post-mortem brains with CSVD and VaD.

Appendix A List of Publications

Co-authored publications that include data generated as part of this thesis

MacGregor Sharp M, Saito S, Keable A, Gatherer M, Aldea R, Agarwal N, et al. Demonstrating a reduced capacity for removal of fluid from cerebral white matter and hypoxia in areas of white matter hyperintensity associated with age and dementia. Acta Neuropathol Commun. 2020;8(1):131. This publication is appended as appendix A and includes data generated from chapter 5.

Co-authored publications in which some of the data has been presented in the main introduction

Hawkes CA, Gatherer M, **MacGregor Sharp M**, Dorr A, Yuen HM, Kalaria R, et al. Regional differences in the morphological and functional effects of aging on cerebral basement membranes and perivascular drainage of amyloid-beta from the mouse brain. Aging cell. 2013;12(2):224-36. (**see figure 1.7**)

Morris AW, **MacGregor Sharp M**, Albargothy NJ, Fernandes R, Hawkes CA, Verma A, et al. Vascular basement membranes as pathways for the passage of fluid into and out of the brain. Acta Neuropathol. 2016;131(5):725-36. (**see Figures 1.13 & 1.16**)

Dobson H, **MacGregor Sharp M**, Cumpsty R, Criswell TP, Wellman T, Finucane C, et al. The perivascular pathways for influx of cerebrospinal fluid are most efficient in the midbrain. Clin Sci (Lond). 2017;131(22):2745-52. (**see Figures 1.14**)

Diem AK, **MacGregor Sharp M**, Gatherer M, Bressloff NW, Carare RO, Richardson G. Arterial Pulsations cannot Drive Intramural Periarterial Drainage: Significance for Abeta Drainage. Front Neurosci. 2017;11:475. (**see Figures 1.17**)

MacGregor Sharp M, Bulters D, Brandner S, Holton J, Verma A, Werring DJ, et al. The fine anatomy of the perivascular compartment in the human brain: relevance to dilated perivascular spaces in cerebral amyloid angiopathy. Neuropathol Appl Neurobiol. 2018. (**see Figure 1.18**)

Criswell TP, **MacGregor Sharp M**, Dobson H, Finucane C, Weller RO, Verma A, et al. The structure of the perivascular compartment in the old canine brain: a case study. Clin Sci (Lond). 2017;131(22):2737-44. (**see Figure 1.19**)

Appendix B PUBLICATION - Demonstrating a reduced capacity for removal of fluid from cerebral white matter and hypoxia in areas of white matter hyperintensity associated with age and dementia

MacGregor Sharp *et al. Acta Neuropathologica Communications* (2020) 8:131
https://doi.org/10.1186/s40478-020-01009-1

Acta Neuropathologica
Communications

RESEARCH Open Access

Demonstrating a reduced capacity for removal of fluid from cerebral white matter and hypoxia in areas of white matter hyperintensity associated with age and dementia

Matthew MacGregor Sharp[1†], Satoshi Saito[1†], Abby Keable[1†], Maureen Gatherer[1], Roxana Aldea[1,2], Nivedita Agarwal[3], Julie E. Simpson[4], Stephen B. Wharton[4], Roy O. Weller[1] and Roxana O. Carare[1*]

Abstract

White matter hyperintensities (WMH) occur in association with dementia but the aetiology is unclear. Here we test the hypothesis that there is a combination of impaired elimination of interstitial fluid from the white matter together with a degree of hypoxia in WMH. One of the mechanisms for the elimination of amyloid-β (Aβ) from the brain is along the basement membranes in the walls of capillaries and arteries (Intramural Peri-Arterial Drainage – IPAD). We compared the dynamics of IPAD in the grey matter of the hippocampus and in the white matter of the corpus callosum in 10 week old C57/B16 mice by injecting soluble Aβ as a tracer. The dynamics of IPAD in the white matter were significantly slower compared with the grey matter and this was associated with a lower density of capillaries in the white matter. Exposing cultures of smooth muscle cells to hypercapnia as a model of cerebral hypoperfusion resulted in a reduction in fibronectin and an increase in laminin in the extracellular matrix. Similar changes were detected in the white matter in human WMH suggesting that hypercapnia/hypoxia may play a role in WMH. Employing therapies to enhance both IPAD and blood flow in the white matter may reduce WMH in patients with dementia.

Keywords: White matter hyperintensities, Laminin, Fibronectin, Intramural periarterial drainage

Introduction

White Matter Hyperintensities (WMH) on magnetic resonance imaging (MRI) occur in the cerebral hemispheres mainly in elderly patients and are particularly associated with dementia [1]. Hyperintensity on MRI suggests that there is fluid in the white matter and is typically referred to as leukoaraiosis on CT [2, 3]. Various mechanisms for the aetiology of WMH have been proposed, they include ischaemia/hypoxia as a result of arteriosclerotic small vessel disease [1] loss of axons in the white matter associated with deposition of tau protein in parent neurons in the overlying grey matter [2] and a failure of elimination of interstitial fluid (ISF) from the affected white matter along peri-capillary and peri-arterial drainage routes [4].

The brain has no conventional lymphatic vessels. Early physiological studies using radio-iodinated tracers have shown that fluid, soluble metabolites and tracers drain along the walls of cerebral arteries to cervical lymph nodes and only an estimated 10–15% leaks into the CSF

---

* Correspondence: rcn@soton.ac.uk

†Matthew MacGregor Sharp, Satoshi Saito and Abby Keable contributed equally to this work.

[1]Faculty of Medicine, University of Southampton, Tremona Road, Southampton SO16 6YD, UK
Full list of author information is available at the end of the article

© The Author(s). 2020 **Open Access** This article is licensed under a Creative Commons Attribution 4.0 International License, which permits use, sharing, adaptation, distribution and reproduction in any medium or format, as long as you give appropriate credit to the original author(s) and the source, provide a link to the Creative Commons licence, and indicate if changes were made. The images or other third party material in this article are included in the article's Creative Commons licence, unless indicated otherwise in a credit line to the material. If material is not included in the article's Creative Commons licence and your intended use is not permitted by statutory regulation or exceeds the permitted use, you will need to obtain permission directly from the copyright holder. To view a copy of this licence, visit http://creativecommons.org/licenses/by/4.0/. The Creative Commons Public Domain Dedication waiver (http://creativecommons.org/publicdomain/zero/1.0/) applies to the data made available in this article, unless otherwise stated in a credit line to the data.

[5, 6]. Detailed anatomical studies of this lymphatic drainage pathway have shown that soluble tracers, including soluble amyloid-β (Aβ), drain from the extracellular spaces of the brain along basement membranes (BM) in the walls of cerebral capillaries and then continue out of the brain along BMs that surround smooth muscle cells in the tunica media of arteries [7]. This drainage pathway is termed the Intramural Peri-Arterial Drainage (IPAD) pathway [8]. Aβ in the extracellular spaces of the brain is taken up by perivascular macrophages, micoglia and astrocytes, crosses into the blood via low density lipoprotein related protein − 1 (LRP1) and also enters the IPAD pathways [9]. IPAD becomes less efficient with advancing age, leading to the accumulation of insoluble Aβ in the BMs of the IPAD pathways as cerebral amyloid angiopathy (CAA) [10, 11]. The elimination of soluble Aβ is severely impaired in Alzheimer's disease (AD) with a rise in levels of soluble Aβ in the brain parenchyma suggesting that a loss of homeostasis in the extracellular spaces of the brain accompanies dementia in AD [12].

It appears, therefore, that two of the major functions of arteries, arterioles and capillaries in the brain are (a) maintaining blood flow with the supply of nutrients and immune cells to brain tissues and (b) drainage of interstitial fluid and soluble metabolites from the brain to cervical lymph nodes by the IPAD pathways to maintain homeostasis in the brain [13, 14]. Changes that occur in cerebral arteries and arterioles associated with age, such as arteriosclerosis and CAA, affect both blood flow and IPAD and may induce both ischaemia/hypoxia and loss of homeostasis due to impaired elimination of ISF and soluble metabolites from the brain along IPAD pathways.

The process of IPAD ceases upon cardiac arrest [7], therefore it was initially assumed that IPAD was driven by the pulsation force of cerebral vessels [15]. However, mathematical simulations by Diem et al. confirmed that this would not provide sufficient motive force [16]. More recently, new mathematical models and in-vivo 2 photon microscopy on awake mice suggest that it is vasomotion generated by cycles of contraction and relaxation of smooth muscle cells that drives IPAD. Vasomotion induces deformations of the BM, effectively opening and closing a valve like system allowing for flow of IPAD in the direction of the vasomotion wave [17, 18]. Motive force of vascular smooth muscle cells decreases with age and in CAA, resulting in hypoperfusion, ischaemia and a failure of IPAD [17, 19, 20].

Cerebrovascular BM consist of a fine extracellular matrix (ECM) of glycoproteins and proteoglycans that ensheath the abluminal side of endothelia separating the endothelia from pericytes or smooth muscle cells and pericytes or smooth muscle cells from astrocytes, encircling the different cell types [21]. Each cell type contributes to ECM production. The ECM consists of highly crosslinked complexes of collagen IV, laminin, nidogen/entactin, fibronectin and heparan sulphate proteoglycan. Remodelling of the ECM is a common feature in ageing and neuropathological conditions [22, 23]. Experimental work in rodents demonstrates that ischaemia in the white matter is characterised by an upregulation of the extracellular matrix proteins laminin and fibronectin [24–26] but it is not known if similar changes occur in human white matter. As BMs are key to IPAD, remodelling of the ECM associated with ischaemia will likely have an impact on the IPAD pathways.

In this study we aim to firstly ascertain if ISF and solutes are eliminated from the white matter by IPAD. We use young adult wild-type mice to compare the drainage of amyloid-β (1–40) from hippocampal grey matter and the white matter tracts of the corpus callosum. We then use human post-mortem brains with WMH to compare the levels of extracellular matrix proteins fibronectin and laminin with those of age-matched controls. Finally, we apply hypercapnia to model hypoxic hypoperfusion and analyse the production of fibronectin and laminin by cultured human brain vascular smooth muscle cells (HBVSMC). Involvement of failure of IPAD in the aetiology of WMH has previously been deduced largely from circumstantial evidence and involvement by association. Direct evidence is difficult to obtain, especially from post-mortem human brain tissue. In this study we seek more direct evidence for the involvement of failure of IPAD in the aetiology of WMH. We show evidence of hypoxia in the white matter in WMH and we also demonstrate, experimentally, a reduced capacity of IPAD in the white matter compared with grey matter.

We test two hypotheses: *Hypothesis 1:* The dynamics of IPAD in the cerebral white matter differ from IPAD in the grey matter of the hippocampus. The hypothesis is tested by a) comparing the density of capillaries in grey and white matter and b) injecting soluble Aβ as a tracer independently into the grey matter of the hippocampus and into the white matter of the corpus callosum of mice and comparing the dynamics of drainage of tracer along IPAD from each of these regions of the brain. *Hypothesis 2:* Changes induced by hypercapnia as a model of hypoxia in the extracellular matrix of vascular smooth muscle cells are similarly expressed in human white matter exhibiting WMH. In order to test Hypothesis 2 we selected two proteins in the BMs of smooth muscle cells, a) laminin and b) fibronectin and established the effects of hypercapnia as a model of hypoxiaon cultures of vascular smooth muscle cells. We then compared the changes observed in culture with the changes in extracellular matrix in WMH.

Materials and methods

Stereotaxic injections of amyloid-β (1–40) HiLyte Fluor 555 into mouse hippocampus (grey matter) and corpus callosum (white matter) and quantification of IPAD

All procedures were carried out in accordance with animal care guidelines stipulated by the United Kingdom Animals (Scientific Procedures) Act 1986, Home Office licence P12102B2A. 10-week-old C57/BL6 wild-type mice ($n = 10$) were anaesthetised with Isoflurane mixed with concentrated O_2 (1.7 L min-1) (induced with 3%, maintained using 2%). Isoflurane was used rather than injectable anaesthetics based on our previous study which showed that isoflurane is better at maintaining a more physiologically normal heart rate and oxygen saturation level [8]. The level of anaesthesia was monitored by using pedal withdrawal reflex response. A rectal probe and homoeothermic blanket and temperature control system (BASi) were used to regulate internal body temperature at 37 °C. Lacri-lube ointment was applied to the eyes to preserve cornea during anaesthesia.

Anaesthetised mice were placed in a KOPH instruments stereotaxic frame (Model 900) and the head secured with jaw bars. A midline incision was performed and a Tech2000 Micromotor drill (RAM Products, INC) with 0.7 mm burr was used to create a burr hole in the skull above the injection site (hippocampal grey matter - Anterior-Posterior - 2 mm; Medial-Lateral 1.5 mm; Dorsal-Ventral - 1.7 mm, $n = 5$ or corpus callosum (white matter) - Anterior-Posterior – 2 mm; Medial-Lateral 0.5 mm; Dorsal-Ventral - 1.3 mm, $n = 5$) (Fig. 1). 0.5 μl of 100 μM amyloid-β (1–40) HiLyte Fluor 555 (Cambridge Bioscience) was injected into either the hippocampus or corpus callosum using a Hamilton Neuros Syringe with a 33 gauge needle (Essex Scientific Laboratory Supplies Ltd.) and Microinjection syringe pump (UMP3T-1; World Precision Instruments) at a rate of 0.25 μl min-1. The syringe was left in situ for 2 min for bolus diffusion and to prevent reflux. The tracers were left to drain for a further 5 min and then the mouse was terminally anaesthetised with pentobarbitone (200 mg/kg) and intracardially perfused with 0.01 M phosphate buffered saline (PBS) followed by 4% Paraformaldehyde (PFA) in 0.01 M PBS, pH 7.4 at a rate of 5 ml/min. Brains were dissected and post fixed for 6 h in fresh 4% PFA in 0.01 M PBS, pH 7.4 at 4 °C and then cryoprotected in 30% sucrose in distilled H_2O at 4 °C for a further 48 h. Brains were embedded in OCT compound and then sectioned into 20 μm coronal slices using a Leica CM1860 UV cryostat. Sections were collected on to SuperFrost Plus™ adhesion slides (Thermo Scientific™, 10,149,870) and viewed using a Zeiss Axioskop 2 fitted with a rhodamine filter to identify the section containing the site of injection. In our previous studies we showed that, in mice, the drainage of Aβ40 occurs predominantly in a posterior direction and can be visualised in the walls of blood vessels as close as 200 μm to the injection site [10]. We therefore chose coronal sections 200 μm posterior to the injection site for immunohistochemistry.

Sections were washed 2 × 3 mins in 0.01 M PBS, pH 7.4 and then blocked in 15% goat serum (Sigma 9023) for 1 h at room temperature. Sections were then incubated in rabbit anti-collagen IV 1/400 in 0.01 M PBSt (AbCam, ab6586) and anti-smooth muscle actin (SMA) FITC conjugated 1/200 in 0.01 M PBSt (Sigma, F3777) overnight in a moist chamber at 4 C. Sections were then

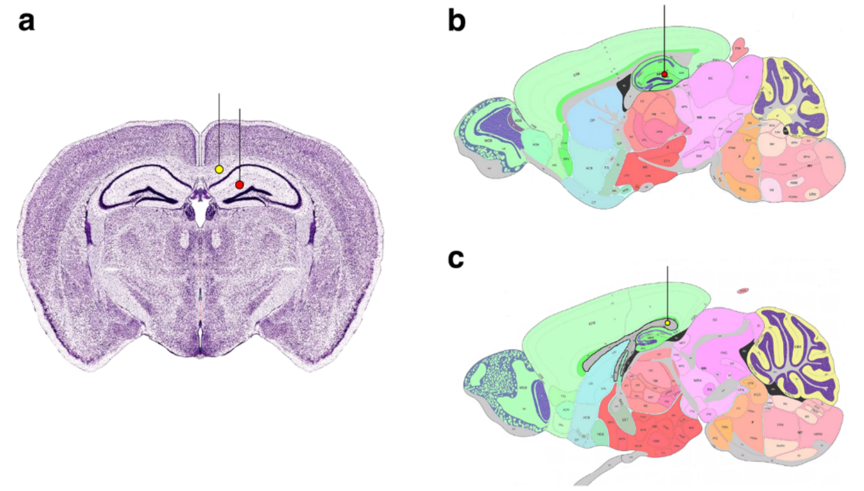

Fig. 1 Stereotaxic Injection sites. Injections were performed Anterior-Posterior – 2 mm from the Bregma represented by the red dot (hippocampus) and yellow dot (corpus callosum) in **(a)**. Sagittal slices show the injection site for the hippocampus (Anterior-Posterior - 2 mm; Medial-Lateral 1.5 mm; Dorsal-Ventral 1.7 mm), red dot in **(b)** and corpus callosum (Anterior-Posterior -2 mm; Medial-Lateral 0.5 mm; Dorsal-Ventral - 1.3 mm), yellow dot in **(c)**. Images adapted from www.mouse.brain-map.org

Appendix B

washed 3 × 10 mins in 0.01 M PBS and incubated in conjugated secondary antibody goat antirabbit Alexa Fluor 633 0.01 M PBSt (ThermoFisher Scientific, A-21070) for 1 h at room temperature. Sections were further incubated in 1% Sudan Black for 5 min to remove auto fluorescence before being mounted in Mowiol Citifluor and imaged using confocal microscopy.

For each section, tile scans of the left hippocampus or corpus callosum were captured using a Leica SP8 confocal microscope fitted with × 20 objective set at an optical zoom of 1. Laser power and detection windows were kept consistent for all scans. Sequential imaging was used to prevent cross excitation of fluorophores. Quantification of IPAD of Aβ40 HiLyte Fluor 555 injected into the left hippocampus or corpus callosum was performed using a max projection of each tile scan uploaded into Adobe Photoshop CS6. We chose to use maximum projections of each tile scan as they provide a more precise and accurate method to assess IPAD, particularly when assessing vessel density. IPAD was assessed by using Adobe Photoshop CS6 to manually measure vessel density of capillaries, arterioles and venules and counting the number of vessels containing Aβ40 HiLyte Fluor 555 in their vessel walls. Vessel density was calculated by dividing the total number of capillaries, arterioles or venules by the overall surface area (in μm^2) and multiplying this value by 500,000 to be expressed as number of vessels per $0.5 mm^2$. This was also performed for the number of capillaries, arterioles or venules with Aβ40 in their vessel walls. Vessels were identified based on lumen diameter and immunoreactivity to SMA (< 10 μm = capillaries, ≥ 10 μm & SMA positive = arterioles, ≥ 10 μm and SMA negative = venules) [7, 10]. The overall surface area was determined by choosing regions of interest that were based on key anatomical features that could be observed in each section analysed. Regions of interest were outlined using Adobe Photoshop CS6. For the hippocampus, a transverse area from the edge of the suprapyramidal [16] was outlined. For the corpus callosum, the white matter tracts extending from the midline to a point directly above the suprapyramidal blade of the granule cell layer of the hippocampus were outlined. Statistical analysis was performed using SPSS Statistics version 26.0 (IBM) and an independent t-test with significance set at $P < 0.05$.

Assessment of fibronectin and laminin expression in WMH

Human autopsy CNS tissue was obtained from the MRC Cognitive Function and Ageing Study (CFAS) that had a post-mortem MRI confirming white matter hyperintensities [27, 28]. Control cases were from CFAS and Parkinson's UK brain bank. The Parkinson's UK Brain Bank is funded by Parkinson's UK, a charity registered in England and Wales (258197) and in Scotland (SC037554) (Table 1).

Two tissue sections of 10 μm thickness of the white matter from each case (WMH × 10, Control × 11) were deparaffinised and then rehydrated through a graded series of alcohols. Endogenous peroxidase activity was quenched with 3% hydrogen peroxide for 15 min at room temperature. Heat mediated antigen retrieval was then performed by microwaving in 0.01 M citrate buffer (pH 6). After blocking in 15% goat serum (Sigma, 9023) for 1 h at room temperature, sections were incubated in rabbit polyclonal anti-laminin antibody 1/50 (Merck, L9393) or rabbit polyclonal anti-fibronectin antibody 1/400 (Merck,) in 0.01 M PBS with 0.1% triton in a moist chamber at 4 C for 48 h. Sections were then washed 3 × 10 mins in 0.01 M PBS and incubated in goat anti-rabbit IgG 1:200 (Vector Laboratories) in 0.01 M PBS with 0.1% triton for 1 h at room temperature. Sections were further incubated with the alkaline phosphatase substrate (Vector Laboratories, PK-6101) for 1 h at room temperature. Anti-laminin or anti-fibronectin immunoreactivity was visualised by incubating tissue sections in glucose oxidase diaminobenzidine nickel (DAB) solution for 5 mins (Vector Laboratories, SK-4100). Sections were

Table 1 Demographics of cases used in this study. pm delay = postmortem delay in hours

Source	Age	Sex	pm delay /hrs	Category
CFAS	87	F		White matter hyperintensity
CFAS	84	F		White matter hyperintensity
CFAS	78	F		White matter hyperintensity
CFAS	91	F		White matter hyperintensity
CFAS	95	F		White matter hyperintensity
CFAS	91	F		White matter hyperintensity
CFAS	89	M		White matter hyperintensity
CFAS	83	M		White matter hyperintensity
CFAS	73	M		White matter hyperintensity
CFAS	88	F		White matter hyperintensity
CFAS	76	M		Control
CFAS	88	M		Control
CFAS	89	F		Control
CFAS	91	M		Control
Parkinson's UK	77	M	17	Control
Parkinson's UK	90	M	12	Control
Parkinson's UK	93	F	36	Control
Parkinson's UK	92	F	24	Control
Parkinson's UK	96	F	24	Control
Parkinson's UK	85	M	29	Control
Parkinson's UK	79	M	25	Control

then washed, dehydrated, cleared in xylene and coverslipped with DPX (Thermo Scientific).

Tissue sections were examined using an Olympus dot slide microscope. Randomly selected regions (1.7 mm × 2.2 mm) of white matter (1 per slide) were captured from each section and imported into Image J software (National Institutes of Health) [29] to calculate total area stained for either laminin or fibronectin. To account for possible variations in vessel density, the total area of either laminin or fibronectin staining was normalised against the number of vessels in each region. Statistical analysis was performed using SPSS Statistics version 26.0 (IBM) and Student's t test with significance set at $P < 0.05$.

Analysis of fibronectin and laminin production by human brain vascular smooth muscle cells exposed to increased CO_2 levels

Human brain vascular smooth muscle cells (HBVSMC) were obtained from Sciencell (sc-1100). Cells were grown in the smooth muscle cell medium purchased from Sciencell (sc-1101) supplemented with smooth muscle cell growth supplement (sc-1152), 100 U/mL penicillin, 100 μg/mL streptomycin (sc-0503) and 2% foetal bovine serum. Cells were maintained in a humidified atmosphere (5% CO_2/95% air) at 37 C and the medium was refreshed every 2–3 days according to the manufacturer's instructions. To confirm that the cells are indeed smooth muscle cells, we analysed the presence of smooth muscle actin through immunofluorescence with anti-alpha smooth muscle actin 1/200 in 0.01 M PBSt (Sigma, F3777).

We first assessed for cell proliferation and metabolic activity of HBVSMC in either a normoxic environment or conditions of increased CO_2 using a CellTiter 96 aqueous one solution cell proliferation assay kit (Promega, G3582). Cells were seeded into two 96 well plates with poly-L-lysine coated wells at a density of 10^4 cells per well. Plates were incubated for 72 h in either normoxic conditions (5% CO_2, 95% air) or conditions of increased CO_2 (8% CO_2, 92% air) and maintained at 37 °C. 20 μL of MTS reagent was added to the cells and the plates were wrapped in foil and incubated for a further 2 h for the reagent to develop. Blank wells containing no cells were also included and their absorbance value was subtracted from the test wells. Absorbance was measured at 490 nm with a Fluorostar optima plate reader and the results were exported to Microsoft Excel.

We next assessed for expression of laminin or fibronectin from HBVSMC in normoxic and conditions of increased CO_2. HBVSMC were plated onto poly-L-lysine coated coverslips in a 24-well plate at a density of 0.5×10^5 cells per coverslip with 1 mL of smooth muscle medium. Cells were then exposed to either normoxic (5% CO2/95% air) or conditions of increased CO_2 (8% CO_2, 92% air) for 72 h and fixed with 4% paraformaldehyde for 10 min before immunofluorescent staining with either with anti-laminin (Sigma, L9393) or anti-fibronectin (Sigma, F3648) antibodies, diluted to 1:200 and 1:400 in 0.01 M PBS respectively. Cells were examined by using a Leica SP8 confocal microscope and three non-overlapping z-stacks were captured per stained coverslip (each an area of 0.15 mm^2). The fluorescence intensity of laminin and fibronectin staining was calculated using the RGB measure tool in ImageJ. The results from individual images were averaged to give a mean value per coverslip and are based upon data gathered over three independent experimental runs ($n = 3$). Statistical analysis was performed using SPSS Statistics version 26.0 (IBM) and a Mann-Whitney U test with significant set at $P \leq 0.05$.

Results

ISF and solutes are drained from the white matter by IPAD

To determine the pattern of intramural Peri-Arterial Drainage (IPAD) in the white matter, the pattern of drainage of fluorescent Aβ40 injected into the corpus callosum was compared with the drainage of Aβ40 injected into the hippocampus of young adult (10-week-old) C57/Bl6 mice. Immunohistochemistry and confocal microscopy was used to assess differences / similarities in vascular density and IPAD between the hippocampus and corpus callosum.

Qualitative assessment revealed the pattern of IPAD normally observed in the hippocampus [30], characterised by colocalisation of fluorescent Aβ40 with collagen IV within the walls of arterioles and capillaries and few venules and in the parenchyma, mainly in the granule cell layer (Fig. 2). In the corpus callosum, fluorescent Aβ40 was observed mainly along the white matter tracts and colocalising with collagen IV within the walls of capillaries, some arterioles and few venules (Fig. 3).

Quantitative assessment of IPAD revealed significant differences in the density of capillaries and arterioles with Aβ40 in their vessel walls between the hippocampus and corpus callosum. The density of arterioles with Aβ40 in their vessel walls was significantly higher in the hippocampus versus corpus callosum (2.3 vs 0.6 per 0.5 mm^2, $p < 0.05$). Conversely, the density of capillaries with Aβ40 in their vessel walls was significantly higher in the corpus callosum versus hippocampus (1.1 vs. 6.3 per 0.5 mm^2, $p < 0.05$) (Fig. 4).

Previous work by Cavaglia et.al [31] showed regional variation in the density of cerebral capillaries. We observed similar variation with a significant reduction in

Appendix B

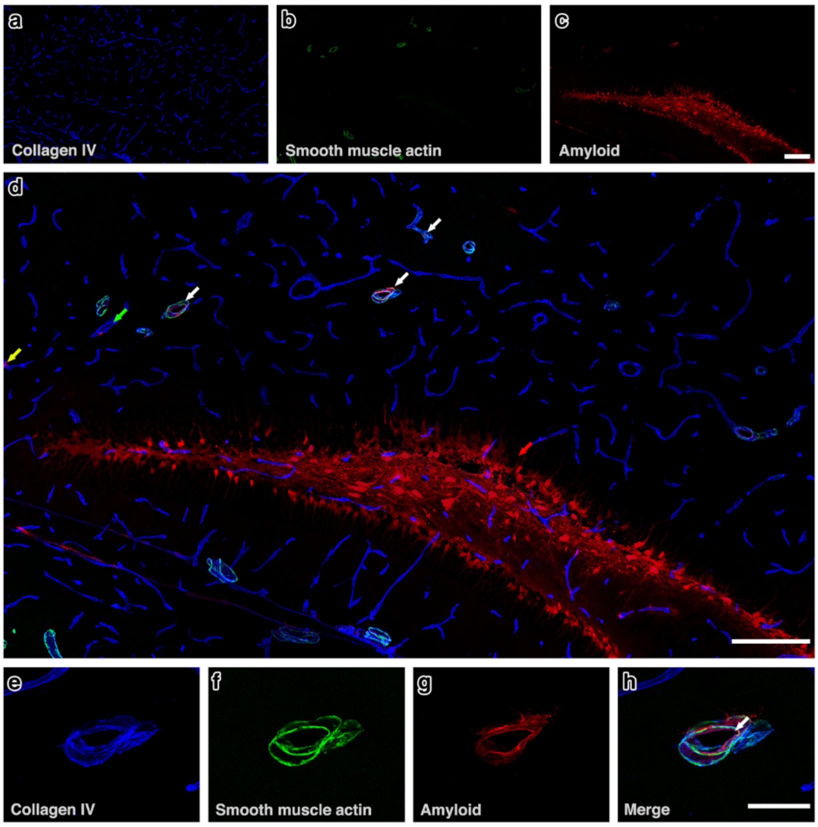

Fig. 2 IPAD in hippocampus. **(a -c)** The distribution of amyloid-β in relation to collagen IV and smooth muscle actin at 7 min after intrahippocampal injection. **c & d)** Amyloid-β **(red)** was observed diffusely distributed in the parenchyma and co-localised **(pink colour)** with collagen IV in the walls of arterioles **(white arrows)**, capillaries **(yellow arrow)** and few venules **(green arrow)**. Representative high power image of an arteriole **(e-h)** shows amyloid-β **(red) (g-h)** in the wall of the blood vessel, indicated by the white arrow in **(h)**. Scale bars **a-d** = 200 μm, **e – h** = 10 μm

the density of capillaries in corpus callosum compared to the hippocampus (84 vs 54.5 per 0.5mm^2, $p < 0.05$) but we observed no significant differences in density of arterioles (4.4 vs. 2.3 per 0.5 mm^2, $p = 0.134$) or venules (1.9 vs.1.1 per 0.5 mm^2, $p = 0.063$) (Fig. 4).

The expression of fibronectin and laminin is altered in human white matter hyperintensities

Experimental work in rodents demonstrate that ischemia in the white matter is characterised by an upregulation of the extracellular matrix proteins laminin and fibronectin [24–26]. Previous work by our group also show that ageing and hypoperfusion lead to a changes in the distribution of laminin and fibronectin in the white matter [10, 32]. To ascertain if similar changes in the distribution occur in the white matter in WMH, we next used immunohistochemistry to assess changes in laminin and fibronectin expression in human brain slices of WMH and age matched control white matter. We observed a significant increase in laminin expression (197.81 μm^2 per vessel vs 126.33 μm^2 per vessel, $p < 0.05$) and a significant decrease in fibronectin expression (199.50 μm^2 per vessel vs 574.22 μm^2 per vessel, $p < 0.005$) in the white matter of subjects with WMH compared to aged-matched controls (Fig. 5).

Expression of Fibronectin and Laminin by human vascular smooth muscle cells is altered with an increase in CO$_2$

Previous mathematical modelling by our group showed that the vasomotion generated by cycles of contraction and relaxation of smooth muscle cells is vital for efficient IPAD [17, 18]. Loss of this function, as seen with ageing and in CAA, results in hypoperfusion, ischaemia and a failure of IPAD [17, 19, 20]. We therefore next investigated whether hypercapnia as a model of hypoperfusion/hypoxia, as in WMH,

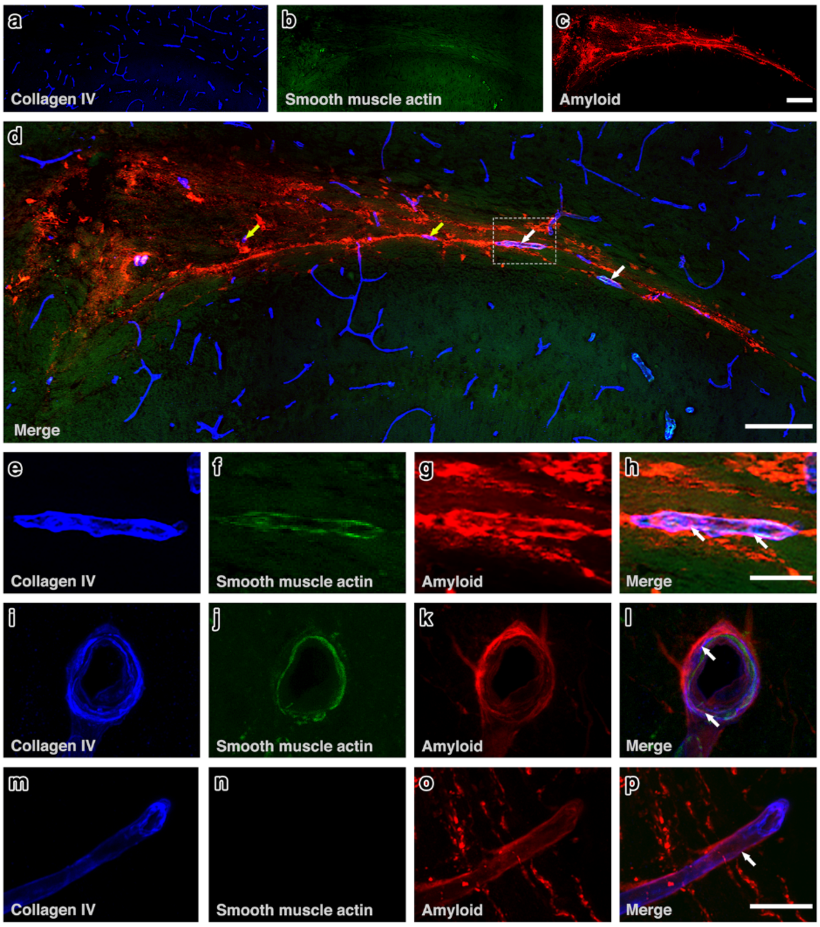

Fig. 3 IPAD in corpus callosum. **(a-c)** Distribution of amyloid-β in relation to collagen IV and smooth muscle actin. Amyloid-β **(red)** was observed along the white matter tracts **(c & d)** and co-localising **(Pink)** with collagen IV in the walls of capillaries **(yellow arrows)** and arterioles **(white arrows)**. **(e-h)** An arteriole in the white matter - see box in **(d)** -showing Aβ in the tunica media. Merging of the blue collagen IV staining in the basement membranes in **(e)** with red amyloid **(g)** produces a pink colour of co-localisation in **(h)**. **(i-l)** A leptomeningeal artery in the hippocampal fissure abutting on to the white matter shows Aβ co-localized **(pink)** with collagen IV in the tunica media **(lower arrow)** and in the adventitia **(upper arrow)**. **(m-p)** shows red Aβ **(arrow)** in the wall of a white matter capillary that is also stained blue for collagen IV in the basement membrane. Scale bars **a-d** = 200 μm, **e – h** = 20 μm **& i –** ***p*** = 10 μm

affects the function of smooth muscle cells. We exposed cultured HBVSMC to an increase in CO_2 and assessed cell proliferation and metabolic activity and production of laminin and fibronectin.

Following 72 h of exposure to increased levels of CO_2, we observed a reduction in MTS absorbance of HBVSMC compared to normoxic conditions but this difference was not significant (0.851 vs. 0.560, $p = 0.631$) (Fig. 6). However, analysis by confocal microscopy and subsequent quantification of laminin and fibronectin expression, revealed a significant increase in expression of laminin in HBVSMC exposed to 8% CO_2 in 92% air ($p \leq 0.05$).. Fibronectin was decreased but not significantly ($p = 0.827$) (Figs. 6 & 7).

Discussion

Of the two major functions of cerebral arteries discussed in this paper in relation to WMH, blood supply to the white matter has received more attention in the literature than elimination of fluid by IPAD. The results of the present study provide evidence that reduced capacity for IPAD from the white matter compared with grey matter together with a degree of hypoxia are involved in the aetiology of WMH.

Appendix B

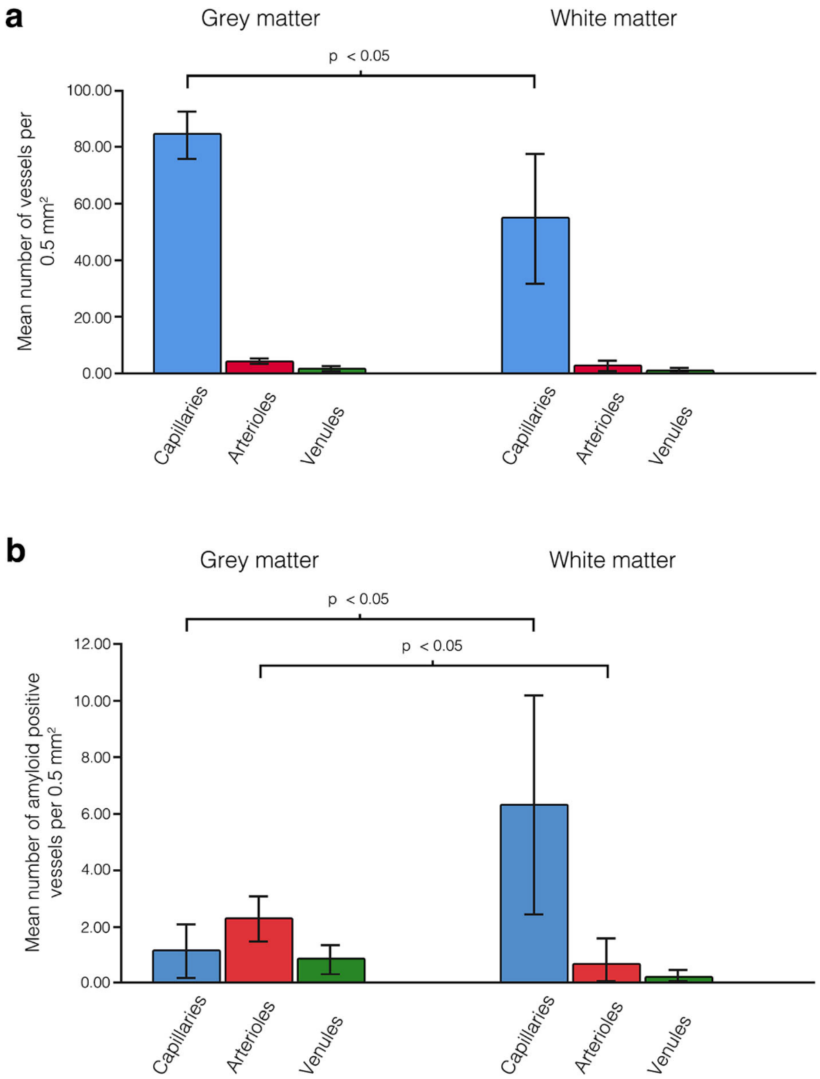

Fig. 4 Comparison of vessel density **(a)** and the density of vessels with fluorescent Aβ in their walls **(b)** between the hippocampus (grey matter) and corpus callosum (white matter). The density of arterioles with fluorescent Aβ in their vessel walls was significantly higher in the hippocampus but the density of capillaries with fluorescent Aβ in their vessel walls significantly higher in the corpus callosum **(b)** despite the significant reduction in density of capillaries in the corpus callosum **(a).** Error bars: +/− 2 SE

Reduced capacity for IPAD in the white matter compared with grey matter

We tested the hypothesis that the dynamics of IPAD in the cerebral white matter differ from those in the grey matter of the hippocampus. There are two major observations in our results that support this hypothesis. We found *First:* that, in rodents, the density of capillaries in the white matter is lower than in the grey matter of the hippocampus. As delivery of nutrients to the brain is via vascular capillaries, the lower density in the white matter suggests a lower capacity in white matter compared to grey matter for the delivery of oxygen and other nutrients. This may result in an increased risk of ischaemia/hypoxia in the white matter over grey matter in the presence of diseases such as arteriosclerosis and CAA in the arteries supplying the white matter; white matter appears to have a lower capacity for delivery of nutrients than grey matter. *Second*: the lower density of capillaries suggests that there is a lower capacity for IPAD in white matter when compared to grey matter. The reduced

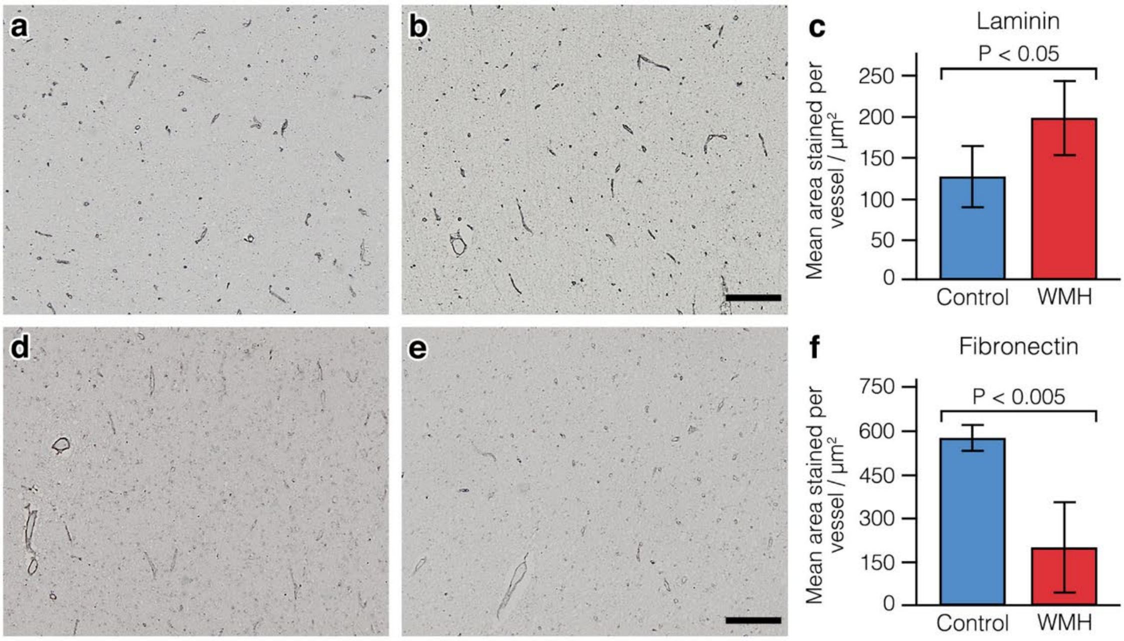
a
b
c
Laminin
P < 0.05
Mean area stained per vessel / µm²
250
200
150
100
50
0
Control
WMH
d
e
f
Fibronectin
P < 0.005
Mean area stained per vessel / µm²
750
600
450
300
150
0
Control
WMH

Fig. 5 Laminin and fibronectin expression in the white matter in subjects with white matter hyperintensities and controls. **a** Representative image of laminin staining in the control group. **b** Representative image of laminin staining in the WMH group. **c** Histogram showing the mean area of laminin staining per vessel. **d** Representative image of fibronectin staining in the control group. **e** Representative image of fibronectin staining in the WMH group. **f** Histogram showing the mean area of fibronectin staining per vessel. Scale bars indicate 200um. Error bars indicate +/− 2 SE

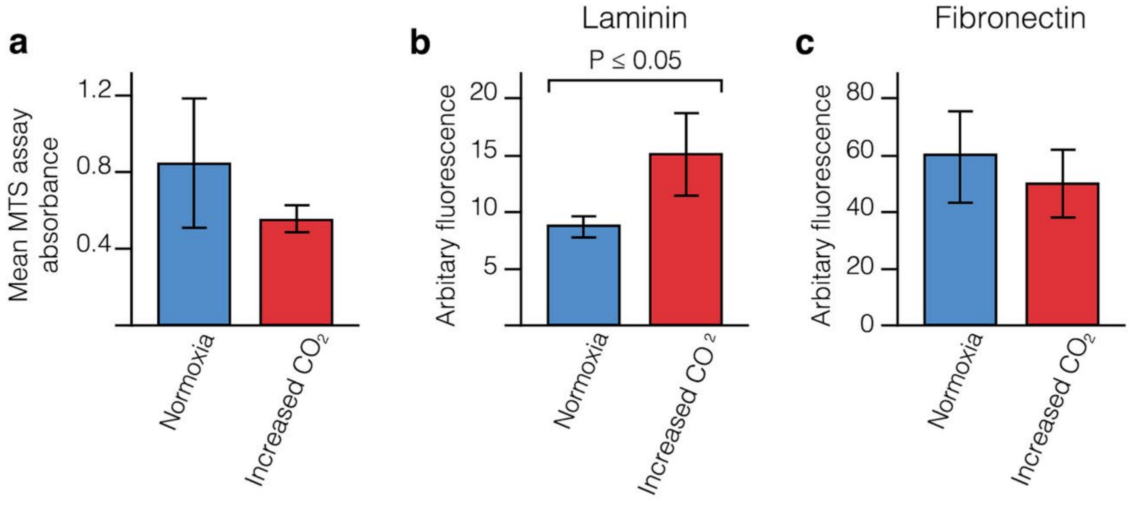

Fig. 6 Mean MTS absorbance and mean fluorescence intensity of HBVSMC exposed to increased levels of CO_2. **a** Mean MTS absorbance was reduced but not significantly.**b** Laminin staining was significantly higher in cultures exposed to increased levels of CO_2 compared to the normoxia cultures ($p \leq 0.05$). **c** There was a trend towards a decrease in the fluorescence intensity of fibronectin staining but this was not statistically significant. Error bars: +/− 1 SE

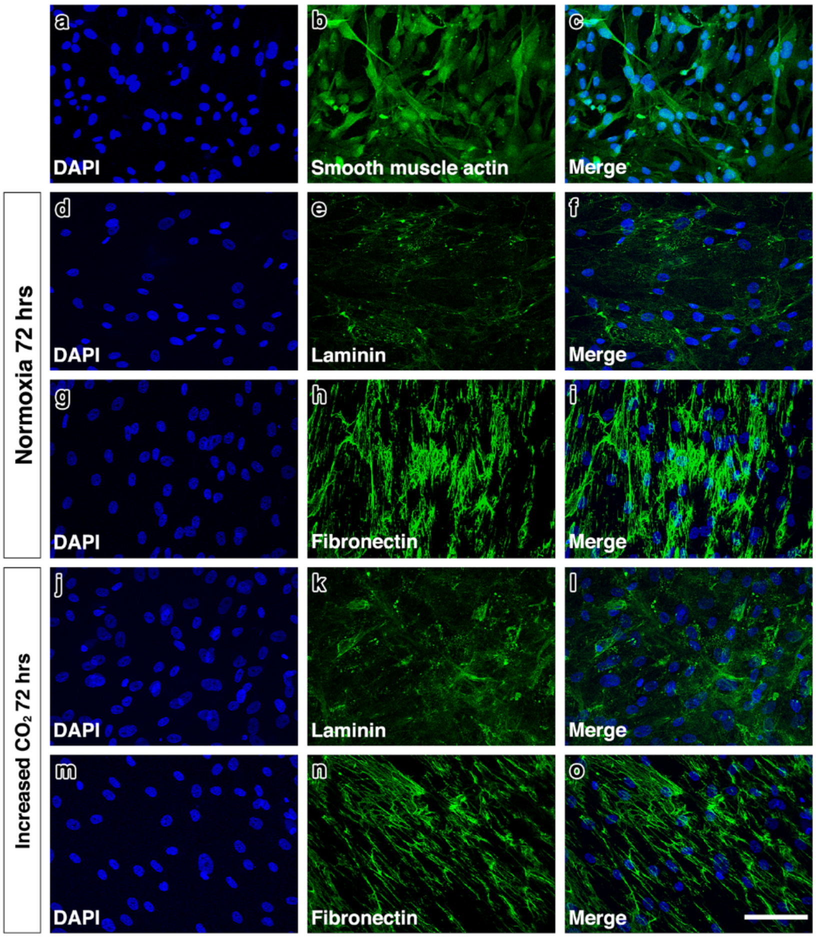

Fig. 7 Laminin and fibronectin staining in HBVSMC cultures after 72 h exposure to normoxia and hypoxia. Reference images **(a – c)** show the presence of smooth muscle actin in the HBVSMCs used in this study. The pattern of laminin staining **(e,k)** was similar in the HBVSMC cultures but there was a significant increase in expression with increased levels of CO_2 **(l)** compared to normoxice cultures **(f)**. Fibronectin staining **(h,n)** had a web-like appearance in both cultures but staining appeared more intense in the normoxic cultures **(i)** compared to cultures exposed to increased levels of CO_2 **(o)**. Cell density, indicated by DAPI stained nuclei **(d, g, j, m)**, did not appear to be altered in normoxic conditions or conditions of increased levels of CO_2. Scale bar = 50 μm

capacity of IPAD is shown in the current tracer experiments. When soluble Aβ was injected as a tracer into the white matter it was cleared more slowly from the capillaries compared to grey matter. A similar effect is seen with increasing age in the grey matter [10]. It seems therefore that the lower capacity of IPAD in the white matter may make it more vulnerable to failure when feeder arteries are affected by age-related changes and CAA that are both known to impede IPAD [4].

In the normal white matter of humans, the total number of capillaries is at least 49% lower compared to the grey matter in humans [33]. We demonstrate a similar reduction in the number of capillaries in the rodent white matter compared to the grey matter. In subjects with WMH, the capillary density decreases further, along with thickening of the capillary wall, leading to hypoperfusion [34]. The ISF entering the capillary bed in the white matter drains towards the coiled, tortuous arterioles situated in the white matter and then into the cortical arterioles [35, 36]. Figure 8 shows the relationship between arteries in cerebral cortex to those in the underlying white matter in the human brain [37]. Most of the blood for the subcortical white matter is supplied by arteries that branch from the leptomeningeal arteries and traverse the cortex, with or without branching, to supply the

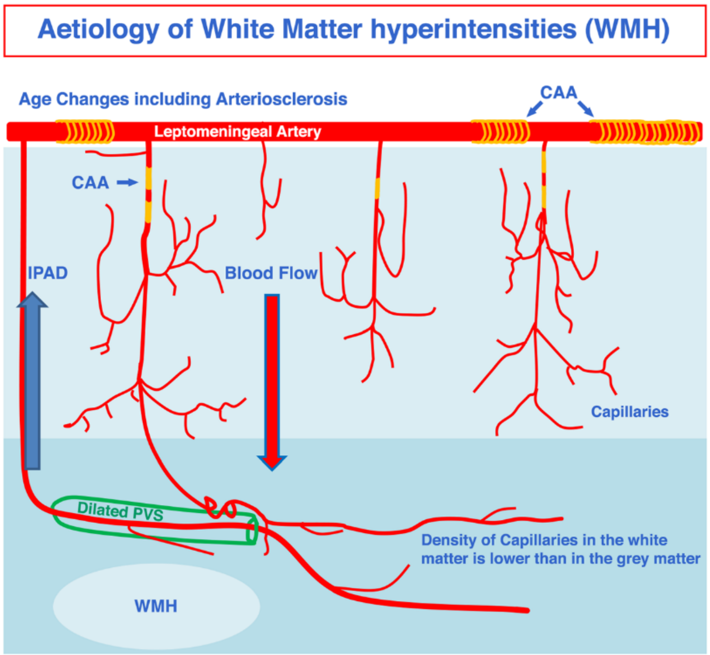
Aetiology of White Matter hyperintensities (WMH)
Age Changes including Arteriosclerosis
CAA
Leptomeningeal Artery
Surface of Brain
CAA
IPAD
Blood Flow
Grey Matter
Capillaries
Dilated PVS
White Matter
Density of Capillaries in the white matter is lower than in the grey matter
WMH

Fig. 8 Aetiology of White Matter Hyperintensities (WMH) in the human brain. Two of the major functions of cerebral arteries, arterioles and capillaries are (**a**) Blood Flow and the supply of nutrients to brain tissues (Red Arrow) and (**b**) Elimination of Interstitial Fluid (ISF) and soluble metabolites from brain tissues along basement membranes within the walls of capillaries and arteries – IPAD (Intramural Peri-Arterial Drainage) (Blue Arrow). Age changes in arteries, such as arteriosclerosis, impair both blood flow and IPAD resulting in ischaemic/hypoxic changes and a reduced drainage of fluid, particularly from the white matter, leading to WMH. A lower density of capillaries in white matter also reduces the capacity for IPAD and may be a causal factor for WMH in the ageing brain. Reduced IPAD is associated with the deposition of Amyloid-β (Aβ) in the IPAD pathways of cortical and leptomeningeal arteries as Cerebral Amyloid Angiopathy (CAA). The capacity of IPAD is further reduced by CAA and is associated with dilated, fluid-containing perivascular spaces (PVS) around arteries in the white matter and with WMH. Diagram adapted from [37]

underlying white matter. Figure 8 also suggests how both blood flow and IPAD could be reduced by the development of arteriosclerosis and CAA in the leptomeningeal and cortical arteries.

There are other pathologies in the white matter that may also reflect a reduced capacity for IPAD in the white matter, supporting the notion that in vivo imaging indicates that water shifts are prominent and represent early changes in WMH [3]. Vasogenic oedema that results from tumours in the brain or subarachnoid haemorrhage mainly involves the white matter [38, 39]. This sugests that fluid dynamics in the white matter may differ from those in the grey matter. In the present study it has been shown that the density of capillaries is lower in the white matter than in grey matter whereas the densities of arterioles is similar. As capillary basement membranes are the entry portals for IPAD by which ISF and solutes drain from brain tissue this relative shortage of capillaries in the white matter may be a factor in the reduced capacity for IPAD. Similarly observations in acute hydrocepahlus support the conclusion that the capacity of IPAD may be lower in white matter than in grey matter. Obstruction of CSF drainage from the cerebral ventricles results in dilatation of the ventricular system and the accumulation of fluid in the periventricular white matter in the acute stages of hydrocephalus with the slowly progressive destruction of white matter fibres and gliosis [40]. The grey matter is only affected to a minor degree by the accumulation of fluid at its junction with the white matter even when the white matter is very severely damaged [41]. These observations support the concept that the capacity of IPAD to eliminate fluid is lower in the white matter than in the grey matter. Our experimental studies focused only on the pattern of IPAD in the corpus callosum of mice, as it is the only part of the white matter that is large enough for intracerebral injections. There may be differences in the pattern of IPAD from the different parts of the white matter (for example subcortical or periventricular), as there are differences in the grey matter reflected also in different patterns of CAA [32, 42].

Our results in post-mortem brains indicate that fibronectin decreases in WMH. The levels of fibronectin were not changed in human cerebral smooth muscle cells subjected to hypercapnia as a model of hypoxic hypoperfusion. This is in contrast to the results obtained in experimental work with rodents, suggesting that human VSMCs react to hypoxia by a reduction in the synthesis of fibronectin, in contrast to rodent VSMCs. Hypoxia in the brain results in an increase matrix metalloproteinase-2 (MMP2) and there is a complex relationship between fibronectin and MMP2 in humans that varies according to the changes in the time from the hypoxic event [43, 44]. Our results in the human brain tissue reflect changes in chronic hypoxia which are considerably different to the experimental hypercapnia in smooth muscle cell lines. As fibronectin is a substrate for α5β1 integrin receptor [2, 45, 46] and both are involved in axonal regeneration, our results support the hypothesis that axonal regeneration is impaired in WMH.

It has been demonstrated in experimental work in rodents that laminin increases after hypoxia [26, 47], but the results in human brains are controversial. Our own results in post-mortem human cortical occipital sections demonstrate that there was no significant difference in the percentage area of collagen IV, laminin or fibronectin in CAA compared to age matched control sections [48]. However, collagen IV, a key glycoprotein component of the BM has been recently shown as increased in human WMH [49]. It may be that the hypoxic environment leads to an increase in laminin synthesis as a compensatory mechanism for the change in homeostasis of the brain, possibly leading to angiogenesis [50].

It has been known for several decades that the majority of the interstitial fluid in the white matter drains along the white matter tracts [51, 52]. In addition to the bulk flow along white matter tracts our study demonstrates that IPAD of soluble Aβ40 is also present in the white matter and occurs preferentially along the walls of capillaries whereas in the grey matter it occurs preferentially along the walls of arteries. The change in pattern of laminin and fibronectin expression in the white matter in WMH does correlate with the changes seen with hypoxia in cultures of VSMCs. However this does not necessarily define the reason for the hypoxia in WMH. The question still remains as to whether the hypoxia is due to poor blood supply or is an effect of the increased fluid in the extracellular spaces separating tissue elements from their oxygen supply in the blood.

Many of the fine details of fluid dynamics within the brain tissue and IPAD await explanation but what seems certain is the involvement of arteries and capillaries not only in the delivery of blood but also in the drainage of fluid and soluble matabolites from the brain. It may be possible therefore to combine therpeutic approaches to resolving ischaemia/hypoxia and failure of IPAD in WMH.

Acknowledgements

Work in the individual CFAS centres is supported by the UK NIHR Biomedical Research Centre for Ageing and Age – awarded to Newcastle-upon-Tyne Hospitals Foundation Trust; Cambridge Brain Bank supported by the NIHR Cambridge Biomedical Research Centre; Nottingham University Hospitals NHS Trust; University of Sheffield, Sheffield Teaching Hospitals NHS Foundation Trust and the Sheffield NIHR Biomedical Research Centre; The Thomas Willis Oxford Brain Collection, supported by the Oxford Biomedical Research Centre; The Walton Centre NHS Foundation Trust, Liverpool. We are grateful to the Parkinson's UK Brain Bank. We would like to acknowledge the essential contribution of the liaison officers, the general practitioners, their staff, and nursing and residential home staff. We are grateful to our respondents and their families for their generous gift to medical research, which has made this study possible.

Authors' contributions

MS performed all animal experiments and helped to prepare the manuscript for submission; SS performed the human post-mortem immunohistochemistry; AK performed the cell culture work. MG performed confocal microscopy. JES & SBW selected the post-mortem cases. RA, NA, ROW had important intellectual contributions to the manuscript. ROC designed the study. All authors contributed to the writing of the manuscript. The author(s) read and approved the final manuscript.

Funding

The authors gratefully acknowledge the Stroke Association Priority Programme Award PPA 2016/01, the MRC CFAS grants MRC/G9901400 and MRC U.1052.00.0013, Grant-in-Aid for Japan Society for the Promotion of Science Fellows to SS. 19 J00106 and BBSRC 2014 CASE PhD Studentship.

Availability of data and materials

The datasets used and/or analysed during the current study are available from the corresponding author on reasonable request.

Ethics approval and consent to participate

Human autopsy CNS tissue was obtained from the MRC Cognitive Function and Ageing Study (CFAS, ethical approval 15/SW/0246). Control cases were from CFAS and Parkinson's UK brain bank (REC Reference numbers 15/SW/0246 and 08/MRE09/31 + 5). The Parkinson's UK Brain Bank is funded by Parkinson's UK, a charity registered in England and Wales (258197) and in Scotland (SC037554). All procedures involving animals were carried out in accordance with animal care guidelines stipulated by the United Kingdom Animals (Scientific Procedures) Act 1986, Home Office licence P12102B2A.

Consent for publication

All human data are post-mortem tissue obtained with consent by the MRC CFAS and Parkinson's UK Brain Banks.

Competing interests

The authors declare no competing interests.

Author details

[1]Faculty of Medicine, University of Southampton, Tremona Road, Southampton SO16 6YD, UK. [2]Roche Pharma Research and Early Development (pRED), Pharmaceutical Sciences, Roche Innovation Center Basel, Basel, Switzerland. [3]Hospital Santa Maria del Carmine, Rovereto, Italy. [4]Sheffield Institute for Translational Neurosciences, University of Sheffield, Sheffield, UK.

Received: 17 June 2020 Accepted: 1 August 2020

Published online: 08 August 2020

References

1. Grinberg LT, Thal DR (2010) Vascular pathology in the aged human brain. Acta Neuropathol 119(3):277–290
2. McAleese KE, Walker L, Graham S, Moya ELJ, Johnson M, Erskine D et al (2017) Parietal white matter lesions in Alzheimer's disease are associated with cortical neurodegenerative pathology, but not with small vessel disease. Acta Neuropathol 134(3):459–473
3. Wardlaw JM, Valdes Hernandez MC, Munoz-Maniega S (2015) What are White Matter Hyperintensities Made of? Relevance to Vascular Cognitive Impairment. J Am Heart Assoc 4(6):e001140
4. Weller RO, Hawkes CA, Kalaria RN, Werring DJ, Carare RO (2015) White matter changes in dementia: role of impaired drainage of interstitial fluid. Brain Pathol 25(1):63–78
5. Szentistvanyi I, Patlak CS, Ellis RA, Cserr HF (1984) Drainage of interstitial fluid from different regions of rat brain. AmJ Physiol 246(6 Pt 2):F835–FF44
6. McIntee FL, Giannoni P, Blais S, Sommer G, Neubert TA, Rostagno A et al (2016) In vivo differential brain clearance and catabolism of monomeric and Oligomeric Alzheimer's Abeta protein. Front Aging Neurosci 8:223
7. Carare RO, Bernardes-Silva M, Newman TA, Page AM, Nicoll JA, Perry VH et al (2008) Solutes, but not cells, drain from the brain parenchyma along basement membranes of capillaries and arteries: significance for cerebral amyloid angiopathy and neuroimmunology. NeuropatholApplNeurobiol. 34(2):131–144
8. Albargothy NJ, Johnston DA, MacGregor-Sharp M, Weller RO, Verma A, Hawkes CA et al (2018) Convective influx/glymphatic system: tracers injected into the CSF enter and leave the brain along separate periarterial basement membrane pathways. Acta Neuropathol 136(1):139–152
9. Tarasoff-Conway JM, Carare RO, Osorio RS, Glodzik L, Butler T, Fieremans E et al (2015) Clearance systems in the brain-implications for Alzheimer disease. Nat Rev Neurol 11(8):457–470
10. Hawkes CA, Hartig W, Kacza J, Schliebs R, Weller RO, Nicoll JA et al (2011) Perivascular drainage of solutes is impaired in the ageing mouse brain and in the presence of cerebral amyloid angiopathy. Acta Neuropathol 121(4): 431–443
11. Carare RO, Hawkes CA, Jeffrey M, Kalaria RN, Weller RO (2013) Review: cerebral amyloid angiopathy, prion angiopathy, CADASIL and the spectrum of protein elimination failure angiopathies (PEFA) in neurodegenerative disease with a focus on therapy. Neuropathol Appl Neurobiol 39(6):593–611
12. Weller RO, Hawkes CA, Carare RO, Hardy J (2015) Does the difference between PART and Alzheimer's disease lie in the age-related changes in cerebral arteries that trigger the accumulation of Abeta and propagation of tau? Acta Neuropathol 129(5):763–766
13. Engelhardt B, Carare RO, Bechmann I, Flugel A, Laman JD, Weller RO (2016) Vascular, glial, and lymphatic immune gateways of the central nervous system. Acta Neuropathol 132(3):317–338
14. Engelhardt B, Vajkoczy P, Weller RO (2017) The movers and shapers in immune privilege of the CNS. Nat Immunol 18(2):123–131
15. Weller RO, Djuanda E, Yow HY, Carare RO (2009) Lymphatic drainage of the brain and the pathophysiology of neurological disease. Acta Neuropathol 117(1):1–14
16. Diem AK, MacGregor Sharp M, Gatherer M, Bressloff NW, Carare RO, Richardson G (2017) Arterial pulsations cannot drive intramural Periarterial drainage: significance for Abeta drainage. Front Neurosci 11:475
17. Aldea R, Weller RO, Wilcock DM, Carare RO, Richardson G (2019) Cerebrovascular smooth muscle cells as the drivers of intramural Periarterial drainage of the brain. Front Aging Neurosci 11:1
18. van Veluw SJ, Hou SS, Calvo-Rodriguez M, Arbel-Ornath M, Snyder AC, Frosch MP et al (2020) Vasomotion as a driving force for Paravascular clearance in the awake mouse brain. Neuron. 105(3):549–561 e5
19. Okamoto Y, Yamamoto T, Kalaria RN, Senzaki H, Maki T, Hase Y et al (2012) Cerebral hypoperfusion accelerates cerebral amyloid angiopathy and promotes cortical microinfarcts. Acta Neuropathol 123(3):381–394
20. Barker R, Wellington D, Esiri MM, Love S (2013) Assessing white matter ischemic damage in dementia patients by measurement of myelin proteins. J Cereb Blood Flow Metab 33(7):1050–1057
21. Hallmann R, Horn N, Selg M, Wendler O, Pausch F, Sorokin LM (2005) Expression and function of laminins in the embryonic and mature vasculature. Physiol Rev 85(3):979–1000
22. Horsburgh K, Wardlaw JM, van Agtmael T, Allan SM, Ashford MLJ, Bath PM et al (2018) Small vessels, dementia and chronic diseases - molecular mechanisms and pathophysiology. Clin Sci (Lond) 132(8):851–868
23. Joutel A, Haddad I, Ratelade J, Nelson MT (2016) Perturbations of the cerebrovascular matrisome: a convergent mechanism in small vessel disease of the brain? J Cereb Blood Flow Metab 36(1):143–157
24. Halder SK, Kant R, Milner R (2018) Chronic mild hypoxia promotes profound vascular remodeling in spinal cord blood vessels, preferentially in white matter, via an alpha5beta1 integrin-mediated mechanism. Angiogenesis. 21(2):251–266
25. Halder SK, Kant R, Milner R (1700) Chronic mild hypoxia increases expression of laminins 111 and 411 and the laminin receptor alpha6beta1 integrin at the blood-brain barrier. Brain Res 2018:78–85
26. Hawkes CA, Michalski D, Anders R, Nissel S, Grosche J, Bechmann I et al (2013) Stroke-induced opposite and age-dependent changes of vessel-associated markers in co-morbid transgenic mice with Alzheimer-like alterations. Exp Neurol 250:270–281
27. Fernando MS, O'Brien JT, Perry RH, English P, Forster G, McMeekin W et al (2004) Comparison of the pathology of cerebral white matter with post-mortem magnetic resonance imaging (MRI) in the elderly brain. Neuropathol Appl Neurobiol 30(4):385–395
28. Wharton SB, Simpson JE, Brayne C, Ince PG (2015) Age-associated white Matter lesions: the MRC cognitive function and ageing study. Brain Pathol 25(1):35–43
29. Rueden CT, Schindelin J, Hiner MC, DeZonia BE, Walter AE, Arena ET et al (2017) ImageJ2: ImageJ for the next generation of scientific image data. BMC Bioinformatics 18(1):529
30. Morris AW, Sharp MM, Albargothy NJ, Fernandes R, Hawkes CA, Verma A et al (2016) Vascular basement membranes as pathways for the passage of fluid into and out of the brain. Acta Neuropathol 131(5):725–736
31. Cserr HF, Ostrach LH (1974) Bulk flow of interstitial fluid after intracranial injection of blue dextran 2000. Exp Neurol 45(1):50–60
32. Hawkes CA, Gatherer M, Sharp MM, Dorr A, Yuen HM, Kalaria R et al (2013) Regional differences in the morphological and functional effects of aging on cerebral basement membranes and perivascular drainage of amyloid-beta from the mouse brain. Aging Cell 12(2):224–236
33. Hase Y, Ding R, Harrison G, Hawthorne E, King A, Gettings S et al (2019) White matter capillaries in vascular and neurodegenerative dementias. Acta Neuropathol Commun 7(1):16
34. Mozumder M, Pozo JM, Coelho S, Costantini M, Simpson J, Highley JR et al (2019) Quantitative histomorphometry of capillary microstructure in deep white matter. NeuroImage Clinical 23:101839
35. Nonaka H, Akima M, Hatori T, Nagayama T, Zhang Z, Ihara F (2003) The microvasculature of the cerebral white matter: arteries of the subcortical white matter. J Neuropathol Exp Neurol 62(2):154–161
36. Nonaka H, Akima M, Hatori T, Nagayama T, Zhang Z, Ihara F (2003) Microvasculature of the human cerebral white matter: arteries of the deep white matter. Neuropathology 23(2):111–118
37. Duvernoy HM, Delon S, Vannson JL (1981) Cortical blood vessels of the human brain. Brain Res Bull 7(5):519–579
38. Tiller-Borcich JK, Fike JR, Phillips TL, Davis RL (1987) Pathology of delayed radiation brain damage: an experimental canine model. Radiat Res 110(2):161–172
39. Weimer JM, Jones SE, Frontera JA (2017) Acute cytotoxic and Vasogenic edema after subarachnoid hemorrhage: a quantitative MRI study. AJNR Am J Neuroradiol 38(5):928–934
40. Weller RO, Wisniewski H, Shulman K, Terry RD (1971) Experimental hydrocephalus in young dogs: histological and ultrastructural study of the brain tissue damage 142. J NeuropatholExpNeurol 30(4):613–626
41. Weller RO, Wisniewski H (1969) Histological and ultrastructural changes with experimental hydrocephalus in adult rabbits 151. Brain 92(4):819–828
42. Attems J, Jellinger K, Thal DR, Van Nostrand W (2011) Review: sporadic cerebral amyloid angiopathy. Neuropathol Appl Neurobiol 37(1):75–93
43. Steffensen B, Xu X, Martin PA, Zardeneta G (2002) Human fibronectin and MMP-2 collagen binding domains compete for collagen binding sites and modify cellular activation of MMP-2. Matrix Biol 21(5):399–414
44. Hua Y, Zhang W, Xie Z, Xu N, Lu Y (2016) MMP-2 is mainly expressed in arterioles and contributes to cerebral vascular remodeling associated with TGF-beta1 signaling. J Mol Neurosci 59(3):317–325
45. Matter ML, Zhang Z, Nordstedt C, Ruoslahti E (1998) The alpha5beta1 integrin mediates elimination of amyloid-beta peptide and protects against apoptosis. J Cell Biol 141(4):1019–1030

Appendix B

46. Tom VJ, Doller CM, Malouf AT, Silver J (2004) Astrocyte-associated fibronectin is critical for axonal regeneration in adult white matter. J Neurosci 24(42):9282–9290
47. Yao Y (2019) Basement membrane and stroke. J Cerebral Blood Flow Metab 39(1):3–19
48. Keable A, Fenna K, Yuen HM, Johnston DA, Smyth NR, Smith C et al (2015) Deposition of amyloid beta in the walls of human leptomeningeal arteries in relation to perivascular drainage pathways in cerebral amyloid angiopathy. Biochim Biophys Acta 1862(5):1037–1046
49. Waller R, Baxter L, Fillingham DJ, Coelho S, Pozo JM, Mozumder M et al (2019) Iba-1−/CD68+ microglia are a prominent feature of age-associated deep subcortical white matter lesions. PLoS One 14(1):e0210888
50. Ji K, Tsirka SE (2012) Inflammation modulates expression of laminin in the central nervous system following ischemic injury. J Neuroinflammation 9:159
51. Geer CP, Grossman SA (1997) Interstitial fluid flow along white matter tracts: a potentially important mechanism for the dissemination of primary brain tumors. J Neuro-Oncol 32(3):193–201
52. Cserr HF, DePasquale M, Patlak CS, Pullen RG (1986) Convection of cerebral interstitial fluid and its role in brain volume regulation 28. AnnNYAcadSci. 481:123–134

Publisher's Note

Springer Nature remains neutral with regard to jurisdictional claims in published maps and institutional affiliations.

Ready to submit your research? Choose BMC and benefit from:

- fast, convenient online submission
- thorough peer review by experienced researchers in your field
- rapid publication on acceptance
- support for research data, including large and complex data types
- gold Open Access which fosters wider collaboration and increased citations
- maximum visibility for your research: over 100M website views per year

At BMC, research is always in progress.

Learn more biomedcentral.com/submissions

BMC

Appendix C METHOD FOR CEREBRAL BLOOD FLOW MEASUREMENTS USING ARTERIAL SPIN LABELLING

C.1 Aim

To measure the cerebral blood flow (CBF) in alpha dystrobrevin knockout mice and wild-type (WT) controls using a non-invasive MRI technique (arterial spin labelling (ASL)).

C.2 Method

All mice were induced with 2% isoflurane anaesthetic in a mixture with room air at 1.0 L/min, which was manually adjusted between 1.75 - 1.5% to maintain the respiration rate at ~100 bpm throughout the scan, measured using a pressure pad. The core body temperature was maintained at 37.0 ± 0.5°C throughout the scan, which was monitored using a rectal probe (SA Instruments, New York, USA) and maintained via an adjustable water bath supplied to a mouse heating pad (Bruker BioSpec).

All images were acquired on a horizontal bore 9.4T Bruker preclinical system (BioSpec 94/20 USR) using 440 mT/m gradient set with outer/ inner diameter 205 mm /116 mm respectively (BioSpec B-GA 12S2), a 86 mm volume transit RF coil and a four-channel receiver array coil designed for the mouse brain (Bruker).

A T2-Turbo-RARE sequence was used to acquire anatomical image for slice positioning reference for each animal. Imaging parameters: echo time (TE) = 33 ms; repetition time (TR) = 2500 ms; matrix size = 256 x 256; field-of-view (FOV) = 28 mm x 28 ms; slice thickness = 0.75 mm; slices = 15.

The ASL image acquisition was based on a flow alternating inversion recovery (FAIR) sequence with a single-shot spin-echo (SE) echo planar imaging (EPI) readout. A single slice FAIR protocol was implemented (slice thickness = 2 mm), with a slice selective inversion pulse thickness of 8 mm and a global non-selective pulse (no slice select gradient). Further ASL imaging parameters: TI = 200 ms, 500 ms, 800 ms, 1000 ms, 1500 ms, 2000 ms, 3000 ms, 4000 ms; TE = 10 ms; TR = 10 000 ms; FOV = 25 mm x 25 mm; data matrix = 96 x 96; partial fourier = 32 + 4 lines of k-space; repetitions = 6.

C.3 Theory

Cerebral blood flow (CBF) was assessed by taking the ASL signal, ΔM, at increasing inflow times (TI) using the standard Buxton general kinetic perfusion model [277]:

Appendix C

$$\Delta M = 2M_0 CBF\alpha \exp\left(-\frac{TI}{T1_b}\right)\left((TI - \delta_a)q_{1.} + \tau q_2\right) \tag{1}$$

$$q_1 = \exp(k.TI)\,\frac{\exp(-k\delta_a) - \exp(-kTI)}{k(TI - \delta_a)} \tag{2}$$

$$q_2 = \exp(k.TI).\frac{\exp(-k.\delta_a) - \exp(-k.(\tau + \delta_a)}{k.\tau} \tag{3}$$

$$k = \frac{1}{T1_b} - \frac{1}{T1'} \tag{4}$$

$$\frac{1}{T1'} = \frac{1}{T1} + \frac{CBF}{\lambda} \tag{5}$$

where M_0 is the equilibrium magnetisation from the control signal using the standard recovery model T1 is the longitudinal relaxation of the extravascular tissue [300], is the arterial transit time, α is the inversion efficiency (0.9), $R1_a$ is the longitudinal relaxation rate of the arterial blood, $T1_b$ is longitudinal relaxation of arterial blood, τ is the temporal length of the labelled bolus and λ is the partition coefficient (assumed to have a value of 0.9 ml/g [301]).

Measured Variables/ unit		Assumed Variables & values		
Cerebral blood flow	CBF / ml/100g/min	Longitudinal relaxation of arterial blood	$T1_b$	2.4 s
Longitudinal relaxation	T1 /s	Blood-brain partition coefficient	λ	0.9
Equilibrium magnetization	M_0	Inversion efficiency	α	0.9
Arterial transit time	δ_a/ ms			
Temporal length of labeled bolus	/ s			

Table 1: The measured variables with associated units and the assumed variables with associated value used for the CBF model.

C.4 Data Processing

All imaging data was processed using Matlab 2018 (Mathworks). The cortical and the hippocampal brain regions were manually segmented in each data set. The control data was fitted to the standard recovery model to measure T1 and M_0 in each animal. Mean ASL images were generated by a pairwise subtraction of the control and labelled images, and the ASL signal was extracted from the cortical and hippocampal regions. The CBF model (eq. 1) was fitted to the ASL signal across at each inflow time measuring/ fitting for the CBF, δ_a and τ.

List of References

1. Livingston G, Sommerlad A, Orgeta V, Costafreda SG, Huntley J, Ames D, et al. Dementia prevention, intervention, and care. Lancet. 2017;390(10113):2673-734.

2. Raphael Wittenberg BH, Luis Barraza-Araiza, Amritpal Rehill. Projections of older people with dementia and costs of dementia care in the United Kingdom, 2019–2040 2019 [Available from: https://www.alzheimers.org.uk/sites/default/files/201911/cpec_report_november_2019.pdf.

3. Orrell M, Brayne C, Interdem, Alzheimer E, Alzheimer's Disease I, European Association of Geriatric P. Dementia prevention: call to action. Lancet. 2015;386(10004):1625.

4. (ADI) AsDI. World Alzheimer Report 2015: the Global Impact of Dementia: An Analysis of Prevalence, Incidence, Cost and Trends 2015 [Available from: ADI website. https://www.alz.co. uk/research/WorldAlzheimerReport2015.pdf.

5. (ADI) AsDI. World Alzheimer Report 2019: Attitudes to dementia 2019 [Available from: https://www.alz.co.uk/research/world-report-2019.

6. Plassman BL, Langa KM, Fisher GG, Heeringa SG, Weir DR, Ofstedal MB, et al. Prevalence of Dementia in the United States: The Aging, Demographics, and Memory Study. Neuroepidemiology. 2007;29(1-2):125-32.

7. Skrobot OA, Black SE, Chen C, DeCarli C, Erkinjuntti T, Ford GA, et al. Progress toward standardized diagnosis of vascular cognitive impairment: Guidelines from the Vascular Impairment of Cognition Classification Consensus Study. Alzheimers Dement. 2018;14(3):280-92.

8. Kalaria RN. The pathology and pathophysiology of vascular dementia. Neuropharmacology. 2017.

9. Venkat P, Chopp M, Chen J. Models and mechanisms of vascular dementia. Exp Neurol. 2015;272:97-108.

10. Munoz DG, Weishaupt N. Chapter 5 - Vascular Dementia. The Cerebral Cortex in Neurodegenerative and Neuropsychiatric Disorders. San Diego: Academic Press; 2017. p. 119-39.

11. Yang Y, Estrada EY, Thompson JF, Liu W, Rosenberg GA. Matrix metalloproteinase-mediated disruption of tight junction proteins in cerebral vessels is reversed by synthetic matrix metalloproteinase inhibitor in focal ischemia in rat. J Cereb Blood Flow Metab. 2007;27(4):697-709.

12. Yang Y, Kimura-Ohba S, Thompson J, Rosenberg GA. Rodent Models of Vascular Cognitive Impairment. Translational stroke research. 2016;7(5):407-14.

13. Alsop DC, Dai W, Grossman M, Detre JA. Arterial spin labeling blood flow MRI: its role in the early characterization of Alzheimer's disease. J Alzheimers Dis. 2010;20(3):871-80.

14. Chao LL, Buckley ST, Kornak J, Schuff N, Madison C, Yaffe K, et al. ASL perfusion MRI predicts cognitive decline and conversion from MCI to dementia. Alzheimer Dis Assoc Disord. 2010;24(1):19-27.

15. Horsburgh K, Wardlaw JM, van Agtmael T, Allan SM, Ashford MLJ, Bath Philip M, et al. Small vessels, dementia and chronic diseases – molecular mechanisms and pathophysiology. Clinical Science. 2018;132:851-68.

16. Pantoni L. Cerebral small vessel disease: from pathogenesis and clinical characteristics to therapeutic challenges. Lancet Neurol. 2010;9(7):689-701.

17. Rosenberg GA, Wallin A, Wardlaw JM, Markus HS, Montaner J, Wolfson L, et al. Consensus statement for diagnosis of subcortical small vessel disease. J Cereb Blood Flow Metab. 2016;36(1):6-25.

18. Biessels GJ. Diagnosis and treatment of vascular damage in dementia. Biochim Biophys Acta. 2016;1862(5):869-77.

19. Joutel A, Chabriat H. Pathogenesis of white matter changes in cerebral small vessel diseases: beyond vessel-intrinsic mechanisms. Clin Sci (Lond). 2017;131(8):635-51.

20. Wardlaw JM, Smith EE, Biessels GJ, Cordonnier C, Fazekas F, Frayne R, et al. Neuroimaging standards for research into small vessel disease and its contribution to ageing and neurodegeneration. Lancet Neurol. 2013;12(8):822-38.

21. Lammie GA, Brannan F, Slattery J, Warlow C. Nonhypertensive cerebral small-vessel disease. An autopsy study. Stroke. 1997;28(11):2222-9.

22. Di Marco LY, Venneri A, Farkas E, Evans PC, Marzo A, Frangi AF. Vascular dysfunction in the pathogenesis of Alzheimer's disease--A review of endothelium-mediated mechanisms and ensuing vicious circles. Neurobiol Dis. 2015;82:593-606.

23. Yamada M, Naiki H. Cerebral amyloid angiopathy. Prog Mol Biol Transl Sci. 2012;107:41-78.

24. Yamada M, Tsukagoshi H, Otomo E, Hayakawa M. Cerebral amyloid angiopathy in the aged. J Neurol. 1987;234(6):371-6.

25. Yamada M. Cerebral amyloid angiopathy: emerging concepts. J Stroke. 2015;17(1):17-30.

26. Thal DR, Ghebremedhin E, Rub U, Yamaguchi H, Del Tredici K, Braak H. Two types of sporadic cerebral amyloid angiopathy. J Neuropathol Exp Neurol. 2002;61(3):282-93.

27. Rensink AA, de Waal RM, Kremer B, Verbeek MM. Pathogenesis of cerebral amyloid angiopathy. Brain Res Brain Res Rev. 2003;43(2):207-23.

28. Herzig MC, Winkler DT, Burgermeister P, Pfeifer M, Kohler E, Schmidt SD, et al. Abeta is targeted to the vasculature in a mouse model of hereditary cerebral hemorrhage with amyloidosis. Nat Neurosci. 2004;7(9):954-60.

29. Haass C, Lemere CA, Capell A, Citron M, Seubert P, Schenk D, et al. The Swedish mutation causes early-onset Alzheimer's disease by beta-secretase cleavage within the secretory pathway. Nat Med. 1995;1(12):1291-6.

30. Lehman EJ, Kulnane LS, Lamb BT. Alterations in beta-amyloid production and deposition in brain regions of two transgenic models. Neurobiol Aging. 2003;24(5):645-53.

31. Scheuner D, Eckman C, Jensen M, Song X, Citron M, Suzuki N, et al. Secreted amyloid beta-protein similar to that in the senile plaques of Alzheimer's disease is increased in vivo by the presenilin 1 and 2 and APP mutations linked to familial Alzheimer's disease. Nat Med. 1996;2(8):864-70.

32. Weller RO, Subash M, Preston SD, Mazanti I, Carare RO. Perivascular drainage of amyloid-beta peptides from the brain and its failure in cerebral amyloid angiopathy and Alzheimer's disease. Brain Pathol. 2008;18(2):253-66.

33. Gouras GK. Current theories for the molecular and cellular pathogenesis of Alzheimers disease. Expert reviews in molecular medicine. 2001;2001:1-11.

34. Soontornniyomkij V, Choi C, Pomakian J, Vinters HV. High-definition characterization of cerebral beta-amyloid angiopathy in Alzheimer's disease. Human pathology. 2010;41(11):1601-8.

35. Mawuenyega KG, Sigurdson W, Ovod V, Munsell L, Kasten T, Morris JC, et al. Decreased clearance of CNS beta-amyloid in Alzheimer's disease. Science. 2010;330(6012):1774.

36. Hawkes CA, McLaurin J. Selective targeting of perivascular macrophages for clearance of beta-amyloid in cerebral amyloid angiopathy. Proc Natl Acad Sci U S A. 2009;106(4):1261-6.

37. Wilcock DM, Munireddy SK, Rosenthal A, Ugen KE, Gordon MN, Morgan D. Microglial activation facilitates Abeta plaque removal following intracranial anti-Abeta antibody administration. Neurobiol Dis. 2004;15(1):11-20.

38. Bechmann I, Priller J, Kovac A, Bontert M, Wehner T, Klett FF, et al. Immune surveillance of mouse brain perivascular spaces by blood-borne macrophages. Eur J Neurosci. 2001;14(10):1651-8.

39. Deane R, Sagare A, Hamm K, Parisi M, Lane S, Finn MB, et al. apoE isoform-specific disruption of amyloid beta peptide clearance from mouse brain. J Clin Invest. 2008;118(12):4002-13.

40. Kalaria RN, Premkumar DR, Pax AB, Cohen DL, Lieberburg I. Production and increased detection of amyloid beta protein and amyloidogenic fragments in brain

microvessels, meningeal vessels and choroid plexus in Alzheimer's disease. Brain Res Mol Brain Res. 1996;35(1-2):58-68.

41. Wisniewski HM, Frackowiak J, Mazur-Kolecka B. In vitro production of beta-amyloid in smooth muscle cells isolated from amyloid angiopathy-affected vessels. Neurosci Lett. 1995;183(1-2):120-3.

42. Kiuru S, Salonen O, Haltia M. Gelsolin-related spinal and cerebral amyloid angiopathy. Ann Neurol. 1999;45(3):305-11.

43. Yamada M. Cerebral amyloid angiopathy: an overview. Neuropathology. 2000;20(1):8-22.

44. Greenberg SM, Charidimou A. Diagnosis of Cerebral Amyloid Angiopathy: Evolution of the Boston Criteria. Stroke. 2018;49(2):491-7.

45. Abbott NJ, Ronnback L, Hansson E. Astrocyte-endothelial interactions at the blood-brain barrier. Nat Rev Neurosci. 2006;7(1):41-53.

46. Obermeier B, Daneman R, Ransohoff RM. Development, maintenance and disruption of the blood-brain barrier. Nat Med. 2013;19(12):1584-96.

47. Abbott NJ, Patabendige AA, Dolman DE, Yusof SR, Begley DJ. Structure and function of the blood-brain barrier. Neurobiol Dis. 2010;37(1):13-25.

48. Keaney J, Campbell M. The dynamic blood-brain barrier. FEBS J. 2015;282(21):4067-79.

49. Pardridge WM. Alzheimer's disease drug development and the problem of the blood-brain barrier. Alzheimers Dement. 2009;5(5):427-32.

50. Hainsworth AH, Oommen AT, Bridges LR. Endothelial cells and human cerebral small vessel disease. Brain Pathol. 2015;25(1):44-50.

51. Ransohoff RM, Engelhardt B. The anatomical and cellular basis of immune surveillance in the central nervous system. Nat Rev Immunol. 2012;12(9):623-35.

52. Shechter R, Schwartz M. Harnessing monocyte-derived macrophages to control central nervous system pathologies: no longer 'if' but 'how'. J Pathol. 2013;229(2):332-46.

53. Liu H, Zhang J. Cerebral hypoperfusion and cognitive impairment: the pathogenic role of vascular oxidative stress. Int J Neurosci. 2012;122(9):494-9.

54. Gill R, Tsung A, Billiar T. Linking oxidative stress to inflammation: Toll-like receptors. Free Radic Biol Med. 2010;48(9):1121-32.

55. Wardlaw JM, Smith C, Dichgans M. Mechanisms of sporadic cerebral small vessel disease: insights from neuroimaging. Lancet Neurol. 2013;12(5):483-97.

56. Hallmann R, Horn N, Selg M, Wendler O, Pausch F, Sorokin LM. Expression and function of laminins in the embryonic and mature vasculature. Physiol Rev. 2005;85(3):979-1000.

57. Morris AW, Carare RO, Schreiber S, Hawkes CA. The Cerebrovascular Basement Membrane: Role in the Clearance of beta-amyloid and Cerebral Amyloid Angiopathy. Front Aging Neurosci. 2014;6:251.

58. Kagan HM, Li W. Lysyl oxidase: properties, specificity, and biological roles inside and outside of the cell. J Cell Biochem. 2003;88(4):660-72.

59. Garrod D. Chapter 6 - Cell Adhesion and the Extracellular Matrix. In: Goodman SR, editor. Medical Cell Biology (Third Edition). San Diego: Academic Press; 2008. p. 191-225.

60. Baeten KM, Akassoglou K. Extracellular matrix and matrix receptors in blood-brain barrier formation and stroke. Dev Neurobiol. 2011;71(11):1018-39.

61. Milner R, Hung S, Wang X, Spatz M, del Zoppo GJ. The rapid decrease in astrocyte-associated dystroglycan expression by focal cerebral ischemia is protease-dependent. J Cereb Blood Flow Metab. 2008;28(4):812-23.

62. Heo JH, Han SW, Lee SK. Free radicals as triggers of brain edema formation after stroke. Free Radic Biol Med. 2005;39(1):51-70.

63. Hohenester E, Yurchenco PD. Laminins in basement membrane assembly. Cell Adh Migr. 2013;7(1):56-63.

64. Yurchenco PD. Basement membranes: cell scaffoldings and signaling platforms. Cold Spring Harb Perspect Biol. 2011;3(2).

65. Zarow C, Barron E, Chui HC, Perlmutter LS. Vascular basement membrane pathology and Alzheimer's disease. Ann N Y Acad Sci. 1997;826:147-60.

66. Kalaria RN. Cerebral vessels in ageing and Alzheimer's disease. Pharmacol Ther. 1996;72(3):193-214.

67. Joutel A, Haddad I, Ratelade J, Nelson MT. Perturbations of the cerebrovascular matrisome: A convergent mechanism in small vessel disease of the brain? J Cereb Blood Flow Metab. 2016;36(1):143-57.

68. Uspenskaia O, Liebetrau M, Herms J, Danek A, Hamann GF. Aging is associated with increased collagen type IV accumulation in the basal lamina of human cerebral microvessels. BMC Neurosci. 2004;5:37.

69. Kalaria RN, Pax AB. Increased collagen content of cerebral microvessels in Alzheimer's disease. Brain Res. 1995;705(1-2):349-52.

70. Lepelletier FX, Mann DM, Robinson AC, Pinteaux E, Boutin H. Early changes in extracellular matrix in Alzheimer's disease. Neuropathol Appl Neurobiol. 2017;43(2):167-82.

71. Castillo GM, Ngo C, Cummings J, Wight TN, Snow AD. Perlecan binds to the beta-amyloid proteins (A beta) of Alzheimer's disease, accelerates A beta fibril formation, and maintains A beta fibril stability. J Neurochem. 1997;69(6):2452-65.

72. Cotman SL, Halfter W, Cole GJ. Agrin binds to beta-amyloid (Abeta), accelerates abeta fibril formation, and is localized to Abeta deposits in Alzheimer's disease brain. Mol Cell Neurosci. 2000;15(2):183-98.

73. Bronfman FC, Alvarez A, Morgan C, Inestrosa NC. Laminin blocks the assembly of wild-type A beta and the Dutch variant peptide into Alzheimer's fibrils. Amyloid. 1998;5(1):16-23.

74. Hawkes CA, Gatherer M, Sharp MM, Dorr A, Yuen HM, Kalaria R, et al. Regional differences in the morphological and functional effects of aging on cerebral basement membranes and perivascular drainage of amyloid-beta from the mouse brain. Aging Cell. 2013;12(2):224-36.

75. Christov A, Ottman J, Hamdheydari L, Grammas P. Structural changes in Alzheimer's disease brain microvessels. Curr Alzheimer Res. 2008;5(4):392-5.

76. Peck JA, Stopa EG. Agrin and microvascular damage in Alzheimer's disease. Med Health R I. 2002;85(7):202-6.

77. Shimizu H, Ghazizadeh M, Sato S, Oguro T, Kawanami O. Interaction between beta-amyloid protein and heparan sulfate proteoglycans from the cerebral capillary basement membrane in Alzheimer's disease. J Clin Neurosci. 2009;16(2):277-82.

78. Winkler EA, Bell RD, Zlokovic BV. Central nervous system pericytes in health and disease. Nat Neurosci. 2011;14(11):1398-405.

79. Armulik A, Genove G, Mae M, Nisancioglu MH, Wallgard E, Niaudet C, et al. Pericytes regulate the blood-brain barrier. Nature. 2010;468(7323):557-61.

80. Zhao Z, Nelson AR, Betsholtz C, Zlokovic BV. Establishment and Dysfunction of the Blood-Brain Barrier. Cell. 2015;163(5):1064-78.

81. Ding R, Hase Y, Ameen-Ali KE, Ndung'u M, Stevenson W, Barsby J, et al. Loss of capillary pericytes and the blood-brain barrier in white matter in poststroke and vascular dementias and Alzheimer's disease. Brain Pathol. 2020.

82. Zlokovic BV. The blood-brain barrier in health and chronic neurodegenerative disorders. Neuron. 2008;57(2):178-201.

83. Sofroniew MV. Molecular dissection of reactive astrogliosis and glial scar formation. Trends Neurosci. 2009;32(12):638-47.

84. Okada S, Nakamura M, Katoh H, Miyao T, Shimazaki T, Ishii K, et al. Conditional ablation of Stat3 or Socs3 discloses a dual role for reactive astrocytes after spinal cord injury. Nat Med. 2006;12(7):829-34.

85. Bush TG, Puvanachandra N, Horner CH, Polito A, Ostenfeld T, Svendsen CN, et al. Leukocyte infiltration, neuronal degeneration, and neurite outgrowth after ablation of scar-forming, reactive astrocytes in adult transgenic mice. Neuron. 1999;23(2):297-308.

86. Faulkner JR, Herrmann JE, Woo MJ, Tansey KE, Doan NB, Sofroniew MV. Reactive astrocytes protect tissue and preserve function after spinal cord injury. J Neurosci. 2004;24(9):2143-55.

87. McGraw J, Hiebert GW, Steeves JD. Modulating astrogliosis after neurotrauma. J Neurosci Res. 2001;63(2):109-15.

88. Alvarez JI, Dodelet-Devillers A, Kebir H, Ifergan I, Fabre PJ, Terouz S, et al. The Hedgehog pathway promotes blood-brain barrier integrity and CNS immune quiescence. Science. 2011;334(6063):1727-31.

89. Wosik K, Cayrol R, Dodelet-Devillers A, Berthelet F, Bernard M, Moumdjian R, et al. Angiotensin II controls occludin function and is required for blood brain barrier maintenance: relevance to multiple sclerosis. J Neurosci. 2007;27(34):9032-42.

90. Bell RD, Winkler EA, Singh I, Sagare AP, Deane R, Wu Z, et al. Apolipoprotein E controls cerebrovascular integrity via cyclophilin A. Nature. 2012;485(7399):512-6.

91. Orre M, Kamphuis W, Osborn LM, Melief J, Kooijman L, Huitinga I, et al. Acute isolation and transcriptome characterization of cortical astrocytes and microglia from young and aged mice. Neurobiol Aging. 2014;35(1):1-14.

92. Simpson JE, Ince PG, Haynes LJ, Theaker R, Gelsthorpe C, Baxter L, et al. Population variation in oxidative stress and astrocyte DNA damage in relation to Alzheimer-type pathology in the ageing brain. Neuropathol Appl Neurobiol. 2010;36(1):25-40.

93. Price BR, Norris CM, Sompol P, Wilcock DM. An emerging role of astrocytes in vascular contributions to cognitive impairment and dementia. J Neurochem. 2018;144(5):644-50.

94. Neely JD, Amiry-Moghaddam M, Ottersen OP, Froehner SC, Agre P, Adams ME. Syntrophin-dependent expression and localization of Aquaporin-4 water channel protein. Proceedings of the National Academy of Sciences of the United States of America. 2001;98(24):14108-13.

95. Waite A, Tinsley CL, Locke M, Blake DJ. The neurobiology of the dystrophin-associated glycoprotein complex. Annals of Medicine. 2009;41(5):344-59.

96. Monaco AP, Neve RL, Colletti-Feener C, Bertelson CJ, Kurnit DM, Kunkel LM. Isolation of candidate cDNAs for portions of the Duchenne muscular dystrophy gene. Nature. 1986;323(6089):646-50.

97. Cotton SM, Voudouris NJ, Greenwood KM. Association between intellectual functioning and age in children and young adults with Duchenne muscular dystrophy: further results from a meta-analysis. Dev Med Child Neurol. 2005;47(4):257-65.

98. Bushby KM, Appleton R, Anderson LV, Welch JL, Kelly P, Gardner-Medwin D. Deletion status and intellectual impairment in Duchenne muscular dystrophy. Dev Med Child Neurol. 1995;37(3):260-9.

99. Taylor PJ, Betts GA, Maroulis S, Gilissen C, Pedersen RL, Mowat DR, et al. Dystrophin gene mutation location and the risk of cognitive impairment in Duchenne muscular dystrophy. PLoS One. 2010;5(1):e8803.

100. Flanigan KM. Duchenne and Becker muscular dystrophies. Neurol Clin. 2014;32(3):671-88, viii.

101. Nico B, Tamma R, Annese T, Mangieri D, De Luca A, Corsi P, et al. Glial dystrophin-associated proteins, laminin and agrin, are downregulated in the brain of mdx mouse. Lab Invest. 2010;90(11):1645-60.

102. Nielsen S, Arnulf Nagelhus E, Amiry-Moghaddam M, Bourque C, Agre P, Petter Ottersen O. Specialized Membrane Domains for Water Transport in Glial Cells: High-Resolution Immunogold Cytochemistry of Aquaporin-4 in Rat Brain. The Journal of Neuroscience. 1997;17(1):171.

103. Amiry-Moghaddam M, Xue R, Haug FM, Neely JD, Bhardwaj A, Agre P, et al. Alpha-syntrophin deletion removes the perivascular but not endothelial pool of aquaporin-4 at the blood-brain barrier and delays the development of brain edema in an experimental model of acute hyponatremia. FASEB J. 2004;18(3):542-4.

104. Warth A, Simon P, Capper D, Goeppert B, Tabatabai G, Herzog H, et al. Expression pattern of the water channel aquaporin-4 in human gliomas is

associated with blood-brain barrier disturbance but not with patient survival. J Neurosci Res. 2007;85(6):1336-46.

105. Saadoun S, Papadopoulos MC, Davies DC, Krishna S, Bell BA. Aquaporin-4 expression is increased in oedematous human brain tumours. J Neurol Neurosurg Psychiatry. 2002;72(2):262-5.

106. Ribeiro Mde C, Hirt L, Bogousslavsky J, Regli L, Badaut J. Time course of aquaporin expression after transient focal cerebral ischemia in mice. J Neurosci Res. 2006;83(7):1231-40.

107. Hirt L, Ternon B, Price M, Mastour N, Brunet JF, Badaut J. Protective role of early aquaporin 4 induction against postischemic edema formation. J Cereb Blood Flow Metab. 2009;29(2):423-33.

108. Sun MC, Honey CR, Berk C, Wong NL, Tsui JK. Regulation of aquaporin-4 in a traumatic brain injury model in rats. J Neurosurg. 2003;98(3):565-9.

109. Wilcock DM, Vitek MP, Colton CA. Vascular amyloid alters astrocytic water and potassium channels in mouse models and humans with Alzheimer's disease. Neuroscience. 2009;159(3):1055-69.

110. Moftakhar P, Lynch MD, Pomakian JL, Vinters HV. Aquaporin expression in the brains of patients with or without cerebral amyloid angiopathy. J Neuropathol Exp Neurol. 2010;69(12):1201-9.

111. Yang J, Lunde LK, Nuntagij P, Oguchi T, Camassa LM, Nilsson LN, et al. Loss of astrocyte polarization in the tg-ArcSwe mouse model of Alzheimer's disease. J Alzheimers Dis. 2011;27(4):711-22.

112. Hoshi A, Yamamoto T, Shimizu K, Ugawa Y, Nishizawa M, Takahashi H, et al. Characteristics of Aquaporin Expression Surrounding Senile Plaques and Cerebral Amyloid Angiopathy in Alzheimer Disease. Journal of Neuropathology & Experimental Neurology. 2012;71(8):750-9.

113. Zago W, Schroeter S, Guido T, Khan K, Seubert P, Yednock T, et al. Vascular alterations in PDAPP mice after anti-Abeta immunotherapy: Implications for amyloid-related imaging abnormalities. Alzheimers Dement. 2013;9(5 Suppl):S105-15.

114. Hoshi A, Tsunoda A, Yamamoto T, Tada M, Kakita A, Ugawa Y. Altered expression of glutamate transporter-1 and water channel protein aquaporin-4 in human temporal cortex with Alzheimer's disease. Neuropathol Appl Neurobiol. 2018.

115. Owasil R, O'Neill R, Keable A, Nimmo J, MacGregor Sharp M, Kelly L, et al. The Pattern of AQP4 Expression in the Ageing Human Brain and in Cerebral Amyloid Angiopathy. Int J Mol Sci. 2020;21(4).

116. Stokum JA, Mehta RI, Ivanova S, Yu E, Gerzanich V, Simard JM. Heterogeneity of aquaporin-4 localization and expression after focal cerebral ischemia underlies differences in white versus grey matter swelling. Acta Neuropathol Commun. 2015;3:61.

117. Badaut J, Fukuda AM, Jullienne A, Petry KG. Aquaporin and brain diseases. Biochim Biophys Acta. 2014;1840(5):1554-65.

118. Iliff JJ, Wang M, Liao Y, Plogg BA, Peng W, Gundersen GA, et al. A paravascular pathway facilitates CSF flow through the brain parenchyma and the clearance of interstitial solutes, including amyloid beta. Science translational medicine. 2012;4(147):147ra11.

119. Walz T, Fujiyoshi Y, Engel A. The AQP structure and functional implications. Handb Exp Pharmacol. 2009(190):31-56.

120. Papadopoulos MC, Verkman AS. Aquaporin water channels in the nervous system. Nat Rev Neurosci. 2013;14(4):265-77.

121. Ho JD, Yeh R, Sandstrom A, Chorny I, Harries WEC, Robbins RA, et al. Crystal structure of human aquaporin 4 at 1.8 Å and its mechanism of conductance. Proceedings of the National Academy of Sciences. 2009;106(18):7437-42.

122. Sui H, Han BG, Lee JK, Walian P, Jap BK. Structural basis of water-specific transport through the AQP1 water channel. Nature. 2001;414(6866):872-8.

123. Potokar M, Jorgacevski J, Zorec R. Astrocyte Aquaporin Dynamics in Health and Disease. Int J Mol Sci. 2016;17(7).

124. Lu M, Lee MD, Smith BL, Jung JS, Agre P, Verdijk MA, et al. The human AQP4 gene: definition of the locus encoding two water channel polypeptides in brain. Proceedings of the National Academy of Sciences of the United States of America. 1996;93(20):10908-12.

125. Rash JE, Yasumura T, Hudson CS, Agre P, Nielsen S. Direct immunogold labeling of aquaporin-4 in square arrays of astrocyte and ependymocyte plasma membranes in rat brain and spinal cord. Proc Natl Acad Sci U S A. 1998;95(20):11981-6.

126. Landis DMD, Reese TS. ARRAYS OF PARTICLES IN FREEZE-FRACTURED ASTROCYTIC MEMBRANES. The Journal of Cell Biology. 1974;60(1):316-20.

127. Gonen T, Walz T. The structure of aquaporins. Q Rev Biophys. 2006;39(4):361-96.

128. Rossi A, Moritz TJ, Ratelade J, Verkman AS. Super-resolution imaging of aquaporin-4 orthogonal arrays of particles in cell membranes. Journal of Cell Science. 2012;125(18):4405-12.

129. Verbavatz JM, Ma T, Gobin R, Verkman AS. Absence of orthogonal arrays in kidney, brain and muscle from transgenic knockout mice lacking water channel aquaporin-4. J Cell Sci. 1997;110 (Pt 22):2855-60.

130. Amiry-Moghaddam M, Frydenlund DS, Ottersen OP. Anchoring of aquaporin-4 in brain: molecular mechanisms and implications for the physiology and pathophysiology of water transport. Neuroscience. 2004;129(4):999-1010.

131. Loh NY, Nebenius-Oosthuizen D, Blake DJ, Smith AJ, Davies KE. Role of beta-dystrobrevin in nonmuscle dystrophin-associated protein complex-like complexes in kidney and liver. Mol Cell Biol. 2001;21(21):7442-8.

132. Wagner KR, Cohen JB, Huganir RL. The 87K postsynaptic membrane protein from Torpedo is a protein-tyrosine kinase substrate homologous to dystrophin. Neuron. 1993;10(3):511-22.

133. Carr C, Fischbach GD, Cohen JB. A novel 87,000-Mr protein associated with acetylcholine receptors in Torpedo electric organ and vertebrate skeletal muscle. J Cell Biol. 1989;109(4 Pt 1):1753-64.

134. Blake DJ, Nawrotzki R, Loh NY, Górecki DC, Davies KE. β-dystrobrevin, a member of the dystrophin-related protein family. Proceedings of the National Academy of Sciences. 1998;95(1):241-6.

135. Sadoulet-Puccio HM, Feener CA, Schaid DJ, Thibodeau SN, Michels VV, Kunkel LM. The genomic organization of human dystrobrevin. Neurogenetics. 1997;1(1):37-42.

136. Enigk RE, Maimone MM. Differential expression and developmental regulation of a novel alpha-dystrobrevin isoform in muscle. Gene. 1999;238(2):479-88.

137. Rees MLJ, Lien C-F, Górecki DC. Dystrobrevins in muscle and non-muscle tissues. Neuromuscular Disorders. 2007;17(2):123-34.

138. Loh NY, Ambrose HJ, Guay-Woodford LM, DasGupta S, Nawrotzki RA, Blake DJ, et al. Genomic organization and refined mapping of the mouse β-dystrobrevin gene. Mammalian Genome. 1998;9(11):857-62.

139. Peters MF, O'Brien KF, Sadoulet-Puccio HM, Kunkel LM, Adams ME, Froehner SC. beta-dystrobrevin, a new member of the dystrophin family. Identification, cloning, and protein associations. J Biol Chem. 1997;272(50):31561-9.

140. Blake DJ, Hawkes R, Benson MA, Beesley PW. Different dystrophin-like complexes are expressed in neurons and glia. J Cell Biol. 1999;147(3):645-58.

141. Blake DJ, Nawrotzki R, Loh NY, Gorecki DC, Davies KE. beta-dystrobrevin, a member of the dystrophin-related protein family. Proc Natl Acad Sci U S A. 1998;95(1):241-6.

142. Ambrose HJ, Blake DJ, Nawrotzki RA, Davies KE. Genomic organization of the mouse dystrobrevin gene: comparative analysis with the dystrophin gene. Genomics. 1997;39(3):359-69.

143. Blake DJ, Nawrotzki R, Peters MF, Froehner SC, Davies KE. Isoform diversity of dystrobrevin, the murine 87-kDa postsynaptic protein. J Biol Chem. 1996;271(13):7802-10.

144. Sadoulet-Puccio HM, Khurana TS, Cohen JB, Kunkel LM. Cloning and characterization of the human homologue of a dystrophin related phosphoprotein

found at the Torpedo electric organ post-synaptic membrane. Hum Mol Genet. 1996;5(4):489-96.

145. Lien CF, Hazai D, Yeung D, Tan J, Fuchtbauer EM, Jancsik V, et al. Expression of alpha-dystrobrevin in blood-tissue barriers: sub-cellular localisation and molecular characterisation in normal and dystrophic mice. Cell Tissue Res. 2007;327(1):67-82.

146. Lien CF, Mohanta SK, Frontczak-Baniewicz M, Swinny JD, Zablocka B, Gorecki DC. Absence of glial alpha-dystrobrevin causes abnormalities of the blood-brain barrier and progressive brain edema. J Biol Chem. 2012;287(49):41374-85.

147. Ueda H, Baba T, Terada N, Kato Y, Fujii Y, Takayama I, et al. Immunolocalization of dystrobrevin in the astrocytic endfeet and endothelial cells in the rat cerebellum. Neurosci Lett. 2000;283(2):121-4.

148. Attwell D, Laughlin SB. An energy budget for signaling in the grey matter of the brain. J Cereb Blood Flow Metab. 2001;21(10):1133-45.

149. Aspelund A, Antila S, Proulx ST, Karlsen TV, Karaman S, Detmar M, et al. A dural lymphatic vascular system that drains brain interstitial fluid and macromolecules. J Exp Med. 2015;212(7):991-9.

150. Louveau A, Smirnov I, Keyes TJ, Eccles JD, Rouhani SJ, Peske JD, et al. Structural and functional features of central nervous system lymphatic vessels. Nature. 2015;523(7560):337-41.

151. Hladky SB, Barrand MA. Mechanisms of fluid movement into, through and out of the brain: evaluation of the evidence. Fluids Barriers CNS. 2014;11(1):26.

152. Brinker T, Stopa E, Morrison J, Klinge P. A new look at cerebrospinal fluid circulation. Fluids Barriers CNS. 2014;11:10.

153. Weed LH. Studies on Cerebro-Spinal Fluid. No. IV : The dual Source of Cerebro-Spinal Fluid. J Med Res. 1914;31(1):93-118 11.

154. Weller RO, Kida S, Zhang ET. Pathways of fluid drainage from the brain--morphological aspects and immunological significance in rat and man. Brain Pathol. 1992;2(4):277-84.

155. Kida S, Pantazis A, Weller RO. CSF drains directly from the subarachnoid space into nasal lymphatics in the rat. Anatomy, histology and immunological significance. Neuropathol Appl Neurobiol. 1993;19(6):480-8.

156. Ma Q, Ries M, Decker Y, Müller A, Riner C, Bücker A, et al. Rapid lymphatic efflux limits cerebrospinal fluid flow to the brain. Acta Neuropathologica. 2018.

157. Rennels ML, Gregory TF, Blaumanis OR, Fujimoto K, Grady PA. Evidence for a 'paravascular' fluid circulation in the mammalian central nervous system, provided by the rapid distribution of tracer protein throughout the brain from the subarachnoid space. Brain Res. 1985;326(1):47-63.

158. Iliff JJ, Wang M, Zeppenfeld DM, Venkataraman A, Plog BA, Liao Y, et al. Cerebral arterial pulsation drives paravascular CSF-interstitial fluid exchange in the murine brain. J Neurosci. 2013;33(46):18190-9.

159. Xie L, Kang H, Xu Q, Chen MJ, Liao Y, Thiyagarajan M, et al. Sleep drives metabolite clearance from the adult brain. Science. 2013;342(6156):373-7.

160. Morris AW, Sharp MM, Albargothy NJ, Fernandes R, Hawkes CA, Verma A, et al. Vascular basement membranes as pathways for the passage of fluid into and out of the brain. Acta Neuropathol. 2016;131(5):725-36.

161. Dobson H, Sharp MM, Cumpsty R, Criswell TP, Wellman T, Finucane C, et al. The perivascular pathways for influx of cerebrospinal fluid are most efficient in the midbrain. Clin Sci (Lond). 2017;131(22):2745-52.

162. Mestre H, Kostrikov S, Mehta RI, Nedergaard M. Perivascular spaces, glymphatic dysfunction, and small vessel disease. Clin Sci (Lond). 2017;131(17):2257-74.

163. Plog BA, Nedergaard M. The Glymphatic System in Central Nervous System Health and Disease: Past, Present, and Future. Annu Rev Pathol. 2017.

164. Abbott NJ. Evidence for bulk flow of brain interstitial fluid: significance for physiology and pathology. Neurochemistry International. 2004;45(4):545-52.

165. Bakker EN, Bacskai BJ, Arbel-Ornath M, Aldea R, Bedussi B, Morris AW, et al. Lymphatic Clearance of the Brain: Perivascular, Paravascular and Significance for Neurodegenerative Diseases. Cell Mol Neurobiol. 2016.

166. Smith AJ, Yao X, Dix JA, Jin BJ, Verkman AS. Test of the 'glymphatic' hypothesis demonstrates diffusive and aquaporin-4-independent solute transport in rodent brain parenchyma. Elife. 2017;6.

167. Cserr HF, Ostrach LH. Bulk flow of interstitial fluid after intracranial injection of Blue Dextran 2000. Experimental Neurology. 1974;45(1):50-60.

168. Carare RO, Bernardes-Silva M, Newman TA, Page AM, Nicoll JA, Perry VH, et al. Solutes, but not cells, drain from the brain parenchyma along basement membranes of capillaries and arteries: significance for cerebral amyloid angiopathy and neuroimmunology. Neuropathol Appl Neurobiol. 2008;34(2):131-44.

169. Carare RO, Aldea R, Agarwal N, Bacskai BJ, Bechman I, Boche D, et al. Clearance of interstitial fluid (ISF) and CSF (CLIC) group-part of Vascular Professional Interest Area (PIA): Cerebrovascular disease and the failure of elimination of Amyloid-beta from the brain and retina with age and Alzheimer's disease-Opportunities for Therapy. Alzheimers Dement (Amst). 2020;12(1):e12053.

170. Hawkes CA, Hartig W, Kacza J, Schliebs R, Weller RO, Nicoll JA, et al. Perivascular drainage of solutes is impaired in the ageing mouse brain and in the presence of cerebral amyloid angiopathy. Acta Neuropathol. 2011;121(4):431-43.

171. Sudduth TL, Powell DK, Smith CD, Greenstein A, Wilcock DM. Induction of hyperhomocysteinemia models vascular dementia by induction of cerebral microhemorrhages and neuroinflammation. J Cereb Blood Flow Metab. 2013;33(5):708-15.

172. Schreiber S, Bueche CZ, Garz C, Kropf S, Angenstein F, Goldschmidt J, et al. The pathologic cascade of cerebrovascular lesions in SHRSP: is erythrocyte accumulation an early phase? J Cereb Blood Flow Metab. 2012;32(2):278-90.

173. Held F, Morris AWJ, Pirici D, Niklass S, Sharp MMG, Garz C, et al. Vascular basement membrane alterations and beta-amyloid accumulations in an animal model of cerebral small vessel disease. Clin Sci (Lond). 2017;131(10):1001-13.

174. Bueche CZ, Hawkes C, Garz C, Vielhaber S, Attems J, Knight RT, et al. Hypertension drives parenchymal beta-amyloid accumulation in the brain parenchyma. Ann Clin Transl Neurol. 2014;1(2):124-9.

175. Hawkes CA, Gentleman SM, Nicoll JA, Carare RO. Prenatal high-fat diet alters the cerebrovasculature and clearance of beta-amyloid in adult offspring. J Pathol. 2014.

176. Arbel-Ornath M, Hudry E, Eikermann-Haerter K, Hou S, Gregory JL, Zhao L, et al. Interstitial fluid drainage is impaired in ischemic stroke and Alzheimer's disease mouse models. Acta Neuropathol. 2013.

177. Weller RO, Djuanda E, Yow HY, Carare RO. Lymphatic drainage of the brain and the pathophysiology of neurological disease. Acta Neuropathol. 2009;117(1):1-14.

178. Diem AK, MacGregor Sharp M, Gatherer M, Bressloff NW, Carare RO, Richardson G. Arterial Pulsations cannot Drive Intramural Periarterial Drainage: Significance for Abeta Drainage. Front Neurosci. 2017;11:475.

179. Aldea R, Weller RO, Wilcock DM, Carare RO, Richardson G. Cerebrovascular Smooth Muscle Cells as the Drivers of Intramural Periarterial Drainage of the Brain. Front Aging Neurosci. 2019;11:1.

180. van Veluw SJ, Hou SS, Calvo-Rodriguez M, Arbel-Ornath M, Snyder AC, Frosch MP, et al. Vasomotion as a Driving Force for Paravascular Clearance in the Awake Mouse Brain. Neuron. 2020;105(3):549-61 e5.

181. Zhang J, Li Y, Chen ZG, Dang H, Ding JH, Fan Y, et al. Glia protein aquaporin-4 regulates aversive motivation of spatial memory in Morris water maze. CNS neuroscience & therapeutics. 2013;19(12):937-44.

182. Fan Y, Liu M, Wu X, Wang F, Ding J, Chen J, et al. Aquaporin-4 promotes memory consolidation in Morris water maze. Brain Struct Funct. 2013;218(1):39-50.

183. Ding JH, Sha LL, Chang J, Zhou XQ, Fan Y, Hu G. Alterations of striatal neurotransmitter release in aquaporin-4 deficient mice: An in vivo microdialysis study. Neurosci Lett. 2007;422(3):175-80.

184. Fan Y, Zhang J, Sun X-L, Gao L, Zeng X-N, Ding J-H, et al. Sex- and region-specific alterations of basal amino acid and monoamine metabolism in the brain of aquaporin-4 knockout mice. Journal of Neuroscience Research. 2005;82(4):458-64.

185. Aoki-Yoshino K, Uchihara T, Duyckaerts C, Nakamura A, Hauw JJ, Wakayama Y. Enhanced expression of aquaporin 4 in human brain with inflammatory diseases. Acta Neuropathol. 2005;110(3):281-8.

186. Sinclair C, Kirk J, Herron B, Fitzgerald U, McQuaid S. Absence of aquaporin-4 expression in lesions of neuromyelitis optica but increased expression in multiple sclerosis lesions and normal-appearing white matter. Acta Neuropathol. 2007;113(2):187-94.

187. Ikeshima-Kataoka H, Abe Y, Abe T, Yasui M. Immunological function of aquaporin-4 in stab-wounded mouse brain in concert with a pro-inflammatory cytokine inducer, osteopontin. Mol Cell Neurosci. 2013;56:65-75.

188. Papadopoulos MC, Verkman AS. Aquaporin-4 gene disruption in mice reduces brain swelling and mortality in pneumococcal meningitis. J Biol Chem. 2005;280(14):13906-12.

189. Fan Y, Kong H, Shi X, Sun X, Ding J, Wu J, et al. Hypersensitivity of aquaporin 4-deficient mice to 1-methyl-4-phenyl-1,2,3,6-tetrahydropyrindine and astrocytic modulation. Neurobiol Aging. 2008;29(8):1226-36.

190. Gakuba C, Gaberel T, Goursaud S, Bourges J, Di Palma C, Quenault A, et al. General Anesthesia Inhibits the Activity of the "Glymphatic System". Theranostics. 2018;8(3):710-22.

191. Manley GT, Fujimura M, Ma T, Noshita N, Filiz F, Bollen AW, et al. Aquaporin-4 deletion in mice reduces brain edema after acute water intoxication and ischemic stroke. Nat Med. 2000;6(2):159-63.

192. Papadopoulos MC, Verkman AS. Aquaporin-4 and brain edema. Pediatr Nephrol. 2007;22(6):778-84.

193. Papadopoulos MC, Binder DK, Verkman AS. Enhanced macromolecular diffusion in brain extracellular space in mouse models of vasogenic edema measured by cortical surface photobleaching. FASEB J. 2005;19(3):425-7.

194. Bloch O, Auguste KI, Manley GT, Verkman AS. Accelerated progression of kaolin-induced hydrocephalus in aquaporin-4-deficient mice. J Cereb Blood Flow Metab. 2006;26(12):1527-37.

195. Feng X, Papadopoulos MC, Liu J, Li L, Zhang D, Zhang H, et al. Sporadic Obstructive Hydrocephalus in Aqp4 Null Mice. Journal of neuroscience research. 2009;87(5):1150-5.

196. Hsu MS, Seldin M, Lee DJ, Seifert G, Steinhauser C, Binder DK. Laminar-specific and developmental expression of aquaporin-4 in the mouse hippocampus. Neuroscience. 2011;178:21-32.

197. Wen H, Nagelhus EA, Amiry-Moghaddam M, Agre P, Ottersen OP, Nielsen S. Ontogeny of water transport in rat brain: postnatal expression of the aquaporin-4 water channel. Eur J Neurosci. 1999;11(3):935-45.

198. Badaut J, Nehlig A, Verbavatz J, Stoeckel M, Freund-Mercier MJ, Lasbennes F. Hypervascularization in the magnocellular nuclei of the rat hypothalamus: relationship with the distribution of aquaporin-4 and markers of energy metabolism. J Neuroendocrinol. 2000;12(10):960-9.

199. Binder DK, Nagelhus EA, Ottersen OP. Aquaporin-4 and epilepsy. Glia. 2012;60(8):1203-14.

200. Pérez E, Barrachina M, Rodríguez A, Torrejón-Escribano B, Boada M, Hernández I, et al. Aquaporin expression in the cerebral cortex is increased at early stages of Alzheimer disease. Brain Research. 2007;1128:164-74.

201. Rodriguez A, Perez-Gracia E, Espinosa JC, Pumarola M, Torres JM, Ferrer I. Increased expression of water channel aquaporin 1 and aquaporin 4 in Creutzfeldt-Jakob disease and in bovine spongiform encephalopathy-infected bovine-PrP transgenic mice. Acta Neuropathol. 2006;112(5):573-85.

202. Papadopoulos MC, Manley GT, Krishna S, Verkman AS. Aquaporin-4 facilitates reabsorption of excess fluid in vasogenic brain edema. FASEB J. 2004;18(11):1291-3.

203. Haj-Yasein NN, Vindedal GF, Eilert-Olsen M, Gundersen GA, Skare Ø, Laake P, et al. Glial-conditional deletion of aquaporin-4 (Aqp4) reduces blood–brain water

uptake and confers barrier function on perivascular astrocyte endfeet. Proceedings of the National Academy of Sciences of the United States of America. 2011;108(43):17815-20.

204. Yao X, Hrabětová S, Nicholson C, Manley GT. Aquaporin-4 Deficient Mice have Increased Extracellular Space Without Tortuosity Change. The Journal of neuroscience : the official journal of the Society for Neuroscience. 2008;28(21):5460-4.

205. Kimelberg HK. Current concepts of brain edema. Review of laboratory investigations. J Neurosurg. 1995;83(6):1051-9.

206. Pirici I, Balsanu TA, Bogdan C, Margaritescu C, Divan T, Vitalie V, et al. Inhibition of Aquaporin-4 Improves the Outcome of Ischaemic Stroke and Modulates Brain Paravascular Drainage Pathways. Int J Mol Sci. 2017;19(1).

207. Klatzo I. Evolution of brain edema concepts. Acta Neurochir Suppl (Wien). 1994;60:3-6.

208. Weller RO, Hawkes CA, Kalaria RN, Werring DJ, Carare RO. White matter changes in dementia: role of impaired drainage of interstitial fluid. Brain Pathol. 2015;25(1):63-78.

209. Fenske A, Samii M, Reulen HJ, Hey O. Extracellular space and electrolyte distribution in cortex and white matter of dog brain in cold induced oedema. Acta Neurochir (Wien). 1973;28(1):81-94.

210. Aarabi B, Long DM. Dynamics of cerebral edema. The role of an intact vascular bed in the production and propagation of vasogenic brain edema. J Neurosurg. 1979;51(6):779-84.

211. Wardlaw JM, Valdes Hernandez MC, Munoz-Maniega S. What are White Matter Hyperintensities Made of? Relevance to Vascular Cognitive Impairment. J Am Heart Assoc. 2015;4(6).

212. Grinberg LT, Thal DR. Vascular pathology in the aged human brain. Acta Neuropathol. 2010;119(3):277-90.

213. McAleese KE, Walker L, Graham S, Moya ELJ, Johnson M, Erskine D, et al. Parietal white matter lesions in Alzheimer's disease are associated with cortical neurodegenerative pathology, but not with small vessel disease. Acta Neuropathol. 2017;134(3):459-73.

214. Wardlaw JM, Valdes Hernandez MC, Munoz-Maniega S. What are white matter hyperintensities made of? Relevance to vascular cognitive impairment. J Am Heart Assoc. 2015;4(6):001140.

215. Charidimou A, Meegahage R, Fox Z, Peeters A, Vandermeeren Y, Laloux P, et al. Enlarged perivascular spaces as a marker of underlying arteriopathy in intracerebral haemorrhage: a multicentre MRI cohort study. J Neurol Neurosurg Psychiatry. 2013;84(6):624-9.

216. Banerjee G, Kim HJ, Fox Z, Jager HR, Wilson D, Charidimou A, et al. MRI-visible perivascular space location is associated with Alzheimer's disease independently of amyloid burden. Brain. 2017;140(4):1107-16.

217. MacGregor Sharp M, Bulters D, Brandner S, Holton J, Verma A, Werring DJ, et al. The fine anatomy of the perivascular compartment in the human brain: relevance to dilated perivascular spaces in cerebral amyloid angiopathy. Neuropathol Appl Neurobiol. 2018.

218. Criswell TP, Sharp MM, Dobson H, Finucane C, Weller RO, Verma A, et al. The structure of the perivascular compartment in the old canine brain: a case study. Clin Sci (Lond). 2017;131(22):2737-44.

219. Gooch J, Wilcock DM. Animal Models of Vascular Cognitive Impairment and Dementia (VCID). Cell Mol Neurobiol. 2016;36(2):233-9.

220. Wilcock DM. Chapter 43 - Animal Models of Vascular Cognitive Impairment and Dementia. In: Ram JL, Conn PM, editors. Conn's Handbook of Models for Human Aging (Second Edition): Academic Press; 2018. p. 577-85.

221. Kaiser D, Weise G, Moller K, Scheibe J, Posel C, Baasch S, et al. Spontaneous white matter damage, cognitive decline and neuroinflammation in middle-aged hypertensive rats: an animal model of early-stage cerebral small vessel disease. Acta Neuropathol Commun. 2014;2:169.

222. Jandke S, Garz C, Schwanke D, Sendtner M, Heinze HJ, Carare RO, et al. The association between hypertensive arteriopathy and cerebral amyloid angiopathy in spontaneously hypertensive stroke-prone rats. Brain Pathol. 2018;28(6):844-59.

223. Price BR, Wilcock DM, Weekman EM. Hyperhomocysteinemia as a Risk Factor for Vascular Contributions to Cognitive Impairment and Dementia. Front Aging Neurosci. 2018;10:350.

224. Baumbach GL, Sigmund CD, Bottiglieri T, Lentz SR. Structure of cerebral arterioles in cystathionine beta-synthase-deficient mice. Circ Res. 2002;91(10):931-7.

225. Weiss N, Heydrick SJ, Postea O, Keller C, Keaney JF, Jr., Loscalzo J. Influence of hyperhomocysteinemia on the cellular redox state--impact on homocysteine-induced endothelial dysfunction. Clin Chem Lab Med. 2003;41(11):1455-61.

226. Kamath AF, Chauhan AK, Kisucka J, Dole VS, Loscalzo J, Handy DE, et al. Elevated levels of homocysteine compromise blood-brain barrier integrity in mice. Blood. 2006;107(2):591-3.

227. Li JG, Pratico D. High levels of homocysteine results in cerebral amyloid angiopathy in mice. J Alzheimers Dis. 2015;43(1):29-35.

228. Kumar-Singh S, Pirici D, McGowan E, Serneels S, Ceuterick C, Hardy J, et al. Dense-core plaques in Tg2576 and PSAPP mouse models of Alzheimer's disease are centered on vessel walls. Am J Pathol. 2005;167(2):527-43.

229. Winkler DT, Bondolfi L, Herzig MC, Jann L, Calhoun ME, Wiederhold KH, et al. Spontaneous hemorrhagic stroke in a mouse model of cerebral amyloid angiopathy. J Neurosci. 2001;21(5):1619-27.

230. Ellis RJ, Olichney JM, Thal LJ, Mirra SS, Morris JC, Beekly D, et al. Cerebral amyloid angiopathy in the brains of patients with Alzheimer's disease: the CERAD experience, Part XV. Neurology. 1996;46(6):1592-6.

231. Nico B, Paola Nicchia G, Frigeri A, Corsi P, Mangieri D, Ribatti D, et al. Altered blood-brain barrier development in dystrophic MDX mice. Neuroscience. 2004;125(4):921-35.

232. Bagdatlioglu E, Porcari P, Greally E, Blamire AM, Straub VW. Cognitive impairment appears progressive in the mdx mouse. Neuromuscul Disord. 2020;30(5):368-88.

233. Chen A, Akinyemi RO, Hase Y, Firbank MJ, Ndung'u MN, Foster V, et al. Frontal white matter hyperintensities, clasmatodendrosis and gliovascular abnormalities in ageing and post-stroke dementia. Brain. 2016;139(Pt 1):242-58.

234. Steiner E, Enzmann GU, Lin S, Ghavampour S, Hannocks MJ, Zuber B, et al. Loss of astrocyte polarization upon transient focal brain ischemia as a possible mechanism to counteract early edema formation. Glia. 2012;60(11):1646-59.

235. Zhou J, Kong H, Hua X, Xiao M, Ding J, Hu G. Altered blood-brain barrier integrity in adult aquaporin-4 knockout mice. Neuroreport. 2008;19(1):1-5.

236. Djukic B, Casper KB, Philpot BD, Chin LS, McCarthy KD. Conditional knock-out of Kir4.1 leads to glial membrane depolarization, inhibition of potassium and glutamate uptake, and enhanced short-term synaptic potentiation. J Neurosci. 2007;27(42):11354-65.

237. Moore SA, Saito F, Chen J, Michele DE, Henry MD, Messing A, et al. Deletion of brain dystroglycan recapitulates aspects of congenital muscular dystrophy. Nature. 2002;418(6896):422-5.

238. Ikeshima-Kataoka H, Abe Y, Abe T, Yasui M. Immunological function of aquaporin-4 in stab-wounded mouse brain in concert with a pro-inflammatory cytokine inducer, osteopontin. Molecular and Cellular Neuroscience. 2013;56:65-75.

239. Grady RM, Grange RW, Lau KS, Maimone MM, Nichol MC, Stull JT, et al. Role for alpha-dystrobrevin in the pathogenesis of dystrophin-dependent muscular dystrophies. Nat Cell Biol. 1999;1(4):215-20.

240. Kurek-Gorecka AM, Sobczakb A, Rzepecka-Stojkod A, Gorecki MT, Wardas M, Pawlowska-Goral K. Antioxidant activity of ethanolic fractions of Polish propolis. Z Naturforsch C. 2012;67(11-12):545-50.

241. Truett GE, Heeger P, Mynatt RL, Truett AA, Walker JA, Warman ML. Preparation of PCR-quality mouse genomic DNA with hot sodium hydroxide and tris (HotSHOT). Biotechniques. 2000;29(1):52, 4.

242. Bohm SV, Constantinou P, Tan S, Jin H, Roberts RG. Profound human/mouse differences in alpha-dystrobrevin isoforms: a novel syntrophin-binding site and promoter missing in mouse and rat. BMC Biol. 2009;7:85.

243. Sharp MM, Page A, Morris A, Weller RO, Carare RO. Quantitative Assessment of Cerebral Basement Membranes Using Electron Microscopy. Methods in molecular biology (Clifton, NJ). 2017;1559:367-75.

244. MacGregor Sharp M, Criswell TP, Dobson H, Finucane C, Verma A, Carare RO. Solving an Old Dogma: Is it an Arteriole or a Venule? Front Aging Neurosci. 2019;11:289.

245. Albargothy NJ, Johnston DA, MacGregor-Sharp M, Weller RO, Verma A, Hawkes CA, et al. Convective influx/glymphatic system: tracers injected into the CSF enter and leave the brain along separate periarterial basement membrane pathways. Acta Neuropathol. 2018.

246. Rueden CT, Schindelin J, Hiner MC, DeZonia BE, Walter AE, Arena ET, et al. ImageJ2: ImageJ for the next generation of scientific image data. BMC Bioinformatics. 2017;18(1):529.

247. MacGregor Sharp M, Saito S, Keable A, Gatherer M, Aldea R, Agarwal N, et al. Demonstrating a reduced capacity for removal of fluid from cerebral white matter and hypoxia in areas of white matter hyperintensity associated with age and dementia. Acta Neuropathol Commun. 2020;8(1):131.

248. Albargothy NJ, Sharp MM, Gatherer M, Morris A, Weller RO, Hawkes C, et al. Investigating the Lymphatic Drainage of the Brain: Essential Skills and Tools. Methods in molecular biology (Clifton, NJ). 2017;1559:343-65.

249. Wolf RL, Detre JA. Clinical neuroimaging using arterial spin-labeled perfusion magnetic resonance imaging. Neurotherapeutics. 2007;4(3):346-59.

250. Petcharunpaisan S, Ramalho J, Castillo M. Arterial spin labeling in neuroimaging. World J Radiol. 2010;2(10):384-98.

251. Daneman R, Zhou L, Kebede AA, Barres BA. Pericytes are required for blood-brain barrier integrity during embryogenesis. Nature. 2010;468(7323):562-6.

252. Jin BJ, Smith AJ, Verkman AS. Spatial model of convective solute transport in brain extracellular space does not support a "glymphatic" mechanism. J Gen Physiol. 2016;148(6):489-501.

253. Smith AJ, Jin BJ, Verkman AS. Muddying the water in brain edema? Trends Neurosci. 2015;38(6):331-2.

254. Farkas E, De Jong GI, de Vos RA, Jansen Steur EN, Luiten PG. Pathological features of cerebral cortical capillaries are doubled in Alzheimer's disease and Parkinson's disease. Acta Neuropathol. 2000;100(4):395-402.

255. Dewing JM, Carare RO, Lotery AJ, Ratnayaka JA. The Diverse Roles of TIMP-3: Insights into Degenerative Diseases of the Senescent Retina and Brain. Cells. 2019;9(1).

256. Woessner JF, Jr. MMPs and TIMPs--an historical perspective. Mol Biotechnol. 2002;22(1):33-49.

257. Meighan SE, Meighan PC, Choudhury P, Davis CJ, Olson ML, Zornes PA, et al. Effects of extracellular matrix-degrading proteases matrix metalloproteinases 3 and 9 on spatial learning and synaptic plasticity. J Neurochem. 2006;96(5):1227-41.

258. Nagy V, Bozdagi O, Matynia A, Balcerzyk M, Okulski P, Dzwonek J, et al. Matrix metalloproteinase-9 is required for hippocampal late-phase long-term potentiation and memory. J Neurosci. 2006;26(7):1923-34.

259. Weekman EM, Wilcock DM. Matrix Metalloproteinase in Blood-Brain Barrier Breakdown in Dementia. J Alzheimers Dis. 2016;49(4):893-903.

260. Michaluk P, Kolodziej L, Mioduszewska B, Wilczynski GM, Dzwonek J, Jaworski J, et al. Beta-dystroglycan as a target for MMP-9, in response to enhanced neuronal activity. J Biol Chem. 2007;282(22):16036-41.

261. Sturchler-Pierrat C, Abramowski D, Duke M, Wiederhold KH, Mistl C, Rothacher S, et al. Two amyloid precursor protein transgenic mouse models with Alzheimer disease-like pathology. Proc Natl Acad Sci U S A. 1997;94(24):13287-92.

262. Brown WR, Moody DM, Thore CR, Challa VR, Anstrom JA. Vascular dementia in leukoaraiosis may be a consequence of capillary loss not only in the lesions, but in normal-appearing white matter and cortex as well. J Neurol Sci. 2007;257(1-2):62-6.

263. Hase Y, Ding R, Harrison G, Hawthorne E, King A, Gettings S, et al. White matter capillaries in vascular and neurodegenerative dementias. Acta Neuropathol Commun. 2019;7(1):16.

264. Mozumder M, Pozo JM, Coelho S, Costantini M, Simpson J, Highley JR, et al. Quantitative histomorphometry of capillary microstructure in deep white matter. Neuroimage Clin. 2019;23:101839.

265. Moody DM, Thore CR, Anstrom JA, Challa VR, Langefeld CD, Brown WR. Quantification of afferent vessels shows reduced brain vascular density in subjects with leukoaraiosis. Radiology. 2004;233(3):883-90.

266. Lee GD, Aruna JH, Barrett PM, Lei DL, Ingram DK, Mouton PR. Stereological analysis of microvascular parameters in a double transgenic model of Alzheimer's disease. Brain Res Bull. 2005;65(4):317-22.

267. Zhang Y, Chao FL, Zhang L, Jiang L, Zhou CN, Chen LM, et al. Quantitative study of the capillaries within the white matter of the Tg2576 mouse model of Alzheimer's disease. Brain Behav. 2019;9(4):e01268.

268. Christie R, Yamada M, Moskowitz M, Hyman B. Structural and functional disruption of vascular smooth muscle cells in a transgenic mouse model of amyloid angiopathy. Am J Pathol. 2001;158(3):1065-71.

269. Hsiao K, Chapman P, Nilsen S, Eckman C, Harigaya Y, Younkin S, et al. Correlative memory deficits, Abeta elevation, and amyloid plaques in transgenic mice. Science. 1996;274(5284):99-102.

270. Davis J, Xu F, Deane R, Romanov G, Previti ML, Zeigler K, et al. Early-onset and robust cerebral microvascular accumulation of amyloid beta-protein in transgenic

mice expressing low levels of a vasculotropic Dutch/Iowa mutant form of amyloid beta-protein precursor. J Biol Chem. 2004;279(19):20296-306.

271. Vinters HV, Gilbert JJ. Cerebral amyloid angiopathy: incidence and complications in the aging brain. II. The distribution of amyloid vascular changes. Stroke. 1983;14(6):924-8.

272. Enciu A-M, Constantinescu SN, Popescu LM, Mureşanu DF, Popescu BO. Neurobiology of Vascular Dementia. Journal of Aging Research. 2011;2011:401604.

273. Joris PJ, Mensink RP, Adam TC, Liu TT. Cerebral Blood Flow Measurements in Adults: A Review on the Effects of Dietary Factors and Exercise. Nutrients. 2018;10(5).

274. Iadecola C. The Neurovascular Unit Coming of Age: A Journey through Neurovascular Coupling in Health and Disease. Neuron. 2017;96(1):17-42.

275. Kisler K, Nelson AR, Rege SV, Ramanathan A, Wang Y, Ahuja A, et al. Pericyte degeneration leads to neurovascular uncoupling and limits oxygen supply to brain. Nat Neurosci. 2017;20(3):406-16.

276. Matsuda H, Maeda T, Yamada M, Gui LX, Tonami N, Hisada K. Age-matched normal values and topographic maps for regional cerebral blood flow measurements by Xe-133 inhalation. Stroke. 1984;15(2):336-42.

277. Buxton RB, Frank LR, Wong EC, Siewert B, Warach S, Edelman RR. A general kinetic model for quantitative perfusion imaging with arterial spin labeling. Magn Reson Med. 1998;40(3):383-96.

278. Amiri M, Pouliot P, Bonnery C, Leclerc PO, Desjardins M, Lesage F, et al. An Exploration of the Effect of Hemodynamic Changes Due to Normal Aging on the fNIRS Response to Semantic Processing of Words. Front Neurol. 2014;5:249.

279. Ambarki K, Wahlin A, Zarrinkoob L, Wirestam R, Petr J, Malm J, et al. Accuracy of Parenchymal Cerebral Blood Flow Measurements Using Pseudocontinuous Arterial Spin-Labeling in Healthy Volunteers. AJNR Am J Neuroradiol. 2015;36(10):1816-21.

280. Bangen KJ, Nation DA, Clark LR, Harmell AL, Wierenga CE, Dev SI, et al. Interactive effects of vascular risk burden and advanced age on cerebral blood flow. Front Aging Neurosci. 2014;6:159.

281. Attems J, Jellinger K, Thal DR, Van Nostrand W. Review: sporadic cerebral amyloid angiopathy. Neuropathol Appl Neurobiol. 2011;37(1):75-93.

282. Carare RO, Hawkes CA, Jeffrey M, Kalaria RN, Weller RO. Review: cerebral amyloid angiopathy, prion angiopathy, CADASIL and the spectrum of protein elimination failure angiopathies (PEFA) in neurodegenerative disease with a focus on therapy. Neuropathol Appl Neurobiol. 2013;39(6):593-611.

283. Keable A, Fenna K, Yuen HM, Johnston DA, Smyth NR, Smith C, et al. Deposition of amyloid beta in the walls of human leptomeningeal arteries in relation to perivascular drainage pathways in cerebral amyloid angiopathy. Biochim Biophys Acta. 2016;1862(5):1037-46.

284. de Bruijn RF, Ikram MA. Cardiovascular risk factors and future risk of Alzheimer's disease. BMC Med. 2014;12:130.

285. O'Brien JT, Thomas A. Vascular dementia. The Lancet. 2015;386(10004):1698-706.

286. Santos CY, Snyder PJ, Wu WC, Zhang M, Echeverria A, Alber J. Pathophysiologic relationship between Alzheimer's disease, cerebrovascular disease, and cardiovascular risk: A review and synthesis. Alzheimers Dement (Amst). 2017;7:69-87.

287. Ighodaro ET, Abner EL, Fardo DW, Lin AL, Katsumata Y, Schmitt FA, et al. Risk factors and global cognitive status related to brain arteriolosclerosis in elderly individuals. J Cereb Blood Flow Metab. 2017;37(1):201-16.

288. Mathiisen TM, Lehre KP, Danbolt NC, Ottersen OP. The perivascular astroglial sheath provides a complete covering of the brain microvessels: an electron microscopic 3D reconstruction. Glia. 2010;58(9):1094-103.

289. Zeppenfeld DM, Simon M, Haswell JD, D'Abreo D, Murchison C, Quinn JF, et al. Association of Perivascular Localization of Aquaporin-4 With Cognition and Alzheimer Disease in Aging Brains. JAMA Neurol. 2017;74(1):91-9.

290. Viji Babu PK, Radmacher M. Mechanics of Brain Tissues Studied by Atomic Force Microscopy: A Perspective. Front Neurosci. 2019;13:600.

291. Tiller-Borcich JK, Fike JR, Phillips TL, Davis RL. Pathology of delayed radiation brain damage: an experimental canine model. Radiat Res. 1987;110(2):161-72.

292. Weimer JM, Jones SE, Frontera JA. Acute Cytotoxic and Vasogenic Edema after Subarachnoid Hemorrhage: A Quantitative MRI Study. AJNR Am J Neuroradiol. 2017;38(5):928-34.

293. Weller RO, Wisniewski H, Shulman K, Terry RD. Experimental hydrocephalus in young dogs: histological and ultrastructural study of the brain tissue damage 142. J NeuropatholExpNeurol. 1971;30(4):613-26.

294. Weller RO, Wisniewski H. Histological and ultrastructural changes with experimental hydrocephalus in adult rabbits 151. Brain. 1969;92(4):819-28.

295. Heuer E, Jacobs J, Du R, Wang S, Keifer OP, Cintron AF, et al. Amyloid-Related Imaging Abnormalities in an Aged Squirrel Monkey with Cerebral Amyloid Angiopathy. J Alzheimers Dis. 2017;57(2):519-30.

296. Piazza F, Winblad B. Amyloid-Related Imaging Abnormalities (ARIA) in Immunotherapy Trials for Alzheimer's Disease: Need for Prognostic Biomarkers? J Alzheimers Dis. 2016;52(2):417-20.

297. Cole GM, Yang F. CAA in Transgenic Mouse Models of Alzheimer’s Disease. In: Verbeek MM, de Waal RMW, Vinters HV, editors. Cerebral Amyloid Angiopathy in Alzheimer’s Disease and Related Disorders. Dordrecht: Springer Netherlands; 2000. p. 295-311.

298. Jakel L, Van Nostrand WE, Nicoll JAR, Werring DJ, Verbeek MM. Animal models of cerebral amyloid angiopathy. Clin Sci (Lond). 2017;131(19):2469-88.

299. Sanchez-Mendoza EH, Carballo J, Longart M, Hermann DM, Doeppner TR. Implantation of Miniosmotic Pumps and Delivery of Tract Tracers to Study Brain Reorganization in Pathophysiological Conditions. J Vis Exp. 2016(107):e52932.

300. McRobbie D. W., Moore E. A. MRI From Picture to Proton 2nd, editor: Cambridge University Press; 2006

301. Herscovitch P, Raichle ME. What is the correct value for the brain--blood partition coefficient for water? J Cereb Blood Flow Metab. 1985;5(1):65-9.